Cryo-Electron Microscopy to Investigate Molecular Dynamics and Conformational Changes in Protein Complexes

DISSERTATION

Zur Erlangung des

DOKTORGRADES DER NATURWISSENSCHAFTEN (DR. RER. NAT.)

der Fakultät für Biologie und vorklinische Medizin

der Universität Regensburg

vorgelegt von

Veronika Heinz (geb. Wirth)

aus München

im Jahr 2022

Das Promotionsgesuch wurde eingereicht am:

Die Arbeit wurde angeleitet von:
Prof. Christine Ziegler

Unterschrift:

Dedicated to the best dad in the world.

We miss you!

"It is very easy to answer many of these fundamental biological questions;

you just look at the thing!"

(Richard P. Feynman, 1959)

This thesis is composed of the following publications, preprints and manuscripts:

Publication 1:

Heinz, V.*, Jäckel, W.*, Kaltwasser, S., Cutugno, L., Bedrunka, P., Graf, A., Reder, A., Michalik, S., Dhople, V. M., Madej, M. G., Conway, M., Lechner, M., Riedel, K., Bange, G., Boyd, A., Völker, U., Lewis, R. J., Marles-Wright, J., Ziegler, C. & Pané-Farré, J. (2022): The *Vibrio vulnificus* stressosome is an oxygen-sensor involved in regulating iron metabolism. *Commun. Biol.* 5, 622.

My contributions to the publication are data analysis, interpretation and writing, as explained in detail in III. 1 PUBLICATION 1. The publication is presented in chapter VIII. PUBLICATION 1.

Preprint 1:

Heinz, V*., Güler, G.*, Leone, V., Madej, M. G., Maksimov, S., Gärtner, R. M., Rudi, O., Hamdi, F., Kastritis, P. L., Mäntele, W., Krämer, R., Forrest, L. R., Perez, C. & Ziegler, C. (2022): Osmotic stress response in BetP: How lipids and K^+ team up to overcome downregulation. (Preprint available at *bioRxiv*).

My contributions to this study are sample preparation, data collection and analysis as well as writing the manuscript, as stated in III. 2 PREPRINT 1. The preprint can be found in chapter IX. PREPRINT 1.

Manuscript 1:

Heinz, V., Rachel, R. & Ziegler, C.: Application of STEM tomography to investigate smooth ER morphology under stress conditions. (Manuscript to be submitted to *J. Struct. Biol.*)

In this project, I am fully responsible for all steps of sample preparation, data collection and analysis as well as manuscript drafting, as explained in III. 3 Manuscript 1. The full manuscript can be found in chapter X. MANUSCRIPT 1.

Moreover, I am grateful for having the possibility to contribute to many other projects, some of which are also published and listed in VI. 1 OWN PUBLICATIONS.

Table of contents

List of abbreviations

2D	two-dimensional
3D	three-dimensional
AB	antibody, antibodies
AHT	Anhydrotetracyclin
APS	Ammonium persulfate
ATF6	activating transcription factor 6
BC	betweenness centrality
BCA	Bicinchoninic acid
BCIP	5-Brom-4-chlor-3-indoxylphosphat
BF	bright field
BiP	binding immunoglobulin protein
BSA	bovine serum albumin
CCD	charge-coupled device
CL	condensor lens
CLEM	correlative light and electron microscopy
CMOS	complementary metal-oxide semiconductor
cryo-EM	cryo-electron microscopy
C_S	spherical aberration
CV	column volume(s)
d	day(s)
DDM	*n*-dodecyl-β-D-maltoside
DDSA	Dodecenylsuccinic anhydride
DED	direct electron detector
DF	dark field
DIBMA	di-isobutylene-maleic acid
DLS	dynamic light scattering
DMF	Dimethylformamide

DMP 30	2,4,6-Tris(dimethylaminomethyl)phenol
DQE	detective quantum efficiency
DTT	Dithiothreitol
EDTA	Ethylenediaminetetraacetic acid
eIF2α	eukaryotic transcription factor 2 (α subunit)
EM	electron microscopy
ER	endoplasmic reticulum
ERAD	ER-associated degradation
ET	electron tomography
FBS	fetal bovine serum
FCS	fetal calf serum
FEG	field emission gun
FIB	focused ion beam
FOV	field of view
FS	freeze substitution
FSC	Fourier shell correlation
FTIR	Fourier transform infrared (spectroscopy)
g	gram(s)
GA	Glutar-di-aldehyde
h	hour(s)
H_2O_{bidest}	distilled water
H_2O_{milli}	Millipore-purified water
HEK	human embryonic kidney
HMG-CoA reductase	3-hydroxy-3-methylglutaryl coenzyme A reductase
HPF	high-pressure freezing
IRE1	inositol requiring 1
ISR	integrated stress response
kDa	kilo Dalton
keV	kilo electron Volts

LB_{Carb}	LB – Carbenicillin
lN_2	liquid nitrogen
mA	milli Ampere
MAM	mitochondria-associated membrane
MC	modularity class
MD	molecular dynamics
mDa	mega Dalton
min	minute(s)
mL	milli liter
MNA	Methyl nadic anhydride
msALDH	microsomal aldehyde dehydrogenase
msec	milli second(s)
MS	mass spectrometry
MSP(s)	membrane scaffold protein(s)
NBT	Nitro Blue Tetrazolium
nm	nanometers
OD_{600}	optical density (at λ = 600 nm)
ON	overnight
OSER	organized smooth ER
p. a.	pro analysi
PAGE	polyacrylamide gel electrophoresis
PbCi	lead citrate
PC-2	polycystin 2
PERK	PKR-like ER kinase
pL	pico liter
POPC	1-palmitoyl-2-oleoyl-*sn*-glycero-3-phophocholine
POPG	1-Palmitoyl-2-Oleoyl-*sn*-Glycero-3-[Phospho-rac-(1-glycerol)]
PVDF	polyvinyl-difluorid

rER	rough endoplasmic reticulum
ROI	region of interest
RT	room temperature
Salipro(s)	Saposin lipo-protein(s)
SDS	Sodium Dodecyl Sulphate
sec	second(s)
SEC	size exclusion chromatography
SEM	scanning electron microscopy
sER	smooth endoplasmic reticulum
SIRT	Simultaneous Iterative Reconstruction Technique
SMA	styrene-maleic acid
smFRET	single molecule fluorescence resonance energy transfer
SNR	signal to noise ratio
SOC	super optimal broth with catabolite repression
SPA	single particle analysis
SSNR	spectral signal to noise-ratio
STAS	Sulfate Transporter and Anti-Sigma factor antagonist
STEM	scanning-transmission electron microscopy
TBS	TRIS buffered saline
TEM	transmission electron microscopy
TEMED	Tetramethylethylenediamine
TM/TMs	transmenbrane helix / transmembrane helices
TRIS	Tris(hydroxymethyl)aminomethane
u	unit
UAc	uranyl acetate
UFo	uranyl formate
UPR	unfolded protein response
V	Volt(s)
v/v	volume per volume

w/v	weight per volume
WT	wild type
XBP1	X-box binding protein 1
λ	wavelength
µL	micro liter
σ^B	SigmaB (transcription factor)

Amino acid abbreviations

amino acid	one letter code	three letter code
Alanine	A	Ala
Cysteine	C	Cys
Aspartic acid	D	Asp
Glutamic acid	E	Glu
Phenylalanine	F	Phe
Glycine	G	Gly
Histidine	H	His
Isoleucine	I	Ile
Lysine	K	Lys
Leucine	L	Leu
Methionine	M	Met
Asparagine	N	Asn
Proline	P	Pro
Glutamine	Q	Gln
Arginine	R	Arg
Serine	S	Ser
Threonine	T	Thr
Valine	V	Val
Tryptophan	W	Trp
Tyrosine	Y	Tyr

List of figures

List of tables

Abstract

Stress can be considered as one of the most fundamental aspects in life, and all living organisms are constantly exposed to a variety of different stress situations. Thus, efficient stress sensing and reaction mechanisms are crucial for their survival. Stress response mechanisms are as diverse as the causative stimuli and oftentimes cross-linked forming a versatile reaction network, to ensure the cells' survival under critical situations. Notably, stress response mechanisms play a major role in pathogenicity, virulence and disease. Pathogenic Bacteria are permanently facing environmental pressure originating from the host's defense systems or drug treatments, while mutations in eukaryotic stress response systems have been shown to cause a large number of severe human diseases such as diabetes, cancer or Parkinson's and Alzheimer's disease. A profound molecular knowledge on the respective mechanisms is thus the inevitable prerequisite towards a global understanding of this fundamental aspect of life, paving the way for the development of new drugs or therapeutic approaches.

Within this thesis, various aspects of stress response mechanisms in three different systems were investigated using state-of-the-art electron microscopy techniques. First, I set out to solve the structure of the *Vibrio vulnificus* stressosome complex, a key player in the bacterial environmental stress response. Currently, there is no structural data available for any gram-negative stressosome. A medium-resolution cryo-electron microscopy (cryo-EM) structure of the minimal complex could be obtained, which features an exceptional symmetry break originating from its unique, regulatory stoichiometry. Based on the structural data, it was possible to propose an activation mechanism and to pinpoint a number of significant differences in comparison to gram-positive stressosome complexes. Undoubtedly, the structure contributes a major piece of information necessary to understand stress sensing and signal transduction in this human pathogen. This study was complemented by a number of physiological and phylogenetic experiments contributed by our co-workers, and published recently (VIII. PUBLICATION 1).

The second project focused on the gram-positive soil bacterium *Corynebacterium glutamicum*, a prime model organism for investigations of the bacterial osmostress response. Sensing of hyper-osmotic stress and regulation of the respective stress response in *C. glutamicum* are simultaneously performed by BetP, a conformationally asymmetric-

trimeric secondary active transporter able to import the compatible solute betaine. Two stimuli are identified to initiate the full osmostress response in BetP, namely an elevated cytoplasmic K^+ concentration and a loosely defined 'membrane stimulus'. Despite the availability of functional data on BetP regulation, structural information especially of the down-regulated state and the subsequent transition events are absent. Using single particle cryo-EM analysis, I was able to provide high-resolution structures of the down-regulated and a transition state, which elucidated a number of important structural features not described so far. It could be shown that down-regulated BetP adopts a symmetric arrangement stabilized by antight cytoplasmic interaction network of the sensory domain, further strengthened by Cardiolipin molecules located at regulatory lipid binding sites. These constraints are released upon stress sensing, as demonstrated by fourier transform infrared (FTIR) spectroscopy and molecular dynamics simulation (MD) data contributed by our co-workers, resulting in the well-established, asymmetric-trimeric structures previously known. The wealth of new data on the down-regulated state allowed to propose a detailed regulation mechanism and to further sharpen the previously vague picture of the membrane stimulus. The data are summarized and presented in IX. PREPRINT 1.

A third topic of this thesis was the three dimensional investigation *via* dual-axis scanning transmission electron microscopy (STEM) tomography of crystalloid-ER structures we identified before in human embryonic kidney (HEK) cells upon over-expression of polycystin-2 (PC-2). In this study presented in X. MANUSCRIPT 1, I was further able to proof the presence of ER whorls, and to obtain high-resolution three-dimensional (3D) reconstructions of the two different ER morphotypes. These data provided unmatched insights into the cellular ER interaction partners and clearly demonstrated the dynamic nature of the organelle even under stress situations. A detailed discussion of the identified morphological features in their respective cellular context finally allowed for the description of the organellar membrane architecture at a high level of detail.

Lastly, the discussion addresses the electron microscopy techniques and instruments used and contains an outlook on further perspectives for the projects. Overall, this thesis yielded intriguing mechanistic insights into the versatile bacterial and eukaryotic stress response mechanisms, reflecting their manifold nature ultimately converging to a common outcome.

Zusammenfassung

Stress stellt einen fundamentalen Bestandteil des Lebens an sich dar, und alle Lebewesen sind kontinuierlich den unterschiedlichsten Stress-Situationen ausgesetzt. Ein effizientes Erkennen von Stress und die jeweiligen Reaktionen darauf sind daher überlebensnotwendig. Die Stressantworten sind dabei so vielfältig wie die entsprechenden Stimuli und oftmals eng miteinander verflochten; so entsteht ein höchst wirksames Reaktionsnetzwerk, welches das Überleben von Organismen in kritischen Situationen sicherstellt. Insbesondere in Bezug auf Pathogenität, Virulenz und Krankheit spielen solche Mechanismen eine große Rolle. Beispielsweise werden pathogene Bakterien permanent von Abwehrmechanismen des Wirtsorganismus oder durch medikamentöse Behandlung unter Druck gesetzt. Zudem ist bekannt dass Mutationen in eukaryotischen Stressabwehr-Systemen schwere Krankheiten wie Diabetes, bestimmte Formen von Krebs, Alzheimer oder die Parkinson'sche Krankheit auslösen können. Ein molekulares Verständnis der zugrunde liegenden Mechanismen ist daher der notwendige erste Schritt auf dem Weg zur Entwicklung neuer Wirkstoffe oder therapeutischer Ansätze.

Im Rahmen dieser Arbeit wurden verschiedene Aspekte von Stressantwort-Mechanismen in drei Systemen mit Hilfe aktuellster elektronenmikroskopischer Techniken untersucht. Zuerst ist es gelungen, die Struktur des Stressosom-Komplexes aus *Vibrio vulnificus* aufzuklären, einem zentralen Komplex der bakteriellen Umweltstress-Antwort. Strukturelle Daten gram-negativer Stressosom-Komplexe waren bis zu diesem Zeitpunkt nicht verfügbar. Die erzielte kryo-EM Struktur mittlerer Auflösung des Minimal-Komplexes zeigt einen außergewöhnlichen Symmetrie-Bruch, welcher in der einzigartigen Stöchiometrie mit regulierender Funktion begründet ist. Basierend auf den strukturellen Daten konnten ein Aktivierungs-Mechanismus vorgeschlagen, sowie signifikante Unterschiede zu gram-positiven Stressosom-Komplexen aufgezeigt werden. Somit stellt die Struktur unzweifelhaft einen bedeutsamen Beitrag zum Verständnis der Stress-Wahrnehmung und Signalübersetzung in diesem humanpathogenen Bakterium dar. Die Studie konnte durch eine Reihe physiologischer und phylogenetischer Experimente unserer Mitautoren ergänzt und kürzlich veröffentlicht werden (VIII. PUBLICATION 1).

Das zweite Projekt beschäftigte sich mit dem gram-positiven Boden-Bakterium *Corynebacterium glutamicum*, einem Modellorganismus zur Untersuchung der bakteriellen

Osmostress-Antwort. In *C. glutamicum* werden sowohl die Wahrnehmung von hyperosmotischem Stress als auch die Regulation der entsprechenden Antwort durch BetP erreicht, einem konformationell asymmetrisch-trimeren Sekundärtransporter welcher für den Import des kompatiblen Solutes Betain verantwortlich ist. Zwei Stimuli werden benötigt, um die vollständige Stress-Antwort auszulösen: eine erhöhte cytoplasmatische K^+-Konzentration, sowie ein vage definierter „Membran-Stimulus“. Trotz zahlreicher Daten zur Regulation von BetP fehlen strukturellen Informationen zum herunterregulierten Zustand. Mithilfe der kryo-EM Einzelteilchenanalyse konnte ich hochauflösende Strukturen des herunterregulierten sowie eines Übergangs-Zustandes beitragen, die wichtige strukturelle Details aufklärten. Es zeigte sich, dass BetP im herunterregulierten Zustand symmetrisch ist, und dass dieser Zustand durch ein enges, cytoplasmatisches Interaktionsnetzwerk der Sensor-Domänen stabilisiert wird, welches wiederum durch Cardiolipin-Moleküle an regulatorischen Lipid-Bindestellen verstärkt wird. Daten unserer Co-Autoren bestätigten, dass dieser Zustand unter Stressbedingungen schrittweise gelöst wird, was in der bekannten, asymmetrischen Struktur resultiert. Diese Daten – zusammengefasst in IX. PREPRINT 1 – sind die Basis für einen detaillierten Regulations-Mechanismus und ermöglichten auch eine genauere Definition des Membranstimulus.

Ein dritter Gegenstand dieser Arbeit bestand in der dreidimensionalen Untersuchung von durch PC-2 Überexpression in HEK-Zellen verursachten kristalloid-ER Strukturen mittels Doppelachsen-STEM-Tomografie. In dieser Studie, nachzulesen in X. MANUSCRIPT 1, konnte ich zudem die Existenz von sog. ER whorls nachweisen, sowie hochauflösende 3D-Rekonstruktionen der beiden Morphotypen erzielen. Diese Daten gewährten bisher unbekannte Einblicke in das intrazelluläre Interaktions-Netzwerk und zeigten klar die hochdynamischen Eigenschaften dieses Organells, sogar unter Stressbedingungen, auf. Eine präzise Darstellung der jeweiligen morphologischen Charakteristika in ihrem zellulären Umfeld ermöglichte schließlich die Beschreibung der Membranarchitektur der Organellen mit einem bisher nicht gekannten Detailgrad.

Schließlich beschäftigt sich die Diskussion mit einem Vergleich der verschiedenen elektronenmikroskopischen Techniken und Methoden, welcher auch einen Ausblick auf zukünftige Experimente erlaubt. Zusammengefasst war es im Rahmen dieser Arbeit möglich, vielfältige Einblicke in unterschiedliche Stressantwort-Mechanismen zu erhalten, die schlussendlich jedoch erfolgreich ein gemeinsames Ziel verfolgen.

I. Introduction

I. 1 A focus on stress – stress response mechanisms

Life is constant adaptation – the bacterial stress response

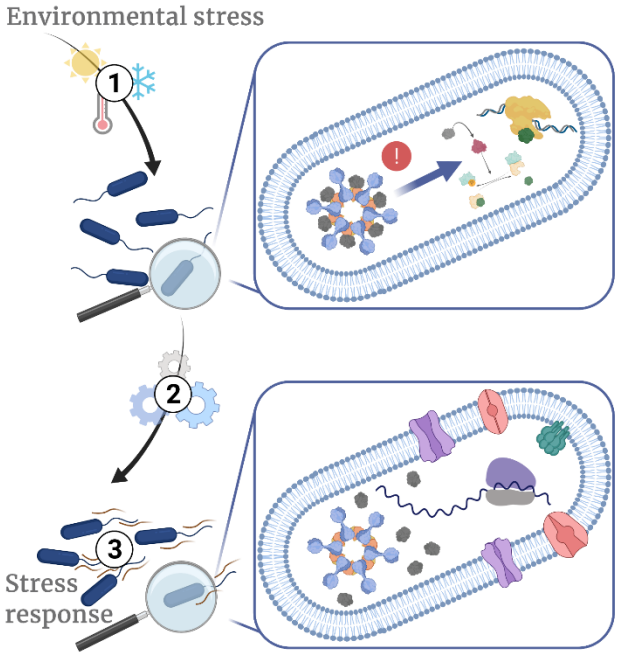

Figure 1: The bacterial stress response

Bacterial cells are constantly exposed to different types of environmental stress. Thus, they possess versatile stress response mechanisms that are initiated upon sensing of the stress stimulus and help the cells to survive under critical conditions.

As all organisms, Bacteria are constantly exposed to stress situations. Altered environmental conditions, a lack of resources or inter- and intra-species competition represent only few of the many possible threatening settings. Consequently, Bacteria have a strong need for efficient sensing, integration and reaction to a number of different stress stimuli; a fast stress response is crucial for their survival (FIGURE 1). This becomes even more important in pathogens, which constantly have to cope with their host's defense systems. Thus, stress response mechanisms play an essential role in virulence and are also discussed in the context of the development of multidrug resistance (Hengge, 2000; Giuliodori *et al.*, 2007). It should also be considered that in most cases, not only a single cell but rather the whole bacterial community is exposed to the same type of stress situation. From this perspective it is not surprising that a considerable ratio of the overall stress response in Bacteria can be related to e.g. quorum sensing or biofilm formation (Giuliodori *et al.*, 2007; Bremer & Kraemer, 2019). This may ultimately result in a global effort of the bacterial community with the potential power to subsequently transform their own environment, e.g. *via* targeted uptake or release of

specific compounds, nutrients, or energy (Schimel *et al.*, 2007). In conclusion, stress response systems represent key players in the interaction of Bacteria with their environment, and are considered vital for their survival. Some of the most prominent stress response systems include the two component systems (Stock *et al.*, 2000); the cold shock response initiating the transcription of nucleic acid binding proteins and chaperones (Giuliodori *et al.*, 2007); or the general stress response system, characterized by the contribution of a sigma factor (Gottesmann, 2019).

From a general perspective, the process of a stress response can be described by three well-defined, subsequent steps, illustrated in FIGURE 1: 1) stress stimulus perception, 2) signal transduction, and 3) initiated stress response. However, although the nature and consecutive order of events are well defined, studying stress response systems remains challenging due to the multitude of different settings and components involved. Stress stimuli can be as diverse as temperature changes, mechanical stress, desiccation, extreme pH values, light, exposure to toxic substances, and many others. Stress sensing thus requires a number of different receptors appropriate for the respective stimulus, and adapted to the bacterial background the same time. Not only the type, but also the extent of stress needs to be determined by the cell. This often requires the presence of multiple sensing systems receiving different signals. Thus, an important feature of many stress response systems is their ability to integrate various signals (introduced in more detail in chapter I. 2 THE STRESSOSOME, A BACTERIAL SIGNAL INTEGRATION AND TRANSDUCTION HUB), to cross-talk with each other and to coordinate the cells' reaction(s). The respective readout must be reliably translated into an intrinsic cellular response. Signal transduction is often achieved *via* protein phosphorylation or conformational changes. Consequently, bacterial stress response mechanisms are manifold and not solely dependent on the stimulus, but also on the physiological properties of the cells. As an example, gram-negative Bacteria are considered more sensitive to osmostress caused by drought or humidity (further illustrated in chapter I. 3 OSMOSTRESS REGULATION IN CORYNEBACTERIUM GLUTAMICUM) than gram-positive Bacteria, which is attributed to the significantly different composition of their respective cell walls (Schimel *et al.*, 2007). A common theme in this respect is the co-operative action of regulated, osmosensory membrane transporters on the one hand, and mechanosensitive channels on the other hand to maintain intracellular solute homeostasis (Wood, 2011). In case a fast response is required, reactions on protein-level such as the up-regulation of transporters or activation of ion channels are common. In contrast, long-term

responses initiated by constant environmental pressure comprise the transcription of genes e.g. encoding for ion channels, transporters or chaperones (Kraemer, 2010; Bremer & Kraemer, 2019). Ultimately, the bacterium's resources are re-allocated from growth to survival pathways (Schimel *et al.*, 2007). Finally, it should be considered that a single stimulus may initiate more than one response, resulting in a network of tightly interconnected events.

Stress in Eukaryotes

Naturally, eukaryotic cells feature a much higher degree of complexity than bacterial ones. Primarily, this is evident from their cellular architecture and the presence of multiple organelles, subdividing eukaryotic cells into different compartments. Similarly, a high degree of complexity is also reflected in the assembly of cells constituting organs or tissues, usually consisting of various cell types with specialized functions. Consequently, also stress response mechanisms are more diverse in Eukaryotes. Factors triggering a stress response in eukaryotic cells are equally diverse and can be of external or internal origin. They include e.g. a lack of nutrients or essential amino acids, hypoxia, oxidative stress, ER stress (discussed in chapter I. 4 MEMBRANE STRESS IN EUKARYOTIC CELLS) or altered environmental temperatures, but also infection by pathogens, inflammation or drug treatment. Remarkably, the responses to all types of stimuli converge in a common mechanism, the integrated stress response (ISR) (Ron, 2002; Pakos-Zebrucka *et al.*, 2016). Its core element is the phosphorylation of the eukaryotic transcription factor 2 (eIF2α), which results in a general down-regulation of protein biosynthesis, while certain genes supporting the regeneration of the cell are up-regulated (Lu *et al.*, 2004). These measures target to restore cellular homeostasis; however, under extended stress conditions, they may ultimately initiate apoptosis. The overwhelming variety of factors influencing the eukaryotic stress response renders it nearly impossible to draw a complete, global picture of the ISR and its downstream effects for an entire organism. On the other hand, a detailed understanding of the underlying mechanisms is key for drug development or treatment of the many diseases caused by imbalances in the ISR, such as e.g. diabetes, various forms of cancer, or arthritis. In conclusion, studying single aspects of the ISR in the cellular or organellar context is considered a good strategy towards a molecular understanding of the eukaryotic stress response.

I. 2 The stressosome, a bacterial signal integration and transduction hub

The general stress response in *Bacillus subtilis*

The general stress response of the gram-positive Bacterium *B. subtilis* can be divided into three major parts, defined by the type of stress stimulus that the cell experiences. The first part comprises the reaction to low temperatures, but is hardly investigated (Brigulla *et al.*, 2003; Hecker *et al.*, 2007). The second branch of the stress response pathway is activated in threatening situations caused by energy depletion. Under such conditions, the protein RsbQ provides a co-factor necessary for the maturation of RsbP, which in turn activates a partner-switching cascade *via* de-phosphorylation of RsbV (Kaneko *et al.*, 2005; Hecker *et al.*, 2007; Gottesmann, 2019). Under environmental stress conditions, the same partner-switching cascade is orchestrated by the stressosome, a high-molecular weight complex composed of the proteins RsbR (co-antagonist), RsbS (antagonist) and RsbT, a kinase (FIGURE 2). For RsbR, five paralogs are known today, namely RsbRA, RsbRB, RsbRC,

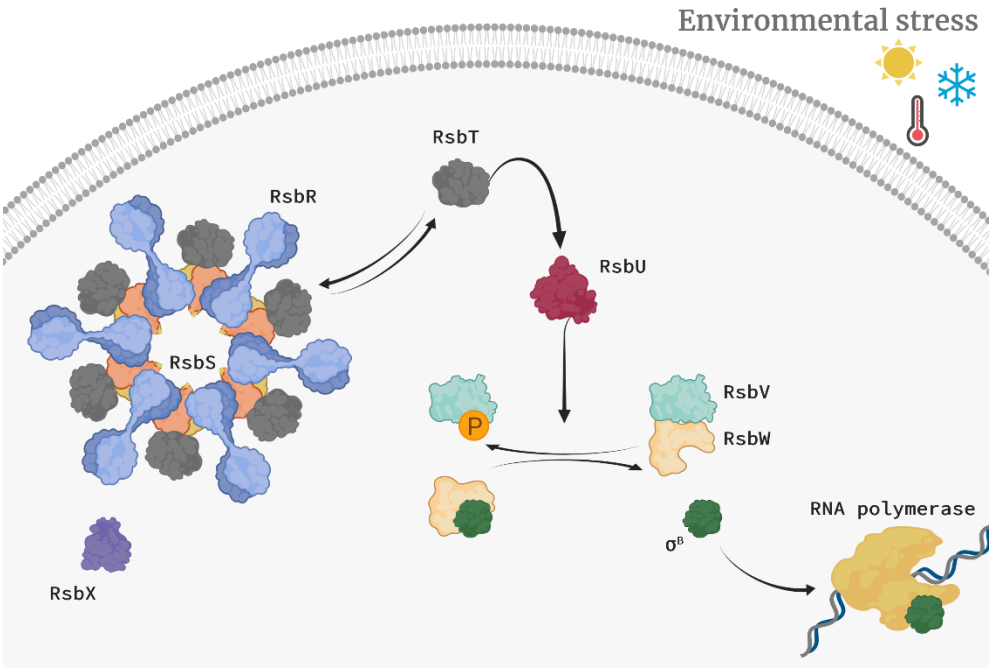

Figure 2: The environmental stress response pathway in B. subtilis

Environmental stress in *B. subtilis* is sensed and transduced by the stressosome, a macromolecular complex built from the proteins RsbS, RsbR and RsbT. Upon stress perception, RsbT phosphorylates the complex and dissociates. Free RsbT, in turn, activates RsbU, which results in the formation of a RsbV:RsbW complex. To this end, σ^B dissociates from RsbW and finally activates the RNA polymerase, to initiate the full downstream stress response.

RsbRD (Kim *et al.*, 2004b; Delumeau *et al.*, 2006) and the blue-light receptor YtvA (Gaidenko *et al.*, 2006). Immunofluorescence localization studies on *B. subtilis* revealed the presence of a constant number of ~20 stressosome complexes per cell both under non-stressed and stressed conditions (Marles-Wright *et al.*, 2008). It was thus concluded that the stressosome functions as versatile signaling hub, with the capability to sense and integrate different types of stress stimuli (Marles-Wright *et al.*, 2008; Marles-Wright & Lewis, 2008, 2010).

The stressosome itself is activated by a multi-stage phosphorylation cascade of highly conserved Threonine and Serine residues upon perceiving a stress signal (FIGURE 3) (Kim *et al.*, 2004a; Hecker *et al.*, 2007). In the absence of environmental stress, only Thr171 in RsbR is phosphorylated. Upon moderate stress, Ser59 in RsbS is phosphorylated by RsbT, and under severe stress conditions, Thr205 in RsbR is being phosphorylated additionally (Hecker *et al.*, 2007; Eymann *et al.*, 2011). Consequently, these phosphorylation events result in the dissociation of the switch kinase RsbT from the complex, which in turn leads to the activation of the environmental phosphatase RsbU (Hecker *et al.*, 2007; Marles-Wright & Lewis, 2010). Subsequently, de-phosphorylation of RsbV by RsbU allows for the formation of an RsbV:RsbW complex, resulting in the release of the transcription factor SigmaB (σ^B) from RsbW. Binding of σ^B to the RNA polymerase of *B. subtilis* finally initiates the transcription of over 150 down-stream genes of the σ^B regulon, accomplishing the cell's environmental stress response. Analysis of the chromosomal organization downstream the regulator of the sigma-operon in many bacterial genera points to diverse roles of the stressosome e.g. in the regulation of aerotaxis, biofilm formation or secondary messenger biosynthesis (Marles-Wright & Lewis, 2008). Resetting of the activated

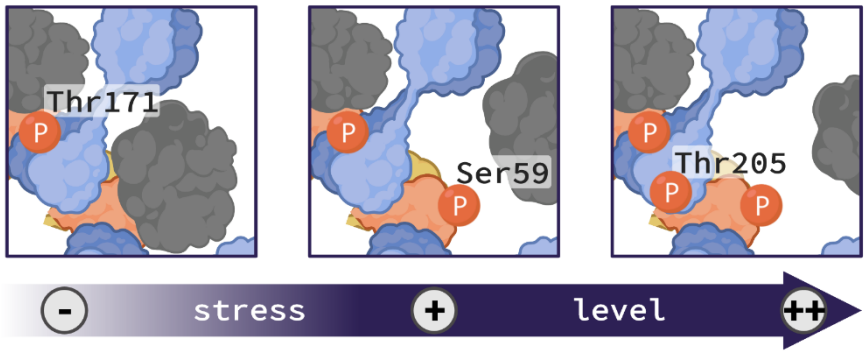

Figure 3: Activation of the B. subtilis *stressosome*

In the absence of environmental stress, only Thr171 in RsbR is phosphorylated. At increasing stress levels, Ser59 in RsbS gets phosphorylated by RsbT as well, and under extreme stress conditions, Thr205 in RsbR is ultimately being phosphorylated as well, which initiates the full stress response.

stressosome is achieved *via* de-phosphorylation of the complex by the feedback phosphatase RsbX, which counteracts the kinase RsbT (Hecker *et al.*, 2007; Marles-Wright & Lewis, 2010) (FIGURE 2). In conclusion, σ^B controls a versatile stress response system in *B. subtilis*, but it is also conserved at a variable degree in other gram-positive Bacteria. The latter was also shown for the RsbRST module (Hecker *et al.*, 2007; Marles-Wright & Lewis, 2010). Recently, σ^B is also discussed in the light of oxidative stress protection (Tran & Bonilla, 2021). From a more global perspective, sigma factors are also key players the general stress response in gram-negative Bacteria; however, their regulation is significantly different (Gottesmann, 2019).

The gram-positive stressosome – structure and assembly

By far the most intensely studied stressosome complex is the one found in the gram-positive soil bacterium *B. subtilis*. The self-assembly of macromolecular complexes by the *B. subtilis* RsbR and RsbS proteins was first described in 2003 (C.-C. Chen *et al.*, 2003). The stoichiometry of the *in vitro* complex was reported to be 3:1 (RsbR:RsbS). The study also showed that only the oligomeric RsbRS complex is able to bind the kinase RsbT, while RsbR or RsbS alone do not. Analysis of the formed RsbRS and RsbRST complexes by negative stain electron microcopy revealed the presence of six-fold symmetric, spherical particles with a diameter of approximately 20 nm. Notably, Chen and co-workers were also able to show complex formation of RsbRS *in vivo*. A number of following studies revealed the formation of 'mixed' complexes, consisting of RsbS in various combinations with the RsbR paralogues, namely purified RsbRA:RsbRB:RsbS complexes (Kim *et al.*, 2004b); RsbRB:RsbRC:RsbRD:RsbS complexes detected *in vitro* (Delumeau *et al.*, 2006); and RsbRA:RsbRB:RsbS:YtvA complexes (Gaidenko *et al.*, 2006). In summary, there is comprehensive evidence that the *B. subtilis* stressosome complex is formed by the STAS domain protein RsbS in combination with one or more RsbR paralogs. Consequently, it was reasoned that the resulting, multi-protein complexes would feature a certain degree of flexibility and that the RsbR N-terminal domain (N-RsbR) may play a role in stress sensing (Delumeau *et al.*, 2006).

Structural investigations revealed that the C-terminal part of RsbR and the entire RsbS protein adopt the Sulfate Transporter and Anti-Sigma factor antagonist (STAS) domain fold. This ancient and highly conserved domain architecture was described in 2000 and is characterized by four beta strands, forming the scaffold of the domain, and a typical, handle-like C-terminal region (FIGURE 4a; (Aravind & Koonin, 2000)). STAS domains are found in a variety of proteins with remarkably different functions, including anti-sigma factor antagonists, nucleotide-binding, sensing, metabolism, nutrient transport, kinases or transcription factors. They are either found as STAS domain-only proteins (e.g. RsbS), or multi-domain proteins fused to other domains of variable functions (e.g. RsbR) (Sharma *et al.*, 2011). N-RsbR adopts the globin fold, as revealed by J. W. Murray and co-workers. Their crystal structure of the *B. subtilis* N-RsbR dimer is depicted in FIGURE 4b, and was found to exhibit structural similarities to hemoglobins, globins and the globin-coupled sensor protein HemAT from *B. subtilis* (Murray *et al.*, 2005). Despite these structural parallels, however, no evidence was found for heme-binding of N-RsbR. Indeed, the characteristic heme-binding pocket found e.g. in HemAT is not pronounced - virtually locked - in N-RsbR. In addition, it lacks a number of conserved amino acids commonly found in bacterial hemoglobins, including a heme-proximal histidine residue (Murray *et al.*, 2005). Further evidence for dimerization of the N-RsbR domain was also provided for the *M. thermoacetica* N-RsbR domain (Quin *et al.*, 2012). The non-heme globin fold is also adopted by the other N-RsbR paralogues, with YtvA being the notable exception. While it does exhibit the characteristic C-terminal STAS domain fold, the N-terminal part of the *B. subtilis* YtvA was shown to contain a blue-light sensing LOV (light – oxygen – voltage) domain (Losi *et al.*, 2002; Ávila-Pérez *et al.*, 2006; Gaidenko *et al.*, 2006; Engelhard *et al.*,

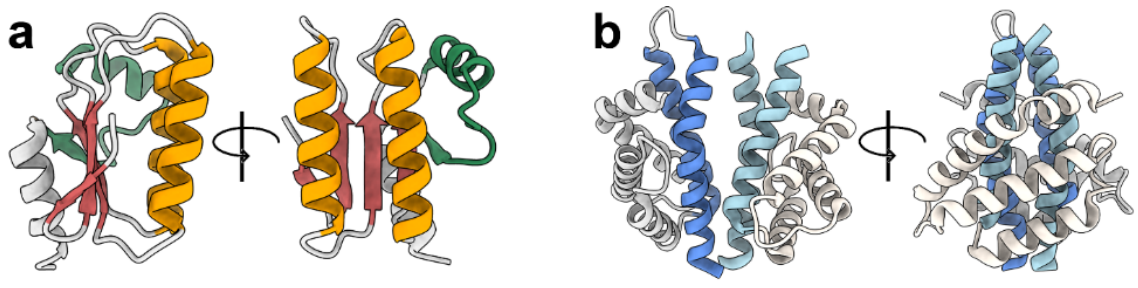

Figure 4: Protein components of the minimal stressosome complex

a) A single monomer of the *Moorella thermoacetica* RsbS protein (PDB-ID: 2VY9) is depicted from two viewing angles. The four characteristic, central beta strands are colored in red, two hairpin helices in orange. The C-terminus forms a typical, handle-like domain shown in green. b) The *B. subtilis* N-RsbR domain (PDB-ID: 2BNL) is shown as a dimer from two viewing angles. The protein adopts a globin fold, with the dimer interface formed by the two C-terminal helices depicted in different shades of blue.

2013). The C-terminal STAS domain and the N-terminal sensory domain of the RsbR paralogs are interconnected by two parallel alpha helices. A study on YtvA signaling provided evidence for signal transduction from the sensory domain *via* the linker helices towards the STAS domain. However, their protein construct did not comprise the STAS domain itself, so the exact signal transduction mechanism remains elusive (Moeglich & Moffat, 2007).

A first, prototypic structure for the entire *in vitro B. subtilis* stressosome complex was published by J. Marles-Wright and co-workers in 2008 (FIGURE 5). Using cryo-EM single-particle analysis (SPA), they were able to determine the structure of the RsbRS complex core to 6.5 Å, the minimal RsbRS complex to 8.0Å and the ternary RsbRST complex to 8.3 Å, respectively. The study further revealed the presence of 2-, 3- and 5-fold symmetry in the complex (Marles-Wright *et al.*, 2008; Marles-Wright & Lewis, 2010). The resolution in the complex core was sufficient to fit *M. thermoacetica* RsbS monomers into the density, and it could be shown that the stressosome core is formed by RsbS and RsbR STAS domain dimers arranged in pseudo-icosahedral symmetry. The cryo-EM density map of the minimal complex revealed the positions of the turret-like N-RsbR domains protruding from

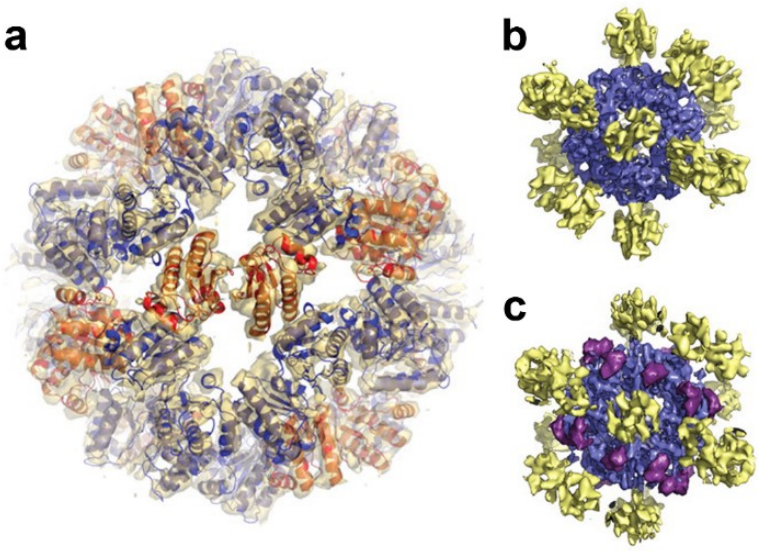

Figure 5: Molecular architecture of the B. subtilis *stressosome*

a) The cryo-EM density map of the icosahedral-symmetric *B. subtilis* RsbRS STAS domain core at a resolution of 6.5Å is depicted with 60 RsbS monomers docked into the density map. b) The cryo-EM reconstruction of the minimal RsbRS complex reached a resolution of 8.0Å. The complex core is depicted in blue, the N-RsbR turrets (yellow) are arranged in a D2 symmetric fashion. c) The ternary RsbRST complex reached a resolution of 8.3Å. Additional densities for RsbT (purple) are observed positioned above the RsbS dimers. Reproduced from (Marles-Wright *et al.*, 2008).

the core arranged in D2 symmetry. It was thus concluded that the stoichiometry of the complex is 20:10 $RsbR_{dimers}$:$RsbS_{dimers}$ (Marles-Wright *et al.*, 2008; Marles-Wright & Lewis, 2008). The density of the ternary complex finally revealed the localization of 20 RsbT proteins, positioned above the RsbS monomers (Marles-Wright *et al.*, 2008). A recent cryo-EM study on the *B. subtilis* RsbRA:RsbS minimal complex confirms these results, and highlights the observation of a mixture of symmetries originating from the stressosome assembly in the STAS domain core (Kwon *et al.*, 2019). Until 2021, further structural information on stressosome complexes is restricted to another gram-positive organism, *Listeria monocytogenes*. The structure of the RsbRST complex was solved to 3.38 Å in icosahedral symmetry and confirmed the general complex architecture as described for *B. subtilis* (Williams *et al.*, 2019). Lastly, the structure of the close relative *Listeria innocua* was contributed in 2022 (Miksys *et al.*, 2022). Structural information on architecture and assembly of the gram-positive stressosome complex are further summarized in TABLE 1.

Table 1: Architecture and assembly of gram-positive stressososmes

organism	**reference**	**symmetry**	**resolution**	**$RsbR_{dimers}$:$RsbS_{dimers}$**
B. subtilis	(Marles-Wright *et al.*, 2008)	I	6.5Å / 8.0Å	20:10
		D2	8.3Å	
B. subtilis	(Kwon *et al.*, 2019)	I	4.1Å	20:10 (D2) 22:8 (C1)
		D2	7.3Å	
		C1	9.1Å	
L. monocyto-genes	(Williams *et al.*, 2019)	I	3.38Å	20:10
		C1	4.48 Å	
L. innocua	(Miksys *et al.*, 2022)	I	3.45 Å	20:10
		D2	3.87 Å	

The gram-negative stressosome

In contrast to the wealth of structural and functional knowledge on the gram-positive stressosome complex, information on its gram-negative counterpart are sparse. The presence of an RsbRST module for members of the genus *Vibrio* was reported in 2005 (Pané-Farré *et al.*, 2005). The first example for a gram-negative stressosome complex was described in 2016 by X. Jia and co-workers. They investigated the *in vitro* assembled *Vibrio*

brasiliensis RsbRST complex, a close relative of the human pathogen *Vibrio vulnificus*. Dynamic light scattering (DLS) experiments pointed to a significantly larger complex of 30.2 nm in comparison to the *B. subtilis* RsbRS stressosome. Another striking difference was proposed with respect to the putative phosphorylation sites: no phosphorylation could be shown for RsbS (Jia *et al.*, 2016). Altered/shifted phosphorylation sites were also reported in 2005 for the *V. vulnificus* RsbS protein (Pané-Farré *et al.*, 2005). The STAS domain of the *V. brasiliense* RsbR protein also seems not to by phosphorylated, while two phosphorylated residues (Ser178 and Thr182) were reported in the linker helices connecting the STAS domain and the N-RsbR sensor domain (Jia *et al.*, 2016). Analogously to the gram-positive stressosome complex, phosphorylation of the *V. brasiliensis* RsbRS complex is presumably achieved *via* the kinase RsbT. The sensory N-RsbR domain was demonstrated to bind heme, and the presence of Fe^{II} was shown to significantly increase the overall kinase activity of RsbT. From the results, it was concluded that N-RsbR most likely represents an O_2 sensor, and that stressosome signaling in *V. brasiliensis* is O_2-dependent (Jia *et al.*, 2016). Heme-binding sensor-globin RsbR proteins are present in all members of the *V. brasiliensis* clade, while non-heme globin domain proteins are found in gram-positive bacteria, pointing towards significant differences in the stressosome sensing and signaling process between gram-positive *vs*. gram-negative Bacteria on a more global view. Despite the above-mentioned studies, however, information on the gram-negative stressosome complex is rare. In particular, structural data are entirely absent. Further investigations, especially of the complex structure and assembly, are thus of great interest and will allow for a mechanistic interpretation of functional data. Ultimately, these informations are required to pinpoint the differences between the gram-positive and gram-negative stressosome complexes, and contribute to a global understanding of the bacterial environmental stress response.

I. 3 Osmostress regulation in *Corynebacterium glutamicum*

Osmotic stress in Bacteria

Osmotic stress, i.e. a change of the extracellular osmolality, is considered one of the most dangerous situations bacterial cells are frequently exposed to. The cellular hydration status changes only within seconds after the initiation of an osmotic shift (Wood, 2011). Under non-stressed conditions, the cytoplasmic solute concentration is significantly higher than the extracellular one. The resulting osmotic gradient is therefore continuously counterbalanced by the hydrostatic turgor pressure of the cell, preventing uncontrolled water influx and maintaining homeostasis. From the cellular perspective, osmostress manifests in two contrary scenarios (FIGURE 6). Under hypo-osmotic conditions, the extracellular solute concentration decreases, e.g. caused by a rain shower. Analogously, hyper-osmotic conditions result in an increase of the extracellular solute concentration, which can for instance be caused by draught. Both scenarios are equally threatening for the cell, since they result in the instant and uncontrolled flux of water across the cellular membrane towards the compartment of higher osmotic pressure, abolishing homeostasis.

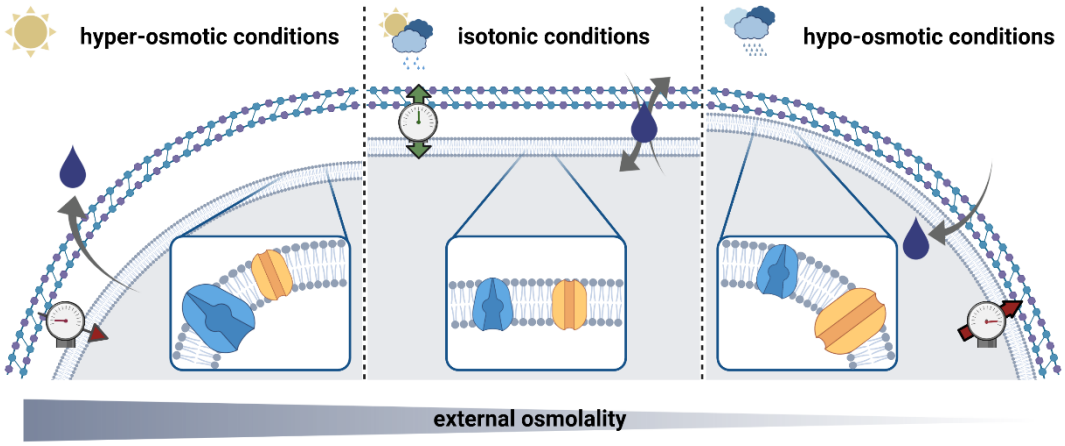

Figure 6: Osmostress in Bacteria

From the bacterial point of view, osmostress manifests in two contrary scenarios: hyper-osmotic conditions (left panel) are caused e.g. by draught and result in water efflux from the cell. In contrast, hypo-osmotic conditions (right panel) happen e.g. after a rain shower and consequently lead to water influx. Both scenarios are equally dangerous for the cell, since they cause immediate and drastic changes in hydrostatic turgor pressure and intracellular solute concentration. Under homeostatic conditions (middle panel), turgor pressure and water flux across the cellular membrane are in balance and kept constant by the concerted basal activity of membrane transporters and mechanosensitive channels (blue and orange in insets, respectively). Under osmostress conditions, either transporters or channels are up-regulated to counter-act the respective threat.

As the immediate and inevitable consequence, the cytoplasm would either shrink (hyper-osmotic stress) or swell (hypo-osmotic stress). Both scenarios result in an altered cellular turgor pressure as well as dramatic changes of the intracellular solute concentrations along with disturbed molecular crowding. In any scenario the chemical nature of the respective solute(s) is not relevant, but only their total concentration (Giuliodori *et al.*, 2007). In every case, the described consequences of osmotic stress would severely impair the cell's metabolic and catalytic activities.

Since Bacteria are not able to actively transport water across their membranes in either direction, they have developed a number of different strategies to evade critical situations caused by osmostress. A hypo-osmotic shift requires a very fast reaction of the cell, since it experiences the danger of bursting due to an increased turgor pressure. This process could be happening within only a few milliseconds (Booth, 2014). Owing to their fast response, channel proteins such as mechanosensitive channels are considered the most important emergency systems to initiate solute efflux under such conditions. In the opposite case, a common strategy to counteract hyper-osmotic conditions is the accumulation of compatible solutes in the cytoplasm, since Bacteria cannot actively re-hydrate by water-uptake. Compatible solutes are small, highly soluble, electro-neutral organic compounds such as sugars, betaine, ectoine, amino acids or polyols, with the property to compensate the lack of water. In addition, they act as osmolytes and have a protective function for cellular components. Naturally, they must be compatible with the cellular biochemistry. From an energetic point of view, compatible solute uptake is strongly favored over *de novo* biosynthesis; e.g. the synthesis of one ectoine molecule consumes at least 20x more energy than its uptake (Bremer & Kraemer, 2019). A similar strategy is the import of high ion concentrations (e.g. K^+), which is primarily found in salt-tolerant microbes (Gunde-Cimerman *et al.*, 2018).

Bacteria are not able to directly sense changes in external osmolality; thus, complementary types of stimuli must be existent (Bremer & Kraemer, 2019). Suitable stimuli are sensed either in the cytoplasm or in proximity of the cellular membrane to initiate the stress response within the cell, and many proteins involved in the osmostress response are in fact membrane proteins. Hence, a contribution of the cellular membrane or the respective membrane lipids to stress sensing and/or regulation is logical. Different types of membrane-transmitted stimuli have been reported to regulate membrane proteins. On the one hand, lipids can act as 'bulk' on the embedded proteins, transmitting forces *via* lateral membrane

pressure or curvature. This is the case e.g. for mechanosensitive channels, with Piezo1 being a well-studied example (Haselwandter & MacKinnon, 2018). Specific and direct lipid-membrane protein interactions, in contrast, are less well investigated. One example for such interactions is the osmosensing transporter ProP in *E. coli*, which has been found to co-localize at the cellular poles harboring an increased Cardiolipin concentration (Romantsov *et al.*, 2009; Romantsov & Wood, 2016). Other membrane-transmitted stimuli are reported to originate from the membrane composition and -charge (Bremer & Kraemer, 2019). An intriguing concept was proposed by J. M. Wood, who suggested that the entire cellular membrane could serve as an "[…]osmosensing antenna" (Wood, 1999, 2011) with increased total surface, amplifying the stress stimulus subsequently sensed by membrane-embedded osmosensory proteins.

Osmostress regulation in *Corynebacterium glutamicum*

The gram-positive soil bacterium *Corynebacterium glutamicum* is considered a model organism for studying the bacterial osmostress response. As a reaction to hyper-osmotic stress, it imports betaine *via* the transporter BetP, one out of five secondary active transporters responsible for compatible solute uptake in *C. glutamicum* (Ruebenhagen *et al.*, 2001). Even when down-regulated, BetP imports a certain amount of betaine (Botzenhardt *et al.*, 2004). The contrary process, betaine release from the cell, is performed by MscCG, a mechanosensitive channel. It was shown that both processes occur simultaneously, enabling fine-tuning of the steady-state cytoplasmic betaine concentration (Boerngen *et al.*, 2010). Notably, both the functions of an osmo-sensor and of an osmo-regulator are synergized within BetP (Ruebenhagen *et al.*, 2000). Consequently, BetP is considered an excellent target to study the osmostress response. Under hyper-osmotic conditions, the already established system composed of BetP and MscCG is able to react very fast and can efficiently adapt to the extent of osmotic stress. Consequently, betaine transport in *C. glutamicum* follows the so-called pump and leak-model (Boerngen *et al.*, 2010).

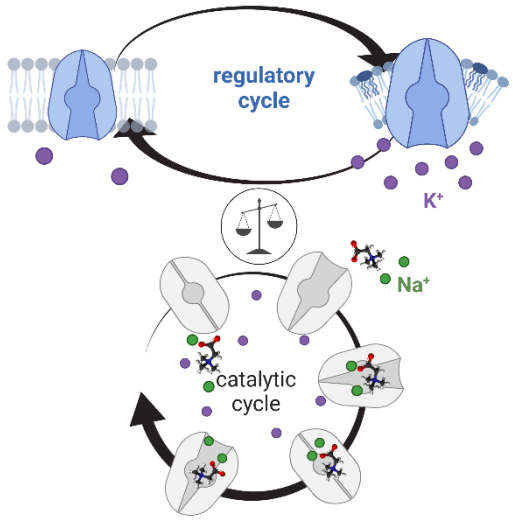

Figure 7: Transport regulation in BetP

The BetP catalytic and regulatory cycles are tightly coupled to each other. Transport activity scales relative to the amount of hyper-osmotic stress sensed. While detailed information about substrate transport are available, the mechanism of regulation is less well understood.

Two types of stimuli are required to fully up-regulate BetP. The primary stimulus was identified to be an elevated cytoplasmic K^+ concentration, which is in turn the consequence of high external osmolality under hyper-osmotic conditions (Ruebenhagen *et al.*, 2001; Schiller, Kraemer, *et al.*, 2004; Schiller, Ruebenhagen, *et al.*, 2004; Ge *et al.*, 2011). The second stimulus, however, is less well defined. From a general point of view, it can be attributed to changes in membrane properties. Membrane surface charge and lipid composition have been shown to contribute to the stimulus (Schiller *et al.*, 2006; Oezcan *et al.*, 2007; Maximov *et al.*, 2014). Notably, the *C. glutamicum* membrane exclusively consists of negatively charged lipids (Hoischen & Kraemer, 1990; Schiller *et al.*, 2006). An altered lateral membrane pressure was similarly discussed in this context; however, this parameter is experimentally hardly accessible. Thus, the precise nature of the membrane stimulus remains vaguely defined. Down-regulation and adaptation of BetP as a consequence of the hyper-osmotic stress response are poorly understood (Botzenhardt *et al.*, 2004). The collective stimuli are constantly fine-tuning the magnitude of regulation in BetP. This so-called 'regulatory cycle' acts in turn as a scale for the transport activity of the protein, described by the catalytic cycle (FIGURE 7). It should be emphasized that both cycles act and react as a functional entity to facilitate stress sensing, signal transduction and stress response (Ziegler *et al.*, 2010). Consequently, detailed information on both cycles is the inevitable prerequisite for a comprehensive, mechanistic understanding of the hyper-osmotic stress response in *C. glutamicum*.

Structure and substrate transport of BetP in the up-regulated state

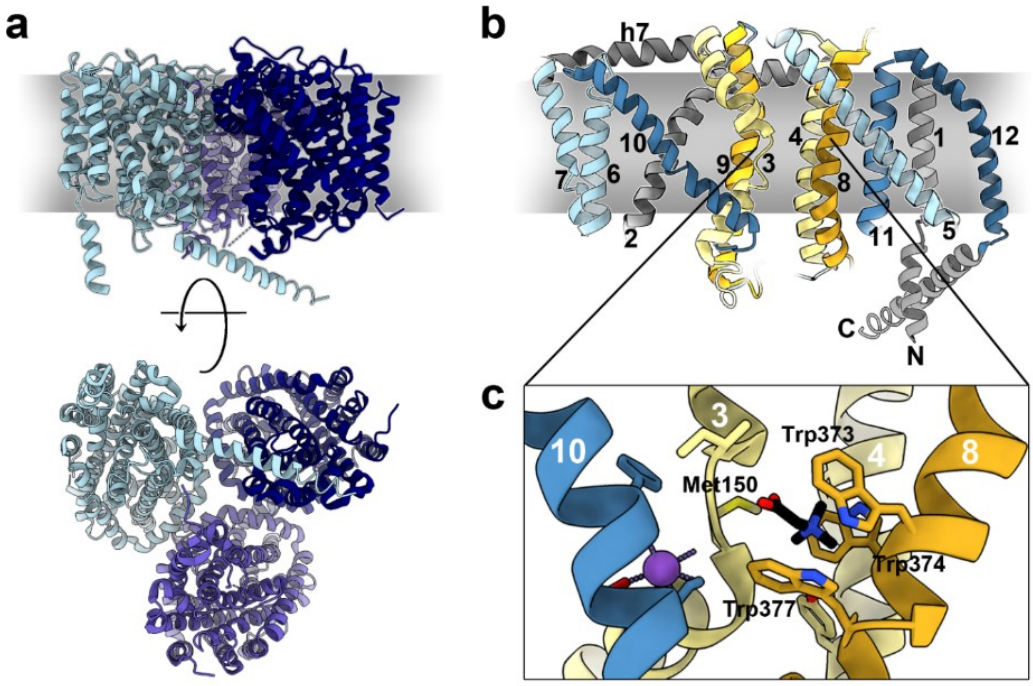

Figure 8: Crystal structure of BetP in the up-regulated state

a) The crystal structure of BetP (PDB-ID: 4AIN; (Perez *et al.*, 2012)) in the presence of betaine and Na^+ reveals the trimeric architecture and asymmetric nature of BetP. Only the C-terminal domain in protomer A (light blue) is fully extended, making contact to protomer C (navy blue). b) Topology model of a single BetP protomer. The transporter core of the protein is formed by TMs 3, 4, 8 and 9 (khaki/gold), the coupling scaffold is built by TMs 5 – 7 and 10 – 12 (blue). Helices attributed to the LeuT fold repeat 1 are colored in bright shading, helices attributed to repeat 2 in dark color shading, reypectively. c) The binding site for betaine (black) is formed by residues in TMs 4 and 8, forming a characteristic tryptophan box (Trp373, Trp374 and Trp377). Met150, located in the unwound glycine stretch in TM3 contributes to the sodium (purple sphere) Na2 binding site, together with residues located in TM10.

A number of crystal structures obtained under different conditions are available for BetP, consistently showing the transporter assembling as an asymmetric homo-trimer in an up-regulated state (FIGURE 8a). Each BetP protomer consists of 12 trans-membrane (TM) helices (TMs 1 – 12), an amphipathic helix (h7), the mostly unordered N-terminal domain and an α-helical C-terminal domain, both located at the cytoplasmic side. Contact between the protomers is mediated by h7 at the periplasmic side of the trimer, TM2, and the C-terminal domains at the cytoplasmic side, respectively (Ressl *et al.*, 2009; Ziegler *et al.*, 2010; Perez, Khafizov, *et al.*, 2011; Korkmaz *et al.*, 2013). An overview of selected structural and functional elements identified in BetP is presented in TABLE 2.

Table 2: Structural and functional elements in BetP

Domain architecture			
element	**location**	**function(s)**	**reference(s)**
N-terminus	N-term	regulation modulator	(Ott *et al.*, 2008)
C-terminal domain	C-term	osmo-sensor & -regulator; trimer contact	(Ruebenhagen *et al.*, 2000) (Schiller *et al.*, 2006) (Ott *et al.*, 2008) (Ziegler *et al.*, 2010)
transporter core	TMs 3, 4, 8, 9	concerted movement during conformational cycling; substrate binding sites located at core/scaffold interface	(Yamashita *et al.*, 2005) (Khafizov *et al.*, 2010) (Ziegler *et al.*, 2010) C. Perez et al, 2012b
transport scaffold	TMs 5 -7, 10 - 12		
repeat 1	TMs 3 - 7	related by pseudo-twofold symmetry axis	(Yamashita *et al.*, 2005) (Khafizov *et al.*, 2010) (Ziegler *et al.*, 2010)
repeat 2	TMs 8 - 12		
helix 7, TM2	h7, TM2	trimer contact	(Ott *et al.*, 2008) (Ziegler *et al.*, 2010)
Glycine stretch	Gly149-Met150-Gly151-Ile152-Gly153	provides structural flexibility during conformational cycling	(Ressl *et al.*, 2009) (Ziegler *et al.*, 2010) (Perez, Koshy, *et al.*, 2011) (Perez *et al.*, 2012)
Substrate binding sites			
element	**location**	**function(s)**	**reference(s)**
S1	Trp373, Trp374, Trp377*	betaine binding (tryptophan box)	(Ressl *et al.*, 2009) (Ziegler *et al.*, 2010) (Perez, Koshy, *et al.*, 2011) (Perez *et al.*, 2012)
Na2	Ala147, Met150, Phe464, Thr467, Ser468	Na^+ binding	(Khafizov *et al.*, 2012) (Perez *et al.*, 2012)
Na1‘	Thr246, Thr250, Phe380, Thr499	Na^+ binding	(Khafizov *et al.*, 2012) (Perez *et al.*, 2012)

*: along with other aromatic residues in TM3 & TM8 lining the substrate pathway

BetP adopts the LeuT fold (Yamashita *et al.*, 2005), with TMs 3 – 7 and TMs 8 – 12 organized as two symmetry-related, structurally homologous, inverted repeats. While TMs 3, 4, 8 and 9 represent the central four-helix bundle harboring the substrate binding sites, TMs 5 – 7 and TMs 10 – 12 form the stabilizing scaffold of the transporter (FIGURE 8b) (Khafizov *et al.*, 2010; Ziegler *et al.*, 2010). The C-terminal domain protrudes into the

cytoplasm and has both sensory and regulatory properties (Ruebenhagen *et al.*, 2000; Kraemer & Morbach, 2004; Schiller *et al.*, 2006; Ott *et al.*, 2008; Ziegler *et al.*, 2010), with the osmosensory residues located within the terminal 12 – 23 amino acids (H. Peter *et al.*, 1998). The asymmetry of the BetP trimer is primarily determined by the orientation and the degree of α-helical fold of the C-terminal domains. While the helix is fully folded and protruding towards the cytoplasm in protomer A, it exhibits a different orientation and degree of order in the other protomers, respectively (Ressl *et al.*, 2009). The N-terminal domain has been shown to modulate BetP regulation *via* interactions with the C-terminal domain (Ott *et al.*, 2008), and is oriented towards TM1 of the neighboring protomer (Ressl *et al.*, 2009). Direct interactions of the C-terminal domain with the N-terminus were demonstrated, along with interactions between the C-terminal domain and a number of cytoplasmic loops, namely loop 2 (L2), loop 4 (L4) and loop 8 (L8) (Ott *et al.*, 2008). Betaine uptake by BetP follows the so-called alternating-access mechanism (Forrest *et al.*, 2011), with the catalytic cycle switching between outward-facing, occluded and inward-facing states (FIGURE 7). Conformational cycling is thought to be largely facilitated by an unwound segment in TM3, designated the Glycine stretch (Perez *et al.*, 2012). The unfolded section allows for independent tilting and rotational movement of the upper and lower part of the helix, resulting in a mutual opening and closing of the upper and lower transporter gates, respectively (Perez *et al.*, 2012). Met150, located in the Glycine stretch, is also involved in sodium coordination, pointing to a key role of this structural element during conformational cycling, originating from its conformational flexibility (Perez, Koshy*, et al.*, 2011).

Substrate binding in BetP is mediated by residues found in the transporter core. Trp373, Trp374 and Trp377 form a tryptophan box coordinating the betaine trimethylammonium group by cation-π-interactions (FIGURE 8c) (Perez *et al.*, 2012) and are elements of the conserved signature sequence of the BCCT family members (Kappes *et al.*, 1996; Saier, 2000; Ziegler *et al.*, 2010). Betaine transport in BetP is driven by the membrane potential and a sodium gradient, and both substrates are symported in a 1:2 (betaine:Na^+) stoichiometry (Farwick *et al.*, 1995; Ressl *et al.*, 2009). Two Na^+ binding sites were predicted from structural data and *in silico* analyses (Khafizov *et al.*, 2012; Perez *et al.*, 2012; Perez *et al.*, 2014). The first site, named Na2, is evident from a crystal structure resolving the coordinated Na^+ ion (FIGURE 8c) (PDB-ID: 4AIN; (Perez *et al.*, 2012)), and the presence of a Na^+ ion was additionally confirmed by molecular dynamics simulations

and mutagenesis (Khafizov *et al.*, 2012). The second Na^+ binding site, named Na1', is formed by residues located in TMs 5, 8 and 11, and was proposed based on conclusions drawn from the twofold pseudo-symmetric axis present in LeuT fold adopting proteins. In addition, the predicted Na1' binding site could be to some extent confirmed by mutagenesis of the involved residues and by MD simulations (TABLE 2) (Khafizov *et al.*, 2012).

As pointed out before, regulation of BetP requires a membrane stimulus (Oezcan *et al.*, 2005; Oezcan *et al.*, 2007). In line with this observation, a number of palmitoyl-oleoyl phosphatidyl glycerol (POPG) lipids could be resolved in one of the BetP crystal structures (FIGURE 9) (PDB-ID 4C7R; (Koshy *et al.*, 2013)). They were either located in the trimer center, or as annular lipids at the trimer periphery. Several lipid binding sites were identified, a majority located at the C-terminal domains, the trimer interface in TM2 and h7, and in the cytoplasmic part of TM3, mimicking the cellular membrane bilayer. In summary, most lipids were found in close association with helices involved in transport and/or regulation; notably, one fatty acid chain exhibited a direct interaction with Met150 (Koshy *et al.*, 2013). In a follow-up study using FTIR spectroscopy, it was concluded that the BetP-lipid interactions alter significantly during the regulatory cycle (Gueler *et al.*, 2016). Taken together, these results once more highlight the role of lipids in the regulation of BetP, and further emphasize the need for structural data of the down-regulated state. While transport activity in BetP is structurally and functionally well characterized, detailed data on the regulatory cycle are largely missing.

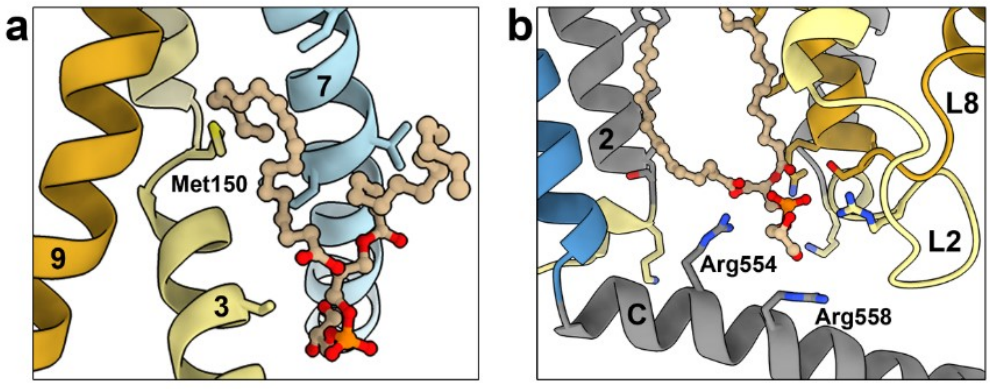

Figure 9: Protein-lipid interactions in BetP

a) A POPG lipid (tan) was resolved at the Glycine stretch located in TM3 (khaki), coordinated by Met150 (PDB-ID: 4C7R; (Koshy *et al.*, 2013)). b) Another POPG lipid was found coordinated by residues in the C-terminal domain of protomer A and in loops L2 and L8 in protomer C, respectively.

I. 4 Membrane stress in eukaryotic cells

Stress in eukaryotic membrane systems

Unlike Bacteria, eukaryotic cells contain multiple, confined compartments and in general feature a much higher degree of complexity. Eukaryotic organelles, such as nucleus, mitochondria or vacuoles, are separated from their surrounding by particular membranes. In addition, the cell comprises several endogenous membrane-built organelles, e.g. the endoplasmic reticulum (ER) or the Golgi apparatus. The major functions of organellar membranes are to maintain different chemical milieus tailored to the requirement of the particular compartment, and to provide a reaction platform for manifold cellular processes. The extent, shape or number of the respective organelles are adjusted to the cells' requirements and can be adapted in response to altered environmental conditions (Schuck *et al.*, 2009). Communication between organelles is achieved either *via* direct fusion or contact, or *via* budding and fusion of membrane vesicles acting as shuttles for different types of cargo. Naturally, membrane-confined organelles are very sensitive to stress; thus, it is not surprising that a network of versatile stress response mechanisms has evolved in Eukaryotes to maintain cellular homeostasis. One of the best studied examples is the unfolded protein response (UPR), initiated upon ER stress caused by the presence of incorrectly folded proteins in the ER lumen (reviewed by e.g. (Schroeder & Kaufman, 2005)). The ER is not only responsible for lipid biosynthesis, but also for protein folding and post-translational modifications of all proteins entering the secretory pathway upon protein biosynthesis. Properly folded proteins are then shuttled to the Golgi apparatus for transport to their final destination, while incorrectly folded proteins are marked for targeted degradation (Ellgaard *et al.*, 1999), or exported to the cytosol and degraded by the proteasome *via* the ER-associated degradation (ERAD) pathway (M. H. Smith *et al.*, 2011).

The unfolded protein response (UPR) pathway

The excessive accumulation of misfolded proteins triggers stress – and consequently the corresponding stress response – in the ER (FIGURE 10). Three different proximal stress sensor proteins are present in the ER membrane, which under non-stressed conditions bind the chaperone BiP (binding immunoglobulin protein). In the presence of unfolded proteins,

BiP dissociates from the sensors which in turn renders them active. The fastest response is initiated by the sensor protein PERK (PKR-like ER kinase). Upon dissociation of BiP, PERK dimerizes and auto-phosphorylates (Harding & Ron, 2002). The subsequent signaling cascade has two major outputs: on the one hand, translation of most proteins is rapidly attenuated, with the aim of reducing the burden of unfolded proteins in the ER. On the other hand, PERK activation induces the translation of ATF4, which in turn regulates the expression of apoptosis-related proteins on a longer timescale (Schroeder & Kaufman, 2005; Walter & Ron, 2011). Similar to PERK, also the second sensory protein IRE1 (inositol requiring 1) dimerizes and auto-phosphorylates upon BiP dissociation. The IRE1 pathway is found in all eukaryotes, which emphasizes its global importance in stress regulation. In mammals, activated IRE1 affects expression of the transcription factor XBP1 (X-box binding protein 1) *via* splicing of the XBP1 mRNA (Harding & Ron, 2002). The downstream IRE1 – XBP1 pathway aims at increasing the ER capacity by up-regulating the transcription of genes responsible for ER growth, lipid biosynthesis, protein maturation and export from the ER (Walter & Ron, 2011; Brown & Naidoo, 2012). The third UPR stress response pathway is controlled by activating transcription factor 6 (ATF6). Upon BiP release, ATF6 migrates to the Golgi apparatus and is being cleaved. The resulting ATF6α

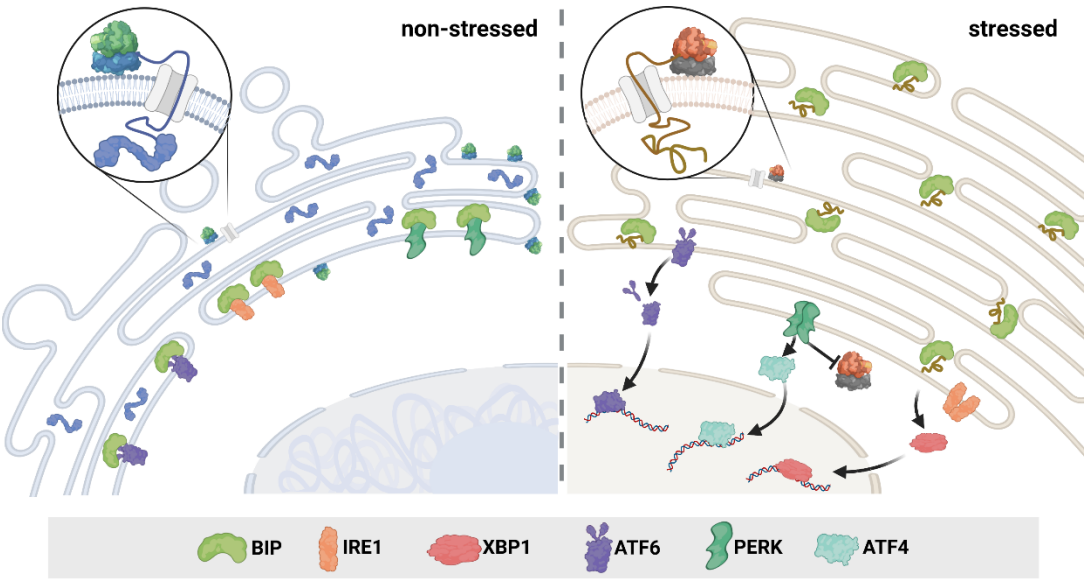

Figure 10: The unfolded protein stress response

Under normal conditions, proteins are folded and post-translationally modified in the ER, and consequently transported further *via* the Golgi apparatus (left). If misfolded proteins accumulate in the ER lumen, the UPR is initiated (right). BIP binds the unfolded proteins, liberating the transmembrane proteins IRE1, PERK and ATF6, and thereby initiates a manifold ER stress response (see main text).

fragment enters the nucleus and initiates expression of chaperones such as BiP. Thus, the purpose of the ATF6 pathway is to enhance the overall ER protein folding output (Okada *et al.*, 2002). H. P. Harding and D. Ron ranked the three UPR response pathways according to their reaction rate and output as follows: the fast and immediate response of the ER upon UPR is an attenuation of protein synthesis to reduce the folding burden on the ER (PERK). At a second stage and longer timescale, protein expression is up-regulated with the aim to globally enhance ER performance (IRE1, ATF6). Under continued, severe UPR stress conditions, however, apoptosis can be initiated to ultimately protect the organism (PERK – ATF4) (Harding & Ron, 2002). P. It was concluded that the regulation of UPR-induced transcription factors in higher Eukaryotes exhibits a certain degree of redundancy, which can be attributed to the necessity of the cell to carefully balance global ER activity (Walter & Ron, 2011). This is further emphasized by the fact that UPR-deficient cells are not able to maintain ER homeostasis (Schuck *et al.*, 2009).

ER morphology

Within eukaryotic cells, the ER is in charge of a variety of different tasks, such as lipid biosynthesis, protein folding and post-translational modification, protein quality control or Ca^{2+} storage. Consequently, the ER is divided into several functional sub-domains, and it could be demonstrated that these occur simultaneously within the same cell, fulfilling their different tasks (Borgese *et al.*, 2006). It is thus not surprising that a considerable number of remarkably diverse morphologies have been described for this single organelle. A first distinction of different ER types is generally determined by its localization. Basically, the perinuclear ER comprises the nuclear envelope, while the peripheral ER is found throughout the cytoplasm (Voeltz *et al.*, 2002). According to the presence or absence of ribosomes attached to the cytosolic ER membrane leaflet, the ER can be classified into rough (ribosome-decorated) or smooth (ribosome-free) ER (rER and sER), respectively. In most cell types, these two distinct ER forms are not spatially separated and occur simultaneously (Borgese *et al.*, 2006). In many cases, rER is formed by ER sheets, while sER oftentimes exhibits a tubular shape (Schuck *et al.*, 2009). Due to its role in protein biosynthesis, the presence of ribosomes at the rER surface is not surprising. As described above, under homeostatic conditions protein synthesis, folding, post-translational modification and transfer to the Golgi apparatus are well balanced. In response to the UPR,

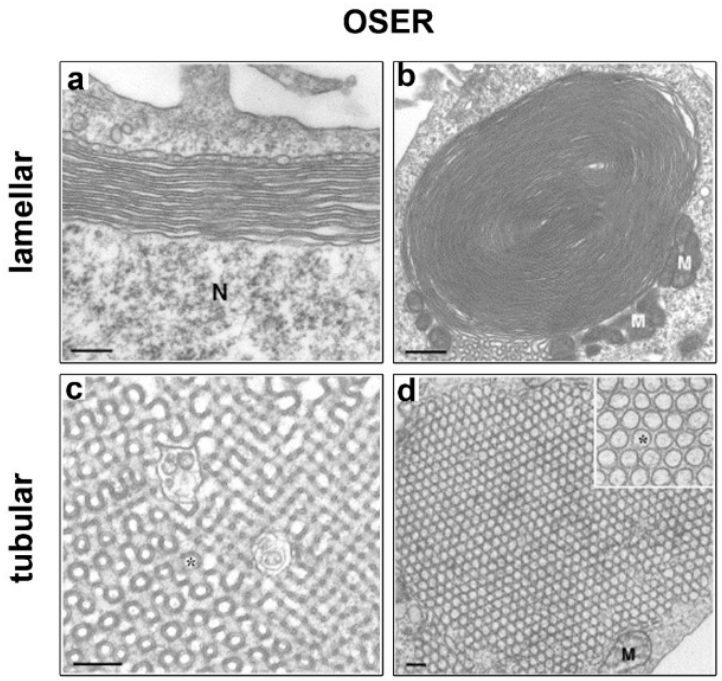

Figure 11: OSER morphology

OSER can be subdivided into two categories: lamellar (top row) and tubular (bottom row) ER structures. Examples for lamellar OSER are karmellae (a) and whorls (b), while tubular OSER can exhibit sinusoidal (c) or crystalloid (d) shapes. Scale bars (a, c, d) = 200 nm, (b) = 600 nm; N = nucleus, M = mitochondria, * = ER luminal space. Reproduced and modified from (Borgese *et al.*, 2006).

however, protein biosynthesis is attenuated while the global ER capacity is expanded. This is achieved *via* the synthesis of large, continuous ER sheets located in the cytoplasm, which can later be transformed into tubular structures and vice versa. Both morphotypes have been found to be equally suitable to alleviate ER stress. (Schuck *et al.*, 2009). Consequently, the ER membrane is able to remodel and adapt dynamically to the new situation, and multiple morphological types of the so-called organized smooth ER (OSER) have been described (FIGURE 11) (Snapp *et al.*, 2003). Stacked sER cisternae are categorized with respect to their subcellular localization as either karmellae (located at the nuclear envelope) or lamellae (located elsewhere) (Wright *et al.*, 1988), while concentrically arranged ER membrane sheets are denominated whorls (Koning *et al.*, 1996). Besides the lamellar morphotypes, also tubular OSER structures are found. Ordered arrays of sinusoidal, tubular OSER can feature cubic or hexagonal symmetries exhibiting extreme membrane curvature, and are thus called crystalloid ER (Yamamoto *et al.*, 1996). Most notably, different types of OSER have not only been found in cells under various stress situations, such as drug treatment or protein overexpression, but also under physiological growth conditions (Snapp *et al.*, 2003). Thus, (re-) organization of the ER is not solely an indication for stress, but also reflects the ability of the cell to adapt to different physiological situations.

Shaping the ER

The wealth of different ER morphologies (as described above), in combination with the observation of a continuous re-organization of the different ER sub-domains raises questions about the mechanism(s) of ER shaping and stabilization of the resulting structures. Especially for the tubular ER morphotypes, extreme membrane curvature has been consistently documented (Chin *et al.*, 1982; Anderson *et al.*, 1983; Yamamoto *et al.*, 1996; Snapp *et al.*, 2003), and it has been suggested that they may represent different stages of sER differentiation (Takei *et al.*, 1994). Deformation of the ER membrane is also required for fusion and fission processes, which are mandatory for proper ER function (Kozlov *et al.*, 2010). Therefore, it is very unlikely that these structures assemble spontaneously. A number of cellular components have been proposed to participate in ER shaping, namely different membrane lipid species, integral membrane proteins, internal or external scaffolding proteins, cytoskeleton elements, and the insertion of amphipathic protein helices into the membrane (FIGURE 12) (McMahon & Gallop, 2005). Indeed, it was reported that reticulon- and reticulon-like protein-oligomers make major contributions to the ER tubular shape *via* insertion of hydrophobic components of the reticulon-domains into the cytoplasmic ER membrane leaflet (Voeltz *et al.*, 2006; Hu *et al.*, 2008). As a consequence, the occurrence of lamellar OSER types was attributed to an imbalance of the reticulon capacity upon ER growth (Schuck *et al.*, 2009). Undoubtedly, all of the above-mentioned mechanisms play a role in ER shaping, the most widely studied among them probably being the interaction of the ER membrane

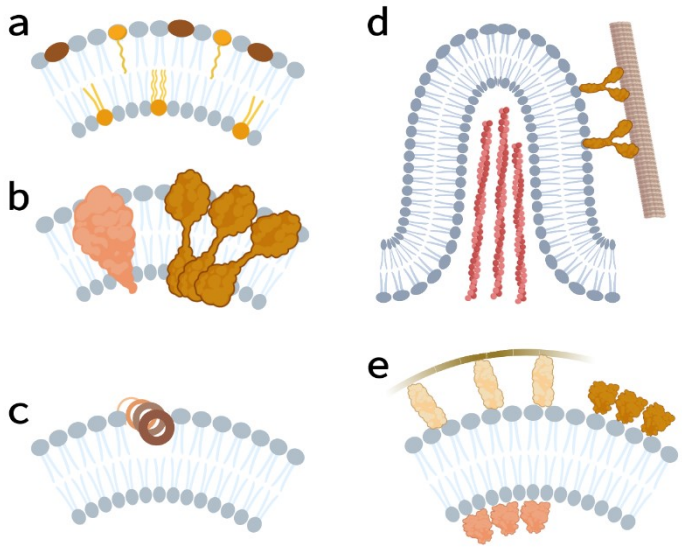

Figure 12: Mechanisms of ER shaping

Different options are discussed in literature that may enable the extreme curvature of ER membrane. a) Membrane lipid headgroup or acyl chain composition. b) Integral membrane protein shape and/or oligomerization. c) Insertion of amphipathic helices in the outer membrane leaflet. d) Actin or microtubule cytoskeleton. e) Indirect or direct (positive/negative) scaffolding. Drawn after (McMahon & Gallop, 2005).

with integral membrane proteins (FIGURE 12b). This, in turn, can be attributed to the fact that mutations within ER-associated proteins can lead to a multitude of severe diseases. As an example, mutations in the PERK kinase have been shown to trigger the development of diabetes (Harding & Ron, 2002). Similarly, misfolded UPR chaperone proteins may accumulate into plaques or fibrils within the brain, causing Parkinson's or Alzheimer's disease (Brown & Naidoo, 2012). As opposed to a broad understanding of biochemical and molecular biological details of the UPR, high-resolution structural information on ER differentiation and its intracellular context, however, is sparse and largely restricted to two-dimensional (2D) TEM images. Consequently, 3D data are needed to be able to interpret the molecular information within a profound, morphological background. Solely the combination of molecular, biochemical and structural data will allow for a global mechanistic understanding of the whole process of ER shaping upon stress sensing.

I. 5 Aims of this thesis

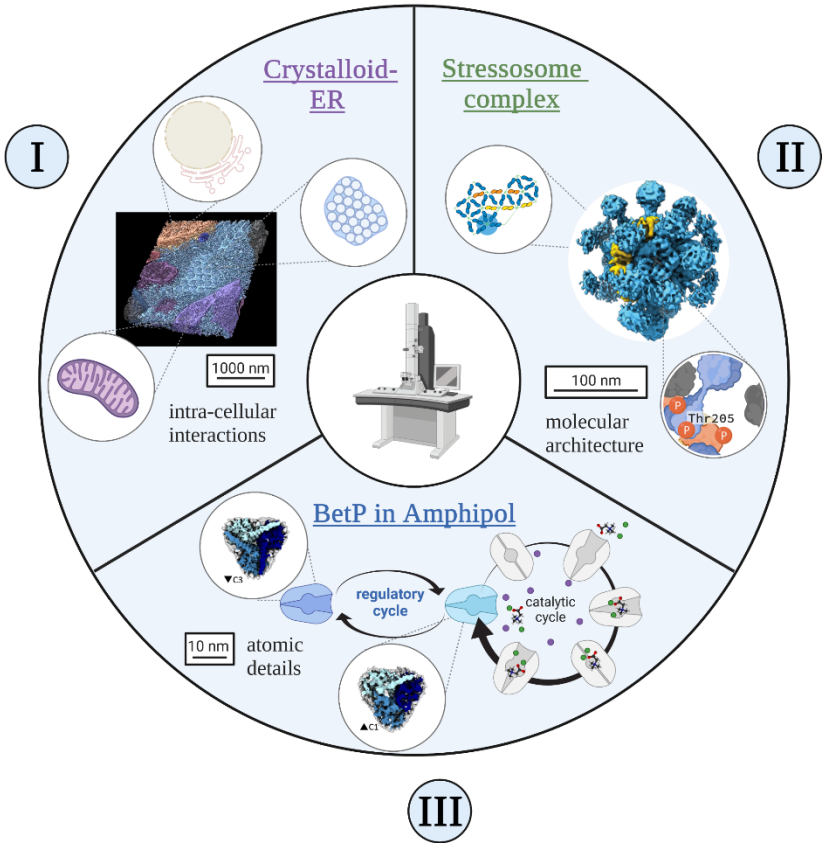

Figure 13: A focus on stress

The results obtained in course of thesis aim to shed light on three different aspects of one fundamental biological question: How do organisms sense and react upon stress? Although many details of bacterial and eukaryotic stress response mechanisms are well understood, it is often structural information that is ultimately missing to elucidate the whole process. Electron microscopy in all of its multiple flavors is thus a key method to investigate molecular mechanisms within their biological context and at different size scales.

Electron microscopy (EM) is a prime tool for the investigation of dynamic processes on a wide resolution range. Today, objects in the size of eukaryotic organelles, e.g. mitochondria or single prokaryotic cells, can be investigated by EM as well as isolated, single proteins with a molecular weight far below 100 kilo Dalton (kDa) (FIGURE 13 I, II and III). In this thesis, two different approaches are applied to cover the whole resolution range. For imaging cellular dynamics on organelle level, dual-axis STEM tomography following high pressure-freezing, freeze substitution and sectioning was selected. The aim of part I is to obtain 3D structural information of the crystalloid ER previously identified in HEK cells upon overexpression of PC-2. In particular, the ultrastructural organization of this ER morphotype is in the focus of the study. Moreover, putative intracellular interaction partners should be identified, to shed light on the differentiation of this unique organelle

and on its role within the cellular machinery. The three dimensional information will bridge the gap between the molecular-functional understanding and the complex architecture of the crystalloid-ER, and may ultimately provide valuable insights into its biogenesis, differentiation and impact within and on the cell.

In addition, single particle cryo-EM of isolated, vitrified proteins was selected to study the molecular architecture of large macro-molecular protein complexes at intermediate resolution, and to investigate the regulation of reconstituted membrane proteins at atomic resolution. In part II, it is aimed to obtain a structure of the minimal *V. vulnificus* RsbRS stressosome complex. Structural similarities or differences revealed in comparison with its gram-positive counterpart may give valuable mechanistic insights into complex assembly and regulation. The *V. vulnificus* RsbRS structure would represent the first example for a gram-negative stressosome. Elucidating the molecular mechanism that orchestrates the environmental stress response in this human pathogen may ultimately pave the way for targeted drug design.

In part III, a high-resolution structure of the betaine transporter BetP from *C. glutamicum* in its down-regulated state would be of high value towards a global understanding of osmostress regulation in this model organism. This state could not be observed so far, and consequently an important piece of structural information is missing. A high-resolution structure would help to answer fundamental open questions, in particular about the role of the sensory C-terminal domain, and might help to pinpoint the until now only vaguely defined membrane stimulus required for the full osmostress response in *C. glutamicum*. This unique model system offers the possibility to study stress sensing, signal transduction and reaction the same time, and potentially the obtained results may be transferred from the model organism to other systems as well in the future.

Finally, the wealth of data obtained during the aforementioned projects might also allow for a detailed methodological comparison. Datasets obtained from different microscopes, detectors and imaging modes allow to draw conclusions about imaging strategies for a broad variety of different samples. The selected methods should be evaluated critically with respect to their suitability in providing the required amount of structural information at an appropriate resolution. This comparison and the gained experience will be of high value to design further experiments.

II. Materials and Methods

II. 1 Materials, chemicals, buffers and equipment

Materials and special components

Routine laboratory materials and consumables (e.g. reaction vials, cell culture dishes, gloves …), as well as ordinary chemicals (e.g. NaCl, TRIS, Ethanol…) are considered of manufacturer-independent, constant quality, and thus not further mentioned here. Components explicitly listed in this section, in contrast, are considered relevant for experimental success, which can be attributed to e.g. purity, manufacturer's quality control or the manufacturing process itself.

Lipids

All synthetic lipids were manufactured by Avanti Polar Lipids Inc., Alabaster, USA. Originally sealed lipids were stored at -20 °C. Prepared lipid stock solutions (see RECONSTITUTION INTO MEMBRANE-MIMICKING SYSTEMS) were stored at -20 °C.

POPG (10 mg/mL, in Chloroform)

POPC (10 mg/mL, in Chloroform)

E. Coli Polar Lipid Extract (25 mg/mL, in Chloroform)

Soybean Polar Lipid Extract (10 mg/mL, in Chloroform)

Detergents

The following detergents were purchased in solid form from Anatrace, Maumee, USA and stored at -80 °C. Prepared stock solutions were stored frozen at -20 °C.

DDM: *n*-Dodecyl-β-D-Maltopyranoside (purity ≥ 99%)

Polymers for protein reconstitution

The list of polymers used for the reconstitution of membrane proteins is growing steadily. Thus, apart from well-established systems, many polymers are currently not commercially available for the use in biochemical applications. These were generously provided as free samples from the respective manufacturers.

Amphipol A8-35	Anatrace, Maumee, USA
SMA 1:1 (free sample)	Polyscope Polymers B.V., Geleen, NL
SMA 2:1 (free sample)	Polyscope Polymers B.V., Geleen, NL
DIBMA (Sokalan® CP 9, free sample)	BTC Europe GmbH, Ludwigshafen, DE

Antibiotics

Carbenicillin (stock solution: 100 mg/mL)	Carl Roth GmbH, Karlsruhe, DE
Anhydrotetracycline (stock solution: 2 mg/mL)	Sigma-Aldrich Chemie GmbH, St. Louis, USA
Tetracycline-Hydrochloride (stock solution: 10 mg/mL)	Sigma-Aldrich Chemie GmbH, St. Louis, USA
Penicillin/Streptomycin (stock s.: 10000 u Pen, 10 mg/mL Strep)	Sigma-Aldrich Chemie GmbH, St. Louis, USA

Antibodies

Anti-StrepTag®II IgG1	IBA Lifesciences GmbH, Göttingen, DE
Rabbit anti-Mouse IgG –AP	Sigma-Aldrich Chemie GmbH, St. Louis, USA

Column materials

Strep-Tactin® MacroPrep®	IBA Lifesciences GmbH, Göttingen, DE
Strep-Tactin® Superflow®	IBA Lifesciences GmbH, Göttingen, DE
Strep-Tactin® Sepharose®	IBA Lifesciences GmbH, Göttingen, DE
PD-10 Desalting Columns	GE Healthcare, Little Chalfont, UK

Heavy metal salts for negative staining

Uranyl Acetate	Merck KGaA, Darmstadt, DE
Uranyl Formate	Electron Microscopy Sciences, Hatfield, USA

Others

DNAse I	Roche Diagnostics GmbH, Risch, CH
Pefabloc® SC	Roche Diagnostics GmbH, Risch, CH
Bradford reagent	Sigma-Aldrich Chemie GmbH, St. Louis, USA
PageRuler Prestained Protein Ladder	Thermo Scientific™, Waltham, USA
HMW Native Marker Kit	GE Healthcare, Little Chalfont, UK
Bio Beads SM-2 polystyrene beads	Bio-Rad Laboratories Inc., Hercules, USA
Mica	Plano GmbH, Wetzlar, DE
Sapphire discs	M. Wohlwend GmbH, Sennwald, CH
Life cell carriers	Leica Microsystems GmbH, Wetzlar, DE
Epon™ 812 substitute embedding resin	Fluka Chemie AG, Buchs, CH

Media

Super optimal broth with catabolite repression (SOC) medium (pH 7.0)

2% (w/v)	Tryptone (Bacto)
0.5% (w/v)	Yeast extract (Bacto)
0.05% (w/v)	NaCl
2.5 mM	KCl
10 mM	$MgCl_2$
10 mM	$MgSO_4$
20 mM	Glucose

LB_{Carb} agar plates

1% (w/v)	Tryptone (Bacto)
0.5% (w/v)	Yeast extract (Bacto)
1% (w/v)	NaCl
1.5% (w/v)	Agar

Carbenicillin was added to a final concentration of 50 µg/mL after autoclaving, prior to pouring the plates.

LB_{Carb} medium

1% (w/v)	Tryptone
0.5% (w/v)	Yeast extract
1% (w/v)	NaCl

Carbenicillin was added to a final concentration of 50 µg/mL shortly before inoculation of the medium.

Buffers and reagents

Buffer A (pH 7.5)

50 mM	Tris(hydroxymethyl)aminomethane (TRIS)/HCl
200 mM	NaCl
10% (v/v)	Glycerol
0.05% (v/v)	DDM

Stacking gel buffer (pH 6.8)

0.5 M	TRIS/HCl
0.4% (w/v)	Sodium Dodecyl Sulphate (SDS)

Separating gel buffer (pH 8.8)

1.5 M	TRIS/HCl
0.4% (w/v)	SDS

1*x* Laemmli buffer (pH 8.3)

24 mM	TRIS/HCl
192 mM	Glycine
3.5mM	SDS

6*x* SDS loading buffer (pH 6.3)

600 mM	TRIS/HCl
12% (w/v)	SDS
0.6% (w/v)	Bromophenol blue
60% (v/v)	Glycerol
600 mM	Dithiothreitol (DTT)

10*x* native gel loading buffer

0.1% (w/v)	Ponceau S
50% (v/v)	Glycerol

Coomassie staining solution

0.1% (w/v)	Coomassie Brilliant Blue R-250
10% (v/v)	Acetic acid
40% (v/v)	Ethanol

Coomassie de-staining solution

10% (v/v)	Acetic acid
20% (v/v)	Ethanol

TRIS buffered saline (TBS) (pH 7.5)

150 mM	NaCl
10 mM	TRIS/HCl

Transfer buffer (pH 8.3)

25 mM	TRIS/HCl
190 mM	Glycine
20% (v/v)	Methanol

AP-Buffer (pH 9.0)

100 mM	TRIS/HCl
150 mM	NaCl
1 mM	$MgCl_2$

AB-Mix for native PAGE

48.5% (w/v)	Acrylamide
1.5% (w/v)	Bis-acrylamide

Native gel buffer (pH 7.0)

75 mM	Imidazole
1.5 M	ε-Aminocaproic acid
0.05% (w/v)	DDM

Anode-buffer for native PAGE (pH 7.0)

25 mM	Imidazole

Cathode-buffer for native PAGE (pH 7.0)

7.5 mM	Imidazole
50 mM	Tricine
0.02% (w/v)	Coomassie Brilliant Blue G-250

Freeze-substitution solution A:

0.5% (v/v)	Glutar-di-aldehyde (GA)
0.5% (w/v)	Uranyl acetate (UAc)
5% (v/v)	H_2O
in Acetone	

Freeze-substitution solution B:

0.5% (v/v)	OsO_4
0.25% (w/v)	UAc
5% (v/v)	H_2O
in Acetone	

RIPA-buffer (pH 7.4):

50 mM	Tris/HCl
1% (v/v)	Triton X 100
150 mM	NaCl
5 mM	Ethylenediaminetetraacetic acid (EDTA)
10 % (w/v)	Glycerol

List of instruments

Special lab equipment and instruments used for experiments are summarized in TABLE 3. Electron microscopes, used detectors and the respective configurations are mentioned in II. 4 ELECTRON MICROSCOPY – SINGLE PARTICLE ANALYSIS, II. 5 ELECTRON MICROSCOPY – TOMOGRAPHY and VII. 3 SINGLE PARTICLE DATA ACQUISITION AND PROCESSING PARAMETERS, respectively.

Table 3: List of instruments

instrument	manufacturer	purpose
SunriseTM absorbance reader	Tecan	readout of BCA assay
Hoefer gel electrophoresis apparature	Hoefer Inc.	SDS-PAGE
Biometra Fastblot System	Analytic Jena	Western blotting
PerfectBlueTM twin L system	Peqlab	blue native PAGE
Avanti J 26S-XP centrifuge	Beckman Coulter Inc.	cell harvesting
Optima MAX-XP benchtop ultra-centrifuge	Beckman Coulter Inc.	ultra-centrifugation (small volumes)
Optima XPN-100	Beckman Coulter Inc.	ultra-centrifugation (larger volumes)
ÄKTA™ purifier	GE Healthcare	size exclusion chromatography
Superose 6 Increase 10/300 GL column	GE Healthcare	gel filtration column
CF Cell Disruptor	Constant Systems Ltd.	cell breaking
Lyovac GT2	Leybold Heraeus GmbH	lyophilization
Cressington 208carbon	Tescan GmbH	carbon evaporator
EM PACT2	Leica Microsystems GmbH	high-pressure freezing
AFS2	Leica Microsystems GmbH	freeze substitution
EM UC7	Leica Microsystems GmbH	ultramicrotome
Plasma Cleaner PDC-3XG	Harrick Plasma Inc.	plasma cleaning
Vitrobot Mark IV	Thermo Fisher Scientific	vitrification
Leica EM GP	Leica Microsystems GmbH	vitrification

List of programs and software

The following list (TABLE 4) contains all programs and software packages, the versions that were used in course of this thesis, as well as the respective publications or copyright

information, respectively. 'Current' version indicates that the respective software was updated frequently and several current versions were used throughout the thesis.

Table 4: List of software

Program	Version(s)	Used for	Reference(s) / copyright
EM MENU	current	screening, SPA data acquisition	© TVIPS - Tietz Video and Image Processing Systems GmbH
EM-Tools	current	STEM tomography	© TVIPS - Tietz Video and Image Processing Systems GmbH
SerialEM	current	SPA data acquisition	(Mastronarde, 2003, 2005)
EM2EM	20-Aug-2019	image format conversion	© Image Science Software GmbH
MotionCor2	current	movie frame alignment	(Zheng *et al.*, 2016)
CTFFIND4	current	CTF estimation	(Rohou & Grigorieff, 2015)
RELION	2.0 - current	SPA	(Scheres, 2012a, 2012b)
SIDESPLITTER	current	SPA - refinement	(Ramlaul *et al.*, 2020)
ResMap	current	local resolution estimation	(Kucukelbir *et al.*, 2014)
Scipion	current	Eigenimages	(De la Rosa-Trevín *et al.*, 2016)
Spider	current	Eigenimages	(Frank *et al.*, 1996)
cryoSPARC	current	SPA	© 2021 Structura Biotechnology Inc.
CryoEF	current	orientation distribution assessment	(Naydenova & Russo, 2017)
IMOD	current	tomogram reconstruction	(Kremer *et al.*, 1996)
Gephi	0.9.2	protein interaction network analysis	© 2008-2017 Gephi contributors
SeggeR	1.9.5	cryo-EM mask generation, tomogram segmentation	(Pintilie *et al.*, 2010)
ImageJ	1.53c	data analysis	(Abràmoff *et al.*, 2004)
UCSF Chimera	1.14 (daily build)	data analysis, visualization, figures	(Pettersen *et al.*, 2004)
UCSF ChimeraX	0.9	Visualization, figures	(Goddard *et al.*, 2017)
Adobe Photoshop CS4	11.0	Figures	© 1990-2008 Adobe Systems Inc.
WinCoot	0.8.9.2 EL	model building	(Emsley *et al.*, 2010)
Phenix	1.16-3549	real space refinement	(Adams *et al.*, 2009)
eLBOW	current	ligand restraints	(Moriarty *et al.*, 2009)

II. 2 Protein Biochemistry

Membrane protein expression and purification

Transformation of *E. coli* cells

A 100 µL aliquot of competent *E. coli* cells (*E. coli* DH5α $T1^R$, ThermoFisher Scientific, Waltham, USA) was gently thawed on ice. Plasmid DNA (minimum concentration 100 ng/µL) was also thawed on ice. 20 µL of the cells were transferred into a fresh reaction tube and served as a negative control. 1.5 µL of the plasmid DNA were added to the rest of the cells. Both reaction mixtures were incubated on ice for 30 min. Subsequently, a heat shock was performed for 45 sec at 42 °C, and the cells were incubated on ice for another five min. 1 mL of pre-warmed SOC medium was added to each reaction mixture, and the cells were incubated for 1 h at 37 °C and 200 rpm. Afterwards, the cells were gently spun down for 1 min in a tabletop centrifuge and all but 100 µL of the supernatant was removed. After re-suspending, the cells were spread on 4 pre-warmed LB_{Carb} agar plates as follows: 100 µL of the negative control; 5 µL, 50 µL or the rest of the transformed cells. The plates were incubated ON at 37 °C and screened for the presence of nicely separated *E. coli* colonies the next morning.

Protein expression

For the heterologous protein expression in *E. coli* cells, a pre-culture was prerequisite. First, several colonies from the transformation plate were transferred with a sterile loop into 5 mL of pre-warmed LB_{Carb} medium. The culture vial was incubated at 37 °C and 170 rpm for at least 3 h. From this first culture, six times 0.5 mL were used to inoculate six flasks with 50 mL pre-warmed LB_{Carb} medium. These pre-cultures were incubated ON as described before. The next day, the optical density (OD_{600}) of the pre-culture was determined. If in a range between 3.4 and 3.7, 50 mL of the pre-culture were used to inoculate the main culture of 1 L pre-warmed LB_{Carb} medium (6 flasks in total). The main cultures were incubated as described before. After an OD_{600} of 0.6 was reached, expression of BetP was induced by the addition of Anhydrotetracycline (AHT) to a final concentration of 0.2 mg/L. After

having reached an OD_{600} of 2.1 – 2.4, the cells were harvested *via* centrifugation at 4,000 rpm and 4 °C in an Avanti J 26S-XP centrifuge (rotor JLA8.1000) for 30 min.

Membrane protein purification

The cell pellet was re-suspended in 100 mM TRIS/HCl pH 7.5 supplemented with 0.05% (w/v) DNAse I and 0.24 mg/mL Pefabloc. Subsequently, cells were disrupted in a cell disruptor at 1.8 kbar and 4 °C. Debris was removed *via* centrifugation at 24,000 *x* g and 4 °C for 45 min. The remaining membranes were pelleted *via* ultra-centrifugation in a Optima XPN-100 ultra-centrifuge at 235,000 *x* g and 4 °C for 1 h, followed by re-suspension in 50 mM TRIS/HCl pH 7.5, 10% glycerol to a final concentration of ~50 mg/mL. DDM was added dropwise under gentle stirring to a final concentration of 2% (v/v) to solubilize all membrane proteins. Subsequently, the solubilization mixture was incubated for 30 min at room temperature (RT) under gentle stirring. Then, NaCl was added to a final concentration of 200 mM as described before, and the solution was incubated for an additional 30 min at 4 °C, until the initially cloudy solution had cleared up significantly. The solubilized proteins were separated from membrane debris *via* ultra-centrifugation at 235,000 *x* g at 4 °C for 1 h. For purification of StrepII-tagged BetP, the supernatant was loaded drop-wise to a Strep-column equilibrated with buffer A ON at 4 °C. Five to ten column volumes (CV) of the same buffer were used for washing to remove unbound protein from the column. Finally, BetP was eluted in buffer A supplemented with 5 mM Desthiobiotin in 500 µL fractions. Elution was monitored by the 'quick Bradford assay'. The Bichinonic acid (BCA) assay was used for protein concentration determination of the elution fractions. The purified protein was further reconstituted into different membrane mimicking systems.

Reconstitution into membrane-mimicking systems

Preparation of lipid stocks

For the reconstitution into Nanodiscs with a defined lipid environment, lipid stocks were prepared as follows: the solution of chloroform-dissolved lipids was transferred from the air-tight sealed ampulla into a chloroform rinsed round-bottomed flask. To remove the solvent, the liquid was fumed with gaseous Nitrogen at a constant flow pressure of 0.1 bar

with gentle stirring until chloroform had evaporated completely. Subsequently, the resulting lipid cake was dried in a desiccator for 1 h, to remove last remnants of the solvent from the lipids. The lipid cake was then dissolved in a suitable amount of detergent-containing buffer, to obtain a final concentration of 10 mM – 50 mM. If required, the solution was heated gently in a water bath, until all lipids were dissolved completely. The resulting stock solution should have a slightly opaque appearance without visible precipitates or smear. Finally, aliquots of the prepared lipid stock solution were flash-frozen in lN_2 and stored at -20 °C.

Preparation of DIBMA polymer powder from Sokalan CP 9

A free sample of Sokalan® CP 9 solution was kindly provided by BTC Europe GmbH. The chemical is sold as a cleaning agent, containing di-isobutylene-maleic acid (DIBMA) of unknown purity grade and dissolved in unknown buffer. It was therefore chemically processed, to obtain pure DIBMA powder that could be used to prepare stock solutions in the desired concentrations and buffers. 100 mL of the Sokalan® CP 9 solution were poured into a 1 L beaker. 37% HCl was added dropwise under constant stirring, until DIBMA had precipitated completely. The precipitate was transferred into a fresh beaker and washed thoroughly in H_2O_{milli}, to completely remove remnants of the original solvent. Subsequently, 5 M NaOH was added dropwise, to raise the pH above 9.0 and re-dissolve DIBMA. Precipitation, washing and dissolving of the polymer were performed multiple times, until the precipitate had reached a white, fine-grained appearance that did not change any more during the procedure. Next, the precipitate was transferred to a filter funnel and dried over a vacuum filtering flask. The resulting DIBMA polymer chunks were freeze dried in a lyophilizer ON, and a last drying step was performed for several days over silica gel in a desiccator. Finally, the dried DIBMA nuggets were homogenized using a mortar, resulting in fine-grained, white polymer powder. The purified DIBMA powder was stored in air-tight sealed plastic vials at -80 °C.

Preparation of stock solutions from DIBMA polymer powder

Ready-to-use DIBMA stock solutions were prepared from DIBMA powder purified as described above. The desired amount of DIBMA powder was added to the buffer, and the solution was mixed thoroughly on a rotary shaker for 30 min. The pH of the cloudy solution

was checked using pH paper strips. 5 M NaOH was added dropwise under constant stirring, until the desired pH was reached and the polymer had visibly dissolved. Note that the polymer will only dissolve completely above pH = 8.0. If necessary, the DIBMA solution was sonified for a short period of time in a sonication bath, until the resulting stock solution had a clear and transparent appearance.

Reconstitution into Amphipol A8-35

Amphipols are amphipathic polymers that can be used to replace the detergent micelle after solubilization of membrane proteins. In comparison to detergents, they feature superior membrane mimicking properties. The addition of external lipids is not required (Tribet *et al.*, 1996; Gohon *et al.*, 2006; Le Bon *et al.*, 2018).

A stock solution of 100 µg/µL Amphipol A8-35 was prepared. For reconstitution, detergent-solubilized and affinity-purified protein was mixed with the polymer stock solution in a 1:3 (w/w) ratio of Amphipol:protein. After incubation for 4 h at 4 °C under gentle agitation, 50 mg of Bio Beads were added to the reaction mixture. The sample was further incubated at 4 °C ON with gentle agitation. Subsequently, another batch of 50 mg Bio Beads was added and the sample was incubated for one more hour as described above. Finally, the Bio Beads were removed from the mixture, and size exclusion chromatography (SEC) was performed as a final step of purification and to remove excess Amphipol polymer.

Reconstitution into Salipros

This reconstitution method is based on the use of Saposin A in combination with lipids to substitute the detergent micelle of solubilized membrane proteins. The method was developed by Jens Frauenfeld, and reconstitution of BetP into Saposin-Lipid-Protein particles (Salipros), was kindly perfomed by his team (Salipro Biotech AB, Stockholm, SWE) as a collaboration project. Further information on the reconstitution principle can be found in the respective publications (Frauenfeld *et al.*, 2016; Lyons *et al.*, 2017), and is also discussed in this thesis (IV. DISCUSSION).

Reconstitution into nanodiscs

Reconstitution into nanodiscs represents the 'classic' reconstitution method, well established for functional and structural investigations of membrane proteins in a defined lipid environment. Nanodisc particles are composed of the membrane protein itself, externally added lipids, and circular, α-helical membrane scaffold proteins (MSPs) surrounding the discs. MSPs are distributed in a variety of lengths, allowing for the generation of nanodiscs of defined, different sizes (Bayburt *et al.*, 2002; Ritchie *et al.*, 2009; Bayburt & Sligar, 2010). In this thesis, the variants MSP1E3D1 and MSP2N2, resulting in average disc sizes of ~12 nm and ~16 nm, respectively, were used. The scaffold proteins were expressed, purified and kindly provided by Dr. Pia Berlik and Felix Fischer.

The reaction mixture for the formation of nanodiscs comprises the detergent-solubilized membrane protein, the MSP and the lipids. The components are always mixed in a pre-defined molar ratio, which needs to be carefully optimized. The MSP concentration is usually defined as '1', while the other components are adjusted respectively. E.g., for the formation of nanodiscs with a molar ratio of 0.3:1:100 (membrane protein:MSP:lipids), 1 mg of MSP was used, and the required volumes of concentrated membrane protein and lipid stock solution were calculated according to their respective concentrations.

For nanodisc formation, the determined volumes of membrane protein and lipids were mixed in a 2 mL reaction vial and incubated for 30 min on ice. Subsequently, MSP was added and the mixture was incubated for another 10 min on ice. For a gentle, stepwise removal of the detergent from the reaction mixture, Bio Beads were added in batches of 20 mg Bio Beads per 1 mL of reaction mixture. The first batch was transferred into the reaction vial, and the mixture was incubated on a rotary shaker for 1 h at 4 °C. Subsequently, a second batch of Bio Beads was added, followed by incubation ON as described before. Finally, a third batch of Bio Beads was added and the reaction mixture was incubated for 1 h as described before. Reconstitution success was first inspected visually: if foam was still present on the samples, another batch of Bio Beads was added to remove remnant detergent from the samples. Otherwise, the samples were analyzed and purified further *via* SEC (BIOCHEMICAL AND ANALYTICAL METHODS).

Reconstitution into SMALPs and DIBMALPs

Styrene-maleic acid (SMA) copolymers represent an alternative membrane protein reconstitution method offering the advantage of being detergent-independent. The hydrophobic polymers are added directly to the prepared membranes, and membrane proteins are solubilized and reconstituted into SMA-lipid-particles (SMALPs) simultaneously. Optional, aliphatic di-isobutylene-maleic acid (DIBMA) polymers can be used, which tolerate a broader spectrum of buffer environments (Vargas *et al.*, 2015; Oluwole *et al.*, 2017). An overview of the most important (bio-) chemical properties of the polymers used in this thesis is presented in TABLE 5.

Table 5: Chemical properties of selected SMA and DIBMA polymers

short name	**chemical composition**			**polymer properties**			
	polymer	subunits	subunit ratio	particle sizes [nm]	average molecular weight [g/mol]	pH range	tolerance of divalent cations [mM]
SMA 1:1	styrene-maleic acid	styrene, maleic acid	1:1	10 – 13	~ 5000	≥ 6.5	5
SMA 2:1	styrene-maleic acid	styrene, maleic acid	2:1	10 – 13	~ 7500	≥ 6.5	5
DIBMA	di-isobutylene-maleic acid	di-isobutylene-maleic acid	1:1	18	~ 12000	7.3 – 8.4	35

For the reconstitution into SMALPs/DIBMALPs, membranes were prepared as described in MEMBRANE PROTEIN EXPRESSION AND PURIFICATION. 20% stock solutions of SMA and DIBMA were prepared in 25 mM TRIS/HCl, 200 mM NaCl; these were diluted further as required. For small-scale solubilization tests, 500 µL – 1000 µL of the membrane sample were mixed with the respective volume of the polymer solution and incubated at room temperature (RT) under gentle agitation for the desired period of time. Subsequently, cell debris was removed *via* ultra-centrifugation in a MLA 130 rotor at 70,000 rpm and 15 °C for 45 min. The supernatants were transferred into a fresh reaction vial; the corresponding pellets were re-suspended in 25 mM TRIS/HCl, 200 mM NaCl, restoring the original reaction volume. All samples were analyzed further *via* western blot; samples with a

sufficient solubilization efficiency could be affinity purified as described in MEMBRANE PROTEIN EXPRESSION AND PURIFICATION.

Biochemical and analytical methods

Protein concentration determination - Bradford assay

A fast version of the Bradford assay (Bradford, 1976) was used to check for the presence of protein during purification and reconstitution experiments. For samples with an expectedly high protein content, 2 µL of the sample were diluted with 48 µL of H_2O_{milli} in a 96 well plate. 150 µL of Bradford reagent were added. A color change from brown to blue indicated the presence of protein in the sample. For samples with a lower expected protein content, 5 µL or 10 µL sample volume were used and diluted with 45 µL or 40 µL of H_2O_{milli}, respectively.

Protein concentration determination - Bicinchoninic acid (BCA) assay

The BCA assay (P. K. Smith *et al.*, 1985) was used for an accurate determination of the protein concentration of any sample. The assay was performed using the detergent compatible Thermo Scientific™ Pierce™ BCA™ Protein assay kit, following the manufacturer's instructions. In brief, several appropriate dilutions (in sample buffer) were used for each protein sample. The protein concentration was determined as a fourfold measurement for each dilution. A standard curve (twofold measurement) was performed for each assay using bovine serum albumin (BSA) as protein standard with known concentration. The assay was pipetted in a 96 well plate, and incubated for 30 min at 37 °C. Afterwards, the protein concentration was read out using the Tecan Sunrise™ instrument.

SDS-polyacrylamide gel electrophoresis (PAGE)

Table 6: SDS PAGE gel composition

component	stacking gel (5.7%)	separating gel (12%)
Acrylamide 30%	1.5 mL	8.0 mL
stacking gel buffer	1.5 mL	---
separating gel buffer	---	5 mL
H_2O_{milli}	4.8 mL	7.0 mL
APS 10% (w/v)	100 µL	200 µL
TEMED	10 µL	20 µL

12.0% SDS-gels were cast according to the manufacturer's instructions using the components given in TABLE 6 and stored at 4 °C until usage. The gel was inserted to a Hoefer gel electrophoresis apparature. 1*x* Laemmli buffer (Laemmli, 1970) was added into the chamber. For preparation of protein samples, 6*x* SDS loading buffer was added in a ratio of 1:2 loading buffer : protein sample (to achieve better migration of detergent- and/or lipid-containing membrane protein samples). Samples were mixed thoroughly, incubated for at least 10 min and spun down in a mini benchtop centrifuge. A suitable amount of the protein samples was applied to the pockets of the gel, along with 7 µL of pre-stained protein standard solution. Gels were run for 35 min at 90 mA (constant) and 300 V. The process was monitored by judging the separation of the pre-stained protein standard bands; running time was adjusted accordingly. Subsequently, the gel was removed from the chamber and either used for western blot analysis (see below), or the protein bands were directly visualized by staining with Coomassie staining solution for 30 min with gentle shaking. Afterwards, de-staining of the gel was achieved by several incubation steps in Coomassie de-staining solution and finally H_2O_{milli}. For documentation, pictures of the gel were taken with a standard digital camera.

Western blot

For specific detection of tagged proteins, semi-dry western blot analysis (Towbin *et al.*, 1979) was performed. First, the samples were separated on a SDS gel as described above. Prior to blotting, four sheets of Whatman filter paper were soaked in transfer buffer, the polyvinyl-difluorid (PVDF) blotting membrane (Immobilon-P 0.45 µm, Merck Millipore; Billerica, USA) was activated in methanol. Two sheets of filter paper, the blotting

membrane, the SDS gel and two more sheets of filter paper were assembled in the blotting chamber according to the manufacturer's instructions. Transfer of the protein samples onto the blotting membrane was performed for 35 min at 25 V and 0.2 A (constant). The membrane was subsequently subjected to protein detection *via* antibodies. First, a blocking step was performed with 3% BSA in TBS buffer for 30 min at RT with gentle shaking, to saturate unspecific binding sites. After three short washing steps (10 min in TBS buffer at RT, with gentle shaking), the primary antibody (anti-StrepTag®II IgG1) was applied for 30 min (RT, gentle shaking). Excess antibodies were removed by washing as described before, and the secondary antibody (rabbit anti-Mouse IgG (whole molecule) -alkaline phosphatase) was applied, again for 30 min (RT, gentle shaking). Both antibodies were used in a 1:5,000 dilution. Thereafter, washing was performed as described previously, and the tagged protein bands could be visualized. The membrane was developed with a freshly prepared solution of 50 µL 5-Brom-4-chlor-3-indoxylphosphat (BCIP, 50 mg/mL in 100% Dimethyl-formamide (DMF)) and 100 µL Nitro blue tetrazolium (NBT, 50 mg/mL in 70% DMF), dissolved in 10 mL AP buffer until the bands were clearly visible. The reaction was stopped by the addition of H_2O_{milli}, and the membrane was washed thoroughly in H_2O_{milli} to remove residual developing solution. After drying of the membrane between two sheets of tissue paper, documentation of the tagged protein bands was performed using a standard digital camera.

Blue native PAGE

Blue native PAGE was performed to analyze oligomeric state and native molecular mass of purified and reconstituted membrane proteins. In contrast to SDS-PAGE (as described above), the proteins are separated under native conditions, thereby maintaining their structural and compositional integrity (Schaegger *et al.*, 1994; Wittig & Schaegger, 2009).

Table 7: Blue native PAGE gel composition

Component	stacking gel (4%)	separating gel (5%)	separating gel (13%)
AB-Mix*	1.2 mL	2.1 mL	5.5 mL
native gel buffer	4 mL	7 mL	7 mL
Glycerol 50% (v/v)	---	---	8.4 mL
H_2O_{milli}	6.7 mL	11.8 mL	---
APS 10% (w/v)	100 µL	100 µL	100 µL
TEMED	10 µL	10 µL	10 µL

* is prepared separately and stirred thoroughly until completely dissolved

For native PAGE, gels (TABLE 7) were prepared directly before usage and polymerized for at least 30 min to 1 h. A PerfectBlue™ twin L gel casting base was used to cast 5% to 13% (Acrylamide/Bis-acrylamide) gradient gels according to the manufacturer's instructions, using a home-made gradient mixing device (mechanical workshop, University of Regensburg). After assembly of the gel chamber and mounting of the gel, Anode- and Cathode-buffer were prepared freshly and poured into the respective reservoirs. Protein samples were mixed gently with 10*x* native loading buffer and loaded into the gel pockets. A maximum of 30 µg of protein could be used. 10 µL of the HMW Native Marker protein standard solution were loaded onto the gel as well. Subsequently, the protein samples were separated by electrophoresis at 300 V and 5 mA (constant) ON for at least 18 h under permanent cooling. Thereafter, the protein bands were stained with Coomassie staining solution for 30 min while gently shaking, and de-stained with Coomassie de-staining solution until clearly visible. A last de-staining step was performed in H_2O_{milli}. For documentation, pictures of the gel were taken with a standard digital camera.

Size exclusion chromatography (SEC)

SEC was performed to separate protein samples according to their hydrodynamic volumes as a final step of purification, for analytical comparison of samples, and as well as a method for sample quality control. The respective protein sample was fractionated on a Superose 6 Increase 10/300 GL column connected to an ÄKTA™ purifier system. The ÄKTA™ system and the column were washed and pre-equilibrated with the running buffer prior to the SEC run(s) according to the manufacturer's advice. The protein sample was filtered through a 0.22 µm spin-through filter unit prior to SEC, to remove larger protein aggregates. 200 µL – 450 µL of the protein sample were loaded onto the column per SEC run, depending on the sample concentration. SEC was performed in either 25 mM TRIS/HCl pH 7.5, 100 mM NaCl for cryo-EM SPA of the down-regulated state of BetP, or in 25 mM TRIS/HCl pH 7.5, 200 mM NaCl, 300 mM KCl for cryo-EM SPA of the transition state of BetP. SEC was performed at a flow rate of 0.5 mL/min and fractions of 0.5 mL were collected. A primary analysis of the resulting SEC profiles was executed with the corresponding Unicorn software package (GE Healthcare, Chalfont St Giles, UK) for de-convolution and overlay of chromatograms. For a better comparison of analytical SEC runs, the chromatograms were normalized to a void volume peak retention volume of 8.0 mL prior to overlaying them in Excel (Microsoft Corporation, Redmont, USA).

II. 3 Eukaryotic cell culture

Expression of PC-2 in a stable cell line

For overexpression of wild type (WT) PC-2 in adherent HEK cells, the stable cell line HEK293S GnTI$^-$ as used by M. Wilkes and co-workers was available (Wilkes *et al.*, 2017). Plasma-cleaned TC 60 cell culture dishes, supplied with prepared sapphire discs (see HIGH-PRESSURE FREEZING, FREEZE SUBSTITUTION AND SECTIONING) were used for cultivation. A vital, adherent cell culture was split and used for seeding into the prepared dishes to an initial confluence of at least 10%. Cells were grown in DMEM/F-12 medium (Sigma-Aldrich®, St. Louis, USA), supplemented with 10% fetal bovine serum (FBS), 5 µg/mL Blasticidin, 350 µg/mL G418, and Pen/Strep (55 u/mL Penicillin, 55 µg/mL Streptomycin). Cells were incubated at 37 °C to reach a confluence of 40%; subsequently, protein expression was induced *via* addition of Tetracycline to a final concentration of 3 µg/mL. After 72 h of growth, the cells had reached a confluence of 80% - 90% and were harvested for further analyses as described below. Non-induced cells were grown simultaneously and analyzed in the same way as a negative control.

Cell harvesting for tomography

72 h after induction, PC-2 expressing cells were harvested and prepared for tomography. Growth of cells on the sapphire discs was checked under the light microscope and should reach at least 80% confluence. Furthermore, the cells should be grown as a monolayer and not be grown beneath the sapphire discs. Sapphire discs not fulfilling these criteria were discarded, while discs considered suitable were placed into the set life cell carriers and immediately covered with a small volume (< 5 µL) of cell culture medium to protect the cells. Subsequently, the sapphire disc-life cell carrier assembly was subjected to high-pressure freezing (see HIGH-PRESSURE FREEZING, FREEZE SUBSTITUTION AND SECTIONING). The remaining cells were harvested from the bottom of the cell culture dish *via* a sterile cell scraper, transferred into a sterile reaction vial, flash frozen and stored at -20 °C for subsequent western blot analysis to confirm the expression of PC-2.

Sample preparation for western blot analysis

Frozen cell pellets were thawed and re-suspended thoroughly in 100 µL RIPA-buffer. After 30 min of incubation on ice, cell debris was removed *via* centrifugation in a benchtop centrifuge at 4 °C and 14,000 rpm for 10 min. The supernatant was transferred into a fresh reaction vial, and 20 µL of 6*x* SDS loading buffer were added to each sample. After a short time of incubation at RT, the samples could be used for SDS-PAGE as described in BIOCHEMICAL AND ANALYTICAL METHODS.

II. 4 Electron microscopy – single particle analysis

SPA allows for the 3D analysis of isolated, vitrified single particles and the resulting volumes can be further used for building near-atomic models of the respective protein. To obtain the best resolution possible, the process requires consequent optimization at various experimental steps, as illustrated in FIGURE 14 and explained in the following section.

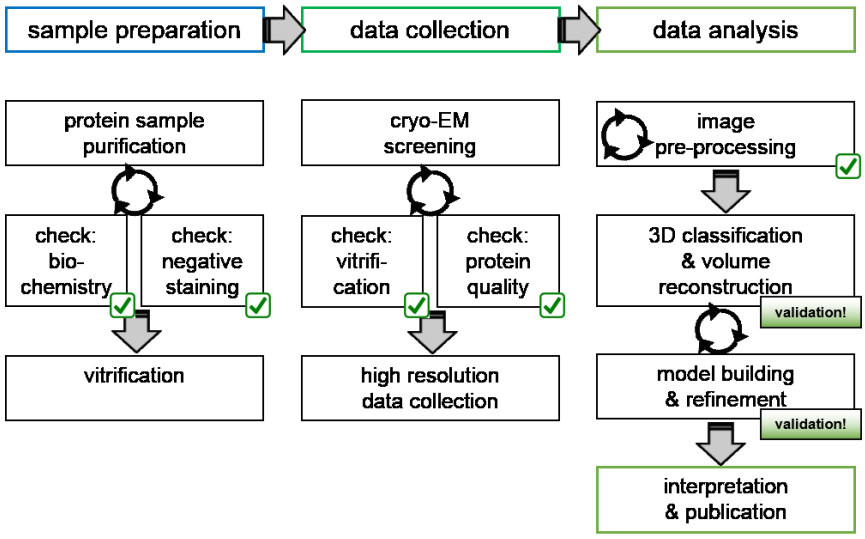

Figure 14: SPA workflow

The SPA workflow comprises a number of experimental steps that have to be carefully optimized to yield the best possible results. Several procedures have to be iteratively repeated, and finally, careful validation is required for a meaningful interpretation of the data.

SPA sample preparation

Preparation of staining solutions

Aqueous solutions of UAc or uranyl formate (UFo) were used for negative staining of protein samples. H_2O_{milli} was pre-warmed to 60 °C to improve solubility of the staining reagent. UAc or UFo powder was added to a final concentration of 2 % (w/v) and dissolved by gentle stirring. 2 - 5 drops of acetic acid were added to the UAc solution to improve solubility and stability. 2 -5 drops of 5 M NaOH were added to UFo solution to increase the pH. The pH of the staining solutions was checked with pH paper strips and should be

around 4.0 for UAc and 4.5 for UFo. Ready-made solutions were filtered through a 0.22 µm syringe filter to remove precipitates and stored at 4 °C in the dark.

Preparation of carbon films

Home-made continuous carbon films were used as sample support for negative staining. The carbon film was prepared by thermal evaporation in a carbon evaporator. A sheet of Mica was freshly cleaved with a razor blade to generate two clean and even surfaces. The Mica sheets were fixed on a glass slide, inserted to the carbon evaporator and the evaporator chamber was evacuated. The film was created on the Mica surface by evaporating material from a carbon rod target at a voltage of 2.6 V. The thickness of the generated films was adjusted to 10 - 15 nm by variation of the evaporation time. The films were left for settling ON, stored dust-protected and could be used from the next day on to coat grids.

Preparation of carbon-coated grids

Carbon-coated grids were used for negative staining of protein samples. A home-made floating device was used for coating. Freshly glow-discharged copper grids (400 mesh; Plano GmbH; Wetzlar, Germany) were lined on a piece of filter paper, placed below water level (H_2O_{milli}) in the floating device. The prepared carbon film was floated off the Mica support on the water surface. By lowering the water level, the film was evenly applied to the grids. Carbon-coated grids were baked at 120 °C for at least 3 h.

Negative staining

Negative staining was used for the investigation of protein samples, as it is commonly accepted as the standard method. The problem of intrinsically low contrast of purified proteins in the electron microscope is bypassed by enclosing the particles with a thin layer of a heavy metal salt. This layer of electron-dense material around the protein creates an area of high contrast surrounding the particles, which appear as bright objects on a dark background (Brenner & Horne, 1959). The method was used for quality control of both protein purification and reconstitution. All staining solutions were spun down in a tabletop centrifuge at 13,000 rpm for at least 10 min prior to usage. For negative staining, 3 µL of

protein sample (concentration: 10 - 20 mAU according to SEC) were applied on a freshly glow-discharged, carbon coated grid and incubated for 60 sec. After adsorption of the sample to the carbon film, the droplet was gently blotted away with filter paper from the edge of the grid. 3 µL of the staining solution were applied immediately as a short washing step. Again, the droplet was blotted from the edge of the grid. 3 µL of staining solution were applied and incubated on the grid for 30 sec for staining. The grid was blotted dry from the bottom and stored in a grid box for further investigation.

Vitrification

Vitrification is considered the state-of-the-art preparation method for SPA today and was established by Nobel laureate Jacques Dubochet and co-workers in the 1980s (Dubochet *et al.*, 1988). For vitrification, the protein solution is applied to a grid, blotted with a filter paper, and the remaining, thin layer of liquid is frozen rapidly in a cryogen. This results in the proteins embedded in vitrified, glass-like ice, since the fast freezing process circumvents the formation of ice crystals in the sample. Artifacts caused by crystalline ice or the presence of staining agents are thus avoided, and the method is suitable to obtain high-resolution cryo-EM images.

Protein samples for SPA were vitrified in a Vitrobot Mark IV or a Leica EM GP plunge freezing device. The environmental chambers of the instruments were pre-equilibrated to 4 °C and maximal humidity. Liquid ethane (Linde GmbH, Pullach, DE) was prepared freshly. Quantifoil® R 1.2/1.3 or R 2/2 copper grids (400 mesh) were used as sample support. The grids were plasma-cleaned for 1 min on each side directly before usage. For sample preparation with the Vitrobot Mark IV, 3.5 µL of the sample were applied to the holey carbon film on the grid manually. In the case of BetP, a sample concentration of 2,000 mAU after SEC, equivalent to 1 mg/mL, was aspired. Subsequently, blotting and plunge-freezing were performed automatically by the machine, without additional wait time. The blot force was always set to zero. Common blotting times yielding good results ranged from 5.0 sec to 6.0 sec. With these settings, a rather steep, yet smooth ice thickness gradient could be reproducibly achieved on the grids, with a sufficient number of holes covered by very thin, vitrified protein sample suitable for high-resolution cryo-EM data collection. For vitrification with the Leica EM GP, 4 µL of the sample were applied to the grid as described before. One-sided blotting at the instrument allowed for use of the blotting

sensor. Typical blotting times ranged from 2.4 sec to 3.2 sec. With this approach, grids of equal ice thickness without a steep thickness gradient could be obtained. The prepared grids were transferred to a cryo-grid box and stored in lN_2 until further usage.

SPA cryo-EM data acquisition

Negative stain screening

For initial investigation of negatively stained samples, a Phillips CM12 (FEI, Hillsboro, USA) transmission electron microscope at an acceleration voltage of 120 keV was used. The samples were documented with a slow-scan charge-coupled device (CCD) -camera (TVIPS0124, 1k *x* 1k pixels, TVIPS GmbH, Gauting, DE) at magnifications between 13,000*x* and 22,000*x*. This setup was used to screen the grids for a suitable particle concentration and adequate staining quality. The software package EM-Menu was used for data acquisition.

Negative stain dataset acquisition

A JEM 2100F (JEOL, Tokyo, JPN) transmission electron microscope, operated at 200 keV, was used for the acquisition of single particle datasets of negatively stained protein samples. On average, 20 to 40 micrographs were collected with a complementary metal-oxide semiconductor (CMOS) camera (TemCam-F416, 4k *x* 4k pixels, TVIPS GmbH, Gauting, DE) at magnifications of 30,000*x* to 50,000*x*. Depending on the magnification, the defocus range was set to -1.0 to -2.5 µm. The software package EM-Menu was used for data acquisition. After conversion to .mrc image format using EM2EM, the micrographs were analyzed further using CTFFIND and RELION.

Cryo-EM data acquisition

All high-resolution single particle cryo-EM datasets were collected with collaboration partners at different electron microscopes and detectors. Already before the start of this thesis, Susann Kaltwasser collected the *Vibrio vulnificus* Stressosome complex dataset manually at the Max-Planck-Institute for Biophysics in Frankfurt/Main (Germany). The Salipro-BetP (WT) data were kindly collected fully automated at the cryo-EM core facility

of the Max Planck Institute for Biochemistry in Martinsried (Germany) by Mike Strauss. The Amphipol-BetP dataset (down-regulated state) collected in the context of this thesis was automatically collected at the Rudolf-Virchow-Centre at the University of Würzburg (Germany) by Bettina Boettcher's group. Finally, the SPA cryo-EM dataset of Amphipol-reconstituted BetP in the transient-active state was collected in Halle with Panagiotis Kastritis' group. Detailed information about electron microscope and detector setup, imaging conditions and the most important processing parameters are given in the appendix (VII. 3 SINGLE PARTICLE DATA ACQUISITION AND PROCESSING PARAMETERS). Taken together, these datasets represent the enormous progress in single-particle cryo-EM data collection, processing and instrumentation in this decade, and highlight its progress and impact on high-resolution structure determination.

SPA reconstruction, validation and interpretation

Analysis of single particle datasets was performed following the brief outline given below, using the indicated software packages and tools. A more detailed description of the individual workflows and reconstruction parameters is given in the respective publication (VIII. PUBLICATION 1) and manuscript (IX. PREPRINT 1) for all significant aspects. An overview of relevant data acquisition and processing parameters, as well as the validation statistics, can be found in the appendix (VII. 3 SINGLE PARTICLE DATA ACQUISITION AND PROCESSING PARAMETERS). A list of all used software packages, their respective versions and the corresponding references is presented in the Materials and methods section (LIST OF PROGRAMS AND SOFTWARE).

Pre-processing

Pre-processing of SPA datasets was performed within the RELION framework. After importing the movies, the movie frames were aligned using MotionCor2; dose-weighting was applied. Subsequently, the contrast transfer function (CTF) was estimated using CTFFIND4. Particle coordinates were initially selected manually from a representative micrograph subset to generate templates for autopicking *via* 2D classification in RELION. The best resulting 2D class averages were then used as templates for reference-based autopicking. Incorrectly picked particles, false positives or junk particles were discarded

during several subsequent rounds of 2D classification. The quality of 2D class averages was judged by the presence of well-defined secondary structure features, and by a good distribution of different orientations ('views') of the particles in the dataset. In the case of sub-optimal classification results or under-populated views, reference-based autopicking and subsequent 2D classification were repeated until satisfactory results could be obtained.

3D classification, reconstruction and post-processing

3D reconstruction from the selected subset of particles was performed either in RELION (*V. vulnificus* stressosome, BetP) or in cryoSPARC (BetP), based on the obtained results. 3D initial models were always created from the dataset, to optimally represent the respective sample. To investigate structural heterogeneity in the datasets, 3D classification in RELION or parallel ab-initio refinement of several models in cryoSPARC were performed. Particles contributing to low-resolution, featureless classes/volumes were again discarded. Subsequently, 3D refinements were as well performed in RELION or cryoSPARC, after a particle subset of sufficient homogeneity was identified. In the case of symmetric refinements, asymmetric volumes were always obtained as a control for the selected symmetry. For refinement of BetP, the SIDESPLITTER algorithm (run *via* the command line, using the RELION external reconstruction feature) often yielded superior results e.g. for unordered or flexible regions of the protein. Careful subtraction of the Amphipol density signal surrounding BetP equally improved the protein density in some cases. Masks for signal subtraction were created and checked in UCSF Chimera using the volume eraser and/or SeggeR tools. As a further control, 2D class averages were created from the subtracted particles and compared with the non-subtracted ones. In addition, maps generated from subtracted particles were carefully inspected in UCSF Chimera to exclude artifacts at the protein periphery originating from signal subtraction. Finally, post-processing of the final maps included masking of the solvent regions and B-factor sharpening. The resulting cryo-EM density maps were finally deposited in the electron microscopy data bank EMDB.

Validation

Several aspects were considered for validation of the quality of SPA density maps. First, the 'gold-standard' Fourier shell correlation (FSC) curve, generated from independently refined half-maps of the dataset, was judged by its shape, and the global resolution of the respective map was obtained according to the FSC = 0.143 criterion. Analysis of the local resolution distribution throughout the map was performed based on results generated with ResMap or the RELION local resolution tool. For an investigation of symmetry components, Eigenimages were created within the Scipion workflow, as described in publication 1 (VIII. PUBLICATION 1). However, also a critical visual inspection of the density map was considered necessary to exclude reconstruction artifacts caused by e.g. too tight masking during refinement or post-processing.

Objective SPA data comparison

For an objective comparison of two SPA datasets, 2D class averages were created following an identical data processing strategy. Initially, the same number of micrographs was chosen for each dataset, and approximately equal numbers of particles were auto-picked in RELION. 2D class averages were computed separately for the datasets, using identical extraction and classification parameters. The resulting class averages were sorted according to the number of particles in the respective classes for easier comparison. The distribution of particles-per-class over the whole dataset can be used to compare the individual imaging conditions. The approach was used to compare linear *vs*. counting imaging mode of the FalconIII detector, as well as datasets collected at 200 keV *vs*. 300 keV acceleration voltage. More details, parameters and plots of this analysis are presented in the discussion of the thesis (IV. DISCUSSION).

Model building

Density maps obtained *via* SPA cryo-EM analysis were used to build atomic models of the respective protein(s). Detailed experimental parameters on modeling and validation can be found in the respective manuscript (IX. PREPRINT 1) and the appendix (VII. 3 SINGLE PARTICLE DATA ACQUISITION AND PROCESSING PARAMETERS).

Model building was performed in COOT. A suitable template was rigid-body-fitted into the cryo-EM density map and adjusted manually. Lipid molecules were added manually into unambiguously identified densities and adjusted. Ligand restraint files were created using eLBOW. Real-space refinement of the model against the density map was subsequently performed in Phenix. Several adjustment-refinement cycles were performed, until satisfactory results could be obtained. Statistics and validation parameters are presented in VII. 3 SINGLE PARTICLE DATA ACQUISITION AND PROCESSING PARAMETERS. Models that are part of a publication or manuscript were deposited in the PDB database.

Protein interaction network analysis

A protein interaction network analysis was performed to obtain an unbiased, objective description of the global interactions of amino acid residues and ligands within a structure. Within the network, each residue is represented by a node, while their interactions are described by the connecting edges. The interaction network facilitates identification of functional sub-domains ('modules') within the protein in a certain state. Consequently, a comparison of networks representing different states allows for conclusions about catalytic or regulatory mechanisms that may otherwise remain speculative. A detailed description of the experimental parameters is also given in IX. PREPRINT 1.

Interactions within the protein structure were determined by the 'find contacts' option in UCSF Chimera. The resulting lists of interacting residues were imported to Gephi, and subsequently, a ForceAtlas was applied to the datasets for at least 10,000 iterations. Two parameters, namely 'betweenness centrality' (BC) and 'modularity class' (MC) were obtained from the interaction network and used for further characterization of the activation states represented by the respective interaction networks. MCs are defined as groups of residues and ligands (inter)acting as functional modules within a protein, while BC can be used as a measure for the global impact of the corresponding residues on the protein. For a better comparison of two states, delta-BC (△BC) values were determined. Visualization of the results of the BC and MC analyses was performed using the 'render by attribute' function in UCSF Chimera.

II. 5 Electron microscopy – tomography

High-pressure freezing, freeze substitution and sectioning

Preparation of sapphire discs

1.4 mm sapphire discs were used for the cultivation of adherent HEK293S GnTI$^-$ cells for subsequent high-pressure freezing and freeze substitution. For cleaning, the sapphire discs were placed on a rubber gel pad and rinsed with 32% HCl for 10 min, subsequently rinsed with 70% EtOH for 10 min, air dried and autoclaved. For cultivation of the cells, the sapphire discs were mounted in a 35 mm cell culture dish with sterile fetal calf serum (FCS). After application of a small FCS droplet to the bottom of the cell culture dish, the disc was placed on top of it with a pair of tweezers and held in place for 2 – 3 min until the droplet had dried completely. When all sapphire discs were mounted, the cell culture dish was sterilized for 2 min in a plasma cleaner, and cells were seeded subsequently.

Preparation of pioloform-coated grids

Pioloform-coated copper grids (P-bar, 150 mesh, Plano GmbH, Wetzlar, DE) were prepared for tomography. 1.5% (w/v) pioloform were dissolved thoroughly in Chloroform p. a. An even, thin pioloform film was produced in a home-made device. The solution was poured into the device, a cleaned glass slide was placed into it and incubated for 30 sec. Thereafter, the pioloform solution was dumped *via* a valve. The film was desiccated for 1 min and then floated on a water (H_2O_{bidest}) surface in a home-made floating device. Chloroform-cleaned, dried grids were placed onto the floating film. Subsequently, both grids and film were removed together from the water surface with a sheet of parafilm, placed into a petri dish, air dried and stored at RT.

High-pressure freezing

To achieve the best ultrastructural preservation possible, high-pressure freezing (HPF) was used for cryo-fixation of cells cultivated on sapphire discs. With this method, the vitrification of thick specimen (up to several hundred µm) is rendered possible.

Consequently, it is suitable for cryo-fixation of eukaryotic cells without the formation of ice crystals. For HPF, cells were grown as a monolayer to ~80% confluence. Cells should be grown exclusively on the surface of the sapphire disc and were checked under the light microscope directly before sample preparation (see also EXPRESSION OF PC-2 IN A STABLE CELL LINE). Life cell carriers were used as support for the sapphire discs. The life cell carrier was picked up with the manipulation tool and its surface was moisturized with sterile FCS. The sapphire disc with the cells facing up was placed into the life cell carrier cavity and covered with sterile cell culture medium. The carrier with the disc was mounted into the HPF pod with the manipulation tool, the pod was closed carefully and inserted into the HPF chamber. Subsequently, cryo-fixation was performed automatically by the HPF machine at 2048 bar and -196 °C. The vitrified sample (including sapphire disc and life cell carrier) was removed from the pod and stored in liquid nitrogen (lN_2) until further processing.

Preparation of solutions and embedding media for freeze substitution (FS):

Freeze-substitution solution A & B for freeze substitution of HPF samples were prepared freshly prior to substitution.

The Epon™ 812 substitute embedding resin was prepared freshly according to the manufacturer's instructions, as outlined in TABLE 8. The first three epoxy resin components (Epon™ 812 substitute, Dodecenylsuccinic anhydride (DDSA) and Methyl nadic anhydride (MNA)) were weighted and mixed thoroughly, before the final component 2,4,6-Tris(dimethyl-aminomethyl)phenol (DMP 30) was added. In particular, it was taken care to mix the components in the correct amount and order, to avoid faulty polymerization or precipitation of the resin during freeze substitution.

Table 8: Embedding resin composition

component	amount	function
Epon™ 812 substitute	23.0 g	resin
DDSA	14.25 g	hardener
MNA	12.4 g	hardener
DMP 30	0.75 g	accelerator

Freeze substitution and resin embedding

Automated freeze substitution was performed in an AFS2 freeze substitution machine to process high-pressure frozen cell monolayers according to the protocol summarized in TABLE 9. During FS, the water contained in the cells is gradually replaced by a solvent (Acetone), while a gentle chemical fixation and en-bloc staining are performed simultaneously. Subsequently, the substitution cocktail is exchanged by pure Acetone. During this procedure, the sample temperature is step-by-step ramped from -196 °C to RT. Lastly, the solvent is incrementally replaced by an epoxy resin, which is finally polymerized. Since en-bloc staining and chemical fixation are performed at low temperatures, freeze substitution generally results in a superior ultrastructural preservation in comparison to conventional methods.

Table 9: Freeze substitution protocol

temperature	**step**	**solution**	**incubation time(s)**
-140 °C	stepwise substitution of intracellular H_2O, mild chemical fixation and en-bloc staining	substitution solution A or B	1 x 30 min
-140 °C to -90 °C		substitution solution A or B	1 x 3 h
-90 °C		substitution solution A or B	1 x 4 h
-90 °C to -60 °C		substitution solution A or B	1 x 3 h
-60 °C		substitution solution A or B	1 x 4 h
-60 °C to -30 °C		substitution solution A or B	1 x 3 h
-30 °C		substitution solution A or B	1 x 4 h
-30 °C to 0 °C		substitution solution A or B	1 x 3 h
0 °C		substitution solution A or B	1 x 3 h
0 °C	removal of substitution solution	Acetone p. a.	2 x 10 min
0 °C to 4 °C		Acetone p. a.	1 x 20 min
4 °C to 25 °C	removal of Acetone and stepwise infiltration with Epon™ 812 substitute embedding resin	Acetone / resin 2 + 1	1 x 1 h
25 °C		Acetone / resin 2 + 1	1 x 1 h
25 °C		Acetone / resin 1 + 1	1 x 2 h
25 °C		Acetone / resin 1 + 2	1 x 16 h
30 °C		resin (fresh)	1 x 2 h
60 °C	resin polymerization	resin	1 x 2 d

Sectioning

Sections of different thickness were produced for different purposes. Ultra-thin (50 nm) sections were used for sample quality screening. Thin sections with a thickness between 200 and 400 nm were used for TEM-tomography. For STEM tomography, thick sections of 800 to 1000 nm are considered appropriate. Prior to sectioning, the gold carriers and sapphire discs were removed thoroughly by alternatingly plunging the resin blocks into hot water (60 °C) and lN_2, until the carriers and sapphire discs stripped off the resin blocks. Subsequently, the block face was trimmed with a razor blade, to obtain a trapezoidal cross section shape required to achieve a ribbon of sections. Subsequently, sectioning was performed on an ultramicrotome with a histo (thin and thick sections) or ultra 35° (ultra-thin sections) diamond knife (Diatome Ltd, Nidau, CH). The sections were picked up from the water surface with an un-coated Cu slot grid, and transferred to a pioloform-coated grid. After blotting dry, the sections and grids were visually inspected under a binocular, and intact grids with well-centered sections were stored in a grid box until further use.

Preparation of sections for tomography

Prior to data collection, the sections on the pioloform-coated grids needed to be prepared for tomography as described in the following. For TEM tomography, fiducial markers were applied onto the 200 nm or 400 nm sections. 15 nm protein A gold fiducials (University of Utrecht, NL) were used in a dilution of 1:40 (v/v) in H_2O_{milli}. The stock solution was diluted freshly before use. The dilution was vortexed thoroughly to reduce aggregation of the fiducial markers. 10 µL droplets of the fiducial solution were placed on a sheet of parafilm. For washing steps, droplets of H_2O_{milli} were placed as well. To apply the gold markers to the section, the grid was placed on top of the fiducial droplet and incubated for 4 min. Afterwards, the grid was incubated briefly on a drop of H_2O_{milli} for washing. Three washing steps were performed, and the grid was finally blotted dry. In this manner, fiducial markers were applied to both sides of the grid subsequently, and the grid was stored in a grid box until further use.

For STEM tomography, fiducial markers were applied to the 800 nm sections as described above. Subsequently, a thin layer of carbon was evaporated onto the section, to generate a conductive surface required for the scanning electron beam. The grid was placed on a rubber foam surface and inserted into the carbon evaporator. A thin carbon film of 2 – 3 nm

thickness was evaporated onto the grid and section surface *via* thermal evaporation. The grids were stored in a grid box until further use. Directly before mounting of the grid into the TEM sample holder, the grid surface was gently cleaned by glow discharging in a plasma cleaner for 30 sec in the 'low' setting, to avoid charging and contaminations during data collection.

Tomography data collection

TEM-tomography

Conventional TEM tomography was used for an initial investigation of thin sections of high-pressure frozen, freeze substituted HEK293S GnTI$^-$ cells to judge the ultrastructural preservation of cells after sample preparation, and to identify putatively interesting regions for STEM tomography on subsequent, thicker sections.

Tomograms were collected on a JEM 2100F (JEOL, Tokyo, JPN) transmission electron microscope, operated at 200 keV with a CMOS camera (TemCam-F416, 4k *x* 4k pixels, TVIPS GmbH, Gauting, DE). For tilt series collection, a high tilt holder tip was used.

Table 10: TEM tomography tilt scheme

	purpose	**tasks**	**acquisition scheme**	
series 1	walking up	focusing tracking	0° to +66°	5° increment
series 2	data acquisition	focusing tracking exposure	+66° to +60°	0.9° increment
			+60° to +12°	↓ continuously increasing increment
			+12° to -15°	2.0° increment
			-15° to -61°	↓ continuously decreasing increment
			-61° to -66°	0.9° increment
series 3	walking down	focusing tracking	-66° to 0°	5° increment

Since plastic sections shrink substantially during data collection (Luther, 2006), the samples were pre-exposed to the electron beam for several minutes ('beam showering').

TEM alignments included eucentric height, high tension center and astigmatism corrections. Subsequently, single-axis tilt series were acquired automatically from +66° to -66° according to a modified Saxton tilt scheme (Saxton *et al.*, 1984) specified in TABLE 10 using EM-Tools. Tracking and focusing were performed outside the region of interest (ROI).

STEM-tomography

STEM tomography, in comparison to conventional TEM tomography, offers the advantage of a much higher depth of focus originating from the different image formation in STEM mode. This allows for the investigation of ticker samples, which ultimately results in a much larger cellular volume to be reconstructed and a better resolution in the Z direction. The collection of dual-axis tomograms reduces the missing wedge artifact in the reconstructed volume, and thus leads to a superior resolution isotropy.

STEM microscopy was performed on a JEM 2100F (JEOL, Tokyo, JPN) electron microscope equipped with both a bright field (BF) and a dark field (DF) STEM detector. For the collection of dual-axis STEM tomograms, a Model 2040 Dual-Axis Tomography holder (Fischione Instruments Inc., Export, USA) was used. Beam showering was performed as described above. The STEM beam (diameter: 1.5 nm) was aligned *via* a Ronchigram generated on the sample support film. A camera length of 20 cm was used, and a 20 µm condensor lens (CL) aperture was inserted and centered. Both BF and DF images were collected simultaneously; brightness and contrast were optimized for BF imaging. Tilt series were recorded automatically from +66° to -66° according to a modified Saxton tilt scheme (Saxton *et al.*, 1984) presented in TABLE 11 using the EM-Tools software package. Eucentric height was adjusted once prior to start data acquisition. After collection of the first tilt series, the sample was rotated in the holder by 90°. Subsequently, a second tilt series was acquired as described before from the same ROI.

Table 11: STEM tomography tilt scheme

	purpose	**tasks**	**acquisition scheme**	
series 1	walking up	focusing tracking	0° to +66°	5° increment
series 2	data acquisition	focusing tracking exposure	+66° to +58°	1.0° increment
			+58° to +15°	continuously increasing increment
			+15° to -15°	2.0° increment
			-15° to -58°	continuously decreasing increment
			-58° to -66°	1.0° increment
series 3	walking down	focusing tracking	-66° to 0°	5° increment

Tomogram reconstruction and visualization

Tomogram reconstruction

TEM and STEM tomograms were reconstructed in IMOD, following the inherent processing pipeline. Prior to processing, the single images were inspected visually, and images featuring sub-average contrast or other anomalies oftentimes present at high tilt angles were discarded. Pre-processing included binning, the generation of an image stack and the removal of X-rays and similar artifacts. Subsequently, the single images in the stack were aligned coarsely by cross-correlation. Fine tuning of the alignment required a fiducial model. It turned out that manual generation and optimization of the fiducial model yielded superior results than automatically generated models. At least 15 fiducial markers were selected from each side of the section, which should be easy to follow throughout the whole tilt series. Fine alignment of the images was then performed iteratively, by manually correcting the positioning of the fiducial markers until all remaining residuals had been resolved. Distortions were removed during later iterations of fine alignment. The 'Local Alignment' option (using 2*x*2 or 3*x*3 patches) often resulted in better overall fine alignments. The aligned stack was subsequently cropped, to optimally fit the ROI into the smallest 3D volume possible. Gold fiducials were removed using the 'Bead Eraser' option. Subsequently, the tomogram was reconstructed from the aligned image stack; using a

Simultaneous Iterative Reconstruction Technique (SIRT) -like filter oftentimes yielded the best results. For dual-axis tomograms, both tomograms were reconstructed following the procedure described above, and subsequently merged using the 'Tomogram Combination' option. Alignment of the two tomograms usually worked best following the 'automatic patch fitting' method. Finally, the tomogram edges were trimmed.

Tomogram segmentation and visualization

For threshold based segmentation of tomograms, the program SeggeR as part of the software package UCSF Chimera was used. The reconstructed tomogram in .mrc format was imported into Chimera, scaled by -1 and binned by a factor of two using the 'Volume Filter' options. The 'Volume Viewer' was utilized to display all planes of the tomogram as a surface. The shown histogram was used to find a suitable threshold for later segmentation. Special attention was paid to appropriate appearance of the membranes. To remove residual noise from the tomogram, the 'Hide Dust' tool was applied. Subsequently, SeggeR was used for automated, threshold based segmentation of the volume into segments or regions. Two or three smoothing steps were performed, and very small regions (< 5 to 30 voxels) were removed. The resulting segmentation dataset was analyzed and refined manually. All regions belonging to one cellular organelle were grouped together. The 'Ungroup' option was used to improve the quality of inaccurately segmented regions. By this procedure, one separate volume was obtained for each organelle or cellular component. The numerous Chimera surface and volume rendering options were then used for final visualization, creation of figures and making movies of the tomograms.

III. Results

III. 1 Publication 1

The *Vibrio vulnificus* stressosome: an oxygen-sensor involved in iron metabolism regulation

The scope of this publication is to provide a global understanding of the *V. vulnificus* minimal stressosome complex. To this end, we deliver phylogenetic, biochemical, physiological and, for the first time, also structural data for a gram-negative Bacterium. These enable us to shed light on the versatile role of the stressosome complex from different perspectives, and allow us to draw mechanistic conclusions about the stressosome-mediated stress response in a human pathogen.

In particular, we were able to pinpoint a number of significant differences of the *in vitro* gram-negative *V. vulnificus* stressosome in comparison to its gram-positive counterparts. A majority of these differences could be attributed to the unique complex assembly and architecture. Our structural analyses elucidated the stoichiometry of the complex, which is different from the one described for gram-positive stressosomes. The concomitant degree of flexibility, originating from a symmetry break in the complex assembly requires a different mechanism of stress sensing and signal transduction, which we propose.

My personal contribution was the analysis and interpretation of the structural data. The intermediate-resolution structures that could be obtained are of comparable quality with the first structure provided for the gram-positive *B. subtilis* stressosomes, and thus of high value for a profound comparison of the two complexes. Further considerations on the data processing strategy, observed difficulties and conclusions can be found in the Discussion part (IV. DISCUSSION) of this thesis and in the publication (VIII. PUBLICATION 1) itself. The obtained insights gained here were also instrumental for structure determination of the *L. innocua* stressosome complex, published in the partner manuscript (Miksys *et al.*, 2022). Moreover, I was significantly involved in drafting and writing the manuscript, as well as in interpretation of the phylogenetic, biochemical and physiological data in the structural context, as stated in the publication/author's contribution section.

III. 2 Preprint 1

Osmotic stress response in BetP: How lipids and K^+ team up to overcome downregulation

Within this project, we investigate fundamental aspects of osmostress regulation by the secondary active transporter BetP in *Corynebacterium glutamicum*. Here, we were able to provide for the first time high-resolution structural data on the down-regulated state, as well as on a transient active state, of BetP. Supported by FTIR and FRET data, these structures enabled us to suggest a detailed regulation mechanism, based on a precise specification of the respective membrane stimulus in the context of structural information.

Within the cryo-EM structure of down-regulated BetP, some unique features could be identified, namely: a true, threefold symmetry along with a significantly altered orientation and different cytoplasmic interaction network of the osmo-sensory C-terminal domain; the presence of Cardiolipin molecules at regulatory lipid binding sites; and a so far undescribed conformation of the Glycine-stretch. The asymmetric structure of the transient-active state represents an intermediate between the down-regulated and crystal structures of up-regulated states. FTIR and FRET analyses contributed a dynamic perspective to the structural data and allowed us to pinpoint the underlying regulatory mechanism, based on unfolding and re-organization of the C-terminal domains.

For this study, I was able to contribute the cryo-EM analyses of the down-regulated and transient active states of BetP, representing the foundation for our mechanistic interpretation. This comprises all required steps, namely protein expression, purification and reconstitution, quality control and cryo-EM analysis. Notably, I succeeded in establishing all aspects of SPA cryo-EM analysis in our group, including sample preparation and screening, but also data analysis and interpretation. Thus, it was a great pleasure for me to also draft, write and illustrate the resulting manuscript. Further considerations, such as a comparison of different reconstitution methods or on the different types of electron microscopes used throughout the study can also be found in the discussion (IV. DISCUSSION) of this thesis. Experimental details are presented in the manuscript (IX. PREPRINT 1).

III. 3 Manuscript 1

Application of STEM tomography to investigate smooth ER morphology under stress conditions

In this study, we investigate the applicability of dual-axis STEM tomography to depict sER morphotypes induced under stress conditions in HEK cells at a high resolution and in their natural cellular environment. In a previous study, we were able to document the formation of crystalloid-ER upon over-expression of PC-2 in HEK cells *via* focused ion beam scanning electron microscopy (FIB-SEM) analysis (Wilkes *et al.*, 2017). However, tracing the single ER membranes was not possible in this dataset. In the present study, we aimed to elucidate the crystalloid-ER membrane architecture by using STEM tomography, which allows the investigation of comparably large cellular sub-volumes at a resolution sufficient to resolve single membranes.

Notably, we succeeded not only in describing the crystalloid-ER morphology, but also detected ER whorls within the cells, which have not been described before for this sample. These findings allowed us to describe a diverse and highly dynamic intracellular interaction network for the different OSER morphotypes, highlighting the cells ability to adapt their metabolism to the respective stress conditions. Importantly, dual-axis STEM tomography proofed suitable to examine the organellar membrane architecture at an unprecedented level of detail in the natural cellular context.

The workflow of sample preparation (cell culture, high pressure-freezing and freeze substitution, sectioning), data recording and tomogram reconstruction is well established at the University of Regensburg (Rachel *et al.*, 2020). Additionally, I evaluated multiple options for tomogram visualization ('segmentation'), with the threshold-based program 'SeggeR' as the match-winning approach (see also TOMOGRAM RECONSTRUCTION AND VISUALIZATION). Thus, I was able to perform all parts of the experiment by myself, realizing an efficient sample and data processing procedure, which also extends to interpretation of the data and drafting of the respective manuscript (see X. MANUSCRIPT 1). An experimental overview is also presented in II. 5 ELECTRON MICROSCOPY – TOMOGRAPHY.

IV. Discussion

IV. 1 Electron microscopy from 2D to 3D

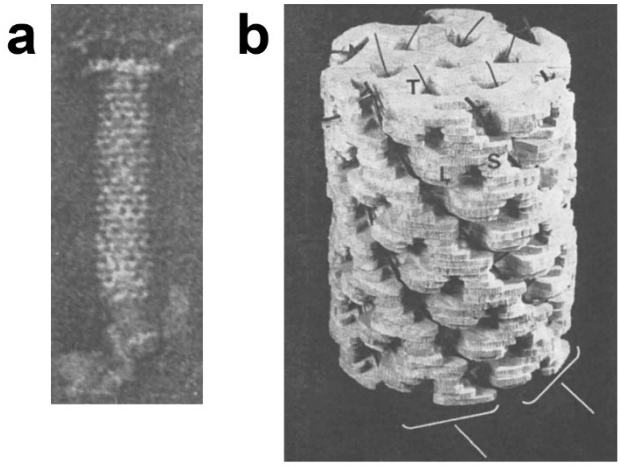

Figure 15: first 3D reconstruction from a TEM micrograph

a) TEM image of an negatively stained bacteriophage T4 tail. b) Balsa wood model of the 3D reconstruction of the phage tail presented in a. Reproduced from (De Rosier & Klug, 1968).

The principle of 3D reconstruction of objects from a series of TEM projection images was established already in 1968 by David J. De Rosier and Aaron Klug (De Rosier & Klug, 1968). They reasoned that different orientations of multiple copies of a protein are present in TEM micrographs of helical symmetric objects. Fourier transformation of these projection images results in a set of Fourier coefficients that can be used to reconstruct the symmetric 3D object *via* subsequent Fourier synthesis. They applied this procedure to an electron micrograph of a negatively stained bacteriophage T4 tail and solved the structure of the extended phage tail from this single electron micrograph to 35 Å (FIGURE 15), taking advantage of the high symmetry of the particle. In addition, they reasoned that the procedure would be applicable also to asymmetric objects by collecting a series of systematically tilted images – this approach is known as electron tomography at present. Alternatively, they suggested to investigate multiple copies of the same asymmetric protein in random orientation, to determine the angles of view by "[…]some form of refinement process" and to obtain a 3D reconstruction from these projections *via* Fourier synthesis (De Rosier & Klug, 1968) – this strategy is applied during single particle cryo-EM reconstruction of protein structures today. Both methods have been successfully applied in this thesis to address diverse biological questions and will be discussed in more detail in the following.

As introduced above, both electron tomography and single particle reconstruction offer the possibility to obtain three-dimensional information from 2D micrographs. There are, however, significant differences with respect to technical aspects, sampled objects and achievable resolution and information content. Both approaches were successfully applied in the course of this thesis to address a variety of scientific questions. SPA could be used to gain insights into protein complex symmetry and stoichiometry (III. 1 PUBLICATION 1), as well as into a yet unidentified regulatory transporter state (III. 2 PREPRINT 1), respectively. Electron tomography, on the other hand, helped to reveal the complex interaction network and proliferation of an organelle in its native, cellular background (III. 3 MANUSCRIPT 1). Thus, alongside the biological insights presented and discussed in the respective publication (VIII. PUBLICATION 1), preprint (IX. PREPRINT 1) and manuscript (X. MANUSCRIPT 1), it is now possible to also provide a more technical comparison of selected aspects of sample preparation, data acquisition and data analysis required by the two approaches. Discussing these considerations is in turn deemed beneficial for subsequent structural biological experiments using electron microscopy.

IV. 2 Samples and sample preparation

Biological samples naturally occur in a large variation of sizes, ranging from several centimeters in eukaryotic organs or tissues to only a few nanometers in isolated proteins. Imaging of such objects in an electron microscope, however, implies a number of constraints to be considered. The mean free path of electrons is limited to 350 nm at an acceleration voltage of 300 keV (Grimm *et al.*, 1998), which in turn restricts the maximum sample diameter to about 1 µm in cryo-EM (Ben-Harush *et al.*, 2010). Consequently, purified protein samples for SPA can be vitrified *via* plunge freezing (Dubochet *et al.*, 1982; Adrian *et al.*, 1984) and imaged right away, while more complex procedures are required to prepare larger specimen for electron microscopy. As an example, high-pressure freezing, freeze substitution and sectioning (Dahl & Staehelin, 1989; Studer *et al.*, 2001; Rachel *et al.*, 2010; Walther *et al.*, 2013; Villinger *et al.*, 2014) as described in II. 5 ELECTRON MICROSCOPY – TOMOGRAPHY were necessary to be able to visualize the crystalloid-ER and whorl structures within HEK cells (see also X. MANUSCRIPT 1). However, both preparation techniques – plunge freezing and high-pressure freezing – follow the same rationale: avoiding the destructive formation of crystalline ice *via* rapid sample vitrification. While this can be achieved solely by fast plunge-freezing in a suitable cryogen for the very thin SPA samples, the additional application of high pressure is required for thicker bulk specimen typically used in cellular electron tomography. High pressure-freezing and subsequent freeze substitution of eukaryotic cell cultures and tissues is a well-established sample preparation method at the Centre for Electron Microscopy / University of Regensburg (Rachel *et al.*, 2010). Sample preparation and vitrification of isolated proteins for SPA cryo-EM structure determination, on the other hand, had to be established in the course of this thesis and will thus be discussed in more detail in the following.

Protein purification and reconstitution are considered key factors to obtain meaningful, high-resolution membrane protein structures, and successful vitrification, in turn, largely depends on sample quality (Lyumkis, 2019; Wu & Lander, 2020b). To retain membrane proteins in a close-to-native state, a number of membrane mimicking systems were introduced in the past years as replacements for the commonly used detergents. Consequently, a selection of different systems was tested in the context of this thesis with

the aim to identify the most suitable one for SPA cryo-EM structure determination of BetP. A schematic overview of these methods is presented in FIGURE 16, and the most important features are briefly summarized in TABLE 12.

Table 12: Membrane mimicking system characteristics

	detergent	**lipid origin**	**scaffold**	**particle shape**
SMA / DIBMA	no	endogeneous	polymer	irregular
Amphipol	yes	endogeneous	polymer	irregular
Salipro	yes	external	protein	irregular
Nanodiscs	yes	external	protein	circular

One of the most recently introduced methods is simultaneous solubilization and reconstitution of membrane proteins by hydrophobic styrene-maleic acid (SMA) or di-isobutylene-maleic acid (DIBMA) polymers (FIGURE 16a) (Dörr *et al.*, 2014; Dörr *et al.*, 2015; Jamshad *et al.*, 2015; Lee *et al.*, 2016; Oluwole *et al.*, 2017; Pollock *et al.*, 2017). This method offers the advantages of being detergent-independent and retaining the protein in the endogeneous membrane environment, highlighted by the 3.2 Å SPA cryo-EM structure of AcrB in its natural lipid bilayer (Qiu *et al.*, 2018). Consequently, a variety of polymers was tested for BetP, to fully exploit their different chemical properties (summarized in TABLE 5, RECONSTITUTION INTO MEMBRANE-MIMICKING SYSTEMS). While sufficient solubilization conditions could be established for all polymers (TABLE 13, VII. 1 SMA AND DIBMA SOLUBILIZATION PARAMETERS), subsequent affinity purification was not successful for any of the tested conditions. One possible explanation could be a putative inaccessibility of the N-terminal StrepII-tag in its native lipid environment. However, since the N-terminal domain is not resolved in the SPA cryo-EM structure, this hypothesis cannot be elaborated on further. Consequently, SMA or DIBMA polymers are considered not suitable for solubilization, reconstitution and affinity purification of BetP.

In contrast to the “native nanodiscs” obtained from the SMA and DIBMA polymers, all other tested methods are based on detergent-solubilized protein. In 2016, the Saposin-lipoprotein (Salipro) technology was introduced (Frauenfeld *et al.*, 2016). In this method,

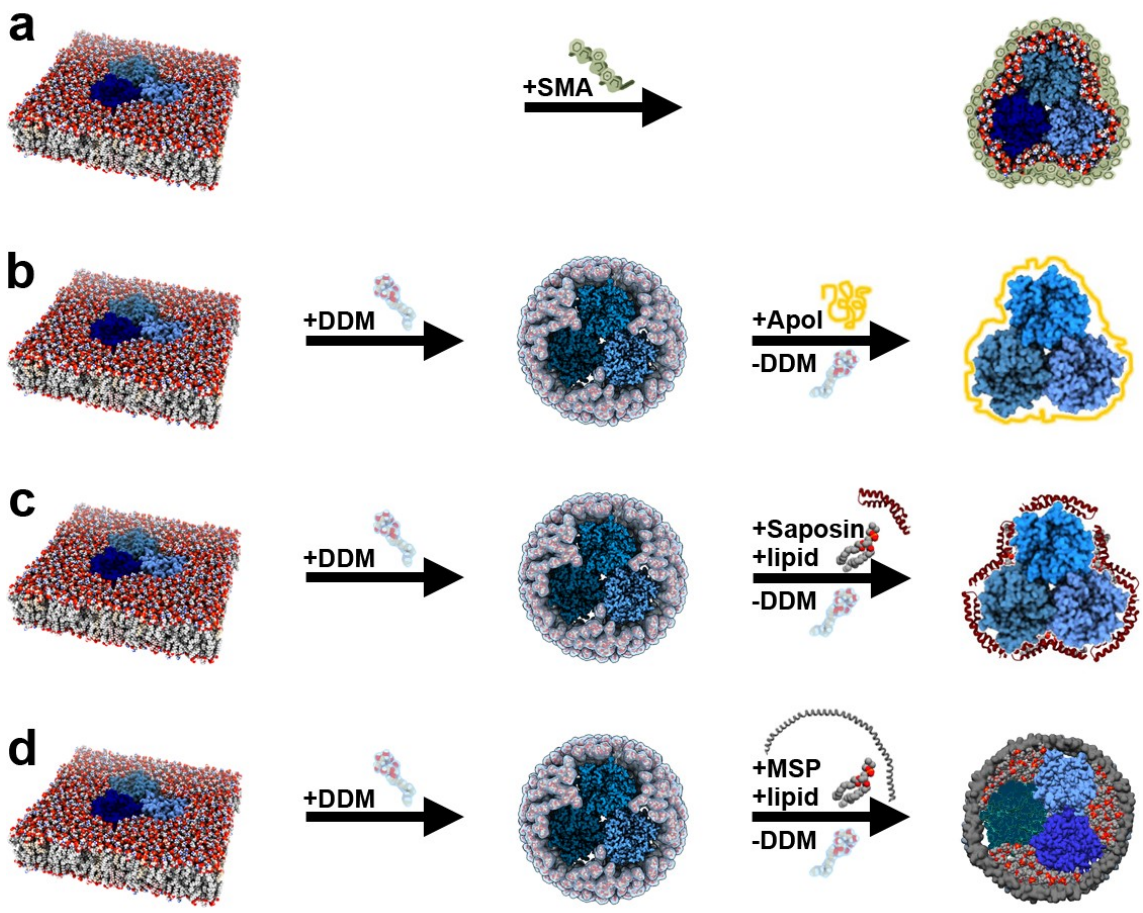

Figure 16: Membrane protein reconstitution methods

Schematic overview of membrane protein reconstitution methods assessed for BetP. a) Simultaneous solubilization and reconstitution into SMA / DIBMA polymers. b) Reconstitution into Amphipol after detergent solubilization. c) Detergent solubilization with subsequent reconstitution into Salipro-particles. d) Reconstitution into nanodiscs after detergent solubilization.

detergent-solubilized membrane proteins are reconstituted and stabilized using a scaffolding protein (Saposin A) in combination with external lipids, accordingly forming the Salipro-particles (FIGURE 16c) (Frauenfeld *et al.*, 2016; Lyons *et al.*, 2017). The method thus comes with the advantage of a user-controlled lipid environment, which was considered of great interest to study lipid-dependent regulation in BetP. BetP-Salipro particles were kindly provided by the group of J. Frauenfeld in a collaboration project and analyzed *via* negative stain and cryo-EM. While negative staining demonstrated evidence for a monodisperse sample, the particles severely suffered from preferred orientation in cryo-EM (FIGURE 20, VII. 2 CRYO-EM OF BETP RECONSTITUTED INTO SALIPROS). 2D class averages revealed the presence of triangular-shaped particles representing the BetP trimer in a top-down projection. The particles featured great level of detail, and secondary structure elements were clearly visible. Tilted or side views, however, were entirely absent

in the dataset, which in turn impeded 3D analysis. Unfortunately, due to the limited amount of sample available, screening and optimization of vitrification parameters were not possible. Thus, other reconstitution options were explored for SPA cryo-EM structure determination.

Nanodiscs with a user-defined lipid environment can also be formed using so-called membrane scaffold proteins (MSPs), resulting in circular nanodiscs of different sizes (FIGURE 16d) (Bayburt *et al.*, 2002; Bayburt & Sligar, 2003; Denisov *et al.*, 2004; Ritchie *et al.*, 2009; Bayburt & Sligar, 2010). This classic reconstitution method is well established in the field and has yielded a large number of high-resolution SPA cryo-EM membrane protein structures, pioneered by various structures from members of the Trp-channel family (Shen *et al.*, 2016; Q. Chen *et al.*, 2017; Guo *et al.*, 2017; Jin *et al.*, 2017; Autzen *et al.*, 2018). Consequently, BetP was reconstituted into nanodiscs and a fluorescence binding assay pointed towards an active protein sample (IX. PREPRINT 1). However, the presence of a sub-population of empty nanodisc particles in the sample could not be excluded with the available biochemical tools. Moreover, successful particle alignment during SPA data processing depends on the presence of a pronounced cytoplasmic protein domain protruding from the uniformly shaped nanodisc density, which is not the case for BetP. This problem was also faced in a collaboration project, where binding of a megabody to the nanodisc-embedded membrane protein was found to be necessary for successful SPA cryo-EM structure determination. However, the obtained resolution was limited by the angular accuracy during reconstruction, caused presumably by small variations in megabody binding in that study (M. F. Peter *et al.*, 2022). Reconstitution of BetP into nanodiscs was thus not pursued further for SPA cryo-EM structure determination.

Coming back to a polymer-based reconstitution method, Amphipol A8-35 was considered as a potentially suitable membrane mimick for BetP. The method is based on detergent-solubilization of the membrane protein and subsequent replacement of the detergent by the Amphipol polymer, without the addition of external lipids (FIGURE 16b) (Tribet *et al.*, 1996; Popot *et al.*, 2003; Popot *et al.*, 2011; Zoonens & Popot, 2014; Zoonens *et al.*, 2014; Le Bon *et al.*, 2018). This, in turn, implies that all lipids resolved in a potential SPA cryo-EM structure must have been co-purified with the protein, and are consequently essential for protein stability and / or function. Indeed, a number of POPG lipids have been resolved in crystal structure PDB-ID 4C7R, proving that a co-purification of BetP with endogenous lipids is possible (Koshy *et al.*, 2013). Another advantage of the Amphipol polymer is its

negative charge, which was considered to be an appropriate mimic of the uncommon, negatively charged *C. glutamicum* membrane (Hoischen & Kraemer, 1990; Schiller *et al.*, 2006). A reconstitution protocol could be successfully established, and two SPA cryo-EM structures in the absence and presence of K^+ could be solved subsequently, including the first structure for the fully down-regulated state (further discussed in IX. PREPRINT 1).

Undoubtedly, the success of SPA cryo-EM structure determination highly depends on the quality of the protein sample. This is all the more the case for membrane proteins, whose structural integrity and functional properties are strongly dependent on proper reconstitution. Thus, chemical properties of the selected scaffold need to be considered with great care, as well as additional components such as detergents or lipids. Moreover, the comparison of reconstitution methods presented above also highlights the necessity to evaluate technical aspects, such as preferred orientation or particle alignment issues. Only the optimal combination of all available options may eventually result in a biologically meaningful structure.

In the case of BetP, Amphipol A8-35 turned out to be the best membrane mimic available. As discussed above, diverse technical difficulties hindered SPA structure determination in SMALPs, Salipros or for nanodisc-embedded BetP. On the other side, the negatively charged Amphipol polymer was shown to be an excellent system to mimic the unusual *C. glutamicum* membrane lipid composition (see also IX. PREPRINT 1). It should also be pointed out here that the functionality of BetP in Amphipol A8-35 was demonstrated *via* Tryptophane fluorescence measurements. In combination with FTIR and MD simulation data, this integrative structural biology approach finally allowed us to suggest, for the first time, a regulation mechanism for BetP based on the SPA cryo-EM structure of the fully down-regulated state (IX. PREPRINT 1). In conclusion, comprehensive screening for suitable reconstitution systems is considered a prerequisite for membrane protein structure determination, and the combination of structural and functional data ultimately allows to elucidate molecular mechanisms at atomic resolution.

IV. 3 Imaging in TEM *vs*. STEM mode

When investigating stress-related topics in eukaryotes, it is oftentimes required to examine not only a single organelle but its whole cellular environment, since stress is a multi-faceted, global stimulus impacting the entire organism. Electron microscopy has been used for this purpose for a long time, due to its superior ability to depict morphological details at high resolution. Significant drawbacks, however, can be posed by technical limitations restricting the achievable information content of a micrograph or dataset. Oftentimes, these are determined by the size of biological objects, exceeding the sample dimensions that can be imaged. Consequently, a number of strategies has been developed in biological electron microscopy in the past to overcome these hurdles.

To circumvent the problem of sample thickness, focused ion beam scanning electron microscopy (FIB-SEM) can be used (Villinger *et al.*, 2012; Narayan *et al.*, 2014; Kizilyaprak *et al.*, 2018; Luckner & Wanner, 2018). In this approach, the sample is commonly embedded in a resin block (see also HIGH-PRESSURE FREEZING, FREEZE SUBSTITUTION AND SECTIONING), which is repeatedly milled by the FIB beam and imaged *via* SEM layer by layer. Thus, subsequent micrographs of the sample can be recorded and stacked, to finally reconstruct, e.g., whole cells. However, since the method is destructive, every sample region can be recorded only a single time, which in turn limits the screening procedure (Walther *et al.*, 2018). Nevertheless, FIB-SEM has become increasingly popular since it provides a unique possibility of imaging large specimen. Areas between 20 – 40 μm^2 and several µm in depth can be observed in a single dataset. The respective field of view (FOV), however, must be chosen from the first imaged layer(s). Thus, identifying smaller ROIs buried in the bulk sample prior to data collection – such as crystalloid-ER and ER whorls investigated in X. MANUSCRIPT 1 – can be difficult using the standard FIB-SEM approach. In our previous study, FIB-SEM was successfully applied to monitor the formation of crystalloid-ER in HEK cells upon over-expression of PC-2, making use of the technique's power to image whole cells in 3D (Wilkes *et al.*, 2017). Due to the large FOV and comparably low magnification, however, it was not possible to trace the organelles complex, membranous network forming the crystalloid-ER in this study. Moreover, the maximum resolution that can be achieved in FIB-SEM experiments is technically limited in the Z-dimension by the layer thickness of the milling FIB beam, which is commonly in the range of down to 5 nm (Rachel *et al.*, 2020).

Thus, in the present study (X. MANUSCRIPT 1) BF STEM tomography was selected as a method to image a comparably large cellular sub-volume at a resolution high enough to unambiguously depict the membrane architecture of the sER morphotypes occurring 72 h after over-expression of PC-2. This approach was pioneered already in 2009, in a study visualizing malaria parasites within human erythrocytes (Hohmann-Marriott *et al.*, 2009), only two years after superior contrast and signal-to-noise ratio (SNR) in STEM tomography in comparison to TEM tomography had been demonstrated (Yakushevska *et al.*, 2007). Due to the different modes of image formation and the altered electron optics configuration of the respective electron microscopes, STEM tomography offers the possibility to investigate samples with a thickness of up to 1 µm, about three times thicker than in the classical TEM tomography approach (Yakushevska *et al.*, 2007; Aoyama *et al.*, 2008; Hohmann-Marriott *et al.*, 2009; Sousa *et al.*, 2011; Wolf *et al.*, 2018). The advantages of STEM tomography for 3D analysis of intracellular, tubular networks – as applied in our own present study – have consequently been explored further by P. Walther and co-workers, who demonstrated the applicability of the method to 1 µm sections not only at 300 keV, but also at 200 keV (Walther *et al.*, 2018).

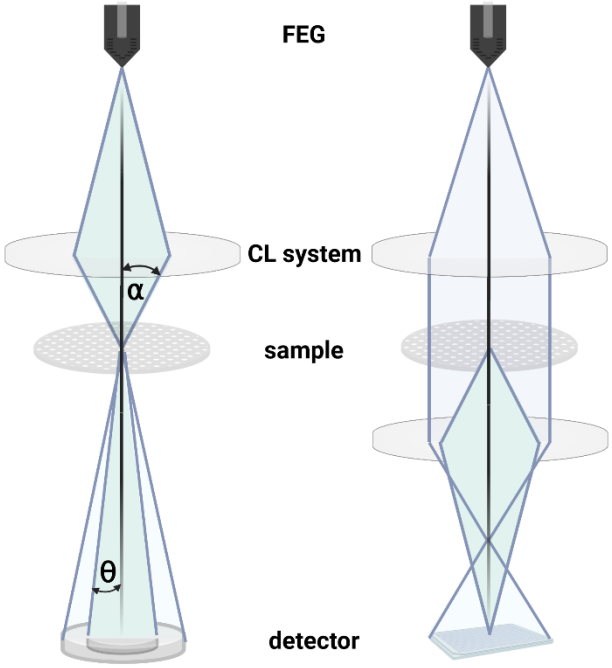

Figure 17: Ray diagrams for STEM and TEM imaging

Left: In STEM mode, the electron beam is focused in the sample plane to a semi-convergence angle α, to scan the FOV pixel by pixel. Electrons with a maximum scattering anlge θ are collected on the BF detector, electrons with a larger scattering angle contribute to the DF image. Right: In phase contrast TEM, the CL system is used to form a parallel elctron beam illuminating the whole FOV. The image is magnified and projected onto a CCD

A comparison of the ray diagrams for STEM and phase contrast TEM imaging is presented in FIGURE 17. Since the electron signal is collected on BF or DF STEM detectors, image forming lenses below the sample plane are not required for STEM imaging, eliminating the deleterious effects of chromatic aberration on image formation and SNR (Hohmann-Marriott *et al.*, 2009; Sousa *et al.*, 2011; Villinger *et al.*, 2012; McBride *et al.*, 2018; Wolf *et al.*,

2018; Rachel *et al.*, 2020). In contrast to the wide, coherent electron beam required for high-resolution, phase contrast TEM imaging (FIGURE 17, right), the convergent electron beam in STEM microscopy is focused in a small probe spot, scanning the FOV (FIGURE 17, left). STEM imaging is thus an incoherent process, and consequently less compromised by inelastic scattering events (Wolf *et al.*, 2018). The same time, both elastically and inelastically scattered electrons can be recorded on the STEM detector(s); thus, in STEM imaging, they both potentially contribute to the signal (Rachel *et al.*, 2020). Moreover, due to the very small semi-convergence angle α of the STEM beam (1 - 2 mrad), the depth of field along the Z-dimension can be substantially increased (Sousa *et al.*, 2011). Consequently, STEM imaging benefits from a much higher depth of focus in comparison to the classical TEM approach. This is highly beneficial especially for tomogram acquisition, since the effective sample thickness increases steadily at higher tilt angles. Considering these technical and methodological advantages, it was assumed that STEM tomography would be a suitable method to analyze the complex membrane architecture of sER morphotypes within a large cellular volume in the context of our current study.

Both the TEM and STEM tomography approach suffer from the 'missing wedge' effect. Since the sample cannot be tilted up to 90°, the reconstructed tomograms lack information in the X-Y plane and undergo artificial feature extension in the Z dimension. This effect was shown to be especially pronounced in elongated objects and membranes oriented perpendicular to the tilt axis (Dierksen *et al.*, 1995; Mastronarde, 1997; Nicastro *et al.*, 2000; Guesdon *et al.*, 2013). This disadvantage can be partially accounted for by dual-axis tomography and subsequent combination of the information obtained in both tilt series during tomogram reconstruction. The lack of information is consequently reduced to a 'missing pyramid', while the information content and resolution isotropy in the combined tomogram increases (Mastronarde, 1997; Guesdon *et al.*, 2013). The power of dual-axis STEM tomography to improve the SNR in the combined tomogram of 1 µm thick sections has been demonstrated by Sousa and co-workers (Sousa *et al.*, 2011). Considering these findings, all datasets presented in the current study (X. MANUSCRIPT 1) were recorded as dual-axis STEM tomograms. With respect to resolution anisotropy, no obvious artifacts were detected in the reconstructed tomograms or the respective visualizations. Furthermore, the resolution in the Z-dimension proved to be sufficient to unambiguously trace and render the membrane network of both tubular and lamellar sER morphothypes.

In summary, dual-axis STEM tomography was successfully applied to characterize the complex membrane architecture of an organelle in its native cellular environment. The resulting 3D reconstructions provide unique insights into the manifold, tight intracellular interaction networks and dynamics of two extraordinary sER morphotypes, namely ER whorls and crystalloid-ER. Moreover, these results once more highlight the superior suitability of high-pressure freezing and freeze substitution to preserve ultrastructural details of eukaryotic cells. In conclusion, the combination of the aforementioned, state-of-the-art sample preparation and imaging techniques proofed suitable to achieve new insights into sER architecture under stress situations at an unprecedented level of detail.

IV. 4 Imaging techniques for SPA

Linear *vs*. counting mode data collection

Transmission electron microscopy has been used to image biological objects for a long time; early examples include e.g. bacterial cells or viruses (Borries *et al.*, 1938; Brenner & Horne, 1959). The introduction of a variety of technical and methodological advances culminated in the so-called "Resolution Revolution" (Kühlbrandt, 2014), and protein structures solved by SPA can reach resolutions below 3 Å routinely today, summarized in (Fernandez-Leiro & Scheres, 2016; Frank, 2017; Cheng, 2018; Nakane *et al.*, 2020; Wu & Lander, 2020b). The introduction of a new generation of direct electron detectors (DEDs), offering different imaging modes, certainly represents a milestone on the way towards crystallographic resolution in SPA.

Exploiting the advantages offered by the DEDs provides the potential to substantially boost the detective quantum efficiency (DQE), a measure for the degradation of the SNR in the images during data recording (Ruskin *et al.*, 2013; McMullan *et al.*, 2014; Wu & Lander, 2020b). When the detector is operated in linear mode, the incident electron signal is straightly digitized by the DED, resulting in a very fast data collection at high total electron doses. However, energy deposition for each electron in the sensor layer follows a stochastic distribution; thus, the DQE of first-generation DEDs was limited to ~60% (Ruskin *et al.*, 2013; McMullan *et al.*, 2016). Individual electrons can only be detected at a much lower illumination intensity with the DED operating in counting mode. Here, subsequent replacement of each incident electron signal with an identical delta function finally yields images with a much better DQE (Ruskin *et al.*, 2013; Cheng, 2018). Thus, there exists a considerable trade-off between data collection speed (linear imaging mode, translating into particle number) and achievable DQE (counting imaging mode, translating into information content), and the respective data collection strategy has to be chosen with great care.

To further investigate this issue, two small test datasets of identical size were collected for Amphipol-reconstituted BetP with the detector operating in either linear or counting mode (TABLE 14). For data quality assessment, 2D class averages were computed for both datasets using the same processing strategy (SPA RECONSTRUCTION, VALIDATION AND

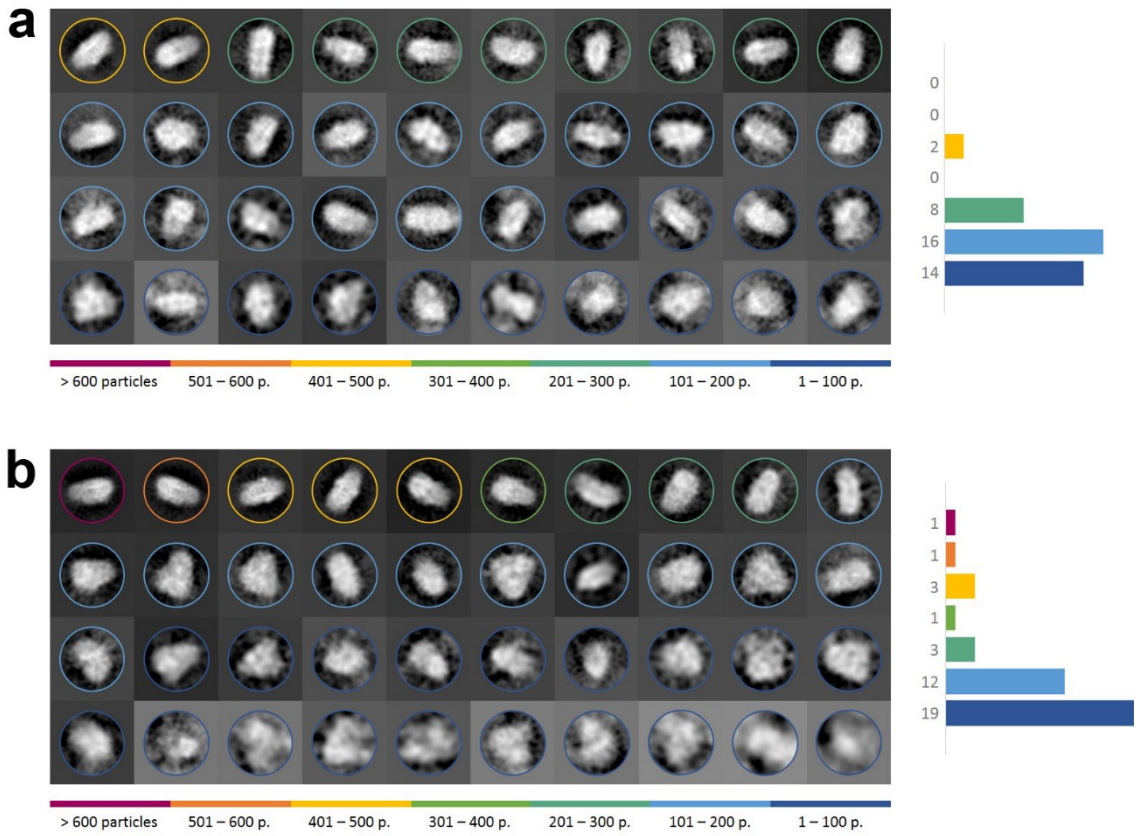

Figure 18: Linear vs. *counting mode*

2D class averages of Amphipol-reconstituted BetP particles, collected with a FalconIII detector in linear (a) or counting mode (b), respectively, collected from the same grid in a single data collection session. The class averages were created from the same number of micrographs, using the same classification strategy. The numbers of particles per class are color-coded.

INTERPRETATION). The results are shown in FIGURE 18a (linear mode) and FIGURE 18b (counting mode), respectively. From the particle-per-class distributions, plotted next to the class averages, it can be readily captured that apparent high-resolution classes are by far more populated in the counting mode dataset, while the linear mode data yielded almost exclusively low-resolution class averages. Since both datasets were collected subsequently from a single grid in the same session, differences in sample quality or microscope performance can be largely excluded to be causative for this finding. The 2D class averages presented here were created using the same number of micrographs for each dataset; however, imaging in linear mode is considerably faster. It was thus concluded that imaging in counting mode is strictly required to collect high-resolution data of Amphipol-reconstituted BetP for subsequent SPA structure determination.

200 keV *vs*. 300 keV data collection

One recent development in the field of cryo-EM SPA is the collection of high-resolution datasets at lower acceleration voltages, initially proposed by K. R. Vinothkumar and Nobel Laureate R. Henderson (Vinothkumar & Henderson, 2016). During this thesis, it was possible to collect multiple cryo-EM SPA datasets of Amphipol-reconstituted BetP at different electron microscopes. This variety of microscope / detector combinations enables a primary comparison of the sampled experimental setups, with the aim to select the most suitable instrument for future experiments. A sound comparison of data collected at 200 keV (BetP in the down-regulated state, see TABLE 14) *vs*. 300 keV (BetP in the transition state, see TABLE 15) is thus of great interest. 2D class averages from subsets of both datasets were created following the same data processing strategy (see SPA RECONSTRUCTION, VALIDATION AND INTERPRETATION). The results are presented in FIGURE 19a (200 keV dataset) and FIGURE 19b (300 keV dataset), respectively. Intriguingly, secondary structure features are more prominent in class averages calculated from the 200 keV dataset, while the overall distribution of particles-per-class is similar in both datasets. The latter argues in favor of both an overall comparable sample quality and a suitable data processing procedure, providing a profound foundation for further discussion.

In general, micrographs collected at lower acceleration voltage exhibit more low-resolution contrast, which is attributed to increased atomic cross sections of the scattered electrons (Lyumkis, 2019; Wu & Lander, 2020a). Consequently, imaging at 200 keV may ameliorate pre-processing procedures such as motion correction, particle picking and 2D classification due to a better visibility of the particles in the micrographs, presumably reflected by the presented 2D class averages (FIGURE 19). Imaging at 300 keV, on the other hand, offers a number of electron optical / physical advantages such as reduced inelastic scattering, smaller defocus spread and minimized specimen charging (Henderson, 1995; Herzik Jr *et al.*, 2017; Lyumkis, 2019; Peet *et al.*, 2019; Wu & Lander, 2020b). Indeed, when comparing the 3D reconstructions obtained from the two datasets, the 300 keV data yielded a higher overall resolution (3.7 Å vs. 4.3 Å; see also IX. PREPRINT 1). Both reconstructions were obtained from a comparable number of particles. However, it needs to be considered that the two structures represent different states of BetP, with the higher-resolution 300 keV reconstruction representing a symmetric and stable conformation, as opposed to the

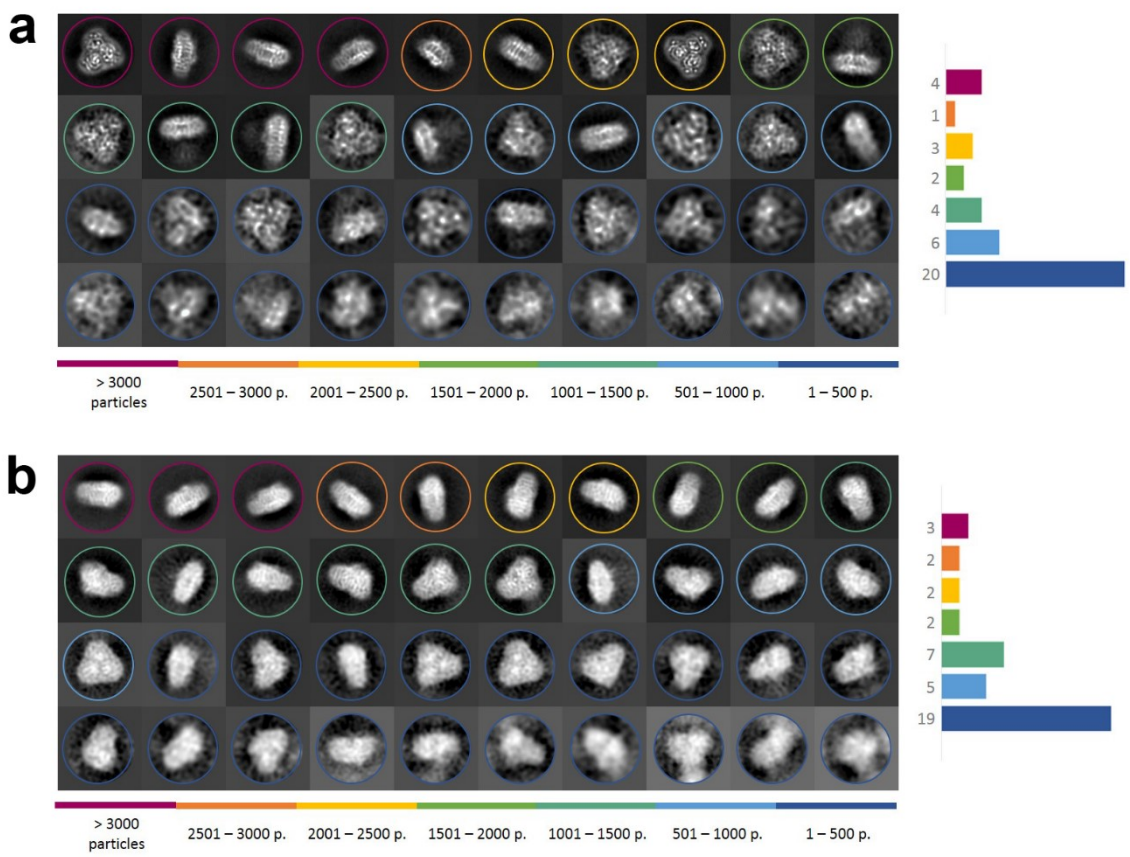

Figure 19: 200 keV vs. *300 keV*

2D class averages of Amphipol-reconstituted BetP particles, collected at 200 keV (a) or 300 keV (b), respectively. The class averages were created from the same number of initially picked particles using the same classification strategy. The numbers of particles per class are color-coded.

asymmetric, flexible conformation observed in the 200 keV dataset. The global resolution of the 3D reconstructions can thus not be used as a measure for dataset quality in this case.

Consequently, with the encouraging 2D classification results for the 200 keV dataset in mind, a comprehensive discussion of recent developments in the field seems reasonable. Firstly, it should be mentioned that a number of high-resolution cryo-EM SPA structures have been solved from 200 keV datasets in the last years, including e.g. the 20S proteasome and rabbit muscle aldolase (Herzik Jr *et al.*, 2017), alcohol dehydrogenase and methemoglobin (Herzik Jr. *et al.*, 2019), mouse apoferritin (Hamdi *et al.*, 2019) or an energy-coupling factor transporter (Thangaratnarajah *et al.*, 2021). A vast majority of those data were collected at medium-class cryo-electron microscopes, such as the Thermo Fisher Glacios or Talos series. While the obvious benefits of these TEMs are clearly the reduced purchase and maintenance costs and better accessibility, they seem to suffer from a less sophisticated electron optics configuration in comparison to the high-end 300 keV TEMs,

e.g. the Thermo Fisher Titan Krios. However, it has also been demonstrated that a number of microscope aberrations can be corrected for at the data processing step (Cash *et al.*, 2020). Lastly, since the introduction of the JEOL JEM-Z200FSC ("cryoARM 200"), a dedicated high-end 200 keV cryo-TEM is commercially available, offering the advantages of a highly coherent and bright cold field emission gun (FEG) electron source (Hamaguchi *et al.*, 2019), in-column energy filtering (Yonekura *et al.*, 2006) and optional Volta phase plate (Danev & Baumeister, 2017; Danev *et al.*, 2017). Pioneering research, e.g. in the groups of K. Namba (Kato *et al.*, 2019) and S. Subramaniam (Merk *et al.*, 2020), proofed the superior eligibility of this unique cryo-TEM for routine, competitive high-resolution SPA cryo-EM structure determination. Since the technical drawbacks have been compensated for in this novel cryo-TEM configuration, it offers the possibility to fully exploit the advantages of imaging at 200 keV, such as superior contrast and reduced radiation damage (Peet *et al.*, 2019). Amphipol-reconstituted BetP, with a molecular weight of 192 kDa, is considered to fully satisfy the sample criteria required to obtain high-resolution data in such experiment (Peet *et al.*, 2019; Wu & Lander, 2020b). In conclusion, considering our own promising preliminary results and recent technical developments and experience from other groups, SPA cryo-EM structure determination at 200 keV is highly promising for membrane protein samples.

IV. 5 SPA cryo-EM reconstruction strategies

It is commonly agreed on that only high sample quality combined with an appropriate data collection strategy will ultimately yield datasets suitable for SPA structure determination at atomic resolution. Major aspects and efforts to achieve high resolution cryo-EM data made throughout this thesis have been outlined above. Consequently, the last step to be discussed here are the data analysis strategies, which will be evaluated in the following. Two studies comprised within this thesis represent SPA projects: The *V. vulnificus* stressosome complex, described in VIII. PUBLICATION 1, and the *C. glutamicum* betaine transporter BetP analyzed in IX. PREPRINT 1. Although the same experimental approach – cryo-EM SPA analysis – had been selected for structure determination in both projects, the target objects feature considerable differences. A detailed analysis of encountered difficulties and the respectively resulting data processing strategies may thus yield valuable insights for future SPA projects.

SPA reconstruction generally relies on averaging of the information contained in thousands of single, cropped particle images. Consequently, under the assumption of equal protein quality and identical particle numbers, homogeneous samples have a greater potential to result in high-resolution averages than heterogeneous ones. In the optimal case, heterogeneity should be carefully addressed already at the sample preparation stage, as discussed in IV. 2 SAMPLES AND SAMPLE PREPARATION for the case of BetP. Here, screening of different membrane protein reconstitution methods and optimization of vitrification parameters reproducibly yielded grids suitable for high-resolution data collection. On the other hand, heterogeneity may also represent an intrinsic, physiological feature of the respective sample, e.g. originating from variations in complex stoichiometry as encountered in the *V. vulnificus* stressosome sample. For this complex, the observed heterogeneity was finally suggested to play a regulatory role by integrating physiological and genomic data into the study (VIII. PUBLICATION 1). This contrasting juxtaposition once more highlights the importance of sample screening and quality control: Intrinsic, functional heterogeneity can only be unambiguously identified when sample preparation artifacts can be in turn excluded. The challenges imposed by the necessity of processing such heterogeneous datasets have been addressed by a number of data processing tools developed over the past years (Serna, 2019), and include e.g. masked classifications and refinements (Scheres, 2016), partial signal subtraction (Bai *et al.*, 2015), localized

reconstructionns (Ilca *et al.*, 2015) or focused refinements, multi-body refinements (Nakane *et al.*, 2018) or 3D variability analysis (Punjani & Fleet, 2021). Consequently, a number of these tools have been applied in course of this thesis to solve the structures of the *V. vulnificus* stressosome complex and the *C. glutamicum* betaine transporter BetP, as outlined in the respective publications and manuscripts (VIII. PUBLICATION 1 and IX. PREPRINT 1).

In both projects, accurate pre-processing – i.e. movie alignment, CTF estimation, particle picking and 2D classification – of the data turned out to be crucial for later successful 3D reconstruction. In the case of the stressosome complex, particle identification in the micrographs is comparably easy, due to their large size and the generally good contrast of soluble proteins. However, the signal of the sensory domains ('turrets') is significantly weaker in comparison to the stressosome core, which in turn complicates the alignment process. Consequently, it was necessary to carefully clean the dataset from broken particles and to thoroughly center them into the box, to finally obtain 2D class averages with well-distinguishable turret densities. Only in 3D reconstructions obtained from particles fulfilling these criteria the turret densities could be prevented from being averaged out. This procedure finally enabled us to describe a set of stoichiometries prevalent in the dataset, putatively reflecting a regulatory mechanism of the *V. vulnificus* stress response (VIII. PUBLICATION 1). In the case of BetP, in contrast, particle picking turned out to be a difficult, yet crucial step of pre-processing, since auto-picking frequently failed to identify the low-abundance top – down-projections ('top views') in the micrographs. The procedure could be optimized by manually selecting top views, followed by 2D classification and subsequent use of the optimized 2D class averages as templates during auto-picking. Only after four iterations of 2D classification and auto-picking, top view class averages exhibiting high-resolution secondary structure features could be obtained. This behavior of the picking algorithm could be explained by the irregular shape of the BetP trimer, featuring large differences in the dimensions of top and side views, which translate into a significantly different distribution of signal *vs*. background noise in the boxed particles. Similarly, only after cleaning the dataset from low-resolution particles, meaningful 3D reconstructions could be obtained. Recognizable secondary structure features in the 2D class averages turned out to be essential for successful 3D refinement.

Intriguingly, both SPA projects share another feature requiring enhanced attention during 3D structure determination, namely the presence of and a certain deviation from symmetry

in the respective oligomeric assemblies or complexes. In the past, it was shown *via* tandem-affinity-purification coupled to mass spectrometry that a large majority of all proteins in budding yeast (>80%) form complexes with at least one interaction partner (Gavin *et al.*, 2006). The same time, a demonstrative computational study based on entries in the PDB database revealed a strong inclination for symmetry in both homo- and heteromeric protein complexes (Levy *et al.*, 2006), which has been attributed in literature to its promotion of e.g. coding efficiency, stability, cooperativity, aggregation protection or efficient folding (Blundell & Srinivasan, 1996; Goodsell & Olson, 2000; Bonjack & Avnir, 2020). Notably, the favored and beneficial formation of symmetric complexes has also been reported for membrane proteins (Forrest, 2015). In line with these basic findings, we were able to show that the *V. vulnificus* stressosome complex features a heteromeric, pseudo-symmetric subunit arrangement interpreted as a regulatory mechanism to dynamically adapt the cell's stress response (see VIII. PUBLICATION 1). For the trimeric and C3 symmetrical transporter BetP, the loss of symmetry upon raising the K^+ concentration in the sample could be shown to be a consequence and functional pre-requisite of transport up-regulation (see IX. PREPRINT 1). For both the stressosome complex and BetP, their respective (pseudo-) symmetric assembly results in the aforementioned, biologically and functionally relevant sample heterogeneity, with BetP exhibiting continuous flexibility and the stressosome complex representing discrete heterogeneity, respectively (Punjani & Fleet, 2021).

From a more general perspective, in both projects a loss or break of symmetry reflects the protein's or complex's ability to react on environmental changes. This strategy – a deviation from perfect symmetry to enable a certain functionality of the respective protein – has been described in literature for a broad variety of diverse biological assemblies, both from structural and functional points of view. E.g., the icosahedral symmetry of bacteriophage capsids or herpes viruses is oftentimes interrupted at a certain 5-fold vertex to allow for the attachment of a portal protein complex required for genome packaging and release (Bhardwaj *et al.*, 2014; Parent *et al.*, 2018). In another, ground-breaking study, the gating-related loss of symmetry under Mg^{2+}-free conditions was demonstrated *via* SPA cryo-EM for the magnesium channel CorA (Matthies *et al.*, 2016). In line with these and other examples, symmetric protein assemblies are regarded as comparably rigid and stable. Consequently, synthetically produced 'designer proteins' are oftentimes bio-engineered as self-assembling, symmetrical oligomers. Applications of those, oftentimes cubic-

symmetric assemblies, comprise e.g. drug encapsulation or exterior display (Cannon *et al.*, 2019).

The characteristic trait of protein monomers to assemble into "[…]near symmetric" oligomers has been analyzed in more detail by M. Bonjack and D. Avnir, who realized that this property is much more pronounced in protein complexes analyzed in solution than in X-ray crystallography (Bonjack & Avnir, 2020). They were furthermore able to narrow down the general source of asymmetry to mainly hydrophilic amino acids along the protein interface(s) around the symmetry axis, which adopt asymmetric orientations to facilitate the formation of stabilizing hydrogen and ionic bonds between the protein monomers (Bonjack & Avnir, 2020). Similarly, we were able to demonstrate an asymmetric localization of lipid molecules located at the interfaces between the BetP protomers (see IX. PREPRINT 1). Moreover, Bonjack and Avnir pointed out that the principle of "[…]near symmetry" was especially obvious and pronounced in the hinge regions of dimeric complexes featuring the domain-swapping mechanism – as it is the case in the asymmetric *V. vulnificus* RsbR dimer (see VIII. PUBLICATION 1). In conclusion, these findings which are perfectly in line with our own observations strengthen the hypothesis that although protein complexes tend to assemble in a symmetric way for the reasons outlined above, it is the subtle deviation from perfect symmetry which enables them to act and function as molecular machines.

V. Concluding remarks and future perspectives

It is evident from the publications and manuscripts achieved throughout this thesis that a number of novel, biologically relevant results and insights could be obtained. However, while some questions could be answered, new queries arose. Undoubtedly, this is a common process driving scientific research in all disciplines. Consequently, in the following section I will elaborate on some of the most urgent follow-up questions from a structural-biological point of view, and also illustrate how emerging techniques and novel electron microscopy methods may help to address these questions.

One of the major results of our research on the *V. vulnificus* stressosome is the description of variable complex stoichiometries, which is interpreted as a possible regulation mechanism to dynamically adapt the cells' stress response to the respective stimulus (see VIII. PUBLICATION 1). In agreement with previous studies, the structural investigations have been performed on *in vitro* assembled stressosome complexes, built from isolated proteins expressed and purified from *E. coli* cells. As a next step, it would thus be of great interest to investigate stressosome complexes in their natural cellular environment. Sub-tomogram averaging represents an increasingly popular method for structure determination of large, macromolecular complexes at intermediate to high resolution from datasets obtained of whole bacterial cells, and should thus be applicable here. Studying complex stoichiometry under different growth conditions would certainly provide new, exciting mechanistic insights. Moreover, we were able to show a cellular response to the iron concentration in the growth medium. In combination with the presence of a heme group in the sensory domain of the RsbR protein, these findings point towards an iron-dependent stressosome activation mechanism. Atomic resolution structures of the oxidized and reduced variants of the RsbR dimer would be key to subsequently elucidate this mechanism. Since RsbR dimers have been demonstrated to form stressosome complexes themselves, X-ray crystallography might be considered as a suitable alternative to cryo-EM SPA structure determination here. In conclusion, our structural and physiological results may pave the way for future, tailored experiments elucidating further details of the versatile stress response mechanism of the human pathogen *V. vulnificus*.

In my second research project, SPA cryo-EM structure determination was successfully used to solve the first structure of the betaine transporter BetP in a down-regulated state (IX.

PREPRINT 1). Together with additional functional and biochemical data, the resulting study represents a prime example for an integrative structural-biological approach and allowed us to suggest a coherent regulation mechanism for BetP. Apart from our current study, a wealth of structural and functional data are already available for BetP under active conditions; molecular and high-resolution structural data on its down-regulated state and the regulation process itself are however less abundant. From this point of view, an atomic resolution SPA cryo-EM structure of BetP in its native lipid bilayer, e.g. embedded into SMALPs, would be of great interest. A complementary study in proteoliposomes might help to further investigate the effect of lateral membrane pressure on the transporter. Since BetP is a model system, structural and mechanistic insights gained from these additional experiments could be transferred to other transporters and would thus provide valuable information for future research on a large variety of membrane proteins.

In a proof of principle study, we were able to demonstrate the excellent suitability of dual-axis STEM tomography to analyze the membrane architecture of sER morphotypes occurring in their natural HEK cell environment upon protein over-expression (X. MANUSCRIPT 1). The description of two very different morphotypes at an unprecedented level of detail allowed for a precise definition of the intracellular interaction network of the organelles, laying a sound foundation for urging questions about intracellular functions, putative tasks and the underlying shaping mechanisms of whorls and crystalloid-ER, respectively. Two different strategies might be pursued in the future to address these questions. First, the function(s) of the sER morphotypes within the cell might be elucidated *via* immuno-labeling studies using different marker proteins (specific for e.g. PC-2, a certain metabolic pathway, sER or rER, etc.) as targets. Notably, correlative light and electron microscopy (CLEM) would represent an appropriate, yet time-consuming alternative technique. Second, establishing a purification protocol for ER membranes from the HEK cells would allow for a large number of biochemical assays to be performed. Kits for gradient-centrifugation based purification of ER microsomes are commercially available; however, the respective protocols certainly need to be adapted and optimized to obtain pure crystalloid-ER and whorl fractions for further experiments. If successful, however, this would allow for e.g. a lipid analysis *via* mass spectroscopy or a purification and reconstitution of PC-2 for SPA cryo-EM structure determination from the respective sER fractions. In summary, the detailed description of the sER morphotypes and their interaction network proofed the applicability of STEM tomography to analyze organellar

ultrastructure within the cellular context, and is furthermore regarded as the basis for future biochemical studies.

Finally, the diverse experiments performed throughout this thesis also allowed for a more technical discussion of the electron microscopy methods used, their suitability for the underlying research questions and the consequential future perspectives for the respective projects. As outlined above, STEM tomography proofed very useful to describe high-resolution ultra-structural details on organelle level. Thus, establishing the method paved the way to extend our research to the cellular level, providing an exciting additional viewing angle for future studies. Furthermore, cryo-EM at 200 keV could be shown to provide data suitable for high-resolution SPA structure determination of membrane proteins. The use of an energy filter or a Volta phase plate may extend the possible resolution range even more. Considering availability and costs in comparison to 300 keV instruments, this approach bears the potential to significantly speed up and facilitate future SPA projects. Lastly, sub-tomogram averaging as a hybrid method combining cryo-electron tomography and SPA reconstruction may ultimately bridge the gap between atomic-resolution structure determination and *in situ* protein analysis. In conclusion, the entity of studies comprised within this thesis illustrates the versatility of diverse electron microscopy techniques to address a broad variety of scientific questions, and highlights the great potential lying in the further developments of the method itself.

VI. References

VI. 1 Own publications

Heinz, V.*, Jäckel, W.*, Kaltwasser, S., Cutugno, L., Bedrunka, P., Graf, A., Reder, A., Michalik, S., Dhople, V. M., Madej, M. G., Conway, M., Lechner, M., Riedel, K., Bange, G., Boyd, A., Völker, U., Lewis, R. J., Marles-Wright, J., Ziegler, C. & Pané-Farré, J. (2022): The *Vibrio vulnificus* stressosome is an oxygen-sensor involved in regulating iron metabolism. *Commun. Biol.* 5, 622.

Heinz, V*., Güler, G.*, Leone, V., Madej, M. G., Maksimov, S., Gärtner, R. M., Rudi, O., Hamdi, F., Kastritis, P. L., Mäntele, W., Krämer, R., Forrest, L. R., Perez, C. & Ziegler, C. (2022): Osmotic stress response in BetP: How lipids and K^+ team up to overcome downregulation. (Preprint available at *bioRxiv*).

Heinz, V., Rachel, R. & Ziegler, C.: Application of STEM tomography to investigate smooth ER morphology under stress conditions. (Manuscript to be submitted to *J. Struct. Biol.*).

Peter, M. F., Depping, P., Schneberger, N., Severi, E., Gatterdam, K., Tindall, S., Durand, A., Heinz, V., König, P.-A., Geyer, M., Ziegler, C., Thomas, G. H. & Hagelueken, G. (2022): Structural and mechanistic analysis of a tripartite ATP-independent periplasmic (TRAP) transporter. *Nat. Comm*. 13:4471.

Leone, V., Bradshaw, R. T., Koshy, C., Lee, P. S., Fenollar-Ferrer, C., Heinz, V., Ziegler, C. & Forrest, L.: Autoregulation of a trimeric transporter involves the cytoplasmic domains of both adjacent subunits. (Preprint available at *bioRxiv*).

Allolio, C., Magarkar, A., Jurkiewicz, P., Baxova, K., Javanainen, M., Mason, P., Sachl, R., Cebecauer, M., Hof, M., Horinek, D., Heinz, V., Rachel, R., Ziegler, C., Schröfel, A. & Jungwirth, P. (2018): Arginine-rich cell-penetrating peptides induce membrane multilamellarity and subsequently enter via formation of a fusion pore. *PNAS,* 115(47): 11923-11928.

Wilkes, M., Madej, M. G., Kreuter, L., Rhinow, D., Heinz, V., De Sanctis, S., Ruppel, S., Richter, R. M., Joos, F., Grieben, M., Pike, A. C. W., Huiskonen, J. T., Carpenter, E. P., Kühlbrandt, W., Witzgall, R. & Ziegler, C. (2017): Molecular Insights into lipid-assisted Ca^{2+} regulation of the TRP channel Polycystin-2. *Nat. Struct. Mol,* 24:123-130.

Heimerl, T., Flechsler, J., Pickl, C., Heinz, V., Salecker, B., Zweck, J., Wanner, G., Geimer, S., Samson, R. Y., Bell, S. D., Huber, H., Wirth, R., Wurch, L., Podar, M. & Rachel, R. (2017): A Complex Endomembrane System in the Archaeon *Ignicoccus hospitalis* Tapped by *Nanoarchaeum equitans*. *Front. Microbiol.,* 8:1072.

Perras, A. K., Wanner, G., Klingl, A., Mora, M., Auerbach, A. K., Heinz, V., Probst, A. J., Huber, H., Rachel, R., Meck, S. & Moissl-Eichinger, C. (2014): Grappling archaea: ultrastructural analyses of an uncultivated, cold-loving archaeon, and its biofilm. *Front. Microbiol.,* 5:397.

VI. 2 Citations

Abràmoff, M. D., Magalhães, P. J., & Ram, S. J. (2004): Image Processing with ImageJ. *Biophotonics Int. ,* 11:36-41.

Adams, P. D., Afonine, P. V., Bunkóczi, G.*, et al.* (2009): *PHENIX*: a comprehensive Python-based system for macromolecular structure solution. *Acta Cryst.,* D66:213–221.

Adrian, M., Dubochet, J., Lepault, J.*, et al.* (1984): Cryo-electron microscopy of viruses. *Nature,* 308:32-36.

Akbar, S., Gaidenko, T. A., Kang, C. M.*, et al.* (2001): New Family of Regulators in the Environmental Signaling Pathway Which Activates the General Stress Transcription Factor sB of *Bacillus subtilis*. *J. Bacteriol.,* 183(4):1329–1338.

Anderson, R. G. W., Orci, L., Brown, M. S.*, et al.* (1983): Ultrastructural Analysis of Crystalloid Endoplasmic Reticulum in UT-1 cells and its Disappearance in Response to Cholesterol. *J. Cell. Sci.,* 63:1-20.

Aoyama, K., Takagia, T., Hirase, A.*, et al.* (2008): STEM tomography for thick biological specimens. *Ultramicroscopy,* 109(1):70-80.

Aravind, L., & Koonin, E. V. (2000): The STAS domain - a link between anion transporters and antisigma-factor antagonists. *Curr.,* 10(2):53-55.

Autzen, H. E., Myasnikov, A. G., Campbell, M. G.*, et al.* (2018): Structure of the human TRPM4 ion channel in a lipid nanodisc. *Science,* 359(6372):228–232.

Ávila-Pérez, M., Hellingwerf, K. J., & Kort, R. (2006): Blue Light Activates the sigB-Dependent Stress Response of *Bacillus subtilis* via YtvA. *J. Bacteriol.,* 188(17):6411–6414.

Bai, X., Rajendra, E., Yang, G.*, et al.* (2015). Sampling the conformational space of the catalytic subunit of human γ-secretase. *eLife*. Retrieved from doi:10.7554/eLife.11182

Bayburt, T. H., Grinkova, Y. V., & Sligar, S. G. (2002): Self-Assembly of Discoidal Phospholipid Bilayer Nanoparticles with Membrane Scaffold Proteins. *Nano Lett.,* 2(8):853-856.

Bayburt, T. H., & Sligar, S. G. (2003): Self-assembly of single integral membrane proteins into soluble nanoscale phospholipid bilayers. *Protein Sci.,* 12:2476–2481.

Bayburt, T. H., & Sligar, S. G. (2010): Membrane protein assembly into Nanodiscs. *FEBS Lett.,* 584:1721–1727.

Ben-Harush, K., Maimon, T., Patla, I.*, et al.* (2010): Visualizing cellular processes at the molecular level by cryo-electron tomography. *J. Cell Sci.,* 123:7-12.

Bhardwaj, A., Olia, A. S., & Cingolani, G. (2014): Architecture of Viral Genome-Delivery Molecular Machines. *Curr Opin Struct Biol.,* 25:1-8.

Blundell, T. L., & Srinivasan, N. (1996): Symmetry, stability, and dynamics of multidomain and multicomponent protein systems. *PNAS,* 93:14243–14248.

Boerngen, K., Battle, A. R., Moeker, N.*, et al.* (2010): The properties and contribution of the *Corynebacterium glutamicum* MscS variant to fine-tuning of osmotic adaptation. *Biochim Biophys Acta,* 1798:2141–2149.

Bonjack, M., & Avnir, D. (2020): The near-symmetry of protein oligomers: NMR-derived structures. *Sci. Rep.,* 10(8367).

Booth, I. R. (2014): Bacterial mechanosensitive channels: progress towards an understanding of their roles in cell physiology. *Curr. Opin. Microbiol.,* 18:16–22.

Borgese, N., Francolini, M., & Snapp, E. (2006): Endoplasmic reticulum architecture: structures in flux. *Curr Opin Cell Biol,* 18(4):358–364.

Borries, B. v., Ruska, E., & Ruska, H. (1938): Bakterien und Virus in Übermikroskopischer Aufnahme. *Klin. Wochenschr.,* 17:921–925.

Botzenhardt, J., Morbach, S., & Kraemer, R. (2004): Activity regulation of the betaine transporter BetP of *Corynebacterium glutamicum* in response to osmotic compensation. *Biochim Biophys Acta,* 1667:229– 240.

Bradford, M. M. (1976): A Rapid and Sensitive Method for the Quantitation of Microgram Quantities of Protein Utilizing the Principle of Protein-Dye Binding. *Anal. Biochem.,* 72:248-254.

Bremer, E., & Kraemer, R. (2019): Responses of Microorganisms to Osmotic Stress. *Annu. Rev. Microbiol.,* 73:313–334.

Brenner, S., & Horne, R. W. (1959): A Negative Staining Method for High Resolution Electron Microscopy of Viruses. *Biochim Biophys Acta,* 34:103-110.

Brigulla, M., Hoffmann, T., Krisp, A.*, et al.* (2003): Chill Induction of the SigB-Dependent General Stress Response in *Bacillus subtilis* and Its Contribution to Low-Temperature Adaptation. *J. Bacteriol.,* 185(15):4305–4314.

Brown, M. K., & Naidoo, N. (2012): The endoplasmic reticulum stress response in aging and age-related diseases. *Front. physiol.,* 3(263):1-10.

Cannon, K. A., Ochoa, J. M., & Yeates, T. O. (2019): High-Symmetry Protein Assemblies: Patterns and Emerging Applications. *Curr. Opin. Struct. Biol.,* 55:77-84.

Cash, J. N., Kearns, S., Li, Y.*, et al.* (2020): High-resolution cryo-EM using beam-image shift at 200 keV. *IUCrJ,* 2020(7):1179–1187.

Chen, C.-C., Lewis, R. J., Harris, R.*, et al.* (2003): A supramolecular complex in the environmental stress signalling pathway of *Bacillus subtilis*. *Mol. Microbiol.,* 49(6):1657–1669.

Chen, Q., She, J., Zeng, W., *et al.* (2017): Structure of mammalian endolysosomal TRPML1 channel in nanodiscs. *Nature,* 550:415-420.

Cheng, Y. (2018): Single particle cryo-EM – how did it get here and where will it go. *Science,* 361(6405):876–880.

Chin, D. J., Luskey, K. L., Anderson, R. G. W., *et al.* (1982): Appearance of crystalloid endoplasmic reticulum in compactinresistant Chinese hamster cells with a 500-fold increase in 3-hydroxy-3-methylglutaryl-coenzyme A reductase. *PNAS,* 79:1185-1189.

Dahl, R., & Staehelin, L. A. (1989): High-pressure Freezing for the Preservation of Biological Structure: Theory and Practice. *J. Electron Microsc. Tech.,* 13:165-174.

Danev, R., & Baumeister, W. (2017): Expanding the boundaries of cryo-EM with phase plates. *Curr. Opin. Struct. Biol.,* 46:87–94.

Danev, R., Tegunov, D., & Baumeister, W. (2017). Using the Volta phase plate with defocus for cryo-EM single particle analysis. *eLife*. Retrieved from

De la Rosa-Trevín, J. M., Quintana, A., Cano, L. d., *et al.* (2016): Scipion: A software framework toward integration, reproducibility and validation in 3D electron microscopy. *J. Struct. Biol.,* 195(1):93-99.

De Rosier, D. J., & Klug, A. (1968): Reconstruction of Three Dimensional Structures from Electron Micrographs. *Nature,* 217:130-134.

Delumeau, O., Chen, C.-C., Murray, J. W., *et al.* (2006): High-Molecular-Weight Complexes of RsbR and Paralogues in the Environmental Signaling Pathway of *Bacillus subtilis*. *J. Bacteriol.,* 188(22):7885–7892.

Denisov, I. G., Grinkova, Y. V., Lazarides, A. A., *et al.* (2004): Directed Self-Assembly of Monodisperse Phospholipid Bilayer Nanodiscs with Controlled Size. *J. Am. Chem. Soc.,* 126(11):3477-3487.

Dierksen, K., Typke, D., Hegerl, R., *et al.* (1995): Three-Dimensional Structure of Lipid Vesicles Embedded in Vitreous Ice and Investigated by Automated Electron Tomography. *Biophys. J.,* 68:1416-1422.

Dörr, J. M., Koorengevel, M. C., Schäfer, M., *et al.* (2014): Detergent-free isolation, characterization, and functional reconstitution of a tetrameric K^+ channel: The power of native nanodiscs. *PNAS,* 111(52):18607–18612.

Dörr, J. M., Scheidelaar, S., Koorengevel, M. C., *et al.* (2015): The styrene–maleic acid copolymer: a versatile tool in membrane research. *Eur Biophys J,* 45:3–21.

Dubochet, J., Adrian, M., Chang, J.-J., *et al.* (1988): Cryo-electron microscopy of vitrified specimens. *Q. Rev. Biophys.,* 21(2):129-228.

Dubochet, J., Chang, J.-J., Freeman, R., *et al.* (1982): Frozen Aqueous Suspensions. *Ultramicroscopy,* 10:55-62.

Ellgaard, L., Molinari, M., & Helenius, A. (1999): Setting the Standards: Quality Control in the Secretory Pathway. *Science,* 286:1882-1888.

Emsley, P., Lohkamp, B., Scott, W. G.*, et al.* (2010): Features and development of *Coot*. *Acta Cryst.,* D66:486–501.

Engelhard, C., Raffelberg, S., Tang, Y.*, et al.* (2013): A structural model for the full-length blue light-sensing protein YtvA from *Bacillus subtilis*, based on EPR spectroscopy. *Photochem. Photobiol. Sci.,* 12:1855–1863.

Eymann, C., Schulz, S., Gronau, K.*, et al.* (2011): In vivo phosphorylation patterns of key stressosome proteins define a second feedback loop that limits activation of *Bacillus subtilis* sB. *Mol. Microbiol.,* 80(3):798–810.

Farwick, M., Siewe, R. M., & Kraemer, R. (1995): Glycine Betaine Uptake after Hyperosmotic Shift in *Corynebacterium glutamicum*. *J. Bacteriol.,* 177(16):4690–4695.

Fernandez-Leiro, R., & Scheres, S. H. W. (2016): Unravelling biological macromolecules with cryo-electron microscopy. *Nature,* 537:339–346.

Forrest, L. R. (2015): Structural Symmetry in Membrane Proteins. *Annu. Rev. Biophys.,* 44:311–337.

Forrest, L. R., Kraemer, R., & Ziegler, C. (2011): The structural basis of secondary active transport mechanisms. *Biochim Biophys Acta,* 1807:167–188.

Frank, J. (2017): Advances in the field of single-particle cryo-electron microscopy over the last decade. *Nat. Protoc.,* 12(2):209-212.

Frank, J., Radermacher, M., Penczek, P.*, et al.* (1996): SPIDER and WEB: Processing and Visualization of Images in 3D Electron Microscopy and Related Fields. *J. Struct. Biol.,* 116(30):190–199.

Frauenfeld, J., Löving, R., Armache, J.-P.*, et al.* (2016): A saposin-lipoprotein nanoparticle system for membrane proteins. *Nat. Methods,* 13(4):345-351.

Gaidenko, T. A., Kim, T.-J., Weigel, A. L.*, et al.* (2006): The Blue-Light Receptor YtvA Acts in the Environmental Stress Signaling Pathway of *Bacillus subtilis*. *J. Bacteriol.,* 188(17):6387–6395.

Gavin, A.-C., Aloy, P., Grandi, P.*, et al.* (2006): Proteome survey reveals modularity of the yeast cell machinery. *Nature,* 440:631–636.

Ge, L., Perez, C., Waclavska, I.*, et al.* (2011): Locating an extracellular K^+-dependent interaction site that modulates betaine-binding of the Na^+-coupled betaine symporter BetP. *PNAS,* 108(43):E890-E898.

Giuliodori, A. M., Gualerzi, C. O., Soto, S.*, et al.* (2007): Review on Bacterial Stress Topics. *Ann. N.Y. Acad. Sci.,* 1113:95–104.

Goddard, T. D., Huang, C. C., Meng, E. C., *et al.* (2017): UCSF ChimeraX: Meeting modern challenges in visualization and analysis. *Protein Sci.,* 27:14-25.

Gohon, Y., Giusti, F., Prata, C., *et al.* (2006): Well-Defined Nanoparticles Formed by Hydrophobic Assembly of a Short and Polydisperse Random Terpolymer, Amphipol A8-35. *Langmuir,* 22(3):1281-1290.

Goodsell, D., & Olson, A. J. (2000): Structural Symmetry and Protein Function. *Annu. Rev. Biophys. Biomol. Struct.,* 29:105-153.

Gottesmann, S. (2019): Trouble is coming: Signaling pathways that regulate general stress responses in bacteria. *J. Biol. Chem.,* 294(31):11685–11700.

Grimm, R., Singh, H., Rachel, R., *et al.* (1998): Electron Tomography of Ice-Embedded Prokaryotic Cells. *Biophys. J.,* 74:1031-1042.

Gueler, G., Gaertner, R. M., Ziegler, C., *et al.* (2016): Lipid-Protein Interactions in the Regulated Betaine Symporter BetP Probed by Infrared Spectroscopy. *J. Biol. Chem.,* 291(9):4295–4307.

Guesdon, A., Blestel, S., Kervrann, C., *et al.* (2013): Single versus dual-axis cryo-electron tomography of microtubules assembled *in vitro*: Limits and perspectives. *J. Struct. Biol.,* 181:169-178.

Gunde-Cimerman, N., Plemenitas, A., & Oren, A. (2018): Strategies of adaptation of microorganisms of the three domains of life to high salt concentrations. *FEMS Microbiol. Rev.,* 42:353–375.

Guo, J., She, J., Zeng, W., *et al.* (2017): Structures of the calcium-activated, non-selective cation channel TRPM4. *Nature,* 552:205-211.

Hamaguchi, T., Maki-Yonekura, S., Naitow, H., *et al.* (2019): A new cryo-EM system for single particle analysis. *J. Struct. Biol.,* 207:40–48.

Hamdi, F., Tüting, C., Semchonok, D. A., *et al.* (2019): 2.7 Å cryo-EM structure of vitrified *M. musculus* H-chain apoferritin from a compact 200 keV cryo-microscope. *PLoS One,* 15(5):e0232540.

Harding, H. P., & Ron, D. (2002): Endoplasmic Reticulum Stress and the Development of Diabetes. *Diabetes,* 51(3):S455-S461.

Haselwandter, C. A., & MacKinnon, R. (2018): Piezo's membrane footprint and its contribution to mechanosensitivity. *eLife,* 7(e41968):1-29.

Hecker, M., Pané-Farré, J., & Voelker, U. (2007): SigB-Dependent General Stress Response in *Bacillus subtilis* and Related Gram-Positive Bacteria. *Annu. Rev. Microbiol.,* 61:215–236.

Henderson, R. (1995): The potential and limitations of neutrons, electrons and X-rays for atomic resolution microscopy of unstained biological molecules. *Q. Rev. Biophys.,* 28(2):171-193.

Hengge, R. (2000): The general stress response in Escherichia coli. In *Bacterial Stress Responses*: ASM Press.

Herzik Jr, M. A., Wu, M., & Lander, G. C. (2017): Achieving better-than-3-Å resolution by single-particle cryo-EM at 200 keV. *Nat. Methods,* 14(11):1075-1078.

Herzik Jr., M. A., Wu, M., & Lander, G. C. (2019): High-resolution structure determination of sub-100 kDa complexes using conventional cryo-EM. *Nat. Commun.,* 10(1032).

Hohmann-Marriott, M. F., Sousa, A. A., Azari, A. A.*, et al.* (2009): Nanoscale 3D cellular imaging by axial scanning transmission electron tomography. *Nat Methods,* 6:729–731.

Hoischen, C., & Kraemer, R. (1990): Membrane Alteration Is Necessary but Not Sufficient for Effective Glutamate Secretion in *Corynebacterium glutamicum*. *J. Bacteriol.,* 172(6):3409-3416.

Hu, J., Shibata, Y., Voss, C.*, et al.* (2008): Membrane Proteins of the Endoplasmic Reticulum Induce High-Curvature Tubules. *Science,* 319(5867):1247-1250.

Ilca, S. L., Kotecha, A., Sun, X.*, et al.* (2015): Localized reconstruction of subunits from electron cryomicroscopy images of macromolecular complexes. *Nat. Commun.,* 6(8843):1-8.

Jamshad, M., Charlton, J., Lin, Y.-P.*, et al.* (2015): G-protein coupled receptor solubilization and purification for biophysical analysis and functional studies, in the total absence of detergent. *Biosci. Rep.,* 35(e00188).

Jia, X., Wang, J.-b., Rivera, S.*, et al.* (2016): An O2-sensing stressosome from a Gram-negative bacterium. *Nat. Commun.,* 7(12381):1-8.

Jin, P., Bulkley, D., Guo, Y.*, et al.* (2017): Electron cryo-microscopy structure of the mechanotransduction channel NOMPC. *Nature,* 547:pages 118–122.

Kaneko, T., Tanaka, N., & Kumasaka, T. (2005): Crystal structures of RsbQ, a stress-response regulator in *Bacillus subtilis*. *Protein Sci,* 14:558–565.

Kappes, R. M., Kempf, B., & Bremer, E. (1996): Three Transport Systems for the Osmoprotectant Glycine Betaine Operate in *Bacillus subtilis*: Characterization of OpuD. *J. Bacteriol.,* 178(17):5071–5079.

Kato, T., Makino, F., Nakane, T.*, et al.* (2019). CryoTEM with a Cold Field Emission Gun That Moves Structural Biology into a New Stage*25*(Suppl 2), 998-999. Retrieved from

Khafizov, K., Perez, C., Koshy, C.*, et al.* (2012): Investigation of the sodium-binding sites in the sodium-coupled betaine transporter BetP. *PNAS*:E3035–E3044.

Khafizov, K., Staritzbichler, R., Stamm, M.*, et al.* (2010): A Study of the Evolution of Inverted-Topology Repeats from LeuT-Fold Transporters Using AlignMe. *Biochemistry,* 49:10702–10713.

Kim, T.-J., Gaidenko, T. A., & Price, C. W. (2004a): In Vivo Phosphorylation of Partner Switching Regulators Correlates with Stress Transmission in the Environmental Signaling Pathway of *Bacillus subtilis*. *J. Bacteriol.,* 186(18):6124–6132.

Kim, T.-J., Gaidenko, T. A., & Price, C. W. (2004b): A Multicomponent Protein Complex Mediates Environmental Stress Signaling in *Bacillus subtilis*. *J. Mol. Biol.,* 341:135–150.

Kizilyaprak, C., Stierhof, Y.-D., & Humbel, B. M. (2018): Volume microscopy in biology: FIB-SEM tomography. *Tissue Cell,* 57:123-128.

Koning, A. J., Roberts, C. J., & Wright, R. L. (1996): Different Subcellular Localization of *Saccharomyces cerevisiae* HMG-CoA Reductase Isozymes at Elevated Levels Corresponds to Distinct Endoplasmic Reticulum Membrane Proliferations. *Mol. Biol. Cell.,* 7:769-789.

Korkmaz, F., Ressl, S., Ziegler, C.*, et al.* (2013): K^+-induced conformational changes in the trimeric betaine transporter BetP monitored by ATR-FTIR spectroscopy. *Biochim Biophys Acta*(1828):1181–1191.

Koshy, C., Schweikhard, E. S., Gaertner, R. M.*, et al.* (2013): Structural evidence for functional lipid interactions in the betaine transporter BetP. *EMBO J,* 32:3096–3105.

Kozlov, M. M., McMahon, H. T., & Chernomordik, L. V. (2010): Protein-driven membrane stresses in fusion and fission. *Trends Biochem. Sci.,* 35(12):699-706.

Kraemer, R. (2010): Bacterial Stimulus Perception and Signal Transduction: Response to Osmotic Stress. *Chem. Rec.,* 10:217–229.

Kraemer, R., & Morbach, S. (2004): BetP of *Corynebacterium glutamicum*, a transporter with three different functions: betaine transport, osmosensing, and osmoregulation. *Biochim Biophys Acta,* 1658:31– 36.

Kremer, J. R., Mastronarde, D. N., & McIntosh, J. R. (1996): Computer Visualization of Three-Dimensional Image Data Using IMOD. *J. Struct. Biol.,* 116(13):71–76.

Kucukelbir, A., Sigworth, F. J., & Tagare, H. D. (2014): Quantifying the local resolution of cryo-EM density maps. *Nat. Methods,* 11(1):63-65.

Kühlbrandt, W. (2014): The Resolution Revolution. *Science,* 343(6178).

Kwon, E., Pathak, D., Kim, H.-u.*, et al.* (2019): Structural insights into stressosome assembly. *IUCrJ,* 6:938–947.

Laemmli, U. K. (1970): Cleavage of Structural Proteins during the Assembly of the Head of Bacteriophage T4. *Nature,* 227:680-685.

Le Bon, C., Marconnet, A., Masscheleyn, S.*, et al.* (2018): Folding and stabilizing membrane proteins in amphipol A8-35. *Methods,* 147:95-105.

Lee, S. C., Knowles, T. J., Postis, V. L. G., *et al.* (2016): A method for detergent-free isolation of membrane proteins in their local lipid environment. *Nat. Protoc.,* 11(7):1149-1162.

Levy, E. D., Pereira-Leal, J. B., Chothia, C., *et al.* (2006): 3D Complex: A Structural Classification of Protein Complexes. *PLoS Comput. Biol.,* 2(11):e155.

Losi, A., Polverini, E., Quest, B., *et al.* (2002): First Evidence for Phototropin-Related Blue-Light Receptors in Prokaryotes. *Biophys. J.,* 82:2627–2634.

Lu, P. D., Harding, H. P., & Ron, D. (2004): Translation reinitiation at alternative open reading frames regulates gene expression in an integrated stress response. *J. Cell Biol.,* 167(1):27–33.

Luckner, M., & Wanner, G. (2018): From Light Microscopy to Analytical Scanning Electron Microscopy (SEM) and Focused Ion Beam (FIB)/SEM in Biology: Fixed Coordinates, Flat Embedding, Absolute References. *Microsc. Microanal,* 24:526–544.

Luther, P. K. (2006): Sample Shrinkage and Radiation Damage of Plastic Sections. In J. Frank (Ed.), *Electron Tomography* (Second Edition ed.). New York: Springer Science+Business Media.

Lyons, J. A., Bøggild, A., Nissen, P., *et al.* (2017): Saposin-Lipoprotein Scaffolds for Structure Determination of Membrane Transporters. *Meth. Enzymol.,* 594:85-99.

Lyumkis, D. (2019): Challenges and opportunities in cryo-EM single-particle analysis. *J. Biol. Chem.,* 294(13):5181-5197.

Marles-Wright, J., Grant, T., Delumeau, O., *et al.* (2008): Molecular Architecture of the "Stressosome," a Signal Integration and Transduction Hub. *Science,* 322:92-96.

Marles-Wright, J., & Lewis, R. J. (2008): The Bacillus subtilis stressosome - A signal integration and transduction hub. *Commun. Integr,* 1(2):182-184.

Marles-Wright, J., & Lewis, R. J. (2010): The stressosome: molecular architecture of a signalling hub. *Biochem. Soc. Trans.,* 38:928–933.

Mastronarde, D. N. (1997): Dual-Axis Tomography: An Approach with Alignment Methods That Preserve Resolution. *J. Struct. Biol.,* 120:343-352.

Mastronarde, D. N. (2003). *SerialEM: A Program for Automated Tilt Series Acquisition on Tecnai Microscopes Using Prediction of Specimen Position*. Paper presented at the Microsc Microanal 9.

Mastronarde, D. N. (2005): Automated electron microscope tomography using robust prediction of specimen movements. *J. Struct. Biol.,* 152:36–51.

Matthies, D., Dalmas, O., Borgnia, M. J., *et al.* (2016): Cryo-EM Structures of the Magnesium Channel CorA Reveal Symmetry Break upon Gating. *Cell,* 164:747-756.

Maximov, S., Ott, V., Belkoura, L.*, et al.* (2014): Stimulus analysis of BetP activation under in vivo conditions. *Biochim Biophys Acta,* 1838:1288–1295.

McBride, E. L., Rao, A., Zhang, G.*, et al.* (2018): Comparison of 3D cellular imaging techniques based on scanned electron probes: serial block face SEM vs. axial bright-field STEM tomography. *J Struct Biol.,* 202(3):216–228.

McMahon, H. T., & Gallop, J. L. (2005): Membrane curvature and mechanisms of dynamic cell membrane remodelling. *Nature,* 438:590-596.

McMullan, G., Faruqi, A. R., & Henderson, R. (2016): Direct Electron Detectors. *Meth. Enzymol.,* 579:1-17.

McMullan, G., R.Faruqi, A., Clare, D.*, et al.* (2014): Comparison ofoptimalperformanceat300keVofthreedirectelectron detectorsforuseinlowdoseelectronmicroscopy. *Ultramicroscopy,* 147:156–163.

Merk, A., Fukumura, T., Zhu, X.*, et al.* (2020): 1.8 A resolution structure of b-galactosidase with a 200 kV CRYO ARM electron microscope. *IUCrJ,* 7:1-5.

Miksys, A., Fu, L., Madej, M. G.*, et al.* (2022): Molecular insights into intra-complex signal transmission during stressosome activation. *Commun. Biol,* 5(621):1-12.

Moeglich, A., & Moffat, K. (2007): Structural Basis for Light-dependent Signaling in the Dimeric LOV Domain of the Photosensor YtvA. *J. Mol. Biol.,* 373:112–126.

Moriarty, N. W., Grosse-Kunstleve, R. W., & Adams, P. D. (2009): electronic Ligand Builder and Optimization Workbench *(eLBOW*): a tool for ligand coordinate and restraint generation. *Acta Cryst.,* D65:1074–1080.

Murray, J. W., Delumeau, O., & Lewis, R. J. (2005): Structure of a nonheme globin in environmental stress signaling. *PNAS,* 102(48):17320–17325.

Nakane, T., Kimanius, D., Lindahl, E.*, et al.* (2018). Characterisation of molecular motions in cryo-EM single-particle data by multibody refinement in RELION. *eLife*. Retrieved from

Nakane, T., Kotecha, A., Sente, A.*, et al.* (2020): Single-particle cryo-EM at atomic resolution. *Nature,* 587:152-156.

Narayan, K., Danielson, C. M., Lagarec, K.*, et al.* (2014): Multi-resolution correlative focused ion beam scanning electron microscopy: Applications to cell biology. *J. Struct. Biol.,* 185:278–284.

Naydenova, K., & Russo, C. J. (2017): Measuring the effects of particle orientation to improve the efficiency of electron cryomicroscopy. *Nat. Commun.,* 18(62):1-5.

Nicastro, D., Frangakis, A. S., Typke, D.*, et al.* (2000): Cryo-electron Tomography of Neurospora Mitochondria. *J. Struct. Biol.,* 129:48-56.

Oezcan, N., Ejsing, C. S., Shevchenko, A., *et al.* (2007): Osmolality, Temperature, and Membrane Lipid Composition Modulate the Activity of Betaine Transporter BetP in *Corynebacterium glutamicum*. *J. Bacteriol.,* 189(20):7485–7496.

Oezcan, N., Kraemer, R., & Morbach, S. (2005): Chill Activation of Compatible Solute Transporters in *Corynebacterium glutamicum* at the Level of Transport Activity. *J. Bacteriol.,* 187(14):4752–4759.

Okada, T., Yoshida, H., Akazawa, R., *et al.* (2002): Distinct roles of activating transcription factor 6 (ATF6) and double-stranded RNA-activated protein kinase-like endoplasmic reticulum kinase (PERK) in transcription during the mammalian unfolded protein response. *Biochem. J.,* 366:585-594.

Oluwole, A. O., Danielczak, B., Meister, A., *et al.* (2017): Solubilization of Membrane Proteins into Functional Lipid-Bilayer Nanodiscs Using a Diisobutylene/Maleic Acid Copolymer. *Angew. Chem. Int. Ed.,* 56:1919 –1924.

Ott, V., Koch, J., Spaete, K., *et al.* (2008): Regulatory Properties and Interaction of the C- and N-Terminal Domains of BetP, an Osmoregulated Betaine Transporter from *Corynebacterium glutamicum*. *Biochemistry,* 47:12208–12218.

Pakos-Zebrucka, K., Koryga, I., Mnich, K., *et al.* (2016): The integrated stress response. *EMBO Rep.,* 17(10):1374-1395.

Pané-Farré, J., Lewis, R. J., & Stuelke, J. (2005): The RsbRST Stress Module in Bacteria: A Signalling System That May Interact with Different Output Modules. *J Mol Microbiol Biotechnol,* 9:65–76.

Parent, K. N., Schrad, J. R., & Cingolani, G. (2018): Breaking Symmetry in Viral Icosahedral Capsids as Seen through the Lenses of X-ray Crystallography and Cryo-Electron Microscopy. *Viruses,* 10(67).

Peet, M. J., Henderson, R., & Russo, C. J. (2019): The energy dependence of contrast and damage in electron cryomicroscopy of biological molecules. *Ultramicroscopy,* 203:125-131.

Perez, C., Faust, B., Mehdipour, A. R., *et al.* (2014): Substrate-bound outward-open state of the betaine transporter BetP provides insights into Na^+ coupling. *Nat. Commun.,* 5(4231).

Perez, C., Khafizov, K., Forrest, L. R., *et al.* (2011): The role of trimerization in the osmoregulated betaine transporter BetP. *EMBO reports,* 12(8):804-810.

Perez, C., Koshy, C., Ressl, S., *et al.* (2011): Substrate specificity and ion coupling in the Na^+/betaine symporter BetP. *EMBO J.,* 30:1221–1229.

Perez, C., Koshy, C., Yildiz, O., *et al.* (2012): Alternating-access mechanism in conformationally asymmetric trimers of the betaine transporter BetP. *Nature,* 4 9 0:126-130.

Peter, H., Burkovski, A., & Kraemer, R. (1998): Osmo-sensing by N- and C-terminal Extensions of the Glycine Betaine Uptake System BetP of *Corynebacterium glutamicum*. *J. Biol. Chem.,* 273(5):2567–2574.

Peter, M. F., Ruland, J. A., Depping, P.*, et al.* (2022): Structural and mechanistic analysis of a tripartite ATP-independent periplasmic TRAP transporter. *Nat. Commun.,* 13(4471):1-15.

Pettersen, E. F., Goddard, T. D., Huang, C. C.*, et al.* (2004): UCSF Chimera—A Visualization System for Exploratory Research and Analysis. *J Comput Chem,* 25:1605–1612.

Pintilie, G. D., Zhang, J., Goddard, T. D.*, et al.* (2010): Quantitative analysis of cryo-EM density map segmentation by watershed and scale-space filtering, and fitting of structures by alignment to regions. *J. Struct. Biol.,* 170(3):427-438.

Pollock, N. L., Lee, S. C., Patel, J. H.*, et al.* (2017): Structure and function of membrane proteins encapsulated in a polymerbound lipid bilayer. *Biochim Biophys Acta Biomembr* . 1860:809–817.

Popot, J.-L., Althoff, T., Bagnard, D.*, et al.* (2011): Amphipols From A to Z. *Annu. Rev. Biophys,* 40:379-408.

Popot, J.-L., Berry, E. A., Charvolin, D.*, et al.* (2003): Amphipols: polymeric surfactants for membrane biology research. *Cell. Mol. Life Sci.,* 60:1559–1574.

Punjani, A., & Fleet, D. J. (2021): 3D Variability Analysis: Resolving continuous flexibility and discrete heterogeneity from single particle cryo-EM. *J Struct Biol.,* 213(2).

Qiu, W., Fu, Z., Xu, G. G.*, et al.* (2018): Structure and activity of lipid bilayer within a membrane-protein transporter. *PNAS,* 115(51):12985–12990.

Quin, M. B., Berrisford, J. M., Newman, J. A.*, et al.* (2012): The Bacterial Stressosome: A Modular System that Has Been Adapted to Control Secondary Messenger Signaling. *Structure,* 20:350–363.

Rachel, R., Meyer, C., Klingl, A.*, et al.* (2010): Chapter 3 - Analysis of the Ultrastructure of Archaea by Electron Microscopy. *Methods Cell Biol.* 96:47-69.

Rachel, R., Walther, P., Maaßen, C.*, et al.* (2020): Dual-axis STEM tomography at 200 kV: Setup, performance, limitations. *J Struct Biol.,* 211(107551).

Ramlaul, K., Palmer, C. M., Nakane, T.*, et al.* (2020): Mitigating local over-fitting during single particle reconstruction with SIDESPLITTER. *J. Struct. Biol.,* 211(107545):1-9.

Ressl, S., Scheltinga, A. C. T. v., Vonrhein, C.*, et al.* (2009): Molecular basis of transport and regulation in the Na^+/betaine symporter BetP. *Nature,* 458:47-52.

Ritchie, T. K., Grinkova, Y. V., Bayburt, T. H.*, et al.* (2009): Reconstitution of Membrane Proteins in Phospholipid Bilayer Nanodiscs. *Meth. Enzymol.,* 464:211-231.

Rohou, A., & Grigorieff, N. (2015): CTFFIND4: Fast and accurate defocus estimation from electron micrographs. *J. Struct. Biol.,* 192:216–221.

Romantsov, T., Guan, Z., & Wood, J. M. (2009): Cardiolipin and the osmotic stress responses of bacteria. *Biochim Biophys Acta,* 1788:2092–2100.

Romantsov, T., & Wood, J. M. (2016): Contributions of Membrane Lipids to Bacterial Cell Homeostasis upon Osmotic Challenge. In O. Geiger (Ed.), *Biogenesis of Fatty Acids, Lipids and Membranes. Handbook of Hydrocarbon and Lipid Microbiology.* Cham: Springer.

Ron, D. (2002): Translational control in the endoplasmic reticulum stress response. *J. Clin. Invest.,* 110:1383–1388.

Ruebenhagen, R., Morbach, S., & Kraemer, R. (2001): The osmoreactive betaine carrier BetP from *Corynebacterium glutamicum* is a sensor for cytoplasmic K^+. *EMBO J,* 20(19):5412-5420.

Ruebenhagen, R., Roensch, H., Jung, H.*, et al.* (2000): Osmosensor and Osmoregulator Properties of the Betaine Carrier BetP from *Corynebacterium glutamicum* in Proteoliposomes. *J. Biol. Chem.,* 275(2):735–741.

Ruskin, R. S., Yu, Z., & Grigorieff, N. (2013): Quantitative characterization of electron detectors for transmission electron microscopy. *J. Struct. Biol.,* 184:385–393.

Saier, M. H. J. (2000): A Functional-Phylogenetic Classification System for Transmembrane Solute Transporters. *Microbiol. Mol. Biol. Rev.,* 64(2):354–411.

Saxton, W. O., Baumeister, W., & Hahn, M. (1984): Three-Dimensional Reconstruction of Imperfect Two-Dimensional Crystals. *Ultramicroscopy,* 13:57-70.

Schaegger, H., Cramer, W. A., & Vonjagow, G. (1994): Analysis of Molecular Masses and Oligomeric States of Protein Complexes by Blue Native Electrophoresis and Isolation of Membrane Protein Complexes by Two-Dimensional Native Electrophoresis. *Anal. Biochem.,* 217(2):220-230.

Scheres, S. H. W. (2012a): A Bayesian View on Cryo-EM Structure Determination. *J. Mol. Biol.,* 415:406–418.

Scheres, S. H. W. (2012b): RELION: Implementation of a Bayesian approach to cryo-EM structure determination. *J. Struct. Biol.,* 180:519–530.

Scheres, S. H. W. (2016): Processing of Structurally Heterogeneous Cryo-EM Data in RELION. In R. A. Crowther (Ed.), *Methods in Enzymology - The Resolution Revolution: Recent Advances In cryoEM* (Vol. 579, pp. 125-157): Academic Press.

Schiller, D., Kraemer, R., & Morbach, S. (2004): Cation specicity of osmosensing by the betaine carrier BetP of *Corynebacterium glutamicum*. *FEBS Letters,* 563:108-112.

Schiller, D., Ott, V., Kraemer, R.*, et al.* (2006): Influence of Membrane Composition on Osmosensing by the Betaine Carrier BetP from *Corynebacterium glutamicum*. *J. Biol. Chem.,* 281(12):7737–7746.

Schiller, D., Ruebenhagen, R., Kraemer, R., *et al.* (2004): The C-Terminal Domain of the Betaine Carrier BetP of *Corynebacterium glutamicum* Is Directly Involved in Sensing K^+ as an Osmotic Stimulus. *Biochem,* 43(19):5583–5591.

Schimel, J., Balser, T. C., & Wallenstein, M. (2007): Microbial Stress-Response Physiology and its Implications for Ecosystem Function. *Ecology,* 88(6):1386–1394.

Schroeder, M., & Kaufman, R. J. (2005): The Mammalian Unfolded Protein Response. *Annu. Rev. Biochem.,* 74:739–789.

Schuck, S., Prinz, W. A., Thorn, K. S., *et al.* (2009): Membrane expansion alleviates endoplasmic reticulum stress independently of the unfolded protein response. *J. Cell Biol.,* 187(4):525–536.

Serna, M. (2019): Hands on Methods for High Resolution Cryo-Electron Microscopy Structures of Heterogeneous Macromolecular Complexes. *Front. Mol. Biosci,* 6(33).

Sharma, A. K., Rigby, A. C., & Alper, S. L. (2011): STAS Domain Structure and Function. *Cell Physiol Biochem,* 28:407-422.

Shen, P. S., Yang, X., DeCaen, P. G., *et al.* (2016): The Structure of the Polycystic Kidney Disease Channel PKD2 in Lipid Nanodiscs. *Cell,* 167:763–773.

Smith, M. H., Ploegh, H. L., & Weissman, J. S. (2011): Road to Ruin: Targeting Proteins for Degradation in the Endoplasmic Reticulum. *Science,* 334:1086-1090.

Smith, P. K., Krohn, R. I., Hermanson, G. T., *et al.* (1985): Measurement of Protein Using Bicinchoninic Acid. *Anal. Biochem.,* 150:76-85.

Snapp, E. L., Hegde, R. S., Francolini, M., *et al.* (2003): Formation of stacked ER cisternae by low affinity protein interactions. *J. Cell Biol.,* 163(2):257–269.

Sousa, A. A., Azari, A. A., Zhang, G., *et al.* (2011): Dual-axis electron tomography of biological specimens: extending the limits of specimen thickness with bright-field STEM imaging. *J Struct Biol.,* 174(1):107–114.

Stock, A. M., Robinson, V. L., & Goudreau, P. N. (2000): Two-Component Signal Transduction. *Annu. Rev. Biochem.,* 69:183–215.

Studer, D., Graber, W., Al-Amoudi, A., *et al.* (2001): A new approach for cryofixation by high-pressure freezing. *J. Microsc.,* 203(3):285-294.

Takei, K., Mignery, C. A., Mugnaini, E., *et al.* (1994): lnositol 1,4,5-Trisphosphate Receptor Causes Formation of ER Cisternal Stacks in Transfected Fibroblasts and in Cerebellar Purkinje Cells. *Neuron,* 12:327-342.

Thangaratnarajah, C., Rheinberger, J., Paulino, C., *et al.* (2021): Insights into the bilayer-mediated toppling mechanism of a folate-specific ECF transporter by cryo-EM. *PNAS,* 118(34).

Towbin, H., Staehelint, T., & Gordon, J. (1979): Electrophoretic transfer of proteins from polyacrylamide gels to nitrocellulose sheets: Procedure and some applications. *PNAS,* 76(9):4350-4354.

Tran, H. T., & Bonilla, C. Y. (2021): SigB-regulated antioxidant functions in gram-positive bacteria. *World J. Microbiol. Biotechnol.,* 37(38).

Tribet, C., Audebert, R., & Popot, J.-L. (1996): Amphipols: Polymers that keep membrane proteins soluble in aqueous solutions. *PNAS,* 93:5047–15050.

Vargas, C., Arenas, R. C., Frotscher, E.*, et al.* (2015): Nanoparticle self-assembly in mixtures of phospholipids with styrene/maleic acid copolymers or fluorinated surfactants. *Nanoscale,* 7:20685–20696.

Villinger, C., Gregorius, H., Kranz, C.*, et al.* (2012): FIB/SEM tomography with TEM-like resolution for 3D imaging of high-pressure frozen cells. *Histochem Cell Biol,* 138:549–556.

Villinger, C., Schauflinger, M., Gregorius, H.*, et al.* (2014): Three-Dimensional Imaging of Adherent Cells using FIB/SEM and STEM. In J. Kuo (Ed.), *Electron Microscopy: Methods and Protocols, Methods in Molecular Biology* (Vol. 1117, pp. 617-638). New York: Springer Science+Business Media.

Vinothkumar, K. R., & Henderson, R. (2016): Single particle electron cryomicroscopy: trends, issues and future perspective. *Q. Rev. Biophys.,* 49(e13):1-25.

Voeltz, G. K., Prinz, W. A., Shibata, Y.*, et al.* (2006): A Class of Membrane Proteins Shaping the Tubular Endoplasmic Reticulum. *Cell,* 124:573–586.

Voeltz, G. K., Rolls, M. M., & Rapoport, T. A. (2002): Structural organization of the endoplasmic reticulum. *EMBO Rep.,* 3(10):944–950.

Walter, P., & Ron, D. (2011): The Unfolded Protein Response: From Stress Pathway to Homeostatic Regulation. *Science,* 334:1081-1086.

Walther, P., Bauer, A., Wenske, N.*, et al.* (2018): STEM tomography of high-pressure frozen and freeze-substituted cells: a comparison of image stacks obtained at 200 kV or 300 kV. *Histochem. Cell Biol.,* 150:545–556.

Walther, P., Schmid, E., & Höhn, K. (2013): High-Pressure Freezing for Scanning Transmission Electron Tomography Analysis of Cellular Organelles. In D. J. Taatjes & J. Roth (Eds.), *Cell Imaging Techniques: Methods and Protocols* (pp. 525-535). New York: Humana Press.

Wilkes, M., Madej, M. G., Kreuter, L.*, et al.* (2017): Molecular insights into lipid-assisted Ca^{2+} regulation of the TRP channel Polycystin-2. *Nat. Struct. Mol,* 24(2):123-132.

Williams, A. H., Redzej, A., Rolhion, N.*, et al.* (2019): The cryo-electron microscopy supramolecular structure of the bacterial stressosome unveils its mechanism of activation. *Nat. Commun.,* 10(3005):1-10.

Wittig, I., & Schaegger, H. (2009): Native electrophoretic techniques to identify protein–protein interactions. *Proteomics,* 9:5214–5223.

Wolf, S. G., Shimoni, E., Elbaum, M.*, et al.* (2018): STEM Tomography in Biology. In E. Hanssen (Ed.), *Cellular Imaging. Biological and Medical Physics, Biomedical Engineering* (pp. 33-60). Cham: Springer.

Wood, J. M. (1999): Osmosensing by Bacteria: Signals and Membrane-Based Sensors. *Microbiol. Mol. Biol. Rev.,* 63(1):230–262.

Wood, J. M. (2011): Bacterial Osmoregulation: A Paradigm for the Study of Cellular Homeostasis. *Annu. Rev. Microbiol.,* 65:215–238.

Wright, R., Basson, M., D'Ari, L.*, et al.* (1988): Increased Amounts of HMG-CoA Reductase Induce "Karmellae": A Proliferation of Stacked Membrane Pairs Surrounding the Yeast Nucleus. *J. Cell Biol.,* 107:101-114.

Wu, M., & Lander, G. C. (2020a): How low can we go? Structure determination of small biological complexes using single-particle cryo-EM. *Curr. Opin. Struct. Biol.,* 64:9-16.

Wu, M., & Lander, G. C. (2020b): Present and Emerging Methodologies in Cryo-EM Single-Particle Analysis. *Biophys. J.,* 119:1281–1289.

Yakushevska, A. E., Lebbink, M. N., Geerts, W. J. C.*, et al.* (2007): STEM tomography in cell biology. *J Struct Biol.,* 159(3):381-391.

Yamamoto, A., Masaki, R., & Tashiro, Y. (1996): Formation of crystalloid endoplasmic reticulum in COS cells upon overexpression of microsomal aldehyde dehydrogenase by cDNA transfection. *J. Cell. Sci.,* 109:1727-1738.

Yamashita, A., Singh, S. K., Kawate, T.*, et al.* (2005): Crystal structure of a bacterial homologue of Na^+/Cl^-dependent neurotransmitter transporters. *Nature,* 437:215-223.

Yonekura, K., Braunfeld, M. B., Maki-Yonekura, S.*, et al.* (2006): Electron energy filtering significantly improves amplitude contrast of frozen-hydrated protein at 300 kV. *J. Struct. Biol.,* 156(3):524-536.

Zheng, S. Q., Palovcak, E., Armache, J.-P.*, et al.* (2016): MotionCor2: anisotropic correction of beam-induced motion for improved cryo-electron microscopy. *Nat. Methods,* 14(4):331-332.

Ziegler, C., Bremer, E., & Kraemer, R. (2010): The BCCT family of carriers: from physiology to crystal structure. *Mol. Microbiol.,* 78(1):13–34.

Zoonens, M., & Popot, J.-L. (2014): Amphipols for Each Season. *J Membrane Biol,* 247:759–796.

Zoonens, M., Zito, F., Martinez, K. L.*, et al.* (2014): Amphipols: A General Introduction and Some Protocols. In I. Mus-Veteau (Ed.), *Membrane Proteins Production for Structural Analysis* (pp. 173-203). New York: Springer.

Further references included within publications/manuscripts:

Abdellatif, M. E. A., Sinzger, C., & Walther, P. (2018): Investigating HCMV entry into host cells by STEM tomography. *J Struct. Biol.*, 204(3):406-419.

Afonine, P. V., Poon, B. K., Read, R. J., et al. (2018): Real-space refinement in PHENIX for cryo-EM and crystallography. *Acta Cryst.*, D(74):531–544.

Akbar, S., Gaidenko, T. A., Kang, C. M., et al. (2001): New Family of Regulators in the Environmental Signaling Pathway Which Activates the General Stress Transcription Factor σB of *Bacillus subtilis*. *J. Bacteriol.*, 183(4):1329–1338.

Andersson, C. E., & Mowbray, S. L. (2002): Activation of ribokinase by monovalent cations. *J. Mol. Biol.*, 315(3):409-419.

Armougom, F., Moretti, S., Poirot, O., et al. (2006): Expresso: automatic incorporation of structural information in multiple sequence alignments using 3D-Coffee. *Nucleic Acids Res.*, 34(W604–W608).

Barth, A. (2000): The infrared absorption of amino acid side chains. *Prog. Biophys. Mol. Biol.*, 74:141–173.

Barth, A., & Zscherp, C. (2002): What vibrations tell us about proteins. *Q. Rev. Biophys.*, 35(4):369–430.

Baumann, O., & Walz, B. (1989): Topography of Ca2+-sequestering endoplasmic reticulum in photoreceptors and pigmented glial cells in the compound eye of the honeybee drone. *Cell Tissue Res.*, 255:511–522.

Baumann, O., & Walz, B. (2001): Endoplasmic reticulum of animal cells and its organization into structural and functional domains. *Int. Rev. Cytol.*, 205:149-214.

Benjamini, Y., & Hochberg, Y. (1995): Controlling the False Discovery Rate: A Practical and Powerful Approach to Multiple Testing. *J. R. Stat. Soc. Series B Stat. Methodol.*, 57(1):289-300.

Best, R. B., Zhu, X., Shim, J., et al. (2012): Optimization of the additive CHARMM all-atom protein force field targeting improved sampling of the backbone φ, ψ and sidechain χ1 and χ2 dihedral angles. *J. Chem. Theory Comput.*, 8(9):3257–3273.

Blankenburg, S., Hentschker, C., Nagel, A., et al. (2019): Improving Proteome Coverage for Small Sample Amounts: An Advanced Method for Proteomics Approaches with Low Bacterial Cell Numbers. *Proteomics*, 19(1900192).

Boël, G., Smith, P. C., Ning, W., et al. (2014): The ABC-F protein EttA gates ribosome entry into the translation elongation cycle. *Nat. Struct. Mol. Biol.*, 21(2):143-151.

Brill, A. L., Fischer, T. T., Walters, J. M., et al. (2020): Polycystin 2 is increased in disease to protect against stress-induced cell death. *Sci. Rep.*, 10(386):1-15.

Burger, U. (2002). Struktur- und Funktionsanalysen am osmotisch regulierten Transporter BetP aus *Corynebacterium glutamicum*. Thesis, *University of Koeln*.

Buser, C., & Walther, P. (2008): Freeze-substitution: the addition of water to polar solvents enhances the retention of structure and acts at temperatures around -60°C. *J. Microsc.*, 230(2):268–277.

Campbell, E. A., Masuda, S., Sun, J. L., et al. (2002): Crystal Structure of the *Bacillus stearothermophilus* Anti-σFactor SpoIIAB with the Sporulation σFactor σF. *Cell*, 108:795–807.

Chen, C.-C., Yudkin, M. D., & Delumeau, O. (2004): Phosphorylation and RsbX-Dependent Dephosphorylation of RsbR in the RsbR-RsbS Complex of *Bacillus subtilis*. *J. Bacteriol.*, 186(20):6830–6836.

Collaborative Computational Project 4 (1994): The CCP4 suite: programs for protein crystallography. *Acta Cryst. D*, 50(5):760–763.

Delumeau, O., Dutta, S., Brigulla, M., et al. (2004): Functional and Structural Characterization of RsbU, a Stress Signaling Protein Phosphatase 2C. *J. Biol. Chem.*, 279(39):40927–40937.

Demarre, G., Guérout, A.-M., Matsumoto-Mashimo, C., et al. (2005): A new family of mobilizable suicide plasmids based on broad host range R388 plasmid (IncW) and RP4 plasmid (IncPα) conjugative machineries and their cognate *Escherichia coli* host strains. *Microbiol. Res.*, 156:245–255.

Distler, U., Kuharev, J., Navarro, P., et al. (2014): Drift time-specific collision energies enable deep-coverage data-independent acquisition proteomics. *Nat. Methods*, 11:167–170.

Eddy, S. R. (2011): Accelerated Profile HMM Searches. *PLoS Comput. Biol.*, 7(10):e1002195.

Elbaum, M. (2018): Quantitative Cryo-Scanning Transmission Electron Microscopy of Biological Materials. *Adv. Mater.*, 30(1706681).

Emsley, P., & Cowtan, K. (2004): *Coot*: model-building tools for molecular graphics. *Acta Cryst.*, D(60):2126-2132.

Fabian, H., & Maentele, W. (2006): Infrared Spectroscopy of Proteins. In J. M. Chalmers & P. R. Griffiths (Eds.), *Handbook of Vibrational Spectroscopy*: John Wiley & Sons Ltd.

Federovitch, C. M., Ron, D., & Hampton, R. Y. (2005): The dynamic ER: experimental approaches and current questions. *Curr. Opin. Cell Biol.*, 17:409-414.

Follmann, M., Becker, M., Ochrombel, I., et al. (2009): Potassium Transport in *Corynebacterium glutamicum* Is Facilitated by the Putative Channel Protein CglK, Which Is Essential for pH Homeostasis and Growth at Acidic pH. *J. Bacteriol.*, 191(9):2944–2952.

Fuchs, S., Pané-Farré, J., Kohler, C., et al. (2007): Anaerobic Gene Expression in *Staphylococcus aureus*. *J. Bacteriol.*, 189(11):4275–4289.

Gaidenko, T. A., Yang, X., Lee, Y. M., et al. (1999): Threonine Phosphorylation of Modulator Protein RsbR Governs its Ability to Regulate a Serine Kinase in the Environmental Stress Signaling Pathway of *Bacillus subtilis*. *J. Mol. Biol.*, 288:29-39.

Gaidenko, T. A., Bie, X., Baldwin, E. P., et al. (2011): Substitutions in the Presumed Sensing Domain of the *Bacillus subtilis* Stressosome Affect Its Basal Output but Not Response to Environmental Signals. *J. Bacteriol.*, 193(14):3588–3597.

Gómez-Rubio, V. (2017): ggplot2 – Elegant Graphics for Data Analysis. *J. Stat. Softw.*, 77(2):1-3.

Goudenège, D., Labreuche, Y., Krin, E., et al. (2013): Comparative genomics of pathogenic lineages of *Vibrio nigripulchritudo* identifies virulenceassociated traits. *ISME J.*, 7:1985–1996.

Grant, S. G. N., Jessee, J., Bloom, F. R., et al. (1990): Differential plasmid rescue from transgenic mouse DNAs into *Escherichia coli* methylation-restriction mutants. *PNAS*, 87:4645-4649.

Haardt, M., Kempf, B., Faatz, E., et al. (1995): The osmoprotectant proline betaine is a major substrate for the binding-protein-dependent transport system ProU of *Escherichia coli* K-12. *Mol. Gen. Genet.*, 246:783-786.

Hardwick, S. W., Pané-Farré, J., Delumeau, O., et al. (2007): Structural and Functional Characterization of Partner Switching Regulating the Environmental Stress Response in *Bacillus subtilis*. *J. Biol. Chem.*, 282(15):11562–11572.

Heide, T. v. d., Stuart, M. C. A., & Poolman, B. (2001): On the osmotic signal and osmosensing mechanismof an ABC transport system for glycine betaine. *EMBO J.*, 20(24):7022-7032.

Jorgensen, W. L., Chandrasekhar, J., & Madura, J. D. (1983): Comparison of simple potential functions for simulating liquid water. *J. Chem. Phys.*, 79(629).

Kabsch, W. (1993): Automatic processing of rotation diffraction data from crystals of initially unknown symmetry and cell constants. *J. Appl. Cryst.*, 26:795-800.

Kang, C. M., Vijay, K., & Price, C. W. (1998): Serine kinase activity of a *Bacillus subtilis* switch protein is required to transduce environmental stress signals but not to activate its target PP2C phosphatase. *Mol. Microbiol.*, 30(1):189–196.

Karimova, G., Pidoux, J., Ullmann, A., et al. (1998): A bacterial two-hybrid system based on a reconstituted signal transduction pathway. PNAS, 95:5752–5756.

Kendall, M. G. (1938): A New Measure of Rank Correlation. *Biometrika*, 30(1/2):81-93.

Kim, Y. R., Lee, S. E., Kim, C. M., et al. (2003): Characterization and Pathogenic Significance of *Vibrio vulnificus* Antigens Preferentially Expressed in Septicemic Patients. *Infect. Immun.*, 71(10):5461–5471.

Kimes, N. E., Grim, C. J., Johnson, W. R., et al. (2012): Temperature regulation of virulence factors in the pathogen *Vibrio coralliilyticus*. *ISME J.*, 6:835–846.

Klauda, J. B., Venable, R. M., Freites, J. A., et al. (2010): Update of the CHARMM All-Atom Additive Force Field for Lipids: Validation on Six Lipid Types. *J. Phys. Chem. B*, 114(23):7830–7843.

Kraemer, R., Lambert, C., Hoischen, C., et al. (1990): Uptake of glutamate in *Corynebacterium glutamicum*. *Eur. J. Biochem.*, 194:929-935.

Lê, S., Josse, J., & Husson, F. (2008): FactoMineR: An R Package for Multivariate Analysis. *J. Stat. Softw.*, 25(1):1-18.

Letunic, I., Doerks, T., & Bork, P. (2015): SMART: recent updates, new developments and status in 2015. *Nucleic Acids Res.*, 43(D257–D260).

Malinauskaite, L., Quick, M., Reinhard, L., et al. (2014): A mechanism for intracellular release of Na^+ by neurotransmitter/sodium symporters. *Nat. Struct. Mol.*, 21(11):1006-1014.

Masaki, R., Yamamoto, A., & Tashiro, Y. (1994): Microsomal Aldehyde Dehydrogenase Is Localized to the Endoplasmic Reticulum via Its Carboxyl-Terminal 35 Amino Acids. J. Cell. Biol., 126(6):1407-1420.

McCoy, A. J., Grosse-Kunstleve, R. W., Adams, P. D., et al. (2007): *Phaser* crystallographic software. *J. Appl. Cryst.*, 40:658–674.

McIntosh, R., Nicastro, D., & Mastronarde, D. (2005): New views of cells in 3D: an introduction to electron tomography. *Trends Cell Bio.*, 15(1):43-51.

Morrison, S. S., Williams, T., Cain, A., et al. (2012): Pyrosequencing-Based Comparative Genome Analysis of *Vibrio vulnificus* Environmental Isolates. *PLoS ONE*, 7(5):e37553.

Musa, Y. R., Baesell, K., Schatschneider, S., et al. (2013): Dynamic protein phosphorylation during the growth of *Xanthomonas campestris* pv. *campestris* B100 revealed by a gel-based proteomics approach. *J. Biotechnol.*, 167(2):111-122.

Oliver, J. D. (2013): *Vibrio vulnificus*: Death on the Half Shell. A Personal Journey with the Pathogen and its Ecology. *Microb. Ecol.*, 65:793–799.

Oliver, J. D. (2015): The Biology of *Vibrio vulnificus*. *Microbiol. Spectr.*, 3(3).

Pané-Farré, J., Quin, M. B., Lewis, R. J., et al. (2017): Structure and Function of the Stressosome Signalling Hub. In J. R. Harris & J. Marles-Wright (Eds.), *Subcell. Biochem.* (Vol. 83): Springer Nature.

Pathak, R. K., Luskey, K. L., & Anderson, R. G. W. (1986): Biogenesis of the Crystalloid Endoplasmic Reticulum in UT-1 Cells: Evidence That Newly Formed Endoplasmic Reticulum Emerges from the Nuclear Envelope. *J. Cell Biol.*, 102:2158-2168.

Pesce, A., Thijs, L., Nardini, M., et al. (2009): HisE11 and HisF8 Provide Bis-histidyl Heme Hexa-coordination in the Globin Domain of *Geobacter sulfurreducens* Globin-coupled Sensor. *J. Mol. Biol.*, 386:246–260.

Petersohn, A., Bernhardt, J., Gehrt, U., et al. (1999): Identification of σ(B)-Dependent Genes in *Bacillus subtilis* Using a Promoter Consensus-Directed Search and Oligonucleotide Hybridization. *J. Bacteriol.*, 181(18):5718–5724.

Pettersson, B. M. F., Nitharwal, R. G., Das, S., et al. (2013): Identification and expression of stressosomal proteins in *Mycobacterium marinum* under various growth and stress conditions. *FEMS Microbiol. Lett.*, 342:98–105.

Philippe, N., Alcaraz, J.-P., Coursange, E., et al. (2004): Improvement of pCVD442, a suicide plasmid for gene allele exchange in bacteria. *Plasmid*, 51:246–255.

Phippen, B. L., & Oliver, J. D. (2017): Impact of hypoxia on gene expression patterns by the human pathogen, *Vibrio vulnificus*, and bacterial community composition in a North Carolina estuary. *GeoHealth*, 1:37-50.

Price, C. W., Fawcett, P., Cérémonie, H., et al. (2001): Genome-wide analysis of the general stress response in *Bacillus subtilis*. *Mol. Microbiol.*, 41(4):757–774.

Ramesh, M., Nitharwal, R. G., Behra, P. R. K., et al. (2021): Intracellular localization of the mycobacterial stressosome complex. *Sci. Rep.*, 11(1060).

Reeves, A., Martinez, L., & Haldenwang, W. (2010): Expression of, and in vivo stressosome formation by, single members of the RsbR protein family in *Bacillus subtilis*. *Microbiology*, 156:990–998.

Remmert, M., Biegert, A., Hauser, A., et al. (2012): HHblits: lightning-fast iterative protein sequence searching by HMM-HMM alignment. *Nat. Methods*, 9:173–175.

Ritchie, M. E., Phipson, B., Wu, D., et al. (2015): *limma* powers differential expression analyses for RNA-sequencing and microarray studies. *Nucleic Acids Res.*, 43(7):e47.

Robert, X., & Gouet, P. (2014): Deciphering key features in protein structures with the new ENDscript server. *Nucleic Acids Res.*, 42(W320–W324).

Schack, V. R., Morth, J. P., Toustrup-Jensen, M. S., et al. (2008): Identification and Function of a Cytoplasmic K^+ Site of the Na^+,K^+-ATPase. *J. Biol. Chem.*, 283(41):27982–27990.

Schneider, T. R., & Sheldrick, G. M. (2002): Substructure solution with SHELXD. *Acta Cryst.*, D(58):1772-1779.

Sikkema, H. R., Noort, M. v. d., Rheinberger, J., et al. (2020): Gating by ionic strength and safety check by cyclic-di-AMP in the ABC transporter OpuA. *Sci. Adv.*, 6(eabd7697).

Steger, R., Weinand, M., Kraemer, R., et al. (2004): LcoP, an osmoregulated betaine/ectoine uptake system from *Corynebacterium glutamicum*. *FEBS Letters*, 573:155–160.

Strahs, G., & Kraut, J. (1968): Low-resolution Electron-density and Anomalous-scattering-density Maps of *Chromatium* High-potential Iron Protein. *J. Mol. Biol.*, 35:503-512.

Suomi, T., & Elo, L. L. (2017): Accurate Detection of Differential Expression and Splicing Using Low-Level Features. In N. Wajapeyee & R. Gupta (Eds.), *Methods Mol. Biol.* (Vol. 1507, pp. 141–151). New York: Humana Press.

Susi, H., & Byler, D. M. (1983): Protein Structure by Fourier Transform Infrared Spectroscopy: Second Derivative Spectra. *Biochem. Biophys. Res. Commun.*, 115(1):391-397.

Thompson, F. L., Li, Y., Gomez-Gil, B., et al. (2003): *Vibrio neptunius* sp. nov., *Vibrio brasiliensis* sp. nov. and *Vibrio xuii* sp. nov., isolated from the marine aquaculture environment (bivalves, fish, rotifers and shrimps). *Int. J. Syst. Evol. Microbiol.*, 53:245–252.

Tohidifar, P., Bodhankar, G. A., Pei, S., et al. (2020): The Unconventional Cytoplasmic Sensing Mechanism for Ethanol Chemotaxis in *Bacillus subtilis*. *mBio*, 11(e02177-20).

Topf, M., Lasker, K., Webb, B., et al. (2008): Protein Structure Fitting and Refinement Guided by Cryo-EM Density. *Structure*, 16:295–307.

Uniprot Consortium (2021): UniProt: The universal protein knowledgebase in 2021. *Nucleic Acids Res.*, 49(D480-D489).

Valley, C. C., Cembran, A., Perlmutter, J. D., et al. (2012): The Methionine-aromatic Motif Plays a Unique Role in Stabilizing Protein Structure. *J. Biol. Chem.*, 287(42):34979–34991.

Venable, R. M., Brown, F. L. H., & Pastor, R. W. (2015): Mechanical properties of lipid bilayers from molecular dynamics simulation. *Chem. Phys. Lipids*, 192:60-74.

Walker, J. A., Rivera, S., & Weinert, E. E. (2017): Mechanism and Role of Globin-Coupled Sensor Signalling. *Adv. Microb. Physiol.*, 71(3):133-169.

Walther, P., & Ziegler, A. (2002): Freeze substitution of high-pressure frozen samples: the visibility of biological membranes is improved when the substitution medium contains water. *J. Microsc.*, 208(1):3–10.

Wen, Y., Kim, I. H., Son, J.-S., et al. (2012): Iron and Quorum Sensing Coordinately Regulate the Expression of Vulnibactin Biosynthesis in *Vibrio vulnificus*. *J. Biol. Chem.*, 287(32):26727–26739.

Webb, B., & Sali, A. (2016): Comparative Protein Structure Modeling Using MODELLER. *Curr. Protoc. Bioinform.*, 54:5.6.1-5.6.37.

Wickham, H. (2016): ggplot2 - Positioning Elegant Graphics for Data Analysis. Cham: Springer.

Wickham, H., Averick, M., Bryan, J., et al. (2019): Welcome to the Tidyverse. *J. Open Source Softw.*, 4(43):1-6.

Williams, T. C., Blackman, E. R., Morrison, S. S., et al. (2014): Transcriptome Sequencing Reveals the Virulence and Environmental Genetic Programs of *Vibrio vulnificus* Exposed to Host and Estuarine Conditions. *PLoS ONE*, 9(12):e114376.

Wood, J. M. (2015): Bacterial responses to osmotic challenges. *J. Gen. Physiol.*, 145(5):381–388.

Xu, F., Du, W., Zou, Q., et al. (2020): COPII mitigates ER stress by promoting formation of ER whorls. *Cell Res.*, 31:141–156.

Yang, X., Kang, C. M., Brody, M. S., et al. (1996): Opposing pairs of serine protein kinases and phosphatases transmit signals of environmental stress to activate a bacterial transcription factor. *Genes Dev.*, 10:2265-2275.

Zhang, W., & Jr., G. N. P. (2003): Structure of the Oxygen Sensor in *Bacillus subtilis*: Signal Transduction of Chemotaxis by Control of Symmetry. *Structure*, 11:1097–1110.

VII. Appendix

VII. 1 SMA and DIBMA solubilization parameters

Table 13: Solubilization conditions for BetP in SMA / DIBMA polymers

polymer	solubilization conditions			solubilization success
	working concentration	incubation time	temperature	
SMA 1:1	1.0% (v/v)	ON	RT	none
	1.0% (v/v)	2 h	RT	poor
SMA 2:1	1.0% (v/v)	ON	RT	ok
	10.0% (v/v)	ON	RT	poor
	0.5% (v/v)	2 h	RT	ok
	1.0% (v/v)	2 h	RT	ok
	2.5% (v/v)	2 h	RT	ok
DIBMA	2.5% - 1.0% - 0.5% - 0.2% (v/v)	2 h	RT	none
	2.5% - 1.0% - 0.5% - 0.2% (v/v)	ON	RT	poor
	2.5% - 1.0% - 0.5% - 0.2% (v/v)	24 h	RT	poor, better at low concentrations
	2.5% - 1.0% - 0.5% - 0.2% (v/v)	3 h	37 °C	poor, better at low concentrations

VII. 2 Cryo-EM of BetP reconstituted into Salipros

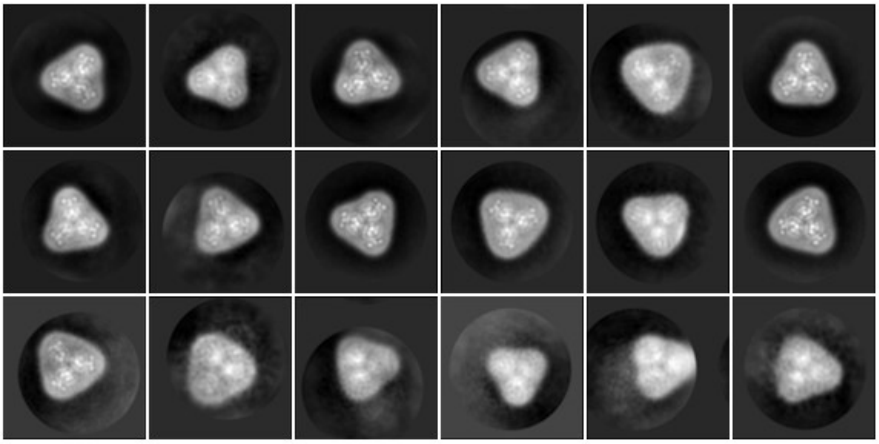

Figure 20: 2D class averages of BetP in Salipros

Selected 2D class averages of BetP reconstituted into Salipro particles, created from 259,106 auto-picked particles. All class averages represent top-down projections of the BetP trimer, revealing great secondary structural details. However, the dataset severely suffers from preferred orientation, since no tilted or side views could be obtained.

VII. 3 Single particle data acquisition and processing parameters

Table 14: Data acquisition and processing parameters for BetP WT in Amphipol A8-35 (downregulated state)

Vitrification parameters	
Sample buffer	20 mM TRIS-HCl pH 7.5, 100 mM NaCl
Sample concentration	1 mg/mL
Sample volume [µL]	3.5
Grid type	Quantifoil R1.2/1.3, Cu 400 mesh
Environmental conditions	4°C / 100% humidity
Blot time [sec]	6
Blot force	0
Data acquisition	
Electron microscope	Titan Krios 'dicke Berta'
Acceleration voltage [keV]	300
Spherical aberration [mm]	2.7
Detector (imaging mode)	Falcon III (counting)
Pixel size [Å]	1.0635
Total e^- dose [$e^-/Å^2$]	82.21
Dose rate [e^-/px/sec]	1.24
Number of fractions	47
Total exposure time [sec]	74.99
Defocus range [µm]	-1.5 to -2.6
Data processing	
Number of movies	1212
Number of picked particles	521461
Particles in final reconstruction	18998
Symmetry	C3
Global map resolution [Å]	3.7
FSC criterion	0.143
Post-processing	auto-sharpening (cryoSPARC)

Table 15: Data acquisition and processing parameters for BetP WT in Amphipol A8-35 (transition state)

Vitrification parameters	
Sample buffer	25 mM TRIS-HCl pH 7.5, 200 mM KCl
Sample concentration	~1.5 mg/mL
Sample volume [µL]	3.5
Grid type	Quantifoil R1.2/1.3, Cu 400 mesh
Environmental conditions	4°C / 100% humidity
Blot time [sec]	5.5
Blot force	0
Data acquisition	
Electron microscope	Glacios
Acceleration voltage [keV]	200
Spherical aberration [mm]	2.7
Detector (imaging mode)	Falcon III (counting)
Pixel size [Å]	0.9613
Total e^- dose [$e^-/Å^2$]	30
Dose rate [e^-/px/sec]	1
Number of fractions	120
Total exposure time [sec]	~ 60
Defocus range [µm]	-0.8 to -2.2
Data processing	
Number of movies	1536
Number of picked particles	542,487
Particles in final reconstruction	18,000
Symmetry	C1
Global map resolution [Å]	4.3
FSC criterion	0.143
Post-processing	B-factor sharpening (B = -20, RELION)

VIII. Publication 1

The article (including supplementary information) can be found at https://doi.org/10.1038/s42003-0 22-03548-w*

communications biology

ARTICLE

https://doi.org/10.1038/s42003-022-03548-w OPEN

The *Vibrio vulnificus* stressosome is an oxygen-sensor involved in regulating iron metabolism

Veronika Heinz[1,10], Wenke Jäckel[2,10], Susann Kaltwasser[3,10], Laura Cutugno[4], Patricia Bedrunka[5], Anica Graf[2], Alexander Reder[6], Stephan Michalik[6], Vishnu M. Dhople[6], M. Gregor Madej[1], Maria Conway[5], Marcus Lechner[5], Katharina Riedel[2], Gert Bange[5], Aoife Boyd[4], Uwe Völker[6], Richard J. Lewis[7,9], Jon Marles-Wright[7,8], Christine Ziegler[1✉] & Jan Pané-Farré[5✉]

Stressosomes are stress-sensing protein complexes widely conserved among bacteria. Although a role in the regulation of the general stress response is well documented in Gram-positive bacteria, the activating signals are still unclear, and little is known about the physiological function of stressosomes in the Gram-negative bacteria. Here we investigated the stressosome of the Gram-negative marine pathogen *Vibrio vulnificus*. We demonstrate that it senses oxygen and identified its role in modulating iron-metabolism. We determined a cryo-electron microscopy structure of the *Vv*RsbR:*Vv*RsbS stressosome complex, the first solved from a Gram-negative bacterium. The structure points to a variation in the *Vv*RsbR and *Vv*RsbS stoichiometry and a symmetry breach in the oxygen sensing domain of *Vv*RsbR, suggesting how signal-sensing elicits a stress response. The findings provide a link between ligand-dependent signaling and an output – regulation of iron metabolism - for a stressosome complex.

[1] Department of Biophysics II/Structural Biology, University of Regensburg, 93053 Regensburg, Germany. [2] Department of Microbial Physiology and Molecular Biology, University of Greifswald, 17487 Greifswald, Germany. [3] Max Planck Institute of Biophysics, Max-von-Laue-Strasse 3, 60438 Frankfurt am Main, Germany. [4] Discipline of Microbiology & Centre for One Health, School of Natural Sciences, Molecular Pathogenesis Research Group, National University of Ireland Galway, Galway, Ireland. [5] Center for Synthetic Microbiology (SYNMIKRO) & Department of Chemistry, Philipps-University Marburg, Karl-von-Frisch-Strasse 14, 35043 Marburg, Germany. [6] Interfaculty Institute for Genetics and Functional Genomics, University Medicine Greifswald, Greifswald, Germany. [7] Biosciences Institute, Newcastle University, Newcastle upon Tyne NE2 4HH, UK. [8] School of Natural and Environmental Sciences, Newcastle University, Newcastle upon Tyne NE1 7RU, UK. [9] Present address: The Royal Society for the Protection of Birds, The Lodge, Potton Road, Sandy, Bedfordshire SG19 2DL, UK. [10] These authors contributed equally: Veronika Heinz, Wenke Jäckel, Susann Kaltwasser. ✉email: christine.ziegler@biologie.uni-regensburg.de; jan.panefarre@chemie.uni-marburg.de

*Reproduced with permission from Springer Nature

Bacteria continuously respond to environmental changes, stress, and, in the case of pathogens, the host. In many bacteria, cellular stress signals are integrated by the stressosome, a high molecular weight signaling complex, first described in the Gram-positive soil bacterium *Bacillus subtilis*[1–3] (Supplementary Fig. 1). The *B. subtilis* stressosome consists of multiple copies of two major components: a small single STAS (sulfate transporter anti sigma factor antagonist) domain protein, RsbS, and at least one out of five RsbR paralogs, which have an N-terminal sensory domain and a C-terminal STAS domain that interacts with RsbS[4–6] to form the stressosome core. The activating signals for the different RsbR paralogs have not yet been identified, with the exception of YtvA, which responds to blue light[7–10]. In the non-stressed state, the protein kinase RsbT is bound to the stressosome core[5]. Upon stress perception by the RsbR sensory domains, RsbT phosphorylates both RsbR and RsbS and is released from the stressosome[11–15]. RsbT then initiates a signaling cascade involving proteins RsbU, RsbV, and RsbW, resulting in sigma factor B (SigB)-dependent up-regulation of the transcription of stress-responsive genes[11,16–20]. Dephosphorylation of RsbS and RsbR by the phosphatase RsbX allows for re-binding of RsbT, and as such 'resets' the sensing state of the stressosome[11,13]. In cryo-electron microscopy (cryo-EM) reconstructions of the *B. subtilis* and the *Listeria monocytogenes* stressosomes, the RsbR:RsbS STAS domain core adopts a pseudo-icosahedral scaffold with the N-terminal sensory domains of RsbR projecting from this as turret-like extensions[5,6,21]. All of these reconstructions were obtained from recombinant proteins, with different methods of reconstituting the stressosome complexes; as a result of this, they show considerable differences in the arrangement of the RsbR proteins in the complex.

Phylogenetic analysis suggests that the extended eight-gene stressosome operon (*rsbRSTUVWsigBrsbX*) encoding the three stressosome proteins (RsbR, RsbS and RsbT) the stressosome feedback-phosphatase (RsbX) and the SigB activation cascade (RsbU, RsbV and RsbW) is not common in nature, and seems restricted to the order Bacillales[22,23]. Instead, a four-gene module (*rsbRSTX*) encoding a minimal stressosome but lacking the *sigB* gene and the SigB activation cascade *(rsbU, rsbV* and *rsbW)*, is widely conserved in diverse bacteria including Cyanobacteria, Bacteroidetes, Proteobacteria, Deinococci and even some archaeal species. The aim of this study was to explore the structure and function of the thus far neglected stressosomes of Gram-negative bacteria. An example for the impact of the four-gene *rsbRSTX* operon was recently described for the γ-Proteobacterium *Vibrio vulnificus*[24], a pathogen associated with high mortality in patients developing infection from sea water through open wounds and by ingestion of contaminated seafood[25]. Whole genome sequencing has shown that the stressosome gene cluster is particularly well conserved in clinical *V. vulnificus* isolates (Biotype 1) and less frequently found in environmental strains (Biotype 2), suggesting that the stressosome may play a role during infection[24,26]. Furthermore, the *rsbRSTX* locus is transcribed during periods of reduced oxygen availability in sea water, showing that the stressosome operon is active in the natural habitat of this pathogen[27]. The *rsbRSTX* gene cluster is also conserved in other important pathogenic *Vibrio* species including *Vibrio coralliilyticus*, causing global coral bleaching[28], *Vibrio nigripulchritudo*, an emerging pathogen of farmed shrimp[29], and *Vibrio brasiliensis*[30] that was isolated from a marine aquaculture environment[31].

Herein we show that starvation in *V. vulnificus* correlates with the expression of stressosome components, and that starvation and oxygen-limitation trigger alterations in the proteome. We also show that *Vv*RsbR and *Vv*RsbS interact in vivo and demonstrate that in vitro, they assemble into a stressosome-like complex that is sensitive to O_2 levels. Finally, we present the first cryo-EM reconstruction of a stressosome complex from a Gram-negative bacterium, assembled from *Vv*RsbR and *Vv*RsbS proteins heterologously co-expressed in *E. coli* and purified under aerobic conditions. The *Vv*RsbR:*Vv*RsbS assembly suggests that *Vv*RsbR:*Vv*RsbS stoichiometries vary, which could serve to adjust the activation threshold upon stress sensing, by changing the surface available for *Vv*RsbT binding. Together, our data link the iron-heme-dependent response of a minimal stressosome to iron-metabolism of an important pathogen, establishing *Vibrio*-type stressosomes as a model system to study stressosome biology from signal sensing to regulatory output.

Results

Starvation-dependent expression of the minimal stressosome. We initially wanted to discover the conditions in which the *V. vulnificus* stressosome is produced. Western-blotting analysis, employing antibodies directed against the *Vv*RsbR protein, clearly showed that this stressosome protein accumulates in defined chemical media in stationary phase cells of *V. vulnificus*, likely induced by the exhaustion of glucose in the growth medium (Fig. 1a, b, c). This is in contrast to *B. subtilis*, where stressosome levels remain relatively constant during growth and stress[32]. Starvation-dependent expression of the stressosome gene cluster and the presumed output module (*Vv*D1-D2) in minimal media was confirmed by analysis of the *VvrsbR*, *VvrsbT*, *VvrsbX*, *VvD1* and *VvD2* transcript levels by Northern-blotting (Supplementary Fig. 2a–c). As the Northern blot experiments show a lower transcription of the stressosome operon in the low iron condition, a possible link between iron-availability and stressosome expression requires further investigation. Taken together, these results show that when *V. vulnificus* grows in a minimal medium the stressosome is expressed upon exhaustion of nutrient and energy sources.

The *Vv*RsbR and *Vv*RsbS proteins form the core of the minimal stressosome. The differences between the *rsbRST*-module of *B. subtilis* and the *rsbRSTX*-module of *V. vulnificus* prompted a detailed analysis of the underlying direct interactions of the proteins involved. To do so, Bacterial-Two-Hybrid (BACTH) assays[33] were performed with the stressosome proteins *Vv*RsbR, *Vv*RsbS, *Vv*RsbT and the predicted stressosome phosphatase *Vv*RsbX. The BACTH assay supported interactions between *Vv*RsbR and *Vv*RsbS, *Vv*RsbS and *Vv*RsbX as well as self-interactions for *Vv*RsbR and *Vv*RsbX (Supplementary Fig. 3a, b). Only weak self-interaction for *Vv*RsbS was observed and reproducible interactions of *Vv*RsbT with *Vv*RsbS or *Vv*RsbR individually were not detected. Lack of VvRsbT binding is in accord with results from the *B. subtilis* stressosome, where the binding of RsbT was dependent on the formation of the RsbR:RsbS complex[3], a condition not captured by the BACTH assay. In addition, BACTH analyses were carried out in aerobic conditions, which might affect the binding of VvRsbT to VvRsbR.

To investigate if in the absence of any obvious RsbR paralogs from the *V. vulnificus* genome sequence, other STAS-domain proteins (VV1_0681, VV1_2658, VV2_1159, VV2_1170) similar in size to RsbS might contribute to stressosome formation, we probed their binding to *Vv*RsbR, *Vv*RsbS and *Vv*RsbT. The BACTH assay did not detect interactions between *Vv*RsbR, *Vv*RsbS or *Vv*RsbT with any of the other four small STAS domain proteins identified in the *V. vulnificus* genome, suggesting that these proteins do not play a role in stressosome formation in this species (Supplementary Figs. 3c–e and 4), and providing support for the specificity of the interactions observed by BACTH.

To investigate whether *Vv*RsbR and *Vv*RsbS interact in vivo, immuno-precipitation experiments were performed with protein

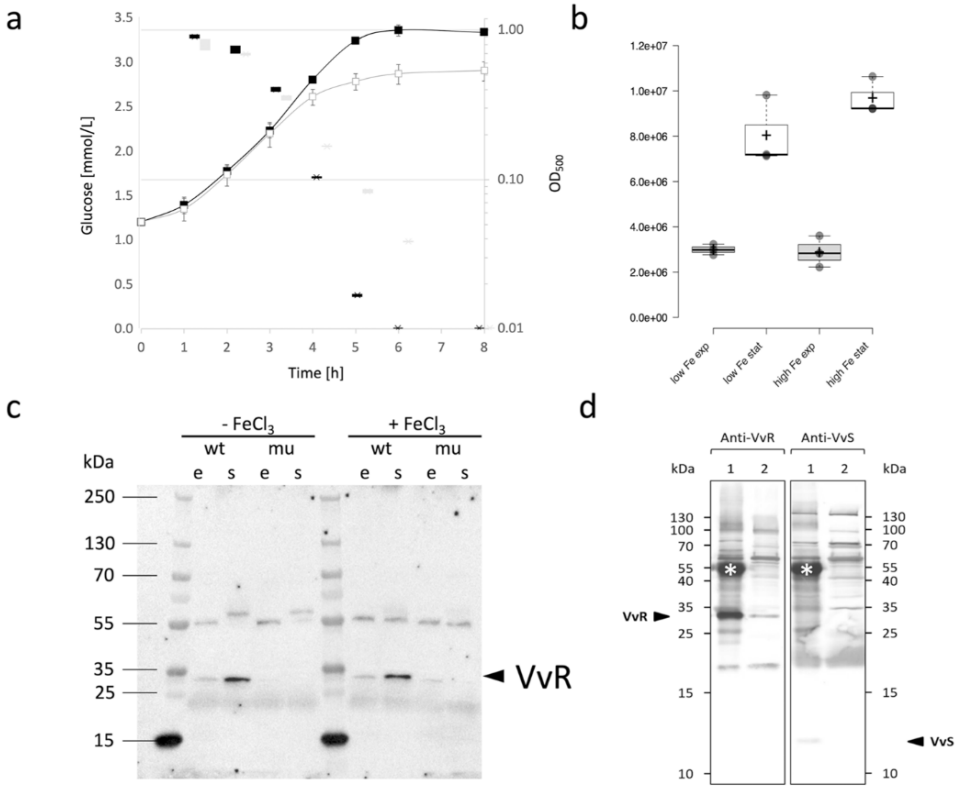

Fig. 1 Stationary phase induction of the *V. vulnificus* stressosome. a *V. vulnificus* was grown in minimal medium with (black symbols) and without (gray symbols) iron supplementation and the cell culture medium was analyzed for glucose consumption: glucose concentration (box plots) and optical density (lines with squares, with error bars showing standard deviations of three independent experiments). In addition, samples for Western blot analysis of *Vv*RsbR were taken during exponential growth and four hours after entry into stationary phase. Quantified *Vv*RsbR signals are shown in (**b**) and a representative uncropped Western blot is shown in (**c**); (e = exponential sample, s = stationary phase sample, wt = *V. vulnificus*) CMCP6 wild type and mu = isogenic ΔRSTX mutant. Box-whisker in (**a**) and (**b**) extend to data points that are less than 1.5 x interquartile ranges away from 1st/3rd quartile (Tukey). **d** For the detection of *Vv*RsbR:*Vv*RsbS complexes, the soluble protein fraction from stationary phase cells grown in iron supplemented minimal medium was subjected to immune precipitation using *Vv*RsbR (*Vv*R) specific polyclonal serum. Precipitated complexes (lane 1) and supernatant from the same precipitation reaction (lane 2) were separated by 1D SDS PAGE and blotted onto membranes. Membranes were then incubated with either anti-*Vv*RsbR (left two lanes) or anti-*Vv*RsbS (*Vv*S) (right two lanes) as primary antibodies. Bound *Vv*RsbR and *Vv*RsbS specific antibodies (arrows) were detected with anti-rabbit IgG. In addition to anti-*Vv*RsbR and anti-*Vv*RsbS the secondary anti-rabbit IgG also detected a band around 55 kDa (asterisk) in the precipitation reaction, which corresponds to the heavy chain of the anti-*Vv*RsbR antibody used for precipitation. Source data for (**a**) and (**b**) are available as supplementary data 1 and the uncropped blot from the immune precipitation experiment (**d**) is shown in Supplementary Fig. 18a.

extracts of *V. vulnificus* cultured in minimal medium in the presence of iron. The clarified *V. vulnificus* cell lysate harvested at early stationary phase was precipitated with protein A-coated magnetic beads pre-incubated overnight with a *Vv*RsbR specific antibody. SDS-PAGE and Western blot analysis of the bound protein-antibody complex with anti-*Vv*RsbR and anti-*Vv*RsbS specific polyclonal sera revealed the simultaneous enrichment of both proteins. The majority of *Vv*RsbR was clearly detected in the immunoprecipitate (Fig. 1d). Analysis with the *Vv*RsbS specific antibody detected a band in the *Vv*RsbR precipitate but not the corresponding supernatant. Thus, *Vv*RsbR and *Vv*RsbS interact in vivo, supporting the hypothesis that stressosome complexes assemble in *V. vulnificus*.

A heme-group in the N-terminal domain of *Vv*RsbR is assembled in *Vv*RsbR:*Vv*RsbS stressosomes. In silico sequence analysis predicted that the N-terminal domain of *Vv*RsbR encodes a heme-dependent globin coupled sensor domain[34]. To validate this prediction, the *Vv*RsbR:*Vv*RsbS complex was produced recombinantly in *E. coli* and the *Vv*RsbR and *Vv*RsbS proteins co-purified as stable stressosome complexes by size-exclusion chromatography (Fig. 2a). The purified *Vv*RsbR:*Vv*RsbS complex showed an intense red color, consistent with the presence of a coordinated heme group (Fig. 2a). Subsequently, a VvRsbR construct of the N-terminal 165 amino acids was produced for recombinant expression in *E. coli*. The purified domain retained the red coloration characteristic of heme binding (Fig. 2b). Under oxidizing conditions, the UV/visible absorbance spectrum of the *Vv*RsbR:*Vv*RsbS complex displayed three distinct peaks typical for a Fe(II)-O_2 heme-dependent globin coupled sensor domain: the Soret peak (414 nm), the α-peak (543 nm) and the β-peak (578 nm)[34]. After deoxygenation with sodium dithionite, the maximum of the Soret peak shifted to 431 nm and the α and β peaks merged into a single peak with a maximum at 556 nm, which is consistent with the Fe(II) form (Fig. 2c). This

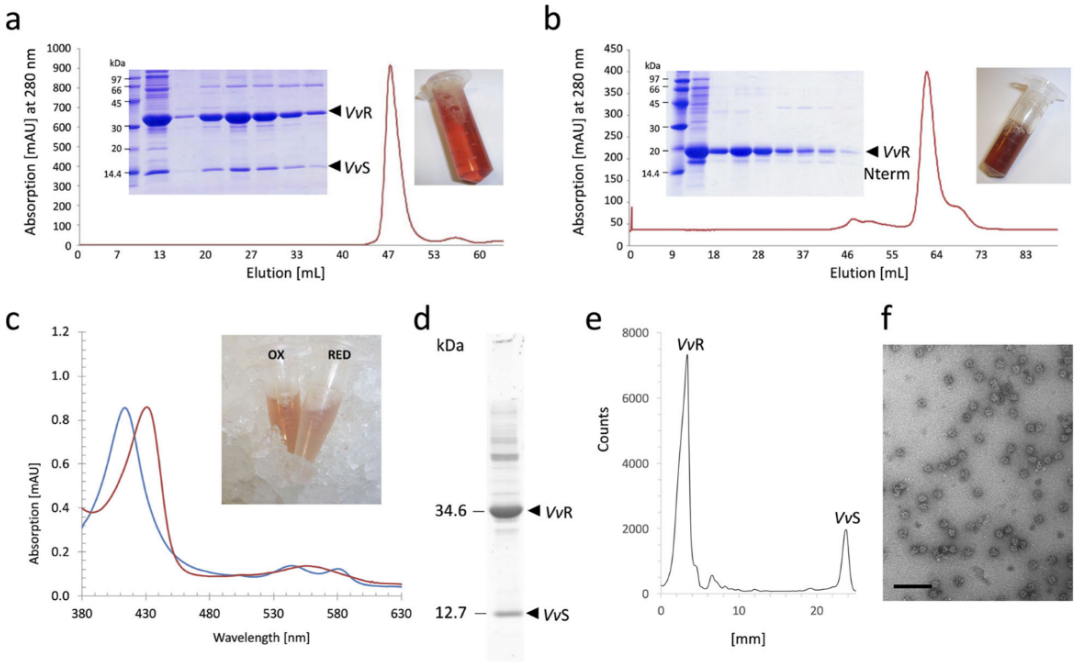

Fig. 2 Biochemical characterization of the *Vv*RsbR:*Vv*RsbS complex. Size exclusion chromatography profiles of the *Vv*RsbR:*Vv*RsbS complex (**a**) and the *Vv*RsbR N-terminal domain (**b**). Insets show Coomassie-stained fractions of the elution maxima after separation by SDS PAGE and the purified protein after concentration: *Vv*RsbR:*Vv*RsbS complex (13 mg/mL) and VvRsbRN-terminal domain (amino acid residues 1–165, 15 mg/mL). **c** Absorption spectra of oxygenated (blue line) and deoxygenated (red line) forms of the *Vv*RsbR:*Vv*RsbS complex. Deoxygenated *Vv*RsbR:*Vv*RsbS samples were prepared by adding sodium dithionite to the protein solutions. Spectra were obtained using a 1 cm path length quartz cuvette and a Biochrom Libra S22 UV-Vis spectrophotometer. The inset shows photographs of protein solutions in oxygenated (OX) and reduced (RED) states. **d** Purified *Vv*RsbR:*Vv*RsbS stressosome complex separated by SDS PAGE (uncropped gel lane) and stained with Krypton (Thermo Scientific). The gel was imaged with a Typhoon fluorescence scanner, with excitation at 532 nm and emission recorded at 560 nm. Band intensities were quantified with ImageQuant (**e**). The calculated ratio between *Vv*RsbR and *Vv*RsbS was 2.4:1. The uncropped gel is shown in Supplementary Fig. 18b. Electron micrographs of negative stained purified *Vv*RsbR:*Vv*RsbS complexes showed homogenously distributed particles (**f**). The size bar represents 100 nm.

shift in the spectrum was accompanied by a change in color of the protein solution from red (oxidized) to yellow (reduced; Fig. 2c). Therefore, the *Vv*RsbR:*Vv*RsbS stressosome complex binds an iron-heme cofactor through the N-terminal sensory domain of *Vv*RsbR, consistent with heme binding of *V. brasiliensis Vb*RsbR[30].

The *V. vulnificus* stressosome is linked to iron metabolism. To investigate the physiological function of the stressosome gene cluster, we investigated the proteome of a Δ*rsbRSTX* mutant in comparison to its isogenic wild type strain. First, we analyzed the proteome of exponentially growing and stationary cells cultured in iron-supplemented medium, a condition leading to strong accumulation of *Vv*RsbR in the stationary phase. Second, to study the predicted association with oxygen signaling, we characterized the proteome of exponentially growing cells transferred to screw top tubes, where hypoxic conditions are established by oxygen depletion of the growing cells (Supplementary Fig. 5a). These comparisons identified a large number of proteins with significantly changed abundance in response to growth phase and oxygen-availability, and confirmed the stationary phase accumulation of *Vv*RsbR and the two potential downstream signaling proteins, *Vv*D1 and *Vv*D2 (Supplementary Fig. 5b). Significantly, the abundance of several proteins differed between the wild type and the Δ*rsbRSTX* mutant in each condition (Supplementary Fig. 5c, Supplementary data 2). The number of proteins with significantly changed abundance (1.5-fold and $p < 0.05$) in the Δ*rsbRSTX* versus wild type comparison was much smaller in exponentially growing cells than in stationary phase cells (Supplementary Fig. 5c). This suggests that a stationary phase signal, correlating with exhaustion of glucose, triggers a strong stressosome response. Following the hypoxic-shift, the lack of the stressosome caused a more pronounced down-regulation than upregulation of proteins in the stressosome mutant at all time points (Supplementary Fig. 5c), pointing to the importance of the stressosome to maintain protein expression in oxygen-restricted conditions. Although in all three conditions—growth, stationary phase and hypoxia—the loss of the stressosome resulted in pronounced changes in protein expression, little overlap in the stressosome-dependent proteomic signatures was observed (Supplementary Fig. 5d, Supplementary data 3 and 4).

Classification of proteins whose abundance was affected by the *Vv rsbRSTX* deletion revealed a functionally diverse set of targets covering various cellular processes e.g. metabolism, biosynthesis of secondary metabolites, cofactors and siderophores, ABC-transport, and signaling (supplementary data 2).

Apart from a great functional diversity of regulated proteins, links between the *Vv rsbRSTX* gene cluster and iron/heavy metal metabolism were observed. Examples of differentially abundant iron-metabolism proteins include the iron-uptake proteins FeoAB

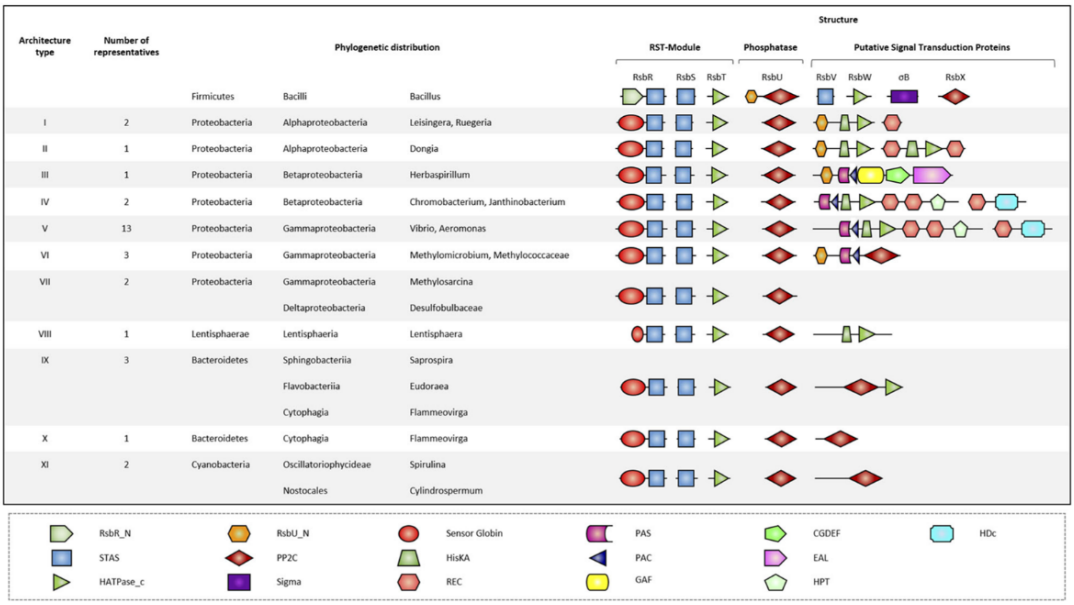

Fig. 3 Phylogenetic distribution of RSTX-modules with a sensor globin coupled RsbR ortholog. The first row shows the domain organization of proteins encoded in the *B. subtilis* SigB operon. Here, the RST-module is followed by a gene encoding the environmental stress phosphatase RsbU. RsbU is activated upon interaction via its N-terminal domain (RsbU_N) with RsbT. Activated RsbU then conveys the signal to the RsbV-RsbW-SigB partner-switching module. RsbX, the last protein encoded in the operon, functions as a feedback phosphatase, reducing stressosome activity by the dephosphorylation of conserved threonine and serine residues in RsbR and RsbS. In contrast to *B. subtilis*, in species encoding a sensor globin coupled R-subunit, the putative feedback phosphatase, RsbX, is encoded immediately downstream of the RST-module thus forming a highly conserved RSTX-module. Based on the domain organization, eleven putative downstream architecture types were identified for these species. Some, but not all, of the downstream-located signaling proteins possess a RsbU_N like domain, supporting the notion that they may indeed function as targets for the RsbT-like protein. Domain abbreviations are as follows: RsbR_N (RsbR non-heme globin N-terminal domain), RsbU_N (RsbU N-terminal domain), PAS (Per- period circadian, Arnt- Ah receptor nuclear translocator, Sim- single-minded protein), GGDEF (Diguanylate cyclase, synthesizes cyclic di-GMP), HDc (Metal dependent phosphohydrolases with conserved 'HD' motif), STAS (Sulfate transporter and anti-sigma factor antagonist), PP2C (Mg^{2+} or Mn^{2+} dependent protein phosphatase 2C), HisKA (His kinase A (phosphoacceptor) domain), PAC (PAS associated C-terminal), EAL (Putative diguanylate phosphodiesterase, called EAL after its conserved residues), HATPase_c (Histidine kinase-like ATPase), Sigma (RNA polymerase sigma subunit), REC (CheY-homologous receiver domain), GAF (cGMP-specific phosphodiesterases, adenylyl cyclases and FhlA) and HPT (Histidine phosphotransfer domain).

(VV1_0148, VV1_0149), vulnibactin[35] siderophore synthesis and uptake proteins (VV2_0830, VV2_0831, VV2_0834, VV2_0835, VV2_0837, VV2_0838, VV2_0842, VV2_0843), ferric iron uptake ABC transporters (VV1_1660, VV1_1663), a TonB iron uptake system (VV2_0363, VV2_0364), a ferritin (VV1_1116), putative heme-iron utilization proteins (VV2_1616, VV2_1617), and proteins with a role in heavy metal resistance (VV2_0850, VV2_0853) (Supplementary Figs. 6–13). Expression of these proteins, except VV2_0850 and VV2_0853 which were upregulated, was lower in Δ*rsbRSTX*, suggesting a specific physiological impact of iron in the stressosome mutant. The link to iron metabolism was particularly evident during stationary phase, while only moderate further downregulation of iron related proteins in the Δ*rsbRSTX* mutant was observed in the hypoxia experiment.

Moreover, a consistent higher upregulation in the stressosome mutant was observed for an uncharacterized ABC-F protein (VV1_0491, between 25 and 29-fold) showing homology to the translation throttle Etta[36]. Additional proteins with a role in translation were differentially regulated in the mutant compared to the wild type. In stationary phase cells of the stressosome mutant we observed upregulation of the ribosome hibernation protein (VV1_0693, 4.7-fold), a peptidyl-tRNA hydrolase (VV1_0258, 4.3-fold) and proteins involved in tRNA biogenesis and modification (VV1_0266, 2.2-fold; VV1_0277,2.1-fold). Finally, a potential translation release factor methyltransferase (VV1_0252, 2.9-fold) and several proteins with a role in tRNA modification (VV1_1251, VV1_2142, VV1_2608; VV1_2926) were present at lower level (1.5 to 1.9-fold) in the mutant, pointing to a potential impact of stressosome activity in modifying translation in *V. vulnificus* (supplementary data 2).

Occurrence and genetic organization of globin coupled sensor containing stressosome gene clusters. Iron-heme binding is a central feature of the stressosome in *V. vulnificus*, and to investigate whether heme-binding globin coupled sensors are a common feature of stressosomes, microbial genomic sequences were analyzed using *V. vulnificus Vv*RsbR as the query (Fig. 3). The search identified many bacterial species possessing a *rsbRSTX*-module with an RsbR-encoded N-terminal globin coupled sensor. These species, ranging from Proteobacteria, Lentisphaerae, Bacteroidetes and Cyanobacteria, reside in aquatic ecosystems, in different types of marine or freshwater habitats. The single domain PP2C type phosphatase encoded in these gene clusters was closely related to RsbX but not RsbU[22]. Thus, these organisms all encode the minimal set of orthologs required to form a functional stressosome: an antagonist RsbS, a co-antagonist RsbR

with sensory function, the switch kinase RsbT, and the feedback phosphatase RsbX. Furthermore, several different types of potential down-stream modules were associated with the *rsbRSTX*-modules, which were usually separated only by a small number of base pairs (Fig. 3). The down-stream module domain organization suggests that in these organisms the stressosome has been adopted to control either: the activity of PP2C-type phosphatases (e.g. *Methylomicrobium*); the level of the secondary-messenger cyclic-di-GMP (e.g. *Vibrio*, *Chromobacterium*, *Herbaspirillum*); or phosphorelays of kinase receiver (HisKA) and transmitter (REC) domain proteins (e.g. *Dogia*, *Ruegeria*).

In some Proteobacteria of the α, β and γ group, the N-terminus of signaling proteins encoded downstream of the RsbX homolog shows significant sequence similarity to the N-terminus of the *B. subtilis* RsbU protein (RsbU_N). Since binding of RsbT to the RsbU_N transmits input from the stressosome to the downstream segment of the cascade regulating SigB in *B. subtilis*[18,19], this observation strongly suggests that these proteins contribute to stressosome dependent signaling. However, for the majority of the down-stream encoded signaling proteins considered in the analysis, including those identified in *V. vulnificus*, no RsbU_N domain was detected. Signaling by the stressosome in these cases could be transmitted through RsbT-dependent phosphorylation of the downstream sensor kinase, which would most likely be a transient interaction as required by a regulatory switch. This explanation is consistent with our failure to produce positive interaction results for VvRsbT and VvD1, the two-component protein encoded directly down-stream of the stressosome module. A screen of complete proteomes available at UniProt for the genus *Vibrio* identified the complete set of stressosome proteins (RsbR, RsbS, RsbT and RsbX) in a surprisingly small number of *Vibrio* species (four out of 38; supplementary data 5): *V. mangrove, V. nigripulchritudo, V. pectenicida* and *V. vulnificus*. These species all share a similar set of potential stressosome downstream regulators. Why stressosomes are restricted to only a few *Vibrio* species, and if this is a common phenomenon in other genera, is presently unknown.

Single particle cryo-EM reconstruction of the *V. vulnificus* *Vv*RsbR:*Vv*RsbS stressosome reveals a new stressosome symmetry and stoichiometry. Negative-stain transmission electron microscopy was performed on the purified *Vv*RsbR:*Vv*RsbS complex (Fig. 2d, e) to assess the formation of stressosome-like structures. The *Vv*RsbR:*Vv*RsbS complex was easily recognizable on micrographs due to its spherical core with several turret-like extensions, highly reminiscent of stressosome complexes from *B. subtilis* and *L. monocytogenes*[5,6,21] (Fig. 2f). Although oxidized and reduced stressosome complexes could be visualized in negative stain, only the oxidized form presented here was suitable for a cryo-EM study.

Quantification of *Vv*RsbR and *Vv*RsbS bands of the heterologously expressed stressosome complex revealed a non-integral *Vv*RsbR:*Vv*RsbS ratio of 2.4:1, suggesting a stoichiometry between *Vv*RsbR and *Vv*RsbS subunits that differs from the 2:1 RsbR:RsbS ratio reported for in vitro assembled *B. subtilis and L. monocytogenes*[5,21] stressosome complexes (Fig. 2d, e). To generate a high resolution structure of the *V. vulnificus* stressosome, and to identify the symmetry and stoichiometry of the *Vv*RsbR:*Vv*RsbS stressosome complex, a cryo-EM reconstruction was initiated from the oxidized stressosome complex (Table 1). Iterative 2D classifications of around 230,000 particles resulted in class-averages displaying a variety of symmetric features in the STAS domain core (supplementary fig. 14). Eigenimage analysis of the 2D classes showed patterns characteristic of icosahedral symmetry: twofold, threefold and fivefold symmetry axes (supplementary fig. 14). These features are especially prominent for the STAS domain core, and less pronounced when analyzing the whole complex. However, a comparison of the experimental 2D class averages with projections of an icosahedral-symmetric reconstruction clearly ruled out icosahedral symmetry for the *Vv*RsbR:*Vv*RsbS stressosome complex (supplementary fig. 14). Simultaneous 3D classification against multiple references with different combinations of two-, three- and five-fold symmetry axes (suggested by the Eigenimage analysis) resulted in a vast majority of particles being sorted into asymmetric (C1) or twofold symmetric (C2, D2) classes. Consequently, the following 3D reconstructions were performed either without applying symmetry (C1), or imposing D2 symmetry, which is supported by the observation of a D2 point-group symmetric arrangement of RsbR in *B. subtilis* stressosomes[5].

In contrast to the organization of the *Bacillus* stressosome, asymmetric reconstructions of the *Vibrio* stressosome show at least two pentagons consisting solely of *Vv*RsbR monomers (Fig. 4), together with pentagons with 4:1 and also 3:2 *Vv*RsbR:*Vv*RsbS stoichiometry, respectively. Thus, the total number of *Vv*RsbR$_2$ dimers in the complex can exceed 20 (Fig. 4), which is in agreement with the experimentally determined, non-integer ratio of 2.4:1 *Vv*RsbR:*Vv*RsbS. C1 refinements of sub-populations of the particles yielded reconstructions with varying

Table 1 Cryo-EM data collection, refinement and validation statistics.

	VvRsbRS complex (EMDB-12676) (PDB 7O01)
Data collection and processing	
Magnification	59000
Voltage (kV)	300
Electron exposure (e–/Å^2)	72
Defocus range (μm)	−1.7 to −5.5
Pixel size (Å)	1.77
Symmetry imposed	D2
Initial particle images (no.)	230,784
Final particle images (no.)	35,647
Map resolution (Å)	8.3
FSC threshold	0.148
Map resolution range (Å)	6.8–13.0
Refinement	
Initial model used (PDB code)	2MWG
Model resolution (Å)	
FSC threshold	0.143
Model resolution range (Å)	8.3
Map sharpening *B* factor (Å^2)	
Model composition	
Non-hydrogen atoms	36384
Protein residues	7356
Ligands	—
B factors (Å^2)	
Protein	mean 269.99
Ligand	none
R.m.s. deviations	
Bond lengths (Å)	0.015
Bond angles (°)	2.573
Validation	
MolProbity score	2.44
Clashscore	22.66
Poor rotamers (%)	0.0
Ramachandran plot	
Favored (%)	88.16
Allowed (%)	11.01
Disallowed (%)	0.83

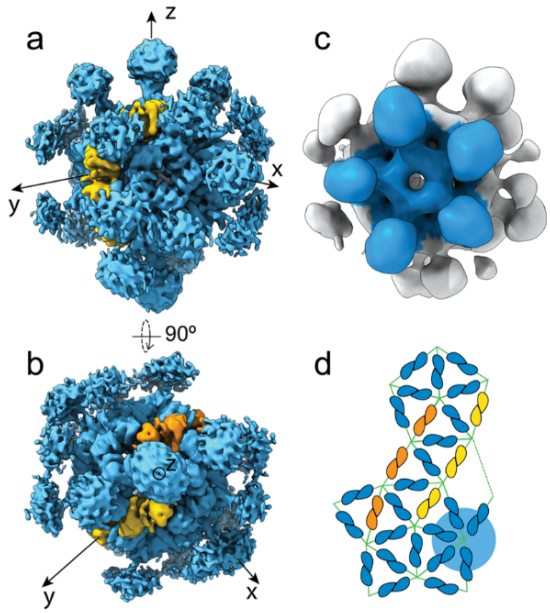

Fig. 4 Cryo-EM reconstruction of the *Vibrio vulnificus* stressosome complex (*Vv*RsbR:*Vv*RsbS) reconstructed in D2 (a, b) and in C1 (c). a The *Vv*RsbR subunits are colored in blue and *Vv*RsbS subunits are shown in yellow and orange. **b** The reconstructed volume reveals an imperfect D2 symmetry. **c** In the volume reconstructed without applying any symmetry operators, pentameric *Vv*RsbR faces are observed (colored blue in c and highlighted by the blue sphere in (**d**)). **d** The 2D representation of the icosahedron pentagonal faces reveal that only 12 hetero-triangular faces are formed in *Vv*RsbR:*Vv*RsbS, while 8 triangular faces are composed entirely of *Vv*RsbR.

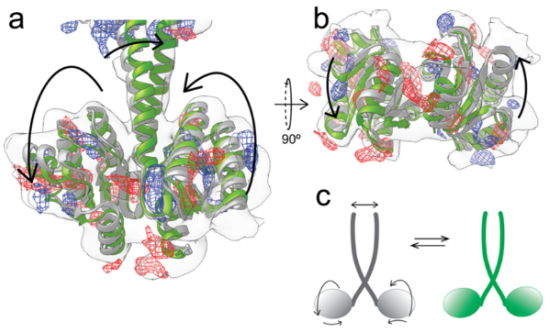

Fig. 5 Conformational changes of the *Vv*RsbR dimer protomers within the *Vv*RsbR:*Vv*RsbS stressosome. Side (**a**) and bottom (**b**) views of a difference map between different *off-axis Vv*RsbR dimers (blue mesh indicates negative difference density, and red mesh indicates positive difference density). The difference map is superposed on an isolated dimer density shown as transparent surface. The green and white ribbon models indicate two putative conformations of the dimer. The schematic (**c**) indicates the changes in the respective positions of the monomers imposed by the transition.

numbers of turrets with an average of 22 ± 3 *Vv*RsbR$_2$ dimers, again clearly pointing towards a variability in *Vv*RsbR:*Vv*RsbS stoichiometry. Consistently, a stoichiometry of 22 RsbR$_2$ dimers was also reported for a recent 4.1 Å recombinant *B. subtilis* stressosome reconstruction[6].

*D2 symmetry break in the VvRsbR:VvRsbS complex*The cryo-EM single particle analysis in C1 symmetry revealed a 24:6 *Vv*RsbR$_2$:*Vv*RsbS$_2$ stoichiometry for the stressosome (Supplementary Fig. 15a). However, when applying D2 symmetry, we observed different reconstruction results depending on where the D2 axis was positioned. Changing the orientation of the D2 axis relating two triangular faces, with respect to the orientation of the x- and y-axes, resulted in changes in the stoichiometry of *Vv*RsbR and *Vv*RsbS, ranging from 20:10 *Vv*RsbR$_2$:*Vv*RsbS$_2$ to 18:12 *Vv*RsbR$_2$:*Vv*RsbS$_2$ (Supplementary Fig. 15b, c). In reconstructions with 20-18 *Vv*RsbR$_2$ dimers, the structural features in the STAS domain core were less prominent and it was not entirely possible to distinguish between *Vv*RsbR and *Vv*RsbS due to a potential misalignment. As expected, the *Vv*RsbR$_2$ dimers located on the D2 axis show symmetric features, while off-axis *Vv*RsbR dimers in all D2 maps exhibited an asymmetric sensory domain. Indeed, a difference map between the two protomers within an asymmetric *Vv*RsbR dimer reveals different states in the sensing domain, the coiled-coil linker helices and the STAS domain (Fig. 5), displaying a 5 Å '*shrugging*' movement. Consequently, both protomers of the *Vv*RsbR are proposed to move either concertedly, in a scissor-like movement, or only one of the protomers moves by skewing one of the linker's coiled-coil helices in the linker.

Interactions within the *Vv*RsbR:*Vv*RsbS:*Vv*RsbT complex. To complement the experimental data on *Vv*RsbR and *Vv*RsbS interactions, and to visualize the interaction with *Vv*RsbT, molecular models of *Vv*RsbR$_2$ and *Vv*RsbS$_2$ dimers and the *Vv*RsbT monomer were built. As stressosome particles were purified under aerobic conditions, and in agreement with the UV/visible absorption spectroscopy data, the sample is oxygen-bound, representing the inactive RsbT binding state of the stressosome[30]. The resolution of the refined D2 map extends below 7 Å in the core assembled from the STAS domains of the *Vv*RsbR and *Vv*RsbS and up to 8–9 Å in the distal N-terminal regions, showing well distinguished linker-helices in *Vv*RsbR and the beta-sheets in *Vv*RsbS in stressosomes with a 24:6 *Vv*RsbR$_2$:*Vv*RsbS$_2$ stoichiometry (supplementary fig. 16). Secondary structure elements in the STAS domain core and the protruding *Vv*RsbR linker helices are thus well defined and allowed for cryo-EM density guided model building of the *Vv*RsbR$_2$ and *Vv*RsbS$_2$ dimers (Fig. 6).

While the contact area between the monomers in *Vv*RsbS$_2$ comprises charged/polar residue chains, the same region in the *Vv*RsbR$_2$ dimer consists exclusively of hydrophobic side-chains (Fig. 6b, e). The charged/polar residues in *Vv*RsbS, e.g., interaction of Ser4-A and Ala6-A with Glu21-B, are likely to establish interactions between the monomers but are not conserved in *Vv*RsbR (Fig. 6c), resulting in a stronger interaction between the monomers of the *Vv*RsbS$_2$ dimer over the *Vv*RsbR$_2$ dimer. Notably, this interaction difference is very well conserved in RsbR and RsbS proteins from different Gram-negative bacteria but not conserved in Gram-positive bacteria (back-to-back submission Miksys *et al.*, in revision, COMMSBIO-21-1365A).

We generated a homology model of *Vv*RsbT and placed it onto the *Vv*RsbR$_2$:*Vv*RsbS$_2$ complex (Fig. 7) using the structure of the SpoIIAB:SpoIIAA complex[37] as a reference. The SpoIIAB serin kinase and its target SpoIIAA are functionally related structural homologs of the RsbT kinase and its RsbS substrate, forming a partner-switching module controlling activity of the sporulation sigma factor, σ^F, in Bacilli[37]. Although the ATP-loop in *Vv*RsbT is slightly shorter compared to related kinases, and consequently *Vv*RsbT is slightly more compact, up to 6 *Vv*RsbT molecules can

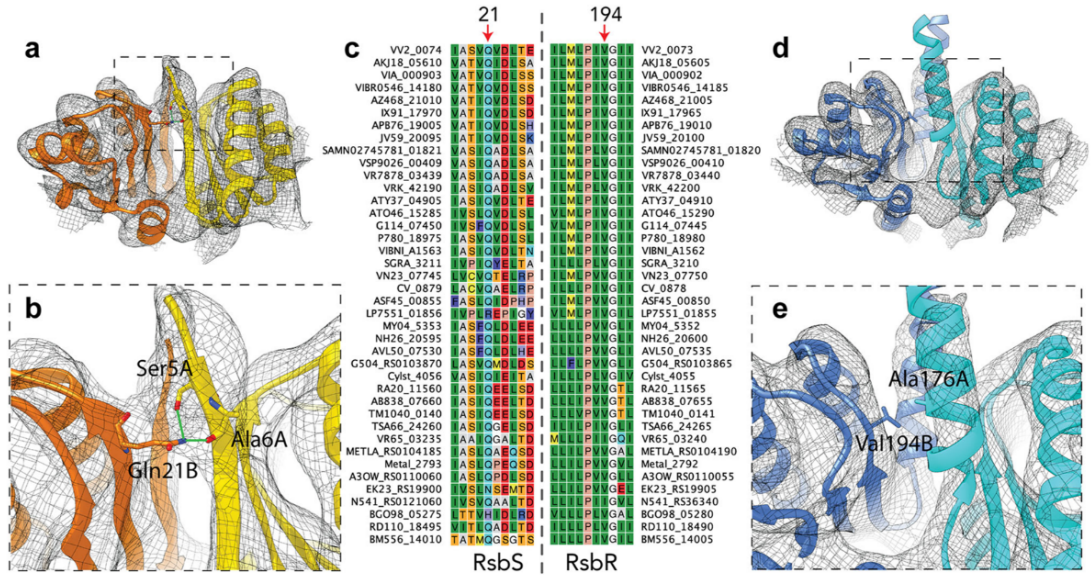

Fig. 6 Interactions within the *Vv*RsbS and *Vv*RsbR STAS-domain interfaces and conservation of the involved residues within Gram-negative Bacteria. **a**, **b** *Vv*RsbS and (**d**, **e**) *Vv*RsbR are shown in different shades of yellow and blue, respectively, fitted into the D2 cryo-EM density map (shown as black mesh). Protomers within the dimers of (**a**) *Vv*RsbS form intradimeric contacts via the β1-sheets (b) that likely result in increased stability of the dimer in comparison to *Vv*RsbR (for the residues contributing to the contacts, carbon atoms are colored blue or yellow/orange respectively, oxygen atoms in red, and nitrogen atoms in dark blue). **c** Gln21 in *Vv*RsbS is conserved in RsbS homologs from other Gram-negative bacteria. **d** Unlike *Vv*RsbS, *Vv*RsbR forms α-helices at the intradimeric interface that continue into the N-terminal turret-forming domain without obvious inter-monomeric contacts. **e** Val194 in *Vv*RsbR is conserved in other RsbR homologs (**c**) and does not feature a clustering of polar sidechains (hydrophobic residues are shown on a green background and polar charged, charged+, charged−, aromatic, are shown on light blue, dark blue, red and violet background, respectively).

be docked to the *Vv*RsbR$_2$:*Vv*RsbS$_2$ and *Vv*RsbS$_2$:*Vv*RsbR$_2$ interface in a stressosome (Fig. 7). There is not a pronounced complementarity of charges between the predicted *Vv*RsbT and *Vv*RsbR binding surfaces, consistent with the necessity of releasing *Vv*RsbT to elicit signal transduction (Supplementary Fig. 17a). In the RsbT bound pose of *Vv*RsbR only Thr233 (structural equivalent to *Bs*RsbR Thr205) would be easily accessible to the ATP-binding site in *Vv*RsbT, the second phosphorylation site in *Vv*RsbR, Ser199 (structural equivalent to *Bs*RsbR Thr175), is inaccessible (Fig. 7). Ser178 and Thr182, for which in vitro phosphorylation was reported for *V. brasiliensis Vb*RsbR[30] are buried within the linker-STAS domain interface in our *Vv*RsbR$_2$ model and would thus not be readily accessible to the *Vv*RsbT kinase in the assembled stressosome (Supplementary Fig. 17b).

Discussion

Biochemical, functional and structural understanding of stressosome complexes is currently restricted to the low-GC Gram-positive *B. subtilis*[5,6] and *L. monocytogenes*[21]. The role of the stressosome in high-GC Gram-positives and Gram-negatives is largely unexplored. Recent pioneering work in *Mycobacterium marinum* showed that expression and cellular localization of stressosomes varies in response to stress and growth conditions in this species[38,39].

The *Vibrio basiliensis* stressosome complex is currently the only example studied from a Gram-negative bacterium. However, expression and phosphorylation of stressosome core protein *Xc*RsbR was also reported in the Gram-negative plant pathogen *Xanthomonas campestris* during transition from the late exponential growth phase to the stationary phase[30,40]. Here, we investigate the stressosome complex of the Gram-negative human pathogen *Vibrio vulnificus*. We show that despite common features and principles shared with stressosomes from Gram-positives (*Bacillus/Listeria*-type), functionally relevant differences can be observed for the stressosome of Gram-negatives (*Vibrio*-type).

Significant differences between the *Bacillus/Listeria* and the *Vibrio* stressosomes are already evident at the genomic level[22]. The *V. vulnificus* genome demonstrates (i) an N-terminal globin coupled sensor of RsbR that is absent from *Bacillus/Listeria*, (ii) lack of a gene encoding RsbU downstream of the *rsbRST* module, (iii) stressosome locus association with genes related to two-component systems, instead of a sigma factor, and (iv) lack of *Vv*RsbR paralogs. Transcriptional analyses of the stressosome locus show that the two predicted downstream encoded signaling proteins, *Vv*D1 and *Vv*D2, follow the same transcription kinetics as the *rsbRSTX* module, supporting the idea that these genetic elements are functionally coupled. Furthermore, transcription of the stressosome locus increased in stationary phase after depletion of the main carbon source, contrasting results obtained for *B. subtilis*[32].

A global proteomics-based profiling of a wild type strain and an isogenic mutant lacking *VvrsbRSTX* was used to identify the physiological function of the stressosome in *V. vulnificus*. Although our proteome analysis detected *Vv*RsbR during all growth conditions in the wild type, showing strongest accumulation during stationary phase in accordance with our Western blot results, there is currently an absence of a direct indicator/reporter for the degree of stressosome activation (e.g. changes in the stressosome phosphorylation pattern). We observed a clear difference in the proteome between wild type and the *ΔrsbRSTX* mutant, which is particularly strong when the stationary phase is triggered by glucose exhaustion in iron-rich medium. A

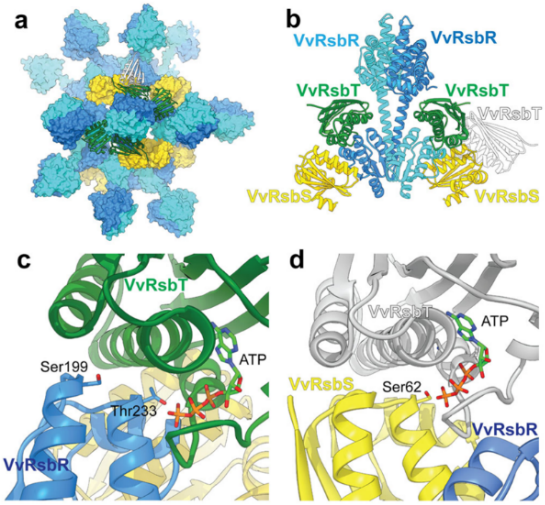

Fig. 7 Interaction of *Vv*RsbT with phosphorylation sites in *Vv*RsbR and *Vv*RsbS. A homology model of *Vv*RsbT was generated and docked to *Vv*RsbR and *Vv*RsbRS. **a** A space-filling model of the *Vv*RsbRS stressosome complex is shown with $VvRsbR_2$ and $VvRsbS_2$ dimers colored in blue and yellow, respectively. *Vv*RsbT (ribbon model) was docked to the $VvRsbR_2$ (*Vv*RsbT in green) or $VvRsbS_2$ (*Vv*RsbT in white). **b** Side view of the $VvRsbR_2$ dimer and two *Vv*RsbS monomers with docked *Vv*RsbT colored as in (**a**). Close-up views show that binding of *Vv*RsbT to neighboring *Vv*RsbR or *Vv*RsbS is possible without steric clashes. The ATP binding site in *Vv*RsbT docked to *Vv*RsbR (**c**) and *Vv*RsbS (**d**) in the stressosome assembly. The respective phosphorylation sites are indicated (carbon atoms in blue or yellow respectively, oxygen atoms in red, and nitrogen atoms in dark blue).

prominent group of proteins linked to iron-metabolism and -uptake showed a consistent decrease in abundance in the stressosome mutant in all growth conditions tested. This finding could point to a reduced requirement for iron in the absence of an active stressosome or in a reduced capacity to induce iron-uptake pathways. At the very least the data suggest that the stressosome alters iron-metabolism in *V. vulnificus;* which could be relevant given the stressosome gene cluster is often associated with clinical isolates of *V. vulnificus*, as high blood iron is a risk factor for the development of severe *V. vulnificus* infection[41]. The oxygen-depletion signature of the mutant showed little overlap with the stationary phase signature. These differences between the oxygen-depletion response and the response to energy limitation might indicate that the *V. vulnificus* stressosome signaling-pathway integrates further signals. Indeed, a recent study linked the aerotaxis globin-coupled sensor domain of HemAT to ethanol-sensing[42], and the presence of a PAS domain in the presumed output module protein VvD1 (VV2_0077) could provide a further entry point into the signaling pathway.

We have determined the cryoEM structure of the stressosome from a Gram-negative organism in three symmetry states, C1, C2 and D2, and compared and contrasted these structural data with prior structural analyses of stressosomes from Gram-positive microbes.

First, the *Bs*RsbR:*Bs*RsbS[5,6] and *Lm*RsbR:*Lm*RsbS[21] stressosome reconstructions share the maximal number of 20 hetero-triangular capsid faces, while *Vv*RsbR:*Vv*RsbS in the most common symmetry, D2, comprises only 12 hetero-triangular faces. Because the *Vv*RsbR turrets prevent access to the STAS core, the 8 *Vv*RsbR homo-triangular faces cannot contribute to *Vv*RsbT binding. Moreover, due to significant differences at the inter-dimeric interaction sites in $VvRsbR_2$:$VvRsbS_2$, it is not possible to fit a second *Vv*RsbT to a *Vv*RsbR at the *Vv*RsbS contact site, as is possible in the *Listeria innocua Li*RsbR:*Li*RsbS structure (Miksys *et al.*, in revision, COMMSBIO-21-1365A). Consequently, only one *Vv*RsbT molecule can be bound at the *Vv*RsbR:*Vv*RsbR interface, suggesting a greatly reduced capacity to interact with *Vv*RsbT. Any variation in the number of hetero-triangular capsid faces would provide an additional regulatory mechanism to titrate bound *Vv*RsbT, thereby modulating the downstream signaling cascade. It should be considered here, however, that the minimal VvRsbR:VvRsbS complex investigated in this study has been heterologously expressed and purified from *E. coli*, which is also the case for all other published stressosome structures. It is thus possible that the stoichiometry adopted by native stressosome complexes is different to these recombinant stressosomes.

Our structural data also provide insight into the mechanism of signal perception and transduction within the $VvRsbR_2$ dimer. Considerable differences between the two monomers in the $VvRsbR_2$ dimer were observed, presumably representing two different states of the *Vv*RsbR protein. This finding is reminiscent of observations previously reported for HemAT[43], an aerotaxis signal transducer protein that shares the heme-binding pocket with the N-terminal sensor domain of *Vv*RsbR. While in its ligand-bound form, the HemAT dimer assumes a highly symmetrical organization, the unoccupied form of the HemAT dimer displays a symmetry breach. This breach in symmetry is manifested in a small helical shift and rotation of the four-helical bundle in the dimerization interface, and more prominent in the ligand binding pocket of one of the two HemAT protomers. Disruption of the HemAT symmetry communicates the ligand binding state to the C-terminal domain of HemAT, and subsequently the downstream elements of the aerotaxis signaling cascade in *B. subtilis*. Asymmetry could be a specific mechanistic feature of oxygen sensing in globin coupled sensors and is reflected by the different states observed for *Vv*RsbR in our structure. Thus, as reported for HemAT, similar structural changes associated with ligand binding by *Vv*RsbR could be communicated by movements of the *Vv*RsbR linker helices and further transmitted to the STAS domain core, affecting the binding position and kinase activity of *Vv*RsbT. This could represent a fundamental aspect of stressosome-dependent signaling and should be considered in future analyses. Finally, we conclude that despite obvious differences in the molecular make-up of stressosome pathways in unrelated organisms, a recurrent theme in stressosome signaling is the global reorganization of the cell physiology to overcome adverse growth conditions.

Methods

Cultivation of bacteria. *V. vulnificus* CMCP6[44] was grown in a chemically defined medium (7.5 mM glucose, 10 mM Na_2HPO_4, 10 mM KH_2PO_4, 0.8 mM $MgSO_4$, 9.3 mM NH_4Cl, 428 mM NaCl, 0.75 µM $FeCl_3$) at 30 °C with 120 rpm agitation. To stabilize the iron during storage, the $FeCl_3$ stock-solution was prepared in 1 N HCl. To neutralize the HCl transferred with the $FeCl_3$, an appropriate volume of 1 N NaOH was added to the final medium to archive final pH 7.0.

Exponentially growing cells from an overnight culture were used to inoculate fresh, pre-warmed medium with a starting OD_{500} of 0.05. To analyze the impact of iron availability on stressosome expression, cells were also grown in medium without iron supplementation. To induced hypoxic conditions, an appropriate amount of exponentially growing cells was transferred to completely fill 50 ml Falcon tubes, leaving no residual air bubbles in the tubes. The filled Falcon tubes were subjected to static incubation at 30 °C and harvested at 30, 60 and 120 min after the shift.

Bacterial two-hybrid screen. For the bacterial two hybrid analyses[33] the coding sequences of *Vv*RsbR (*VV2_0073*), *Vv*RsbS (*VV2_0074*), *Vv*RsbT (*VV2_0075*), *Vv*RsbX (*VV2_0076*) and the predicted STAS domain proteins *VV1_0681*, *VV1_2658*, *VV2_1159* and *VV1_1170* were amplified by PCR from *V. vulnificus* CMCP6 genomic DNA and cloned into the XbaI and KpnI site of pUT18, pUT18C, pKT25 and p25-N to generate N- and C-terminal fusions with the T18

and T25 fragment of the *Bordetella pertussis* adenylate cyclase, CyaA. To test for protein-protein interactions, appropriate plasmid combinations encoding a T18 and a T25 fusion were co-transformed into *E. coli* BTH101 and transformants selected overnight at room temperature (RT) on LB plates supplemented with 50 μg ml^{-1} kanamycin. The next day co-transformants were streaked on LB-agar plates containing 50 μg ml^{-1} kanamycin, 100 μg ml^{-1} ampicillin, 100 μg ml^{-1} X-Gal (5-bromo-4-chloro-3-indolyl-β-D-galactopyranoside), and 0.5 mM IPTG (isopropyl β-D-1-thiogalactopyranoside). Plates were stored in the dark at RT and X-Gal degradation monitored for up to three days. pUT18Czip and pKT25-zip expressing a fusion of T18 and T25 with the leucine zipper of GCN4 were used as a positive control and the pUT18C and pKT25 empty vectors as a negative control. Colonies that turned blue following the above procedure in all three replicates were deemed as positive for protein-protein interactions due to the functional complementation of *cyaA*, which results in the expression of ß-galactosidase and the hydrolysis of X-Gal.

RNA isolation and Northern blot analysis. *V. vulnificus* was harvested by mixing 30 ml cell culture with 10 ml ice-cold killing buffer (20 mM Tris pH = 7.5, 5 mM $MgCl_2$, 20 mM sodium azide) and centrifugation at 21,000 *x* g and 4 °C for 5 min. Isolation of RNA was performed as previously described using the acid-phenol method with modifications as described by Fuchs et al.[45] Briefly, the cells were resuspended in 0.5 ml ice-cold suspension buffer (3 mM EDTA pH 8.0, 200 mM NaCl), mixed with 0.5 ml μl PCI (phenol:chloroform:isoamyl alcohol, 25:24:1) and 0.5 μl glass beads (0.1 mm diameter) and lysed in a Precellys 24 (Peqlab, Erlangen, Germany) with one 30 sec cycle at 6800 rpm. After 5 min centrifugation at 21,000 *x* g the aqueous phase containing the RNA was transferred to a new test tube and mixed with 500 PCI for 5 min in a shaker. The aqueous and the organic phase were separated by centrifugation for 5 min at 21.000 *x* g and the upper, aqueous phase washed once with CI (chloroform:isoamyl alcohol, 24:1). After transfer of the RNA containing phase (usually 0.4 ml) to a new test tube the RNA was precipitated overnight at −20 °C with 1 ml ice-cold ethanol (98%) and 40 μl sodium acetate (3 M). The RNA was pelleted for 30 min at 21,000 *x* g and 4 °C. The RNA pellet was washed with 0.5 ml ice-cold ethanol (70%) and dissolved at RT for 5 to 10 min in 50–200 μl distilled water to reach a final concentration of 1 to 2 μg per μl. RNA was stored at −70 °C.

For Northern blot analyses, total RNA was prepared from three independent experiments. Digoxygenin-labeled RNA probes were synthesized by in vitro transcription using T7 RNA polymerase and appropriate DNA fragments as templates. The DNA fragments were generated by PCR using appropriate primers (supplementary table 1) with chromosomal DNA of *V. vulnificus* CMCP6 as a template. Separation, transfer and detection of RNA were carried out as described previously[45].

Western blot analysis - Polyclonal antibodies against Strep-tagged *Vv*RsbR and *Vv*RsbS were raised in rabbits (Pineda, Berlin, Germany) and affinity- purified using CNBr-activated agarose coupled with the respective target protein.

V. vulnificus cells were re-suspended in 1 ml TE buffer (10 mM Tris/HCl, 1 mM EDTA, pH = 8.0) and disrupted with 0.5 ml glass beads of 0.1 mm diameter in a Precellys 24 (Peqlab, Erlangen, Germany) with two 30 sec cycles at 6800 rpm. To remove glass beads and cell debris the lysate was centrifuged for 15 min at 4 °C and 21,000 *x* g. Afterwards the supernatant was subjected to a second centrifugation step at 4 °C for 10 min at 21,000 *x* g. Protein extracts were stored at −20 °C.

Proteins were separated by 1D SDS-PAGE and transferred to PVDF membranes for 1.5 h at 250 mM and 150 V using standard procedures. *Vv*RsbR and *Vv*RsbS specific sera were used at a 1:5000 and 1:2000 dilution, respectively. Bound anti-*Vv*RsbR and anti-*Vv*RsbS antibodies were detected with a monoclonal alkaline phosphatase conjugated mouse anti-rabbit IgG at 1:200,000 dilution and with NBT and BCIP as substrates.

Co-immunoprecipitation of *Vv*RsbR:*Vv*RsbS. Stationary *V. vulnificus* cells grown in a minimal medium with iron supplement were harvested by centrifugation (10,000 × *g*, RT, 10 min) washed in TE buffer (1 mm EDTA, 10 mM Tris pH = 7.0) and lysed by vigorous agitation in the presence of glass beads (0.1–0.11 mm, Sartorius Stedium Biotech) by two cycles in a Precellys 24 device for 30 s at 6800 rpm (Bertin Technologies) in lysis buffer (1 mM EDTA, 10 mM Tris, 1.0% (v/v) Tween 20). Glass beads and cell debris were removed by two centrifugation steps at 21,000 × *g* at 4 °C for 10 min. The supernatant of the second centrifugation step was used for immuno-precipitation. 0.5 ml of protein solution was mixed with 10 μl *Vv*RsbR antibody (0.5 μg μl^{-1}) and incubated overnight in a rotary shaker at 4 °C. After overnight incubation, protein A coated magnetic beads (Dynabeads, Novex) from 50 μl bead solution were added to the protein antibody mix and incubated for additional 2 h at 4 °C. Beads were collected with help of a magnet and washed three times with 200 μl wash buffer (1x PBS (pH 7.4) and 1% (v/v) Tween 20). The supernatant was stored at −20 °C for further analysis. Antibodies and bound proteins were eluted from the beads by incubation with 20 μl elution buffer (50 mM glycine, pH = 2.8) and 10 μl 3x SDS-PAGE loading buffer for 10 min at 70 °C. Finally, beads were removed by magnetization and the supernatant loaded on a 15% SDS-PAGE for further analysis by Western blotting.

Stressosome mutant construction. In order to study the role of the *V. vulnificus* stressosome in vivo, a knock-out mutant lacking the *Vv*RsbR, *Vv*RsbS, *Vv*RsbT and *Vv*RsbX genes was constructed (*V. vulnificus ΔRSBRSTX*). The synthetic knockout allele (Eurofins) had a deletion from nucleotide 4 of *Vv*RsbR to nucleotide 577 of *Vv*RsbX and was inserted into the pDS132 suicide vector[46] to create plasmid pDS_*ΔRSBRSTX*. The mutagenesis protocol was carried out by bi-parental conjugation of pDS_*ΔRSBRSTX* into *V. vulnificus* CMCP6 and then allowing two consecutive events of homologous recombination. The *E. coli* donor strain chosen for the bi-parental conjugation was β2163[47], auxotrophic for 2,6-Diaminopimelic acid (DAP). *V. vulnificus* CMCP6 and *E. coli* β2163 pDS_*ΔRSBRSTX* were grown overnight at 37 °C in LBN and LB + 25 μg/mL Chloramphenicol + 0.3 mM DAP, respectively. Cultures were washed in LB broth, recipient and donor cells were mixed at a 1:1 ratio (v/v) and spotted onto LB + 0.3 mM DAP agar plates and incubated for 5 h at 37 °C. Chloramphenicol-resistant *V. vulnificus* transconjugants carrying pDS_*ΔRSBRSTX* plasmid name integrated into the chromosome by homologous recombination were selected onto LBN + 5 μg/mL Chloramphenicol. The second event of homologous recombination was triggered by culturing the first recombinant cells in LBN broth without Chloramphenicol. Second recombinant cells were selected onto LBN + 5% sucrose (w/v). Due to the *sacB* gene present in the suicide plasmid, growth in the presence of sucrose can be achieved only after the second event of homologous recombination has efficiently excised the plasmid from the chromosome of *V. vulnificus*. This event can equally generate Wild-Type cells or deletion mutants. To select the stressosome mutant, colonies grown on LBN + 5% sucrose were screened by PCR using *Taq* polymerase (Bioline) and using the primers RSTX_For (5′-GTCACGGGTTGATTGATTCGCAT-3′) and RSTX_Rev (5′-CTCACCGAGACGTAACATATGAATGT-3′), mapping just outside the putative deletion site. The amplification was verified through agarose gel electrophoresis. Two different PCR products, of approximately 300 bp and 2600 bp, were expected for the *ΔRSBRSTX* mutant and WT, respectively. A *ΔRSBRSTX* mutant was selected and the mutation was confirmed through Whole Genome Sequencing (WGS) analysis (MicrobesNG).

Cloning and expression of *V. vulnificus* stressosome proteins. The full-length gene sequences of VvRsbR and VvRsbS were amplified by PCR from genomic DNA of *V. vulnificus* strain CMCP6. In a second PCR, the VvRsbR- and VvRsbS-encoding fragments were fused thereby introducing an additional ribosomal binding site (RBS) between the genes for VvRsbR and VvRsbS. The additional RBS was derived from that found naturally in front of the gene for VvRsbR and necessary to increase heterologous expression of VvRsbS in *E. coli*. The fused DNA fragment was cloned into the BsaI site of pPR-IBA1 (IBA, Göttingen, Germany) yielding pJPF012. For the co-expression of VvRsbR and VvRsbS as untagged proteins, a stop codon was introduced immediately downstream of the VvRsbS coding sequence. For expression and purification of the VvRsbR N-terminal domain the VvRsbR sequence was cloned into pBR-IBA1 using primers that introduced a stop codon within the VvRsbR sequence to yield a construct corresponding to the first 165 amino acids of VvRsbR. All primers are listed in Supplementary Table 1.

For over-expression of *V. vulnificus* stressosome proteins, the plasmid co-expressing *Vv*RsbR and *Vv*RsbS was transformed into *E. coli* TUNER (DE3) cells with ampicillin selection (100 μg ml^{-1}). Transformants were used to inoculate an overnight culture grown at 37 °C and 180 rpm in LB medium supplemented with ampicillin (100 μg ml^{-1}). To start the expression-culture, a two liter Erlenmeyer flask with one liter LB medium supplemented with ampicillin (100 μg ml^{-1}) was inoculated to a starting OD_{600} of 0.05. Cells were grown at 37 °C and 180 rpm overnight without induction. Cells were harvested by centrifugation at 4 °C, for 30 min at 2,130 *x* g and the cell pellet was stored at −80 °C.

For the production of *Vv*RsbR and *Vv*RsbS specific polyclonal sera, the respective full-length sequences were amplified by PCR with primers listed in supplementary table 1 from *V. vulnificus* genomic DNA and cloned as C-terminal Strep-tag fusions into the vector pPR-IBA1 (IBA, Göttingen, Germany) yielding vectors pEB02 and pEB13, respectively. Expression of *Vv*RsbR followed the protocol described above for the expression of the *Vv*Rsb:*Vv*RsbS complex. *Vv*RsbS expressing *E. coli* cells were induced with 1 mM IPTG when the culture reached an OD_{540} of 0.6 and harvested 3 h after induction by centrifugation at 4 °C, for 30 min at 2.130 × *g* and the cell pellet was stored at −20 °C.

Protein purification procedures. The *Vv*RsbR:*Vv*RsbS complex was purified in a three-step procedure. Cells were resuspended in 30 ml low salt buffer (50 mM Tris/HCl, 150 mM NaCl, pH = 8.0) and disrupted by sonication with two cycles of 2 min with a Sonoplus sonicator (Bandelin, Berlin, Germany) with 50 % pulse and 80 % power. Cell debris and insoluble material were pelleted by centrifugation at 34,000 × *g* for 30 min. The cell free extract containing the soluble protein was mixed with solid ammonium sulfate to a final concentration of 15% and incubated for 30 min with stirring at 4 °C. After ammonium sulfate precipitation, the solution was cleared by centrifugation at 34,000 × *g* for 30 min at 4 °C. For further purification, the supernatant containing the *Vv*RsbR:*Vv*RsbS stressosome complex was filtered (0.45 μm) and loaded at a flow-rate of 3 ml min^{-1} onto a Toyopearl Phenyl-650S hydrophobic interaction column (Tosoh, Tokyo, Japan) pre-equilibrated in buffer A (15 % $(NH_4)_2SO_4$, 50 mM Tris/HCl, pH = 8.0). Unbound protein was removed by washing with buffer A, before the column was developed with a 200 ml linear gradient of buffer B (50 mM Tris/HCl, pH = 8.0). Fractions containing the *Vv*RsbR:*Vv*RsbS complex were identified by SDS-PAGE and color

(because of the bound heme), pooled, and concentrated by ultrafiltration with a 30 kDa MWCO centrifugal concentrators (Millipore, Billerica, USA) at 4,000 *x* g and 4 °C before a final purification step by gel filtration chromatography using a HiPrep 16/60 Superdex S-200 column (GE Healthcare). The gel filtration column was pre-equilibrated with running buffer C (150 mM NaCl, 20 mM Tris HCl at pH = 8.0). Fractions of 2 ml were collected at a flow-rate of 1 ml min^{-1}. Fractions containing *Vv*RsbR:*Vv*RsbS were identified by color and stored at 4 °C. Purification of Strep-tagged *Vv*RsbR and *Vv*RsbS using Strep-tag columns was performed according to the protocol of the manufacturer (IBA, Göttingen, Germany).

Measurement of *Vv*RsbR:*Vv*RsbS UV/visible absorption spectra. Purified *Vv*RsbR:*Vv*RsbS complex was diluted to 1.4 µM final concentration in buffer C (150 mM NaCl, 20 mM Tris/HCl at pH = 8.0). Protein concentrations were determined using the Bradford assay. A standard curve using known quantities of bovine serum albumin was generated. The absorption spectra of air-oxidized and dithionite-reduced (0.8 mM final concentration) complexes were recorded with a Biochrom Libra S22 UV/Vis spectrophotometer (Biochrom Ltd.) in a 1 cm path length quartz cuvette in the 250–700 nm range. Measurement of the reduced complex was performed immediately after addition of the reducing agent and 20 minutes later, to re-evaluate the redox state of the sample.

In silico analysis of *V. vulnificus* stressosome proteins. To identify stressosome gene clusters encoding RsbR homologs with an N-terminal globin coupled sensor domain, the *Vv*RsbR (*VV*2_0073) sequence of *V. vulnificus* CMCP6 was used as query in a protein-protein BLAST search (http://blast.ncbi.nlm.nih.gov/Blast.cgi) using default parameters. Hits were checked for the presence of an N-terminal globin coupled sensor domain (Protoglobin, Pfam: PF11563) and a C-terminal Sulfate Transporter and Anti-Sigma factor antagonist (STAS, Pfam: PF01740) domain using the SMART tool for the analysis of protein domain architectures[48]. Next, for protein hits with a Protoglobin-STAS domain architecture, genomic context analyses were manually carried out by inspection of the graphical representation of nucleotide data from the respective bacterial strain at NCBI (http://www.ncbi.nlm.nih.gov/nuccore) to identify complete RST-modules and in addition, to retrieve protein sequences of genes encoded up- and down-stream of the RST-module. Domain composition of all retrieved protein sequences was analyzed with SMART. Sequences were aligned with EXPRESSO[49] and displayed using ESPrit[50]. A manually curated set of bacterial RsbR, RsbS, RsbT and RsbX proteins was used to create a Hidden Markov model for each group and to screen all complete Vibrio proteomes provided by UniProt (release 2021_03) using HMMER (v3.1b2) with an e-value threshold of 1e-10[51,52]. Overlapping hits were resolved based on the model with the more significant e-value.

Proteomic analysis - Cell disruption and protein lysate generation. 16 OD units of cells were harvested by centrifugation, the supernatant was discarded and the resulting pellet was immediately frozen in liquid nitrogen and stored at −80 °C for further preparation. For the cell disruption the pellets were resuspended in 100 µL Tris-HCl 5 mM pH 7.4 containing 5% SDS each and immediately disrupted mechanically using in the Dismembrator/Retsch (ball mill) for 3 min at 2600 rpm (in a 4,8 ml Teflon vessel on liquid nitrogen with an 8 mm diameter steel ball). The cell powder was resuspended with 400 µl of preheated (95 °C) Tris-HCl buffer (5 mM pH 7.4) and the viscous lysate was transferred into a fresh 1.5 mL low bind pre-lubricated Eppendorf tube and shaken for 1 min at 95 °C and 1400 rpm. Then the lysate was cooled to room temperature and 2 µL of a 1 M $MgCl_2$ stock solution (final 4 mM $MgCl_2$) was added. Then 1 µL of a 1:100 diluted benzonase (Pierce Universal Nuclease No#88702) stock solution (final 0.005 U/µL) was added and mixed by short vortexing. The samples were then incubated at room temperature in an ultrasonic bath for 5 min until the viscous lysate was liquefied by complete degradation of DNA and RNA before the raw lysates were centrifuged for 30 min at 17000 g at room temperature. After centrifugation the protein lysate was transferred into a fresh 1.5 mL low bind pre-lubricated Eppendorf tube and the pelleted cell debris was discarded. Protein concentration of the samples was determined using the Micro BCA Protein Assay Kit following the manufacturer's protocol (Pierce, Rockford, IL, USA; prod. No. 23235) using a FLUOstar Omega Plate Reader (BMG Labtech). Samples were always stored at −80 °C. Sample preparation for mass spectrometry measurements was performed using the SP3 protocol as described in Blankenburg et al., 2019[53].

LC-MS analysis. The measurement of samples was performed on a LC-MS/MS platform containing reversed phase nano liquid chromatography (nano Acquity M-class UPLC, Waters corporation) coupled to nano spray ionization tandem mass spectrometry with traveling wave ion mobility using high-definition data independent (HD-MSE) acquisition and enabled with hybrid quadrupole orthogonal acceleration time of flight mass spectrometer (Synapt G2Si, Waters Corporation). The peptide mixture was separated on ACQUITY UPLC® M-Class HSS T3 1.8um, 75um x 200 mm column (Waters Corporation) using mixture of two buffers A and B (Buffer A, 0.1% (v/v) acetic acid in water; Buffer B, 0.1% (v/v) acetic acid in acetonitrile) by formation of a gradient with an increasing concentration of Buffer B at a flow rate of 300 nl/min from 5–26% (v/v) B in 170 min. The eluents sprayed at a voltage of 1.85–1.90 kV using PicoTip emitters (Waters Corporation) while other source parameters (sampling cone 40 V; source off set 80 V; source temperature 800 °C; cone gas 50 l/h; nano gas flow 0.4 bar; and no purge gas) were not changed. The IMS was optimized for wave velocity by ramping with start velocity of 870 m/s to end at 564 m/s that corresponds to separation of GluFib fragments in the drift time range of 0-200 bins. The data acquisition was set up using the program MassLynx™ Software Version V4.1 (Waters Corporation) and it automatically switches between MS and MS/MS (HDMSE) scans that set at scan range 50–2000 m/z were acquired in resolution mode at 20000 with 1 sec scan time. GluFib was injected at an interval of 1 min and was used for calibration. The acquired data was analyzed for protein identifications using the program PLGS v3.3 (Water Corporation) against the FASTA database from Uniprot of *V. vulnificus* CMCP6 strain that contained 4417 sequences, 783 in Swissprot and 3684 in TrEMBL. For spectral processing, low and high energy thresholds of 135, 20 counts and lock mass calibration 785.8456 m/z for GluFib were used. The workflow search parameters contain trypsin as protease, one missed cleavage, carbamidomethyl for cysteine as fixed and oxidation of methionine as variable modifier. The protein quantification was carried out based on the top 3 peptides that had no modifications, pass one match having peptide fragment one and ranked first three highest peptides. The independent identification output by PLGS imported in ISOQuant 1.8[54] for comparison among all samples and quantification was done on proteins that were identified with minimum of two peptides and the protein areas used for subsequent analyses.

Statistics and Reproducibility. The data analysis was performed in R version 4.0.2 using the tidyverse package (version 1.3.0)[55]. Briefly, the IsoQuant protein intensities were median normalized using the global median as reference. The PCA analysis was carried out using the FactoMineR package (version 2.3)[56] with normalized log_2 protein intensities scaled to unit variance. The sample correlation was calculated using Kendalls methodology[57] and displayed using the ggcorrplot package (version 0.1.3)[58]. The statistical analysis was carried out using the PECA package (version 1.24.0)[59] by applying a modified t-test for the pairwise comparisons with proteins having valid protein quantity values in at least 2 replicates, by calculating an empirical Bayes moderated t-statistics using the linear modeling approach implemented in the limma package (version 3.44.3)[60]. The raw p-values (p) were multiple test adjusted (p.fdr) using the Benjamini-Hochberg method[61]. Volcano plots were generated using ggplot2 package (version 3.3.2)[62] with an absolute fold-change cutoff of 1.5 and 0.05 as q-value (adjusted p-value) cutoff. Venn diagrams were drawn using the tool available at: http://bioinformatics.psb.ugent.be/beg/software.

Electron microscopy. For negative stain electron microscopy, 3 µL of the sample were loaded on a freshly glow-discharged, carbon coated grid (400 mesh, SPI Supplies / Structure Probe, Inc). After incubation for 30 sec, excess liquid was blotted away and the sample was stained with 1% Uranyl acetate solution and imaged on a Philips CM120 electron microscope, operated at 120 kV. For vitrification, 3 µL of the purified, oxidized *Vv*RsbRS complex at a concentration of 0.3 mg/mL were applied to glow-discharged Quantifoil holey carbon grids (Quantifoil Micro Tools). The sample was plunge frozen after blotting for 2.5 sec in a Vitrobot at 70% humidity and 10 °C. Grids were immediately transferred to and stored in liquid nitrogen. Cryo-EM data collection was performed manually over multiple sessions on a Tecnai Polara (Thermo Fisher Scientific) cryo-electron microscope (operated at 300 keV), equipped with a Falcon II detector (Thermo Fisher Scientific). Per exposure, 24 subframes were recorded with an exposure time of 1.5 s and an electron dose of 3 $e^-/Å^2$ per subframe. The target defocus range was −1.7 to −5.5 µm. The dataset was recorded at a magnification of ×59,000, resulting in a pixel size of 1.77 Å/px on the sample level.

Unless stated differently, single particle cryo-EM data analysis was performed using RELION-1.4 and RELION-2[63]. Global motion correction was performed in MotionCor[64]. CTF was estimated using CTFFIND4.1[65]. Autopicking yielded a total of 230,784 particles. After multiple rounds of 2D classification and thorough visual inspection of the remaining particles, a subset of 35,647 particles was used for further analyses. Initial models were created by RELION from the data themselves, or obtained from published structures (EMDB-ID 1555). A first 3D refinement was calculated applying icosahedral symmetry. Relion_project was used to calculate random projections from the 3D reconstruction; subsequently, 2D classification was used to obtain a more robust visualization of the most prominent views. A comparison of *Vv*RsbRS 2D class averages and the class averages of the projections revealed significant inconsistencies. Icosahedral symmetry was therefore excluded for *Vv*RsbRS. Eigenimages were calculated from a random subset of particles by SPIDER – PCA using 25 Eigenvectors[66], following the Scipion MDA Workflow[67]. The ten first Eigenimages revealed the presence of 2fold, 3fold and 5fold symmetry in the dataset. Consequently, ten initial models representing different variations of these symmetry groups were created. For supervised multi-reference 3D classification (using 10 classes and C1 symmetry), a.star file[38] pointing to the locations of the initial models was provided as a reference. The resulting distribution of particles in the ten 3D classes showed a strong preference for twofold symmetric classes; higher-symmetry classes were not populated. The final 3D reconstructions were therefore performed applying D2 point group symmetry. Subsequently, to improve the alignment of the STAS-domain core, the regions

containing the sensory domains were masked out and a reconstruction of the core was obtained.

Homology modeling of the *Vv*RsbR2 and *Vv*RsbS2 dimers and model building of the *Vv*RsbR:*Vv*RsbS stressosome complex. Homology detection was performed by HHblits[68] using the query sequences of *Vv*RsbR and *Vv*RsbS separately. The HMM database pdb70 was chosen to search and build multiple query-template alignments. The secondary structure of the query was predicted by PSIPRED and subsequently compared to the actual secondary structure of the database templates. The secondary structure similarity score was used to enhance the alignment quality. A local alignment mode was used to identify remote homologs sharing only a common core, revealing the query and template belonged to the same protein superfamily. Concerning the *Vv*RsbS STAS domain (made up of 115 residues), the HHblits search yielded the RSBS anti-sigma-factor antagonist from *Moorella thermoacetica* (pdb id 3ZXN, DOI:10.2210/pdb3zxn/pdb)[69] as the best candidate to generate a suitable homology model (sequence identity 25%). It was selected due to its high experimental resolution (1.9 Å). The secondary structure score was 14.9, the aligned columns were 115 (no gaps), and the sequence similarity was 0.525. The template sequence is 123 amino acids long, whose first 115 have been used in the alignment with the target. The homologous search of the *Vv*RsbR STAS domain (113 residues) led to the same template detection, suggesting 3ZXN as the most promising one (sequence identity 22%). The secondary structure score was 13.6, the aligned columns were 111 (with initial and final gaps) and the sequence similarity was 0.425. Residues 7 to 117 were used for alignment with the target sequence. Both *Vv*RsbR and *Vv*RsbS were assembled as dimers, in accordance to the template and to the map, using the CHIMERA program. The *Vv*RsbR N-terminal domain (composed of 138 amino acids) was modeled using the globin coupled sensor from *Geobacter sulfurreducens* (pdb id 2W31, DOI: 10.2210/pdb2w31/pdb) as a template, with an experimental resolution of 1.5Å[70]. It shows a sequence identity of 21%, secondary structure score of 118.0 and a sequence similarity of 0.392 with 138 aligned columns (no gaps). The template sequence has a length of 162 amino acids, and those in the range from 13 to 150 were used in the alignment with the target sequence. The linker helix connecting the *Vv*RsbR N-terminus with the C-terminal STAS domain was modeled as a poly-Alanine helix made up of 20 amino acids. It was built using the COOT program[71] and fitted as a dimer into the density map using the FLEX-EM[72] method of the MODELLER program[73]. The three components of *Vv*RsbR (N-terminal sensor domain, linker helix and STAS domain) were assembled in a final, complete $VvRsbR_2$ dimer, fitted into the cryo-EM density map and refined by using phenix.real_space_refine without imposing constraints[74]. The *Vv*RsbS dimer was also fitted into the map. Fitting was performed initially by CHIMERA[75] and then adjusted by FLEX-EM. Copies of the $VvRsbR_2$ and $VvRsbS_2$ dimers were generated and fitted into the asymmetric cryo-EM density map. These global fittings were initially guided by CHIMERA and then refined by phenix.real_space_refine[74].

Reporting summary. Further information on research design is available in the Nature Research Reporting Summary linked to this article.

Data availability

Proteomic data that support the findings of this study are available at MASSive with accession: MSV000087636. The structural data presented in this manuscript has been deposited in the wwPDB with the ID 7O01. The corresponding EM map can be found in the EMDB under the code EMD-12676. Availability of source data is as follows: Fig. 1a, b and supplementary Fig. 5b (Supplementary data 1), proteomic data shown in Supplementary Fig. 5c (Supplementary Data 2) and Fig. 5d (Supplementary Data 3 and 4). The occurrence of stressosome gene clusters in the genus *Vibrio* is summarized in supplementary data 5. All other data are available from the corresponding author on reasonable request. The uncropped blots for Figs. 1d and 2d are presented in Supplementary Fig. 18.

Received: 27 May 2021; Accepted: 31 May 2022;
Published online: 27 June 2022

References

1. Delumeau, O., Chen, C. C., Murray, J. W., Yudkin, M. D. & Lewis, R. J. High-molecular-weight complexes of RsbR and paralogues in the environmental signaling pathway of Bacillus subtilis. *J. Bacteriol.* **188**, 7885–7892 (2006).
2. Kim, T. J., Gaidenko, T. A. & Price, C. W. A multicomponent protein complex mediates environmental stress signaling in Bacillus subtilis. *J. Mol. Biol.* **341**, 135–150 (2004).
3. Chen, C. C., Lewis, R. J., Harris, R., Yudkin, M. D. & Delumeau, O. A supramolecular complex in the environmental stress signalling pathway of Bacillus subtilis. *Mol. Microbiol* **49**, 1657–1669 (2003).
4. Akbar, S. et al. New family of regulators in the environmental signaling pathway which activates the general stress transcription factor σB of Bacillus subtilis. *J. Bacteriol.* **183**, 1329–1338 (2001).
5. Marles-Wright, J. et al. Molecular architecture of the 'stressosome,' a signal integration and transduction hub. *Science* **322**, 92–96 (2008).
6. Kwon, E. et al. Structural insights into stressosome assembly. *IUCrJ* **6**, 938–947 (2019).
7. Murray, J. W., Delumeau, O. & Lewis, R. J. Structure of a nonheme globin in environmental stress signaling. *Proc. Natl Acad. Sci. USA* **102**, 17320–17325 (2005).
8. Gaidenko, T. A., Kim, T. J., Weigel, A. L., Brody, M. S. & Price, C. W. The blue-light receptor YtvA acts in the environmental stress signaling pathway of Bacillus subtilis. *J. Bacteriol.* **188**, 6387–6395 (2006).
9. Gaidenko, T. A., Bie, X., Baldwin, E. P. & Price, C. W. Substitutions in the presumed sensing domain of the Bacillus subtilis stressosome affect its basal output but not response to environmental signals. *J. Bacteriol.* **193**, 3588–3597 (2011).
10. Ávila-Pérez, M., Hellingwerf, K. J. & Kort, R. Blue light activates the σB-dependent stress response of Bacillus subtilis via YtvA. *J. Bacteriol.* **188**, 6411–6414 (2006).
11. Yang, X., Kang, C. M., Brody, M. S. & Price, C. W. Opposing pairs of serine protein kinases and phosphatases transmit signals of environmental stress to activate a bacterial transcription factor. *Genes Dev.* **10**, 2265–2275 (1996).
12. Gaidenko, T. A., Yang, X., Lee, Y. M. & Price, C. W. Threonine phosphorylation of modulator protein RsbR governs its ability to regulate a serine kinase in the environmental stress signaling pathway of Bacillus subtilis. *J. Mol. Biol.* **288**, 29–39 (1999).
13. Chen, C. C., Yudkin, M. D. & Delumeau, O. Phosphorylation and RsbX-dependent dephosphorylation of RsbR in the RsbR-RsbS complex of Bacillus subtilis. *J. Bacteriol.* **186**, 6830–6836 (2004).
14. Kim, T. J., Gaidenko, T. A. & Price, C. W. In vivo phosphorylation of partner switching regulators correlates with stress transmission in the environmental signaling pathway of Bacillus subtilis. *J. Bacteriol.* **186**, 6124–6132 (2004).
15. Eymann, C. et al. In vivo phosphorylation patterns of key stressosome proteins define a second feedback loop that limits activation of Bacillus subtilis σB. *Mol. Microbiol* **80**, 798–810 (2011).
16. Petersohn, A. et al. Identification of σ(B)-dependent genes in Bacillus subtilis using a promoter consensus-directed search and oligonucleotide hybridization. *J. Bacteriol.* **181**, 5718–5724 (1999).
17. Price, C. W. et al. Genome-wide analysis of the general stress response in Bacillus subtilis. *Mol. Microbiol* **41**, 757–774 (2001).
18. Kang, C. M., Vijay, K. & Price, C. W. Serine kinase activity of a Bacillus subtilis switch protein is required to transduce environmental stress signals but not to activate its target PP2C phosphatase. *Mol. Microbiol* **30**, 189–196 (1998).
19. Hardwick, S. W. et al. Structural and functional characterization of partner switching regulating the environmental stress response in Bacillus subtilis. *J. Biol. Chem.* **282**, 11562–11572 (2007).
20. Delumeau, O. et al. Functional and structural characterization of RsbU, a stress signaling protein phosphatase 2C. *J. Biol. Chem.* **279**, 40927–40937 (2004).
21. Williams, A. H. et al. The cryo-electron microscopy supramolecular structure of the bacterial stressosome unveils its mechanism of activation. *Nat. Commun.* **10**, 3005 (2019).
22. Pané-Farré, J., Lewis, R. J. & Stülke, J. The RsbRST stress module in bacteria: a signalling system that may interact with different output modules. *J. Mol. Microbiol. Biotechnol.* **9**, 65–76 (2005).
23. Pané-Farré, J., Quin, M. B., Lewis, R. J. & Marles-Wright, J. Structure and function of the stressosome signalling hub. *Subcell. Biochem* **83**, 1–41 (2017).
24. Williams, T. C., Blackman, E. R., Morrison, S. S., Gibas, C. J. & Oliver, J. D. Transcriptome sequencing reveals the virulence and environmental genetic programs of vibrio vulnificus exposed to host and estuarine conditions. *PLoS One* **9**, e114376 (2014).
25. Oliver, J. D. Vibrio vulnificus: death on the half shell. a personal journey with the pathogen and its ecology. *Microb. Ecol.* **65**, 793–799 (2013).
26. Morrison, S. S. et al. Pyrosequencing-based comparative genome analysis of vibrio vulnificus environmental isolates. *PLoS One* **7**, e37553 (2012).
27. Phippen, B. L. & Oliver, J. D. Impact of hypoxia on gene expression patterns by the human pathogen, Vibrio vulnificus, and bacterial community composition in a North Carolina estuary. *GeoHealth* **1**, 37–50 (2017).
28. Kimes, N. E. et al. Temperature regulation of virulence factors in the pathogen Vibrio coralliilyticus. *ISME J.* **6**, 835–846 (2012).
29. Goudenège, D. et al. Comparative genomics of pathogenic lineages of Vibrio nigripulchritudo identifies virulence-associated traits. *ISME J.* **7**, 1985–1996 (2013).
30. Jia, X., Wang, J., Rivera, S., Duong, D. & Weinert, E. E. An O2-sensing stressosome from a Gram-negative bacterium. *Nat. Commun.* **7**, 12381 (2016).

31. Thompson, F. L. et al. Vibrio neptunius sp. nov., Vibrio brasiliensis sp.nov. and Vibrio xuii sp. nov., isolated from the marine aquaculture environment(bivalves, fish, rotifers and shrimps. *Int. J. Syst. Evol. Microbiol* **53**, 245–252 (2003).
32. Reeves, A., Martinez, L. & Haldenwang, W. Expression of, and in vivo stressosome formation by, single members of the RsbR protein family in Bacillus subtilis. *Microbiology* **156**, 990–998 (2010).
33. Karimova, G., Pidoux, J., Ullmann, A. & Ladant, D. A bacterial two-hybrid system based on a reconstituted signal transduction pathway. *Proc. Natl Acad. Sci. USA* **95**, 5752–5756 (1998).
34. Walker, J. A., Rivera, S. & Weinert, E. E. Mechanism and role of globin-coupled sensor signalling. *Adv. Microb. Physiol.* **71**, 133–169 (2017).
35. Wen, Y., Kim, I. H., Son, J.-S., Lee, B.-H. & Kim, K.-S. Iron and quorum sensing coordinately regulate the expression of vulnibactin biosynthesis in Vibrio vulnificus. *J. Biol. Chem.* **287**, 26727–26739 (2012).
36. Boël, G. et al. The ABC-F protein EttA gates ribosome entry into the translation elongation cycle. *Nat. Struct. Mol. Biol.* **21**, 143–151 (2014).
37. Campbell, E. A. et al. Crystal structure of the Bacillus stearothermophilus anti-σ factor SpoIIAB with the sporulation σ factor σF. *Cell* **108**, 795–807 (2002).
38. Ramesh, M. et al. Intracellular localization of the mycobacterial stressosome complex. *Sci. Rep.* **11**, 10060 (2021).
39. Pettersson, B. M. F. et al. Identification and expression of stressosomal proteins in Mycobacterium marinum under various growth and stress conditions. *FEMS Microbiol. Lett.* **342**, 98–105 (2013).
40. Musa, Y. R. et al. Dynamic protein phosphorylation during the growth of Xanthomonas campestris pv. campestris B100 revealed by a gel-based proteomics approach. *J. Biotechnol.* **167**, 111–122 (2013).
41. Oliver, J. D. The Biology of Vibrio vulnificus. *Microbiol. Spectr.* **3**, VE-0001-2014 (2015).
42. Tohidifar, P. et al. The Unconventional Cytoplasmic Sensing Mechanism for Ethanol Chemotaxis in Bacillus subtilis. *MBio* **11**, e02177-20 (2020).
43. Zhang, W. & Phillips, G. N. Structure of the oxygen sensor in Bacillus subtilis: signal transduction of chemotaxis by control of symmetry. *Structure* **11**, 1097–1110 (2003).
44. Kim, Y. R. et al. Characterization and pathogenic significance of Vibrio vulnificus antigens preferentially expressed in septicemic patients. *Infect. Immun.* **71**, 5461–5471 (2003).
45. Fuchs, S., Pané-Farré, J., Kohler, C., Hecker, M. & Engelmann, S. Anaerobic gene expression in Staphylococcus aureus. *J. Bacteriol.* **189**, 4275–4289 (2007).
46. Philippe, N., Alcaraz, J. P., Coursange, E., Geiselmann, J. & Schneider, D. Improvement of pCVD442, a suicide plasmid for gene allele exchange in bacteria. *Plasmid* **51**, 246–255 (2004).
47. Demarre, G. et al. A new family of mobilizable suicide plasmids based on broad host range R388 plasmid (IncW) and RP4 plasmid (IncPα) conjugative machineries and their cognate Escherichia coli host strains. *Res. Microbiol.* **156**, 245–255 (2005).
48. Letunic, I., Doerks, T. & Bork, P. SMART: Recent updates, new developments and status in 2015. *Nucleic Acids Res* **43**, D257–D260 (2015).
49. Armougom, F. et al. Expresso: automatic incorporation of structural information in multiple sequence alignments using 3D-Coffee. *Nucleic Acids Res* **34**, W604–W608 (2006).
50. Robert, X. & Gouet, P. Deciphering key features in protein structures with the new ENDscript server. *Nucleic Acids Res* **42**, W320–W324 (2014).
51. Eddy, S. R. Accelerated Profile HMM Searches. *PLoS Comput. Biol.* **7**, e1002195 (2011).
52. UniProt Consortium. UniProt: the universal protein knowledgebase in 2021. *Nucleic Acids Res* **49**, D480–D489 (2021).
53. Blankenburg, S. et al. Improving Proteome Coverage for Small Sample Amounts: An Advanced Method for Proteomics Approaches with Low Bacterial Cell Numbers. *Proteomics* **19**, e1900192 (2019).
54. Distler, U. et al. Drift time-specific collision energies enable deep-coverage data-independent acquisition proteomics. *Nat. Methods* **11**, 167–170 (2014).
55. Wickham, H. et al. Welcome to the Tidyverse. *J. Open Source Softw.* **4**, 1686 (2019).
56. Lê, S., Josse, J. & Husson, F. FactoMineR: An R Package for Multivariate Analysis. *J. Stat. Softw.* **25**, (2008).
57. Kendall, M. G. A New Measure of Rank Correlation. *Biometrika* **30**, 81 (1938).
58. Gómez-Rubio, V. ggplot2 - Elegant Graphics for Data Analysis (2nd Edition). *J. Stat. Softw.* **77**, (2017).
59. Suomi, T. & Elo, L. L. Accurate Detection of Differential Expression and Splicing Using Low-Level Features. *Methods Mol. Biol.* **1507**, 141–151 (2017).
60. Ritchie, M. E. et al. limma powers differential expression analyses for RNA-sequencing and microarray studies. *Nucleic Acids Res* **43**, e47 (2015).
61. Benjamini, Y. & Hochberg, Y. Controlling the False Discovery Rate: A Practical and Powerful Approach to Multiple. *Test. J. R. Stat. Soc. Ser. B* **57**, 289–300 (1995).
62. Wickham, H. *ggplot2 -Positioning Elegant Graphics for Data Analysis. Springer* (2016).
63. Scheres, S. H. W. RELION: Implementation of a Bayesian approach to cryo-EM structure determination. *J. Struct. Biol.* **180**, 519–530 (2012).
64. Zheng, S. Q. et al. MotionCor2: anisotropic correction of beam-induced motion for improved cryo-electron microscopy. *Nat. Methods* **14**, 331–332 (2017).
65. Rohou, A. & Grigorieff, N. CTFFIND4: Fast and accurate defocus estimation from electron micrographs. *J. Struct. Biol.* **192**, 216–221 (2015).
66. Frank, J. et al. SPIDER and WEB: Processing and visualization of images in 3D electron microscopy and related fields. *J. Struct. Biol.* **116**, 190–199 (1996).
67. de la Rosa-Trevín, J. M. et al. Scipion: A software framework toward integration, reproducibility and validation in 3D electron microscopy. *J. Struct. Biol.* **195**, 93–99 (2016).
68. Remmert, M., Biegert, A., Hauser, A. & Söding, J. HHblits: Lightning-fast iterative protein sequence searching by HMM-HMM alignment. *Nat. Methods* **9**, 173–175 (2012).
69. Quin, M. B. et al. The bacterial stressosome: A modular system that has been adapted to control secondary messenger signaling. *Structure* **20**, 350–363 (2012).
70. Pesce, A. et al. HisE11 and HisF8 Provide Bis-histidyl heme hexa-coordination in the globin domain of geobacter sulfurreducens globin-coupled sensor. *J. Mol. Biol.* **386**, 246–260 (2009).
71. Emsley, P., Lohkamp, B., Scott, W. G. & Cowtan, K. Features and development of Coot. *Acta Crystallogr. D. Biol. Crystallogr.* **66**, 486–501 (2010).
72. Topf, M. et al. Protein structure fitting and refinement guided by Cryo-EM density. *Structure* **16**, 295–307 (2008).
73. Webb, B. & Sali, A. Comparative protein structure modeling using MODELLER. *Curr. Protoc. Bioinforma.* **54**, 5.6.1–5.6.37 (2016).
74. Afonine, P. V. et al. Real-space refinement in PHENIX for cryo-EM and crystallography. *Acta Crystallogr. Sect. D., Struct. Biol.* **74**, 531–544 (2018).
75. Pettersen, E. F. et al. UCSF Chimera-a visualization system for exploratory research and analysis. *J. Comput. Chem.* **25**, 1605–1612 (2004).

Acknowledgements

This project has received funding from the European Union's Horizon 2020 research and innovation program under the Marie Skłodowska-Curie grant agreement No 721456 to AB, JM-W, RJL, CZ and JP-F, and was supported by a starting grant of the University of Greifswald to JP-F. RJL and JM-W thank the UK BBRSC for funding (BB/G001553/1). We thank Alejandro F. Alice and Jorge H. Crosa (Oregon Health & Science University, Portland) for kindly providing *V. vulnificus* CMCP6. We also thank Christoph Ruess for help with experiments and Michael Hecker and Susanne Engelmann for continuous support and fruitful discussions. Genome sequencing was provided by MicrobesNG (http://www.microbesng.uk) which is supported by the BBSRC (grant number BB/L024209/1).

Author contributions

A.B., R.J.L., J.M.-W., J.P.-F., and C.Z., designed this study and the experiments. Performed experiments, analyzed and visualized the data - *V. vulnificus* experiments: M.C., L.C., A.G., P.B., and J.P.-F.; stressosome biochemistry and cryo-EM: G.B., V.H., W.J., S.K., J.R.L., M.G.M., J.M.-W., J.P.-F., and C.Z.; proteome analysis: K.R., V.M.D., M.L., S.M., J.P.-F., A.R., and U.V.; drafted and edited manuscript V.H., G.B., R.J.L., J.M.-W., J.P.-F., and C.Z. All authors discussed the results and commented on the manuscript.

Funding

Open Access funding enabled and organized by Projekt DEAL.

Competing interests

The authors declare no competing interests.

Additional information

Supplementary information The online version contains supplementary material available at https://doi.org/10.1038/s42003-022-03548-w.

Correspondence and requests for materials should be addressed to Christine Ziegler or Jan Pané-Farré.

Peer review information *Communications Biology* thanks the anonymous reviewers for their contribution to the peer review of this work. Primary Handling Editors: Joanna Timmins, Anam Akhtar and George Inglis. Peer reviewer reports are available.

IX. Preprint 1

The preprint (including supplementary information) can be found at https://www.biorxiv.org/content/10.1101/2022.06.02.493408v1.

Osmotic stress response in BetP: How lipids and K^+ team up to overcome downregulation

Veronika Heinz[1,±], Günnur Güler[2,±], Vanessa Leone[3], M. Gregor Madej[1], Stanislav Maksimov[4], Rebecca M. Gärtner[1], Olga Rudi[1], Farzad Hamdi[5], Panagiotis L. Kastritis[5], Werner Mäntele[6], Reinhard Krämer[4], Lucy R. Forrest[3], Camilo Perez[7#], and Christine Ziegler[1,#]

Affiliations

[1] Department for Structural Biology/Biophysics II, University of Regensburg, Regensburg, Germany

[2] Department of Physics, Izmir Institute of Technology, Izmir, Turkey

[3] National Institute of Neurological Disorders and Stroke, National Institutes of Health, Bethesda, MD, USA

[4] Institute of Biochemistry, University of Cologne, Cologne, Germany

[5] Interdisciplinary Research Center HALOmem & Institute of Biochemistry and Biotechnology, Martin Luther University Halle-Wittenberg, Biocenter, Halle/Saale, Germany

[6]Institute for Biophysics, Johann Wolfgang Goethe-University Frankfurt, Frankfurt am Main, Germany

[7] Biozentrum, University of Basel, Basel, Switzerland

[±] have contributed equally to this work

[#] to whom correspondence should be addressed

Christine.Ziegler@ur.de

Camilo.perez@unibas.ch

Key words

Osmoregulation, protein structure, lipid-protein interactions, CryoEM, FTIR, cardiolipin, curvature stress, membrane transport

Abstract

The trimeric betaine symporter BetP senses an osmotic upshift via its osmosensory C-terminal domain and responds rapidly with a steep increase in transport rate. Full activation requires both an elevated internal K^+ concentration and a yet unknown membrane stimulus. Moreover, the molecular mechanisms of stress sensing and upregulation remain unclear. Here, we show that K^+ binding to BetP *in vivo* is highly cooperative. Using X-ray crystallography, we identify four putative K^+ interaction sites at the C-terminal domains of BetP. Single particle CryoEM on BetP reconstituted in amphipols (AMP-BetP), in the absence of K^+, revealed that the three C-terminal domains are oriented symmetrically near the membrane surface, representing a new downregulated state. The presence of K^+ resulted in asymmetric partial unfolding of the C-terminal domains, which was assigned as an intermediate between the downregulated state and the conformation observed in crystal structures. Attenuated total reflection Fourier transform infrared (ATR-FTIR) spectroscopy in 2D crystals of BetP reveal glutamate/aspartate and tyrosine responses to K^+, in agreement with the identified K^+ interaction sites, as well as specific unfolding events in the C-terminal domain upon activation. A rearrangement of the relative protomer orientations confers upregulation through key structural elements involved in the alternating access of BetP affecting sodium and betaine binding affinities. Although K^+-specific regulation is unique to BetP we discuss unfolding/refolding of sensory domains as a unifying element in hyperosmotic stress response of osmoregulated transporters.

Introduction

The sodium-coupled betaine symporter BetP from the soil bacterium *Corynebacterium glutamicum* is a prime example of a lipid-dependent osmotic stress regulated membrane transporter [1]. BetP transports betaine with high specificity, which under hyperosmotic conditions is accumulated in molar amounts against the concentration gradient into the cytoplasm [2]. The transporter exploits the inward directed sodium gradient across the membrane to energize betaine transport in a stoichiometry of 2 Na^+:1 betaine [3]. It is assumed that BetP senses changes of the physical state of the membrane via its C-terminal domain [1, 4, 5]. Biochemical data suggested that the sensory domain is attached at the membrane surface when BetP is downregulated in the absence of stress [6, 7] and that these specific lipid interactions are released when BetP perceives a stress signal via the membrane [8, 9]. Activation can be partially achieved by increasing K^+ concentrations in proteoliposomes [4, 10], but notably, K^+ alone – i.e., in the absence of the membrane stimulus – is not able to fully activate BetP [7]. *Vice versa*, full transport activity cannot be reached by the membrane stimulus alone [5, 7]. The biochemical properties of the C-terminal domain(s) have been studied extensively during the past decades and it was shown that osmo-stress regulation of BetP is strongly dependent on the helical folding of this osmosensory domain [7, 11]. Transport regulation triggered by hyperosmotic stress was seen in other transporters such as OpuA, a type I ABC importer, which was shown to be gated by ionic strength and inhibited by the second messenger cyclic-di-AMP [12, 13]. The specific requirement of potassium ions during activation and the characteristic helical C-terminal domain was, however, only observed in BetP [7]. In several crystal structures [2, 14-17] BetP appears as a trimer with each protomer in a different conformational state and each osmosensor exhibiting a different degree of helical folding (**Fig. S1**). Consistently, only one of the C-terminal domains, the one involved in crystal contacts, formed a straight alpha-helix. This domain was maximally resolved to Arg586, exhibiting two segments (HC1: Glu552 – Arg568 and HC2: Glu570 – Arg595) separated by an unwound region (**Fig. S1,** chain A). The other two C-terminal domains were resolved in most structures at most to Arg568 and at least to Glu552, respectively. Aside from several arginine residues in HC1 and HC2, Tyr550 in the short linker loop between TM12 and HC1, and Glu572 in HC2 are essential for osmosensing [7]. It was suggested that having positively charged residues in HC1 and HC2 is key to the lipid-dependent down-regulation in BetP. The membrane of *C. glutamicum* consists entirely of negatively charged lipids, with phosphatidylglycerol (PG) and cardiolipin (CL) together contributing nearly 70%. The osmotic activation threshold, directly dependent on the amount of negatively charged lipids in the membrane, shifts to lower osmolalities when BetP is expressed in *E. coli*, which comprises ~70% neutral lipids. Although BetP retains up to eight PG lipids bound mainly in the hydrophobic cavity in the trimer centre none of the C-terminal domains in crystal structures adopts a conformation approaching the membrane; in fact, all three C-terminal helices are pointing around 30° away from the membrane plane. To date, it has not been possible to assign a specific activation state to the crystal structures, and consequently neither a molecular mechanism for stress sensing nor activation could be deduced for BetP.

Here, we present X-ray and Cryo-EM BetP structures in complex with K^+, which allow us to unambiguously assign down-regulated and activated conformations for BetP. By using a combination of functional, structural, spectroscopic, and computational studies, we pinpoint the pivotal role of lipids and K^+ in downregulation and identify unfolding-refolding of the osmosensory C-terminal domain as a key element to overcome

downregulation in response to elevated K^+ concentrations.

Results

K^+ binds to multiple sites in BetP – Regulation of transport activity of BetP as a function of the luminal K^+ concentration was measured under both *in vivo* (*C. glutamicum* cells) and *in vitro* conditions (*E. coli* lipid proteoliposomes) and found to be highly cooperative (**Fig. 1**). The *in vivo* analysis is limited to *C. glutamicum* cells, since only this organism can be grown under extremely low internal potassium concentrations, which is an experimental prerequisite for this investigation [18]. Hill coefficients for K^+ dependent activation were directly deduced from Fig.1 resulting in n = 4.9 ± 0.2 and 5.2 ± 0.2 in *C. glutamicum* cells and proteoliposomes, respectively, suggesting the presence of cooperative K^+ binding in BetP during activation. The corresponding half-activation constants for K^+ were 220 ± 14 mM and 242 ± 15 mM in *C. glutamicum* cells and proteoliposomes, respectively. We therefore considered the K_d as a threshold of activation for subsequent structural and spectroscopic studies. To further characterize the nature of cooperative K^+ binding, we co-crystallized BetP with the K^+ mimic Rb^+.

BetP co-crystallization with Rb^+ – Activation of BetP can also be achieved by Rb^+ and Cs^+ [10]. Rb^+ has a comparable ionic radius (r) to that of K^+ (r^{Rb+} = 166 pm; r^{K+} = 152 pm), so a similar coordination of Rb^+ and K^+ ions in BetP can be assumed. Therefore, we co-crystallized BetP with the K^+ analogue Rb^+ [19, 20] to trace protein-K^+ interaction-sites via anomalous Rb^+ scattering. According to our *in vivo* cooperativity measurements, we used 300 mM K^+ (Rb^+) for co-crystallization, which would be above the K_d in the presence of 1 mM betaine. We solved the structure of the Rb^+-complexed BetP to a resolution of 3.4 Å (**Fig. 2a**). All three protomers adopt an inward-facing open C_i conformation similar to a structure reported previously [2]. Chain A contains a betaine molecule bound close to the S1 site that is coordinated through cation-π interactions with Trp377 similar to previous structures [15]. The C-terminal domain of chain A is resolved as a straight helix as far as residue Arg584 (**Fig. 2a**) and projects towards chain C, which harbours a citrate buffer molecule in the cytoplasmic pathway. The C-terminal domain of chain C is resolved up to residue Arg568 and pointing towards chain B, which adopts an apo state, i.e., neither substrate nor buffer molecule occupies the intracellular pathway.

Anomalous difference Fourier maps were calculated using the CCP4 program FFT [21] and allowed for an unambiguous assignment of Rb^+ in the crystal structure. Four cytoplasmic Rb^+ ions are observed (**Fig. 2a insets**). Three Rb^+ ions are localized at the interface of the crossing C-terminal domains from chains A and C with the first one coordinated by the carboxyl group of Glu552 from the C-terminal domain of chain C, the main chain carbonyl of Ala561 from the C-terminal domain of chain A, and a hydrated Cl^- ion close to the side chain of Arg210 from chain C. A second Rb^+ ion is coordinated by the hydroxyl group of Thr124 from chain C, a water molecule hydrogen-bonding to the main chain carbonyl, and the side chain of Gln557 from the C-terminal domain of chain A, and the third Rb^+ ion is coordinated by the carbonyl of Thr124 and the hydrated Cl^- ion. A fourth Rb^+ ion is coordinated only by residues located in the C-terminal domain of chain C, including the side chain of Gln557 and the hydroxyl group of Tyr553 (**Fig. 2a insets**). To study the contribution of each site to the osmo-regulation activity profile, we performed alanine replacement of the cytoplasmic side chains involved in the Rb^+ interaction sites (**Fig. 2b**). Alanine mutants of residues Thr124, Arg210, Glu552 and Tyr553 exhibit severely altered responses to osmotic stress. While R210A and E552A are no longer regulated, T124A and Y553A show a slight increase in activity at high

osmolalities. The alanine mutant of Gln557 (**Fig. 3a**) retains the ability to respond to osmotic stress although with a significant shift to higher osmolalities resulting at a reduced transport rate. In summary, almost all mutants of the residues participating in the cytoplasmic Rb^+ interaction sites showed impaired osmo-sensing and/or reaction properties compared to WT BetP. The mutagenesis study confirms the Rb^+-interacting residues are essential for activation and that they are located mainly in HC1. Again, the Rb^+ bound structure shows only very slight deviations from structures determined in the absence of Rb^+ / K^+ (e.g., PDB ID 4C7R) suggesting that the ensembles of C-terminal domains, especially the crossing of C-terminal domains of chain A and chain C in the trimer already represent an active conformation with K^+ interaction sites pre-formed. We investigated the C-terminal domain inter-protomeric interactions by measuring the formation of a crosslink between the C-terminal domain and L2 of adjacent protomers mimicking the interaction between Arg558 and Asp131 observed in crystal structures (**Fig. S1**), as a function of osmotic stress (**Fig. 3b**). First, residues Arg565 and Ile130 were replaced with cysteine; this mutant was expressed in *E. coli* cells and the osmotic profile was measured to test whether its activity could still be osmo-regulated. The BetP-R565C/I130C mutant was also regulated by changes in osmotic stress, although the initial activity measured at 200 mOsmol/kg was ~2.5-fold higher than WT, and the overall increase of activity was only 1.5-fold, compared to ~4-fold for the fully regulated WT BetP (**Fig. 3b**). We compared WT and the cross-linked BetP-I130C/R565C using SDS-PAGE and immunoblotting against the N-terminal strepII tag after the addition of the homo-bifunctional cross-linker o-PDM. There is a significant amount of dimeric cross-linked BetP-I130C/R565C at low osmolalities (**Fig. 3b,** blue square), with limited amounts of trimeric protein, whereas at high osmolality the cross-linked protein exists in both dimeric and trimeric forms (**Fig. 3b,** green square). These results indicate that the interaction between the C-terminal domain of one protomer and L2 of an adjacent protomer at this position is characteristic for an activated state. Therefore, we can conclude that the C-terminal conformations observed in crystal structures with and without K^+ represent an active state. There might be several reasons that a down-regulated state cannot be adopted in crystal structures, such as missing lipids in the detergent micelle or the altered activation profile of the crystallization mutant. However, ionic strength and crowding effects during crystallization could simply prevent downregulated conditions. To test this hypothesis, we performed a CryoEM single particle analysis on WT BetP.

The downregulated state of amphipol-reconstituted BetP by CryoEM – Considering the strong effect of negatively charged lipids on BetP activation we reconstituted WT BetP into amphipol A8-35, which due to its carboxyl-groups provides a negatively charged belt around the BetP trimer (**Fig. S2a**). In comparison to BetP reconstituted in *E. coli* proteoliposomes and POPG-MSP nanodiscs, respectively, amphipol-reconstituted BetP (AMP-BetP) showed comparable sodium-dependent betaine binding (**Fig. S2b, Table S1**). Moreover, binding was responsive to K^+ concentrations (**Fig. S2c, Table S1**) with a similar increase in the Hill coefficient to ~2 as observed for BetP reconstituted in proteoliposomes at elevated K^+ concentrations [22]. CryoEM micrographs of AMP-BetP were collected in the absence of K^+ (**Table S2, Fig S3**). Two distinct populations were identified. The larger class showed all three C-terminal domains resolved to comparable length and arranged symmetrically and parallel to the membrane plane (**Fig. S3 a, d**). The second, significantly smaller 3D class resulted in a 3D volume, in which the C-terminal domains were resolved to Arg568, e.g., only

HC1 was folded (**Fig. S3a**). We also investigated the crystallization mutant of BetP (BetP^{cryst} - ΔN29 E_3 44-46 A_3) reconstituted in amphipol by CryoEM. This mutant displayed a higher conformational heterogeneity in which the dominant class adopted an asymmetric conformation with HC1 folded and HC2 unfolded to different degrees, as in the second class of WT BetP (**Fig. S3a, Fig. S4**). The C-terminal orientations in the CryoEM coulomb potential maps of BetP and BetP^{cryst} were more or less like each other but were distinct from the orientation observed in crystal structures (**Fig. S1**).

The C3 map of the symmetrical class of WT BetP reconstructed to 3.7 Å (**Fig. 4a**) was modeled (**Fig. 4b, Table S4**). All three C-terminal domains in the CryoEM structure are resolved to Ala580 and form a straight helix. The cytoplasmic loops L2 and L8 form two short, anti-parallel beta-strands between residues Ile125 – Leu127 (L2) and Gly391 – Ile394 (L8) (**Fig. S5)**. In comparison to crystal structures, we observe a rigid-body rotation of the C-terminal helix around Asp547 by 50˚ towards the outer rim of the trimer (**Fig. S6a**). Simultaneously, the C-terminal domain is tilted upwards by 10˚ towards the membrane plane (**Fig. S6b**). In this orientation it points towards loop 6 (L6) and TM1 of the adjacent protomer (**Fig. S6c, d**). We analysed whether this orientation leads to persistent contacts during µs-scale molecular dynamics (MD) simulations of the BetP trimer inserted into a POPG lipid membrane. In the simulation initiated with the CryoEM orientation of the protomers, the C-terminal domain forms extensive contacts with the cytoplasmic loops L2, L6, L8 and L10 (**Fig. 76 a, b**). These are in stark contrast with the contacts observed in a simulation initiated with an X-ray structure, where only a handful of the contacts with L2 are similar (**Fig. S7 a, b**). Notably, in the CryoEM structure, the protomer distances within the trimer differ by 2.6 Å with respect to the threefold symmetry axis at the cytoplasmic side in comparison to the X-ray structure (e.g., between C_α of Lys121 in chain A, B and C), resulting in a narrower hydrophobic cavity. TM1, TM6 and TM11 are oriented parallel to the membrane normal, while they are tilted away from the membrane normal in X-ray structures (**Fig. S6b)**. During the MD simulations of the trimer in a POPG environment for both X-ray and CryoEM structures, the interprotomer distances evolve during the simulations (**Fig. S7c, d**), suggesting that the lipid bilayer is less constraining than the amphipol conditions; nevertheless, the trimer remains significantly more constrained and symmetric in the CryoEM-derived conformation than in the X-ray structure.

In summary, we assign the symmetrical trimeric state observed for AMP-BetP as a down-regulated conformation, noting that the wildtype AMP-BetP contains a substantial fraction (24.1%) of trimers that are, according to this definition, not in a down-regulated state (**Fig. S3a**). We assign this population to an active state, similar to other asymmetrical trimeric states, in which C-terminal domains differ in degree of helical folding and/or orientation. Unlike the wild-type protein, BetP^{cryst} does not exhibit any population of the fully symmetrical downregulated state when reconstituted in amphipol, although the HC1 helix of the C-terminal domains lies parallel to the membrane, unlike in the crystal structures (**Fig. S4b**). As BetP^{cryst} is partly N-terminal truncated we suggest that the helical stabilization of HC2 required for the fully-symmetric state is normally facilitated by N-terminal interactions. Therefore, BetP^{cryst} can never be entirely down-regulated, consistent with the altered activation profile of this and other N-terminally truncated mutants [1, 14].

Lipid binding to AMP-BetP – Elongated densities identified as lipids are located in the hydrophobic clefts between the protomers and at the trimer perimeter (**Fig. 4**). The lipid densities were assigned as POPG and cardiolipin (CL), respectively. We also detected a similar density for cardiolipin in AMP-BetP^{cryst} (**Fig. S4b**). A

periplasmic POPG ($POPG^{peri}$) is resolved close to the amphipatic helix h7 at a trimerization contact between Trp101 in TM2 and Leu330 in h7 [23], while a cytoplasmic POPG ($POPG^{cyto}$) is found in the hydrophobic cleft coordinated by Lys121 (L2) and by Arg392 and Arg395 (L8) of the counterclockwise adjacent protomer (**Fig. 4c, d**). The cardiolipin fatty acid chains protrude into the cleft formed between protomers (**Fig. 4b, e**), while the cardiolipin phosphate group is nestled into an arginine-binding pocket formed by Arg554, Arg558, Arg562 and Arg565 in the C-terminal domain and by Arg137 in L2. In addition, cardiolipin interacts with $POPG^{cyto}$ and with hydrophobic residues in TM2/TM12/loop 4 (L4) and TM3/TM9/L2 of the protomers flanking the cleft. Being positioned between the cardiolipin molecule and L2, the C-terminal domain of the clockwise adjacent protomer maintains several ionic interactions starting from Arg554 to Ala580 with L2, which is consistent with peptide binding studies [7] (**Fig. 4e**).

Inward-facing conformation in down-regulated AMP-BetP – All three protomers adopt an apo-inward facing state (C_i^{down}), which compared to those observed in crystal structures (C_i^{cryst}), exhibits differences in TM3, TM7, h7 and the cytoplasmic loops L2, L4, L6, and L8 (**Fig. 5a-c**). Differences in TM7 and h7 are correlated with an interaction between Lys300 in L6 and Glu572 of the C-terminal domain of the clockwise adjacent protomer (**Fig. S6d**). Specifically, L6 is stretched out away from the transporter core affecting the orientation of TM7 and h7. L6 and the cytoplasmic tip of TM7 were already identified as key players in conformational cycling in BetP, but also in other LeuT-fold transporters [24]. Mutation of K300A and G301A resulted in inactive BetP mutants, while BetP E572P lost transport regulation [5]. TM3 is separated by a conserved glycine stretch (G149-M150-G151-I152-G153) into two helical segments ($TM3_a$ and $TM3_b$). In AMP-BetP the cytoplasmic $TM3_a$ exhibits a slightly compressed glycine stretch and Met150 points towards the Trp prism interacting with Trp374 (**Fig. 5c**). This rotamer conformation was not observed in C_i^{cryst}, where the Met150 thioether side chain points towards the hydrophobic cleft formed by TM3 and TM7 interacting with the fatty acid chain of a POPG molecule.

To assess the possibility that these two opposite conformations of Met150 are accessible just by a simple side chain reorientation, we analysed multiple µs-scale MD simulations of the AMP-BetP trimers initiated with the orientation of Met150 observed in a crystal structure in the presence of 100 mM and 300 mM K^+. According to a metric of proximity (see Methods section) between Met150 and either Ala313, Ala408 and Trp412 (in TM3 and TM7, X-ray conformation) or Trp373, Trp374 and Trp377 in the Trp prism (EM conformation), the methionine almost exclusively points away from the Trp prism (**Fig. S8a**), although very rare but reversible transitions toward the Trp prism (e.g., CN(EM) values > 2) are observed. This is notable, given the use of a non-polarizable force field in which methionine-aromatic interactions have not been specifically optimized, and suggests that conformational rearrangements of Met150 in the down-regulated conformation are physiologically meaningful. We then investigated the possibility that the alternate conformation of Met150 depends on the orientation of the C-terminal domain. However, simulations carried out with the C-terminal helix oriented as in the X-ray structures did not cause a rearrangement of Met150 to interact with Trp374 (**Fig. S8b**). In summary, the simulations indicate that conformational rearrangements of Met150 observed in the CryoEM structure under down-regulated conditions are not related to the release of C-terminal domain interactions with cytoplasmic loops. Thus, it is possible that lipid interactions contribute to stabilising the unique side chain conformation of Met150 in the down-regulated AMP-BetP.

CryoEM structure of AMP-BetP in the presence of K^+ – To investigate K^+-induced structural changes of AMP- BetP, a CryoEM dataset was collected in the presence of 200 mM KCl (**Fig. S9a-c**, **Table S2**). The CryoEM coulomb potential map in C1 was reconstructed to 4.3 Å. AMP-BetP in the presence of K^+ lacks C3 symmetry in the C-terminal domains, which all exhibit different lengths and orientations reminiscent of what was observed in crystal structures (**Fig. 6a**). Again, one of the C-terminal domains is helically folded until Ala576, while the C-terminal domains in protomers B and C are only resolved until Asn560 and Arg567, respectively with slightly different orientations to each other. We observed a low-resolution connecting density between the N-terminal domain and the C-terminal domain of the counterclockwise adjacent protomer (**Fig. S9d**). K^+-AMP-BetP bridges between C_i^{down} and C_i^{cryst} adopting an intermediate, transient state C_i^{trans}. Differences are detected in L6, which is no longer interacting with the C-terminal domain. In turn the hairpin TM6 – TM7 is shifted towards the periplasmic side. Compared to protomer A (**Fig. 6c**) the C-terminal domain is folded helically until Arg565 still interacting with the cardiolipin molecule in protomers B and C (**Fig. 6d, e**). Moreover, the C-terminal domain in protomer C exhibits a different orientation more like that in crystal structures, which re-positions cardiolipin away from the membrane plane (**Fig. 6e**), which was not observed in $BetP^{cryst}$ in the absence of K^+ (**Fig. S4b**). Compared to C_i^{down}, C_i^{trans} showed a conformation of the glycine stretch and Met150 like the one in C_i^{cryst} confirming the MD simulation results that in the presence of K^+, the orientation of Met150 away from the Trp prism is stabilized (**Fig. S8).** We therefore assign the inward-facing states observed in K^+-AMP-BetP and in BetP crystal structures as pre-activated states.

Network-analysis of the down-regulated and transient states – Regulation in BetP is linked to the trimeric state. A network analysis was performed to identify global changes in interaction patterns in $C_i^{cryst/trans}$ and C_i^{down} within the trimer (**Fig. S10**). Interactions were classified according to a metric that ranks the impact of a residue by the number of global interactions. We screened specifically for residues that changed their interaction pattern when switching from C_i^{down} to C_i^{cryst} (**Fig. 5d**). We detected changes in the intratrimeric contacts in residues located in the beta-strand in L2, which are highly interactive only in C_i^{down}, while residues located in helix h7 at the periplasmic side of the BetP trimer have increased interaction pattern only in C_i^{cryst} (**Fig. 5e**), consistent with our observation of an altered protomer arrangement in downregulated AMP-BetP. With respect to substrate binding Trp371 and Trp377 are global interactors in C_i^{down}, while Trp373 and Trp189 have a higher interaction score in C_i^{cryst} (**Fig. 5f**). Met150 shows equal impact on the global protein structure in both states, which we see in agreement to the importance of both alternating orientations as discussed before. An interaction network analysis including lipid molecules was performed to identify groups of global interactors with the C-terminal domain. In the C_i^{down} state, two possible scenarios were identified. In the first scenario (**Fig. S11a**) the entire C-terminal domain forms a group with the transporter core of the counterclockwise adjacent protomer, while the cardiolipin lipid is grouped with the protomer providing the C-terminal domain. In the second scenario, cardiolipin is associated with the counterclockwise adjacent protomer, but the C-terminal domain is not. In fact, the C-terminal domain is only grouped until the very first segment (Arg558) with its own protomer (**Fig. S11b**). This pattern of partly grouping with the own protomer is maintained in the C_i^{cryst} (**Fig. S11c, d**) suggesting a switch mechanism of C-terminal domain and lipids in BetP to stabilize the cytoplasmic part of the transporter core. Obviously, if the C-terminal domain is not engaged in intratrimeric interactions, it is not part of the

group, which might cause a destabilization of the helical fold.

K^+ activation of lipid reconstituted BetP investigated by ATR-FTIR – The IR-absorbance spectra in the range 1800-1300 cm^{-1} were recorded from BetP in POPG 2D crystals at different concentrations of K^+ (10 mM to 500 mM). For absorbance difference spectra, data were analysed after subtraction of the IR signal recorded in the absence of K^+ (IR [10-500 mM K^+]-IR [0 K^+]) (**Fig. S12a**). The IR signal was further investigated by calculating the 2nd derivative for peak assignment (**Fig. S12b-d**). As vibration/stretching modes of individual residues and secondary structure elements often overlap in wavenumbers, spectra were taken in H_2O and D_2O, respectively, for unambiguous assignments of band position and band shift. This is necessary especially for the absorption of the H–O–H bending vibration at around 1643 cm^{-1} that superimposes with the amide modes (**Fig. S13a, b**). The deconvoluted bands were investigated for a possible assignment (**Fig. S12c, d**) to lipid C=O modes, to the C=O stretching modes of protonated Asp/Glu, to the Amide I region (i.e., to α-helices, unordered structures and loops), to the antisymmetric and symmetric stretching C-N mode of Arg residues, to the antisymmetric and symmetric stretching modes of deprotonated carboxylate groups for Asp/Glu, and to the C-C ring stretching vibrations of Trp residues and protonated/deprotonated Tyr residues, respectively. Multiple changes were observed in the 2nd derivatives (**Fig. S12b-d**) and in the absorbance difference spectra (**Fig. S13**) from 10 – 200 mM (below the K_d of K^+) and from 250 – 500 mM K^+ (above the K_d of K^+). Analysis of the band shifts in the IR region of 1725 – 1700 cm^{-1}, 1585 – 1565 cm^{-1} and 1390 – 1420 cm^{-1} allowed the assignment of distinct shifts in 1745, 1731, and 1715 cm^{-1}, respectively, to changes in H-bonding of protonated Asp/Glu residues (**Fig. 7a**). Wavenumber shifts increased by ~ 6 – 8 cm^{-1} into saturation until 200 mM, followed by a steep decrease between 200 mM and 300 mM back to their initial peak position. Simultaneously, the IR signals originating from deprotonated Asp/Glu residues show the inverse spectral shift. Especially the negative absorbance between 1600 and 1550 cm^{-1} is an indicator of the population of deprotonated Asp/Glu residues. An increase in the population of stronger H-bonded protonated Asp/Glu side chains is only observed at K^+ concentrations < 200 mM (below the K_d of K^+) (**Fig. 1**), while above those concentrations the IR signal rapidly returns to its initial value. We suggest that Asp/Glu residues reporting changes from downregulated to active state might be transiently engaged in K^+ binding as they return to an initial deprotonated state after full activation. We have identified potential K^+-responsive Asp/Glu residues in the network analysis comparing C_i^{down} and the activated $C_i^{cryst/trans}$ states. Asp470 (TM10), Asp543, and Asp547 (TM12) – all accessible from the cytoplasmic side – are strong interactors in the down-regulated state, while Asp131 exhibits a stronger interaction network in the activated state (**Fig. 7d**). Glu552, which is one of the K^+ coordination sites identified in the Rb^+ bound crystal structure and Glu572 have more interaction impact in the active state, Glu132 and Glu396 in L2 and L8 are more dominant in the downregulated state (**Fig. 7e**). Additional recording of the absorbance differences in D_2O buffer confirms that absorbance differences at 1604 – 1587 cm^{-1} (**Fig. S13b**) can be assigned to the antisymmetric and symmetric stretching C-N mode of arginine, respectively, while absorbance differences at 1704 – 1692 and 1614 – 1611 cm^{-1} (**Fig. S12a**) are unambiguously assigned to the C=O mode and NH_2 bending mode of asparagine, respectively (for band assignments see refs. [25-28]). These findings agree with our observation that the cardiolipin molecule remains bound to the Arg binding pocket and moves together with the C-terminal domain (**Fig. 6c-e**) therefore not contributing to the IR difference spectra. This observation would also agree with the

fact that Arg210, which coordinates K^+ indirectly via the chloride ion, is not affected in its conformation by K^+ titration. In the difference spectra, the C-C ring mode of tyrosine, which is a sensitive protonation reporter group, also responds to a K^+ increase (**Fig. 7b**). There is a distinctive upshift for the C-C mode of protonated Tyr (1516.5 cm^{-1}) with a sudden breakdown after 200 mM K^+, reminiscent of the upshift of protonated Asp/Glu residues. However, the C-C mode changes of deprotonated Tyr (1497 cm^{-1}) respond differently to an increase in K^+: the downshift from 10 – 100 mM K^+ is followed by a lag phase between 100 mM – 200 mM K^+. At 200 mM there is a steep bi-phasic increase, surpassing the initial wavenumber of 1496.8 cm^{-1} and reflecting the osmoregulation profile of BetP. Based also on our mutagenesis study (**Fig. 2b**) we assign Tyr553 as one of the key tyrosine residues to K^+ activation (**Fig. 7f**). While most Tyr exhibiting an altered interaction network are located at the periplasmic side of BetP, Tyr550 which is in the beginning of the C-terminal domain, adjacent to the cardiolipin interaction site is another promising candidate albeit not coordinating K^+ directly. The differences in reporter group response might also suggest an order of events triggered by cooperative K^+ binding. We propose that the first action is a reorientation of the osmosensors from membrane bound to intratrimeric C-terminal interactions followed by a stabilization of the helical fold of the now membrane detached C-terminal domain. This two-step mechanism would involve changes in the helical fold which can be compensated at higher K^+ concentrations.

Unfolding of the osmosensor monitored by ATR-FTIR – The IR-difference spectra recorded both in H_2O and D_2O also revealed indeed changes in protein secondary structure (helix, turn and loop) in response to increasing K^+. Several peak shifts in the range of 1660 – 1630 cm^{-1} indicate a change in H-bonding strengths of ordered secondary structures both for membrane buried and solvated α-helices (**Fig. 7c**). A signal absorbing at 1653.5 cm^{-1} increases after a lag phase at 150 mM K^+ to 1654.5 cm^{-1} and saturates at 300 mM K^+. Reportedly, an α-helix with a high number of residues would absorb around 1653 cm^{-1} in H_2O buffer [29], and an upshift indicates weakening or loss of H-bonding in that helix, e.g., it becomes relatively flexible. The observed increase in helix flexibility matches the increase in deprotonated Tyr residues. Simultaneously, a change in the amount of turns and loops can be assigned to the shift in wavenumbers from 1679.5 cm^{-1} to 1681 cm^{-1}, exhibiting a similar hyperbolic increase as the protonated Asp/Glu residues.

To unambiguously assign the observed changes in helical structure, absorbance difference spectra of the de-regulated mutant BetP ΔC45 missing the entire osmosensory domain were recorded at 200 mM and 500 mM K^+ (**Table S6**). The mutant exhibits minor amide I changes together with very subtle spectral alterations in the region for the protonated (above 1700 cm^{-1}) and deprotonated (1600 – 1550 cm^{-1}) Asp/Glu residues, as compared to WT BetP (**Fig. S14**), suggesting that these residues respond to K^+ also in the absence of the osmosensor. Furthermore, an elevated K^+ concentration leads to increased intermolecular β-sheet formation in the BetP ΔC45 mutant, indicated by a positive 1623 cm^{-1} signal. The secondary structural elements reveal a bi-phasic behaviour, too. While no shifts in the signal positions were detected when comparing secondary structural elements in the absence and presence of 500 mM K^+, there is a significant difference of 2 cm^{-1} at 200 mM K^+ in the signal positions assigned to the conformations of loops/turns and in short and 3_{10}-helices. A new peak appears at 1635 cm^{-1}, both in H_2O and D_2O, which can be assigned to unordered structures, short helices, or solvated loops. This peak is absent in BetP ΔC45 (**Table S5**), suggesting an unfolding event of the C-terminal domain.

Discussion

Accumulation of compatible solutes such as betaine by uptake is in the first line of defense when microorganisms face a hyperosmotic shock. Osmoregulated transporters that can sense the amount of stress and can switch accordingly from low basal transport rate to maximal rate play an essential role in immediate response. The sodium-coupled betaine symporter BetP is a prototype of such transporters, as its activity increases to more than 5-fold of the basal rate within a second [1, 30]. Biochemical data have uncovered an amazing causality between the nature of stress stimuli and transport upregulation in BetP with clear dependences on lipid environment and intracellular conditions. In fact, BetP is one of the best studied transporters for which the role in activation of practically every residue has been investigated over the past 20 years [1, 7]. In addition, multiple structures of BetP adopting individual states of the alternating access cycle describe betaine transport in molecular detail [2, 14-17]. Despite all these structural and functional data, the molecular mechanism of stress sensing and regulation in BetP remained largely unknown, mainly since crystal structures showed the osmosensor only partly resolved and pointing away from the membrane. An unambiguous assignment of the three different C-terminal conformations within one BetP trimer in a crystal structure to inactive/active states was not possible.

The combination of methods used in this study finally allows us to gain molecular insights into a complex interplay of lipids and K^+ ions regulating BetP in response to osmotic stress. Functional data showed high cooperativity of K^+ binding. Structural data obtained from both X-ray crystallography and CryoEM single particle analysis conclusively allowed the assignments of down- and up-regulated states and identified regulatory K^+ interaction sites. MD simulations monitored conformational stability and validated structural states, and finally, FTIR allowed us to probe unfolding events of the terminal domains. From these data a mechanism emerges in which the C-terminal domains undergo a molecular switch to change interaction partners within the trimer. But instead of an anticipated rigid body movement, we observe a sequence of unfolding and folding events of the osmosensory helix controlled by lipids and K^+. Concurrently, BetP protomers in the trimer re-orient themselves in the membrane thereby altering protein-protein and lipid-protein interactions to increase flexibility of helices important in transport. One major lipid interaction, which was not observed in crystal structures is with cardiolipin.

Role of cardiolipin – The cardiolipin observed in AMP-BetP is located in a strategical position coordinated by the C-terminal domain and L2 and its presence is correlated with the orientation of the first helical segment HC1. TM12 and the C-terminal helix are connected by an elbow-like short loop around Tyr550 that needs to be flexed to position the C-terminal helix parallel to the membrane plane. Cardiolipin seems to participate in maintaining the orientation of both the elbow-loop and HC1 in the down-regulated state and enables downstream interactions with cytoplasmic loops that play a role in regulation. HC1 and HC2 folding results in the formation of the extended C-terminal helix reaching the adjacent protomer. Consequently, protomer distances are reduced at the cytoplasmic side when compared to the X-ray structures. It appears as if the C-terminal domain pulls two protomers at the cytoplasmic side closer together. Although the trimer packing is not static in MD simulations of these states, the down-regulated conformation is more compact overall. Specifically, proximity of two protomers facilitates contacts between the C-terminal domain and L6. This small loop is a crucial region for closing the cytoplasmic transport pathway in LeuT fold transporters. From our previous structural work and

mutagenesis studies, we confer this loop controls the isomerization from inward to outward, which in symport is a substrate-free step and therefore relies on a low energy barrier. We speculate that the change in protomer-protomer interaction and protomer orientation at elevated K^+ is one of the parameters involved in a cooperativity between betaine binding sites in adjacent protomers [23].
Notably, the downregulated state was not observed in crystal structures. Moreover, neither was cardiolipin, despite the observed density for a cardiolipin molecule in AMP-BetP^{cryst}. We assume that additional washing steps and detergent exchange to Cymal-5 required for crystallization might be responsible for removal of cardiolipin molecules. Interestingly, HC2 in AMP-BetP^{cryst} was not folded, most likely due to missing interactions with the N-terminal domain and L6. Nevertheless, functional data have shown that even after truncation of HC2 (ΔC25) BetP is still regulated, although not to full activity. Together with the lack of a negatively charged lipid bilayer, including the missing CL, the N-terminal truncation might be one of the reasons why BetP^{cryst} always adopts an active state conformation in crystal structures. We therefore conclude that the downregulated state can be characterized by cardiolipin interacting with HC1 lying parallel to the membrane.

The membrane stimulus – Reconstitution in AMP-nanodiscs, mimicking the negatively charged membrane belt surrounding BetP, is to date the only condition enabling studies of structural changes in the C-terminal domain. Aside of cardiolipin we identified another lipid interaction in down-regulated BetP (**Fig. 8**): POPG bound to the periplasmic side of TM2 and h7 in an extended conformation. The negatively charged, peripheral POPG like cardiolipin is in ideal positions to perceive changes in bulk lipids via lipid-lipid interactions, and to subsequently transmit the stimuli to h7. Notably, POPG and cardiolipin densities observed in the CryoEM data obtained at high K^+ remain in contact with h7 and the C-terminal domain, respectively, thereby moving together with h7 and the C-terminal domain. In the active state POPG changes its conformation (**Fig. 8**, hyperosmotic conditions). Under hyperosmotic stress, we suggest that local changes in lipid packing trigger a movement of both lipids via their interaction with bulk lipids, thereby cause the movement of h7 and the C-terminal domain. Altered bulk lipid-lipid interactions may be the consequence of changes in curvature, lateral pressure, or lipid packing, which would directly impact the hydrophobic mismatch at the periphery of the BetP trimer. Curvature changes might result in a concerted movement of POPG and h7 causing a protomer rearrangement. Changes in both cytoplasmic cardiolipin and periplasmic POPG position might even occur simultaneously according to the amount of stress.

How to overcome down-regulation? – The first step in activation is to overcome down-regulation when the stress signal raises above the activation threshold. For BetP, multiple interactions result in a latch-like locking of one protomer by the neighboring C-terminal domain. A comparison of K^+ complexed CryoEM and X-ray structures suggests that the answer lies in cooperative K^+ binding. In the CryoEM structure recorded below the K_d for K^+, the only interaction site that is available for K^+ binding is the one involving Tyr553 and Gln557. By contrast, in the X-ray structure, at concentrations above the K_d the C-terminal domains cross at the point where K^+ interacts with Thr124 and Arg210. Exactly this switch in interaction – from lipid to C-terminal domain crossing – requires a flexible transition, which we suggest can only be achieved by partial unfolding of the osmosensor. FTIR shows indeed a bi-phasic behavior around the K_d of K^+ regarding protonation/deprotonation states of reporter residues and folding/unfolding events; the latter could be unambiguously assigned to the C-terminal domain by comparison to a C-terminally

truncated mutant (ΔC45). This bi-phasic behavior is mirrored in betaine binding studies showing an increase at 200 mM K^+ for sodium and betaine K_d followed by a decrease at 300 mM K^+ (**Table S1**).

Transport activation – Interactions mediated by cardiolipin with the C-terminal domain affect the conformation of TM3 and L6 between TM6 and TM7. While in most LeuT transporters the first helix of the first repeat swings in and out, in BetP $TM3_a$ moves up and down like a mechanical spring [15]. This contraction movement in BetP is facilitated by the glycine stretch, the hallmark of betaine-specific BCCTs [31]. The glycine-stretch harbors the sodium and betaine coordinating residues Ala147, Ala148 and Met150. In the down-regulated form, $TM3_a$ is significantly retracted, with Met150 coordinating Trp374 in the betaine binding site by a non-covalent methionine-aromatic interaction. Such Met-aromatic or aromatic-Met-aromatic bridging interactions are well-established in protein structures as stabilizers [32]. A possible connection between the downregulated conformation of TM3 and the C-terminal osmosensor locking both helices of neighboring protomers might be via the beta sheet formed between L2 (125 – 127) and L8 (396 – 398) ('2' in **Fig. 8**, locked TM3 and the C-terminal domain are shown in red). At the same time, the interaction of the osmosensor with L6 (Lys301 – Val298) affects both L6 and TM7. L6 is stretched into an expanded position ('3' in **Fig. 8**), while on the periplasmic side TM7 and h7 is interacting with POPG ('1'). Notably, TM7, is a scaffold domain helix involved in Na2 coordination via a water molecule [17]. We therefore speculate that the down-regulated state mainly affects the Na2 site, which must be occupied first to stabilize the outward facing state for subsequent betaine binding.

Under down-regulated conditions BetP might thus adopt an energetically much more stable conformation with a higher substrate affinity and a higher energy barrier to overcome during conformational cycling to the outward-facing state than the C_i conformation observed in the presence of K^+ and in all crystal structures.

The role of K^+ – As the concentration of potassium ions in the cytoplasm scales with the external osmolality, K^+ seems like the natural choice as an activator for BetP. However, K^+ binds with a K_d of 220 – 245 mM, a concentration already reached in *C. glutamicum* in the absence of hyperosmotic external stress, which can even reach 800 mM upon stress [18, 33]. Thus, the high potassium content is in general accompanied by high concentrations of glutamate, acting as a counter ion. Consequently, with K^+ as physiological activator ruled out, the question remains what role K^+ plays in activation. FTIR analysis indicates that folding/unfolding of the C-terminal domain is K^+ responsive. K^+ may help to transiently maintain the helical fold of the C-terminal HC1 segment, to allow for the stepwise conformational change in the transporter. The FTIR data also support a conformational change in L2 once the L6-C-terminal interaction is disrupted. Specifically, FTIR spectra for BetP-ΔC45 suggested additional K^+ binding sites in the transporter core, where binding of K^+ might support the isomerization from inward- to outward-facing conformation. For the C-terminal domains, we assume that K^+ is released once the full osmosensor conformational change is achieved. Thus, we suggest a regulatory mechanism based on the symmetry-breaking unfolding/folding of the C-terminal domain affecting both the S1 betaine binding site and sodium binding sites.

Solute molecules such as K^+ and betaine attract water molecules and restrict their freedom to move [34, 35]. An altered water potential within the cell could be an additional osmotic stress stimulus directly sensed by the C-terminal domain of BetP as water molecules are also fundamental components in protein folding by defining hydrophobic interactions. Thus, K^+ bound to the C-terminal domain of BetP might

have the sole purpose of keeping the osmosensor hydrated acting as a water sink (**Fig. 8**) at strategic positions formerly stabilized by lipid interactions. K^+ binding in BetP is achieved by water coordination. For the folding/unfolding of BetP's osmosensor, water potential will play a role also when internal betaine concentration increases during full activation.

Towards a general mechanism in transporter osmoregulation – Osmotic stress induced transport regulation of BetP is considered unique even in the BCCT family as the helical folded osmosensory C-terminal domain is only conserved in *Corynebacteria* species [31]. However, anionic lipids seem to be a common denominator and are found to be crucial in other osmoregulated transporters, e.g., OpuA. OpuA is activated by increasing ionic strength, not specifically responsive to K^+ and downregulated by cyclic-di-AMP binding to the CBS domain [13]. Despite cellular and biochemical differences in structure and transport energetics, CryoEM structures of both BetP and OpuA in downregulated and active conformations show intriguing mechanistic similarities centered around the role of negatively charged lipids. While positively charged Arg and Lys residues in BetP's C-terminal domain – when folded – interact with the membrane to lock the downregulated conformation, OpuA harbours a comparable positively charged cluster in the helix-turn-helix motif in the NBDs, which are located close to the membrane acting as ionic strength sensor. Another striking similarity is that the CBS domains in the OpuA dimer are only ordered when bound to cyclic-di-AMP, otherwise they are natively disordered, thereby linking activation to unfolding of a regulatory domain like that reported here for BetP. In downregulated conditions, both OpuA and BetP adopt inward-facing states apparently stabilized by intra-oligomeric interactions. In OpuA, the CBS domain of one protomer interacts with the NBD of the adjacent protomer, which connects the inhibition site to the ionic strength sensor. For BetP, intradimeric interaction within the trimer, i.e., interaction between two adjacent protomers involving the cytoplasmic loops and the osmosensory C-terminal domain, is key to downregulation and appears to be facilitated by cardiolipin binding.

Conclusions

The molecular switch model of the BetP osmosensor was predicted based on biochemical data about two decades ago; however, it could never be corroborated by structural data. Our comprehensive structural, functional, and dynamic data show that the C-terminal domain, instead of performing a rigid body movement of the entire osmosensory helix, partially unfolds. Changes in membrane curvature or lateral pressure sensed by CL-C-terminal domain interactions and/or POPG-h7 interactions may destabilize multiple cytoplasmic interactions, triggering C-terminal unfolding and disruption of interactions between the C-terminal domain and the transporter helices. Unfolding and lipid interactions of the osmosensory and regulatory domain show striking similarities to what was recently reported for the primary active transporter OpuA. In BetP, this process might be enhanced by changes in the water potential due to elevated K^+ concentrations. The Na2 sodium ion site, and with it the energetics of cycling from inward- to outward-facing conformation, is affected by C-terminal unfolding. There are many open questions about the nature of this up-regulation, especially the role of the enigmatic Na1 site and potential K^+ binding to the transporter itself that will require additional structural investigation in combination with studies on K^+ dependent changes in sodium kinetics.

Acknowledgment

This work was supported in part by the Division of Intramural Research of the NIH, National Institute of Neurological Disorders and Stroke. Anton 2 computer time was

provided by the Pittsburgh Supercomputing Center (PSC) through Grant R01GM116961 from the National Institutes of Health. The Anton 2 machine at PSC was generously made available by D.E. Shaw Research. This work was supported by the Deutsche Forschungsgemeinschaft (DFG, German Research Foundation) through SFBs 699 and 1350. We want to thank the CryoEM core facility namely Bettina Böttcher are the Rudolf-Virchow-Centre at the University of Würzburg. We thank the SLS team at the PSI Villigen, Switzerland for constant support during data collection.

Author contributions: S.M. and R.K. performed cooperativity studies. V.H., M.G.M. and C.P. determined structures, P.K and F.H. collected the Glacios data set, R.G., S.M. and O.R. performed functional experiments, G.G. and W.M. performed FTIR studies, V.L. and L.R.F. carried out MD simulations. G.G., C.P. and C.Z. designed research. C.Z., L.R.F., R.K. and V.H. wrote the manuscript.

Material and Methods

Cell culturing and protein purification – Cell culture and protein preparation methods have been described previously [36]. Uptake of [^{14}C] betaine was measured in *E. coli MKH13* cells [37]. *E. coli* DH5αmcr [38] was used for the heterologous expression of *strep-betP*. Cells were grown at 37°C in LB medium supplemented with carbenicillin (50 µg/ml) and induction was initiated with anhydrotetracycline (200 µg/l). Cells were harvested at 4 °C by centrifugation and resuspended in buffer containing 100 mM Tris-HCl (pH 8.0) and protease inhibitor Pefabloc 0.24 mg/ml. Membranes were isolated from disrupted cells and solubilized with 1.5% β-dodecyl-maltoside (DDM) when purified protein was subsequently crystallized, or 1.0% of the same detergent when protein was reconstituted. The protein was then loaded on a StrepII-Tactin macroprep® column, washed with 50 mM Tris-HCl (pH 7.5), 500 mM NaCl, 8.6% Glycerol, 0.05-0.1% DDM, and eluted with 5 mM desthiobiotin, 50 mM Tris-HCl (pH 7.5), 200 mM NaCl, 8.7% glycerol and 0.6% Cymal-5, if used for crystallization, or 0.05% DDM if used for reconstitution. Prior to crystallization the protein was loaded onto a Superose 6 (GE Healthcare) size-exclusion column equilibrated with 20 mM Tris-HCl (pH 7.5), 200 mM NaCl and 0.6% Cymal-5. This purified protein was concentrated at 4 °C to approx. 10 mg/ml at 3000 g in a Vivaspin tube (Vivascience) with a 100k -molecular-weight cut-off.

Site-directed mutagenesis – The QuickChangeTM kit (Stratagene) and Pfu Turbo DNA polymerase were applied for nucleotide mutagenesis in pASK-IBA5betP [4] and pASK IBA7-betPΔN29-EEE44/45/46AAA [14] plasmids. All the plasmids were fully sequenced and the specific mutations confirmed.

Crystallization and structure determination – BetP-ΔN29/E44E45E46/AAA was co-crystallized with RbCl using two different strategies. In the first strategy the purified protein was pre-incubated with Rb^+ before crystallization trials. Therefore, purified BetP at ~8.0 mg/ml was incubated for 5 min to 16 hours in the presence of RbCl (5 – 300 mM) after which crystallization trials by the hanging drop vapor diffusion method were set. The reservoir solution, containing 100 mM Na-tri-citrate (pH 5.3 – 5.6), 100 mM NaCl, 17 – 24% PEG 400, and purified protein were mixed in 1 µl:1 µl, 1 µl:1.5 µl or 1 µl:2 µl ratios. The second implemented strategy consisted of crystallization trials using a reservoir solution in which the concentration of NaCl originally at 300 mM concentration was systematically replaced by RbCl. The concentration of betaine was varied between 1 and 8 mM. The reservoir solution was composed of 100 mM Na-tri-citrate (pH 5.3 – 5.6), 100 – 300 mM RbCl/NaCl and 17 – 24% PEG 400. Crystals grew at 18 °C and were harvested after at least two weeks. Complete datasets were collected at the tunable beamline (0.6 - 2.1 Å) PXII at the Swiss Light Source (SLS). Fluorescence scans across the

rubidium absorption edge were performed to assess the incorporation of Rb^+ and to determine the wavelength at which the anomalous scattering signal would be maximized. Data sets were collected at a wavelength of 0.81574 Å. The best data sets were collected from crystals grown in 100 mM Na-tri-citrate (pH 5.55), 300 mM RbCl and 22% PEG 400 obtained from protein without preincubation treatment. All data sets were indexed, integrated and scaled using the XDS package [39]. Processing to localize anomalous signals was performed keeping the Friedel mates separate. The quality of the anomalous signal was evaluated according to the anomalous correlation after processing in XDS [40]. The first crystal structure (PDB entry XXX) was determined by molecular replacement using the Phaser program [41], against a structure of BetP (PDB entry 3P03), whereas for the second structure (PDB entry SSS) the model of BetP in a closed conformation (PDB entry 4AIN) was used. Structures were refined using the Phenix refinement program and by manual building with the COOT program until achieving a final refined model after which any improvements of R_{free} and R_{work} factors were observed [42]. An anomalous difference Fourier map was calculated [21] with the CCP4 program FFT in order to identify Rb^+ binding sites [43].

Protein reconstitution into liposomes – Functional reconstitution of BetP and mutants was performed as described [36]. Briefly, liposomes (20 mg phospholipid/ml) from *E. coli* polar lipids (Avanti polar lipids) were prepared by extrusion through polycarbonate filters (100 nm pore-size) and diluted 1:4 in buffer 250 mM KPi (pH 7.5) or Tris 100 mM (pH 7.5), 500 mM KCl. After saturation with Triton X-100, the liposomes were mixed with purified protein at a lipid/protein ratio of 10:1 or 30:1 (w/w). BioBeads at ratios (w/w) of 5 (BioBeads/Triton X-100) and 10 (BioBeads/DDM) were added to remove detergent. Finally, the proteoliposomes were centrifuged and washed before being frozen in liquid nitrogen and stored at –80 °C.

[^{14}C] betaine Transport assays – Uptake of [^{14}C] betaine in *E. coli* cells was performed as described [7]. *E. coli MKH13* cells expressing a particular strep-betP mutant were cultivated at 37 °C in LB medium containing carbenicillin (50 µg/ml) and induced at an OD_{600} of 0.5 by adding anhydrotetracycline (200 µg/l). After 2 h the cells were harvested and washed in buffer containing 25 mM KPi buffer (pH 7.5), 100 mM NaCl, then resuspended in the same buffer containing 20 mM glucose. For uptake measurements the external osmolality was adjusted with KCl. Cells were incubated for 3 minutes at 37 °C before the addition of different concentrations of [^{14}C] betaine. Betaine uptake was measured at various intervals after cell samples were passed through glass fiber filters (APFF02500, Millipore, Schwalbach, Germany), and washed twice with 2.5 ml of 0.6 M KPi buffer. The radioactivity retained on the filters was quantified by liquid scintillation counting. For experiments on K^+ stimulation in intact cells, strep-betP C252T was expressed in *C. glutamicum* strain DHPF [44], and in the same strain glycine betaine import was measured. Cultivation of *C. glutamicum* cells, manipulation and quantification of intracellular K^+ was described previously [45]. To adjust the intracellular K^+ concentration in *C. glutamicum*, K^+-depleted cells were incubated for 10 min at 0.07 – 2.5 mM external KCl prior to the addition of [^{14}C]-betaine. Betaine uptake assays in *C. glutamicum* DHPF were performed as described before [45] at low external osmolality of 0.24 osmol/kg to avoid osmodependent stimulation of BetP. For experiments on K^+ stimulation in proteoliposomes, Strep-BetP C252T was purified and functionally reconstituted as described previously [36]. The internal K^+ concentration was 72 mM, which corresponds to 40 mM KPi buffer at pH 7.5. The internal K^+ concentration was changed by increasing the external osmolality with

sorbitol, which leads to a corresponding reduction of the intraliposomal lumen. The maximal BetP activity was measured in an independent experiment at an internal K^+ concentration of 480 mM.

Expression, purification, and Amphipol-reconstitution of BetP – WT BetP was expressed as described previously [36]. After membrane preparation, membrane proteins were solubilized in 2% (v/v) DDM and Strep II-tagged BetP was affinity purified on a Strep Tactin® column. Reconstitution into Amphipol A8-35 was performed by mixing the polymer stock solution (100 µg/µl) with purified protein in a 1:3 ratio (w/w). After 4 h of incubation, detergent was stepwise removed by addition of BioBeads. Subsequently, the reconstituted protein sample was subjected to SEC in buffer with or without K^+, respectively, and peak fractions were used for SPA CryoEM structure determination without further concentrating of the sample.

Tryptophan fluorescence-binding assay – Binding assays were performed with 100 µg/ml of purified BetP either proteoliposomes, nanodiscs or amphipol A8-35. Betaine concentrations ranged from 0.05 to 15 mM. Tryptophan fluorescence emission between 315 and 370 nm was recorded on a Hitachi F-4500 fluorescence spectrophotometer and averaged over four readings, with the excitation wavelength set to 295 nm and a slit width of 2.5 or 5.0 nm for excitation or emission, respectively. The mean value and standard deviation at the 342 nm emission maximum was plotted for each substrate concentration. Binding constants were derived by fitting with the program GraphPad Prism (version 5.0c for Mac OS X, GraphPad Software Inc., San Diego CA).

CryoEM – For SPA CryoEM structure determination, 3.5 µl of the protein sample were applied to Quantifoil R1.2/1.3 grids, blotted for 5 – 6 sec, and subsequently vitrified in a Vitrobot Mark IV (ThermoFisher Scientific, USA). Datasets were collected at a Titan Krios (ThermoFisher Scientific, USA) operated at 300 keV with a Falcon III camera (ThermoFisher Scientific, USA) in counting mode (BetP in the absence of K^+), or at a Glacios (ThermoFisher Scientific, USA) operated at 200 keV with a Falcon III camera (ThermoFisher Scientific, USA) in counting mode (BetP in the presence of 200 mM K^+). SPA CryoEM data processing was performed according to established procedures in RELION 3.0 and cryoSPARC V2. Symmetric and asymmetric refinements were performed for both datasets, to establish and confirm the correct symmetry, respectively. A model was built into the CryoEM density map of the down-regulated state in COOT and real-space refined in Phenix using PDB 4C7R (chain A) as a template.

Interaction network analysis – Interaction network analysis for BetP were performed. In brief, interactions in the trimeric protein were identified in UCSF Chimera and ranked using the program Gephi 0.9.2 by applying a ForceAtlas. Ligands were excluded from the analysis. Characterization of the resulting interaction networks was performed according to the parameters 'betweenness centrality' (BC) and 'modularity class' (MC), and depicted in UCSF Chimera for visualization. Interactions were classified according to the parameter 'betweenness centrality' (BC). The delta-BC (△BC) values were determined to compare the C_i^{down} *vs.* C_i^{cryst} states, and superposition of |△BC| on the C_i^{down} structure visualizes per-residue changes in global interactions.

FTIR – WT BetP and the C-terminal truncation mutant BetP ΔC45 were expressed and purified as described previously. For subsequent 2D crystallization, a lipid mix mimicking the lipid composition in *C. glutamicum* was solubilized into 1% Decylmaltoside (DM) at a final concentration of 4 mg/ml. Protein - lipid - detergent mixtures were adjusted to contain 2.5 mg/ml protein, 0.15% DM, and an LPR of 0.2 (w/w). After incubating

overnight, the sample was dialyzed at 37 °C for 2 weeks against 500-600 ml of dialysis buffer with BioBeads added. The samples were applied to the ATR diamond, and spectra were recorded with a Vector 22 FTIR spectrometer (Bruker, Germany). Experimental details concerning data recording and analysis are provided in the supplementary methods section.

Molecular dynamics simulations – Molecular dynamics simulations of BetP were carried out for two conformations of the full-length C-terminal domain: either that observed in the crystal structure (4C7R), or that observed in the EM map. In both cases, the rest of the protomer structure was derived from the symmetric all-inward facing crystal structure (4C7R). Each BetP trimer was embedded in a hydrated POPG bilayer, with the concentration of K^+ ions set to either 100 mM or 300 mM. For each system, multiple independent simulations were carried out on Anton2 (with time scales from 2.4 µs to ~7.4 µs) amounting to 24 µs for the crystal structure-derived systems (12 µs for each potassium concentration tested) and 36.7 µs for the systems with the C-terminal domains in the EM orientation (19.9 µs for the 100 mM K^+ system and 16.8 µs for the simulations with 300 mM K^+). All simulations used the CHARMM36 force field [46-48] to describe the protein, lipid, and ions, while the water molecules were represented with TIP3P [49].

To assess whether Met150 adopts the orientation observed in crystal structures or the one observed in the EM structure, we defined two coordination numbers (CN_{crystal} and CN_{EM}):

$$CN_{crystal/EM} = \sum_{ij} \frac{1 - \left({}^{r_{ij}}/_{R}\right)^{10}}{1 - \left({}^{r_{ij}}/_{R}\right)^{20}}$$

where the i and j index refers to the non-hydrogen atoms of the side chains of a given set of residues, r_{ij} is the distance between these atoms and R is the distance cutoff, which was set to 3.5 Å. CN_{crystal} was measured using Met150, Ala313, Ala408 and Trp412 while CN_{EM} was measured using Met150, Trp373, Trp374 and Trp377. Consequently, if the methionine side chain is in close contact with the interaction partners observed in the crystal structure, CN_{crystal} will be larger, whereas if Met150 interacts with the Trp prism, then CN_{EM} will be larger.

References

1. Peter, H., A. Burkovski, and R. Kraemer, *Osmo-sensing by N- and C-terminal Extensions of the Glycine Betaine Uptake System BetP of Corynebacterium glutamicum.* J Biol Chem, 1998. **273**(5): p. 2567–2574.
2. Perez, C., et al., *Substrate specificity and ion coupling in the Na^+/betaine symporter BetP.* The EMBO Journal, 2011. **30**: p. 1221–1229.
3. Farwick, M., R.M. Siewe, and R. Krämer, *Glycine Betaine Uptake after Hyperosmotic Shift in Corynebacterium glutamicum.* J. Bacteriol., 1995. **177**(16): p. 4690–4695.
4. Schiller, D., et al., *The C-Terminal Domain of the Betaine Carrier BetP of Corynebacterium glutamicum Is Directly Involved in Sensing K^+ as an Osmotic Stimulus.* Biochemistry, 2004. **43**(19): p. 5583–5591.
5. Schiller, D., et al., *Influence of Membrane Composition on Osmosensing by the Betaine Carrier BetP from Corynebacterium glutamicum.* The Journal of Biological Chemistry, 2006. **281**(12): p. 7737–7746.
6. Burger, U., *Struktur- und Funktionsanalysen am osmotisch regulierten Transporter BetP aus Corynebacterium glutamicum*. 2002, University of Köln.
7. Ott, V., et al., *Regulatory Properties and Interaction of the C- and N-Terminal Domains of BetP, an Osmoregulated Betaine Transporter from Corynebacterium glutamicum.* Biochemistry, 2008. **47**: p. 12208–12218.
8. Krämer, R. and S. Morbach, *BetP of Corynebacterium glutamicum, a transporter with three different functions: betaine transport, osmosensing, and osmoregulation.* Biochim Biophys Acta, 2004. **1658**: p. 31– 36.
9. Özcan, N., et al., *Osmolality, Temperature, and Membrane Lipid Composition Modulate the Activity of Betaine Transporter BetP in Corynebacterium glutamicum.* J. Bacteriol., 2007. **189**(20): p. 7485–7496.
10. Rubenhagen, R., S. Morbach, and R. Kramer, *The osmoreactive betaine carrier BetP from Corynebacterium glutamicum is a sensor for cytoplasmic K^+.* The EMBO Journal, 2001. **20**: p. 5412-5420.
11. Guler, G., et al., *Lipid-Protein Interactions in the Regulated Betaine Symporter BetP Probed by Infrared Spectroscopy.* The Journal of Biological Chemistry, 2015. **291**(9): p. 4295–4307.
12. Heide, T.v.d., M.C.A. Stuart, and B. Poolman, *On the osmotic signal and osmosensing mechanismof an ABC transport system for glycine betaine.* The EMBO Journal, 2001. **20**(24): p. 7022-7032.
13. Sikkema, H.R., et al., *Gating by ionic strength and safety check by cyclic-di-AMP in the ABC transporter OpuA.* Science Advances, 2020. **6**(eabd7697): p. 1-12.
14. Ressl, S., et al., *Molecular basis of transport and regulation in the Na^+/betaine symporter BetP.* Nature, 2009. **458**(5): p. 47–52.
15. Perez, C., et al., *Alternating-access mechanism in conformationally asymmetric trimers of the betaine transporter BetP.* Nature, 2012. **490**: p. 126–130.
16. Koshy, C., et al., *Structural evidence for functional lipid interactions in the betaine transporter BetP.* The EMBO Journal, 2013. **32**: p. 3096–3105.
17. Perez, C., et al., *Substrate-bound outward-open state of the betaine transporter BetP provides insights into Na^+ coupling.* Nature Communications, 2014. **5**(4231): p. 1-11.
18. Follmann, M., et al., *Potassium Transport in Corynebacterium glutamicum Is Facilitated by the Putative Channel Protein CglK, Which Is Essential for pH Homeostasis and Growth at Acidic pH.* Journal of Bacteriology, 2009. **191**(9): p. 2944–2952.
19. Andersson, C.E. and S.L. Mowbray, *Activation of Ribokinase by Monovalent Cations.* Journal of Molecular Biology, 2002. **315**(3): p. 409-419.

20. Schack, V.R., et al., *Identification and Function of a Cytoplasmic K^+ Site of the Na^+,K^+-ATPase.* The Journal of Biological Chemistry, 2008. **283**(41): p. 27982–27990.
21. Strahs, G. and J. Kraut, *Low-resolution Electron-density and Anomalous-scatteringdensity Maps of Chromatium High-potential Iron Protein.* Journal of Molecular Biology, 1968. **35**: p. 503-512.
22. Ge, L., et al., *Locating an extracellular K^+-dependent interaction site that modulates betaine-binding of the Na^+-coupled betaine symporter BetP.* PNAS, 2011. **108**(43): p. 1-9.
23. Perez, C., et al., *The role of trimerization in the osmoregulated betaine transporter BetP.* EMBO reports, 2011. **12**(8): p. 804-810.
24. Malinauskaite, L., et al., *A mechanism for intracellular release of Na+ by neurotransmitter/sodium symporters.* Nature Structural & Molecular Biology, 2014. **21**: p. 1006–1012.
25. Barth, A. and C. Zscherp, *What vibrations tell us about proteins.* Quarterly Reviews of Biophysics, 2002. **35**(4): p. 369–430.
26. Barth, A., *The infrared absorption of amino acid side chains.* Progress in Biophysics & Molecular Biology, 2000. **74**: p. 141–173.
27. Fabian, H. and W. Mantele, *Infrared Spectroscopy of Proteins*, in *Handbook of Vibrational Spectroscopy*, J.M. Chalmers and P.R. Griffiths, Editors. 2006, John Wiley & Sons Ltd.
28. Korkmaz, F., et al., *K^+-induced conformational changes in the trimeric betaine transporter BetP monitored by ATR-FTIR spectroscopy.* Biochimica et Biophysica Acta (BBA) - Biomembranes, 2013. **1828**(4): p. 1181-1191.
29. Susi, H. and D.M. Byler, *Protein structure by Fourier transform infrared spectroscopy: Second derivative spectra.* Biochemical and Biophysical Research Communications, 1983. **115**(1): p. 391-397.
30. Schiller, D., R. Krämer, and S. Morbach, *Cation specificity of osmosensing by the betaine carrier BetP of Corynebacterium glutamicum.* FEBS Letters, 2004. **563**: p. 108-112.
31. Ziegler, C., E. Bremer, and R. Krämer, *The BCCT family of carriers: from physiology to crystal structure.* Mol. Microbiol., 2010. **78**(1): p. 13–34.
32. Valley, C.C., et al., *The Methionine-aromatic Motif Plays a Unique Role in Stabilizing Protein Structure.* The Journal of Biological Chemistry, 2012. **287**(42): p. 34979–34991.
33. Krämer, R., et al., *Uptake of glutamate in Corynebacterium glutamicum: 1. Kinetic properties and regulation by internal pH and potassium.* Eur. J. Biochem., 1990. **194**: p. 929-935.
34. Wood, J.M., *Osmosensing by Bacteria: Signals and Membrane-Based Sensors.* Microbiol. Mol. Biol. Rev, 1999. **63**(1): p. 230–262.
35. Wood, J.M., *Bacterial responses to osmotic challenges.* J. Gen. Physiol., 2015. **145**(5): p. 381–388.
36. Rubenhagen, R., et al., *Osmosensor and Osmoregulator Properties of the Betaine Carrier BetP from Corynebacterium glutamicum in Proteoliposomes.* The Journal of Biological Chemistry, 2000. **275**(2): p. 735-741.
37. Haardt, M., et al., *The osmoprotectant proline betaine is a major substrate for the binding-protein-dependent transport system ProU of Escherichia coli K-12.* Molecular and General Genetics, 1995. **246**: p. 783–796.
38. Grant, S.G.N., et al., *Differential plasmid rescue from transgenic mouse DNAs into Escherichia coli methylation-restriction mutants.* Proceedings of the National Academy of Sciences of the United States of America, 1990. **87**(12): p. 4645-4649.

39. Kabsch, W., *Automatic processing of rotation diffraction data from crystals of initially unknown symmetry and cell constants.* Journal of Applied Crystallography, 1993. **26**: p. 795-800.
40. Schneider, T.R. and G.M. Sheldrick, *Substructure solution with SHELXD.* Acta Crystallographica Section D, 2002. **58**(10-2): p. 1772-1779.
41. McCoy, A.J., et al., *Phaser crystallographic software.* Journal of Applied Crystallography, 2007. **40**: p. 658–674.
42. Emsley, P. and K. Cowtan, *Coot: model-building tools for molecular graphics.* Acta Crystallographica Section D, 2004. **D60**: p. 2126-2132.
43. Collaborative Computational Project, N., *The CCP4 suite: programs for protein crystallography* Acta Crystallographica Section D, 1994. **50**(5): p. 760–763.
44. Steger, R., et al., *LcoP, an osmoregulated betaine/ectoine uptake system from Corynebacterium glutamicum.* FEBS Letters, 2004. **573**: p. 155–160.
45. Maximov, S., et al., *Stimulus analysis of BetP activation under in vivo conditions.* Biochimica et Biophysica Acta, 2014. **1838**: p. 1288–1295.
46. Best, R.B., et al., *Optimization of the additive CHARMM all-atom protein force field targeting improved sampling of the backbone φ, ψ and sidechain χ1 and χ2 dihedral angles.* Journal of Chemical Theory and Computation, 2012. **8**(9): p. 3257–3273.
47. Klauda, J.B., et al., *Update of the CHARMM All-Atom Additive Force Field for Lipids: Validation on Six Lipid Types.* The Journal of Physical Chemistry B, 2010. **114**(23): p. 7830–7843.
48. Venable, R.M., F.L.H. Brown, and R.W. Pastor, *Mechanical properties of lipid bilayers from molecular dynamics simulation.* Chemistry and Physics of Lipids, 2015. **192**: p. 60-74.
49. Jorgensen, W.L., J. Chandrasekhar, and J.D. Madura, *Comparison of simple potential functions for simulating liquid water.* Journal of Chemical Physics, 1983. **79**(2): p. 926-935.

Figures

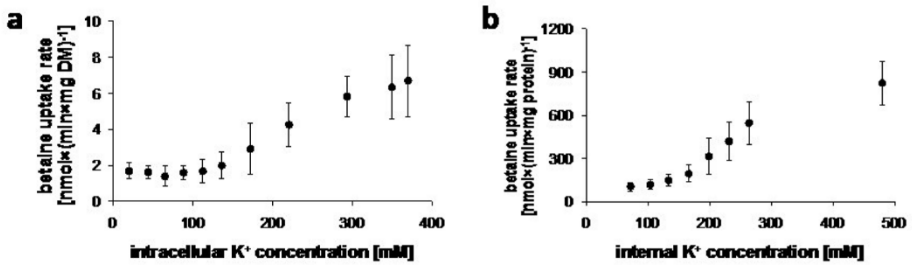

Figure 1. Effect of internal K^+ concentration on BetP activity.
a. [^{14}C]-Betaine uptake rate of BetP expressed in *C. glutamicum* cells. Cytoplasmic K^+ concentration was gradually increased by K^+ uptake into K^+ depleted cells. **b.** [^{14}C]-Betaine uptake rate of BetP reconstituted in liposomes. The internal K^+ concentration was increased by controlled shrinkage of the vesicles in response to addition of hypertonic buffer. All measurements were carried out in triplicate and error bars indicate standard deviation (s.d.).

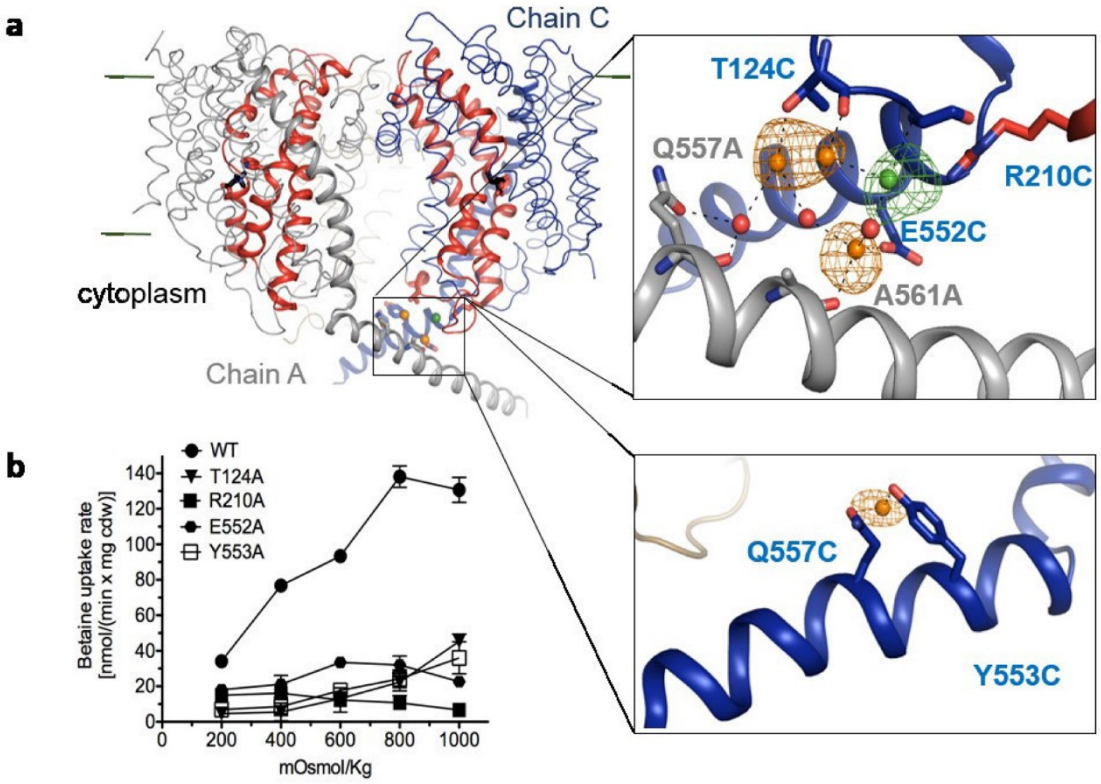

Figure 2. The role of K^+ in the regulation of BetP.
a. Rb^+ binding sites in BetP. Rb^+ ions (orange) and their interaction networks are shown with the anomalous-difference Fourier map (orange) contoured at 4.0σ. The *Fo-Fc* omit map (green) of the coordinating Cl^- ion (green) is contoured at 3.0σ. Water molecules are shown as red spheres. Betaine and citrate are shown in black sticks. **b.** Functional characterization of Rb^+ interaction-sites. Osmotic activation profile of BetP WT expressed in *E. coli MKH13* compared to those of single alanine mutants of residues involved in the formation of Rb^+ interaction sites. All measurements were carried out in triplicate. Error bars indicate s.d.

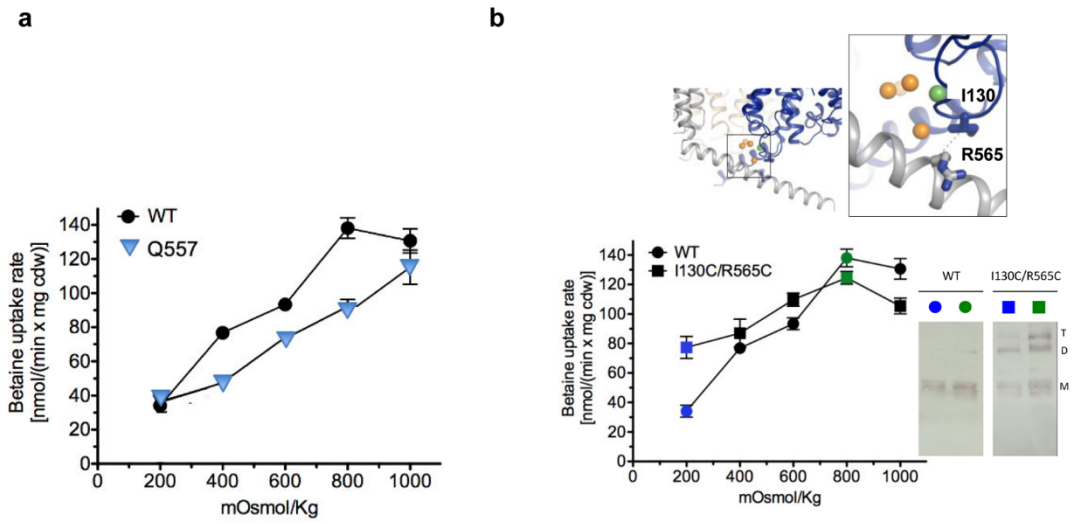

Figure 3. The active state of BetP in crystal structures.
a. Osmotic activation profile of BetP WT expressed in *E. coli MKH13* compared to that of single alanine mutants of Gln557 coordinating Rb^+. All measurements were carried out in triplicate. Error bars indicate s.d. **b.** Osmotic activation profile of BetP WT and the double cysteine mutant I130C/R565C expressed in *E. coli MKH13* cells and western blot of BetP WT and I130C/R565C from membrane vesicles of *E. coli MKH13* cells extracted after incubation in iso-osmotic conditions (blue) or hyper-osmotic conditions (green), in the presence of the homobifunctional cross-linker o-PDM (o-phenylenedimaleimide). T, trimer; D, dimer; M, monomer.

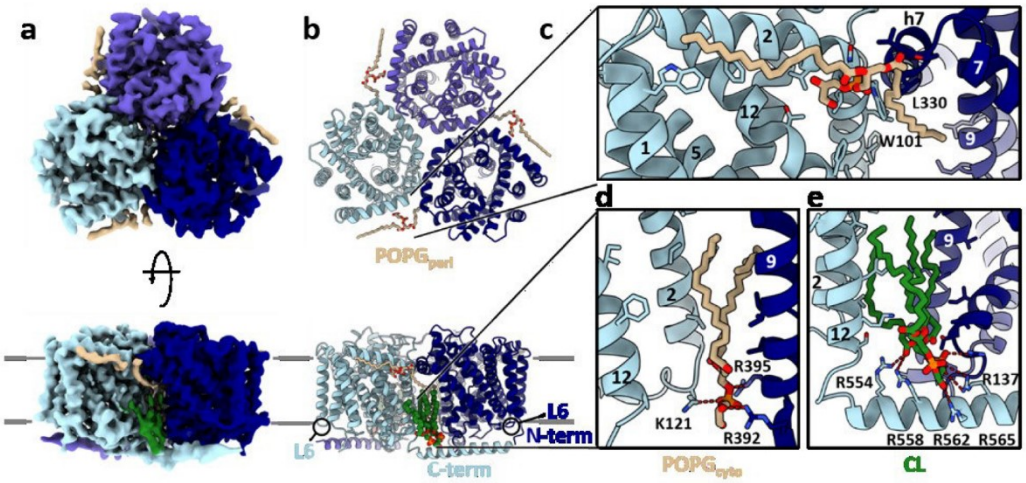

Figure 4. Symmetric cryo-EM structure of BetP in the absence of K^+.
a. Cryo-EM density map of BetP in C3 symmetry at a resolution of 3.7Å according to the FSC = 0.143 criterion. The BetP trimer (protomer A: light blue, protomer B: violet blue, protomer C: navy blue) is depicted in a top- and side-view. Lipid densities located at the hydrophobic cleft at the trimer interface are shown in tan (POPG) or green (CL), respectively. The membrane plane is indicated by grey lines. **b.** An atomic model was built into the density map shown in a. Intra-protomeric contacts involve the N- and C-terminal domains and L6 as well as the lipid molecules. Color coding as in a. **c.** Coordination of the $POPG^{peri}$ molecule with TM1, TM2 and TM12 in protomer A and h7 and TM9 in protomer C. **d.** Coordination of $POPG^{cyto}$ with TM2 and TM12 in protomer A and TM9 in protomer C. **e.** Coordination of CL with TM2, TM12 and the C-terminal domain of protomer A and TM9 and L2 in protomer C.

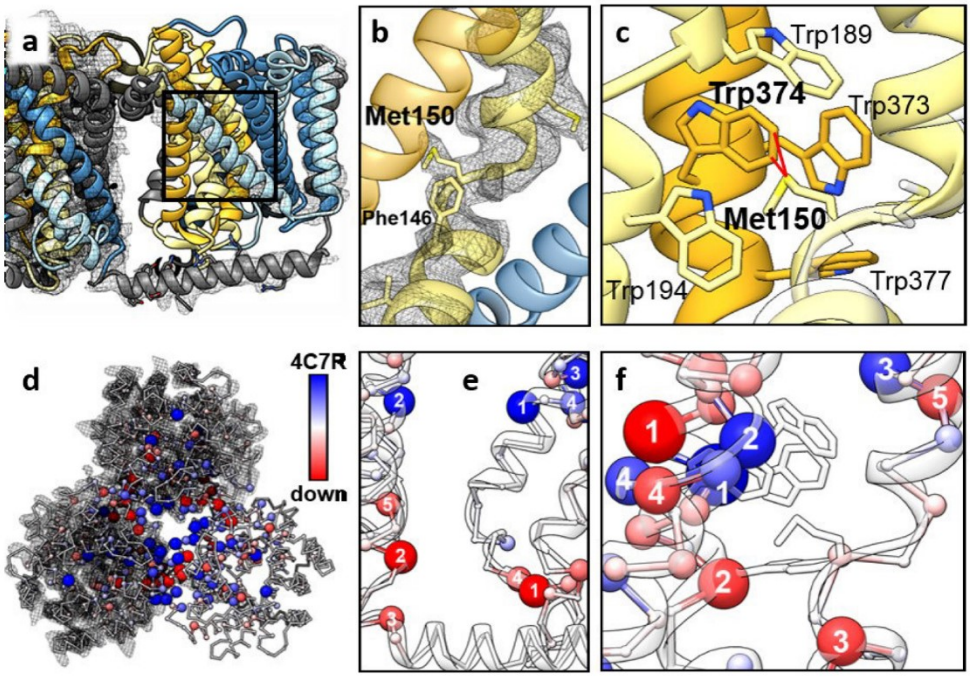

Figure 5. Structural analysis of BetP in the absence of K^+.
a. Superposition of the atomic ribbon model with the cryo-EM density map, illustrating the tight interactions of the C-terminal domain with L2 and L6. A black box highlights the area shown in b and c. **b.** Close up of the glycine-stretch in TM3 (khaki). The atomic model is shown fit into the symmetric cryo-EM density map (black mesh). The neighboring TMs 9 (gold) and 10 (steel blue) are displayed as transparent ribbons. **c.** Superposition of the atomic model (gold/khaki) with crystal structure 4C7R (white). Met150 exhibits a significantly different orientation. In the absence of K^+, the side chain is oriented towards the Trp box (Trp373, Trp374 and Trp377) in TM8 (gold ribbon, black mesh). **d.** Protein interaction network analyses were performed for the symmetric C_i^{down} state and C_i^{cryst} (pdb-ID 4C7R), each without ligands. The difference in global interaction of a specific residue was mapped on the atomic model of C_i^{down} (white ribbon). Blue spheres indicate an increase in interaction in C_i^{cryst}, while red spheres indicated an increase in C_i^{down}. The sphere size corresponds to the number of interactions, i.e., large, red spheres represent residues with a higher interaction score under downregulated conditions. Most global interactors was identified at the trimer interface and in the bundle helices TM3, TM4, TM8 and TM9. **e.** A zoom on the contact region of protomers B and A reveals an altered interaction network at the regulatory C-terminal domain. For the C_i^{down} state (red), residues Arg126.A (1), Ser545.B (2), Tyr550.B (3), Ile125.A (4) and Val541.B (5) are identified as major interactors, while in C_i^{cryst} (blue) Phe112.A (1) and Phe112.B (2) as well as His192.A (3) and Phe110.A (4) contribute to the inter-protomer contact. **f.** A zoom on the Trp box in protomer C reveals an altered interaction profile in the substrate binding pocket: Trp373 (1), Trp189 (2), Tyr157 (3) and His192 (4) were identified as the key residues in C_i^{cryst} (blue). Trp371 (1), Trp377 (2), Phe146 (3), Leu191 (4) and Phe156 (5) exhibit the highest interaction score in C_i^{down} (red).

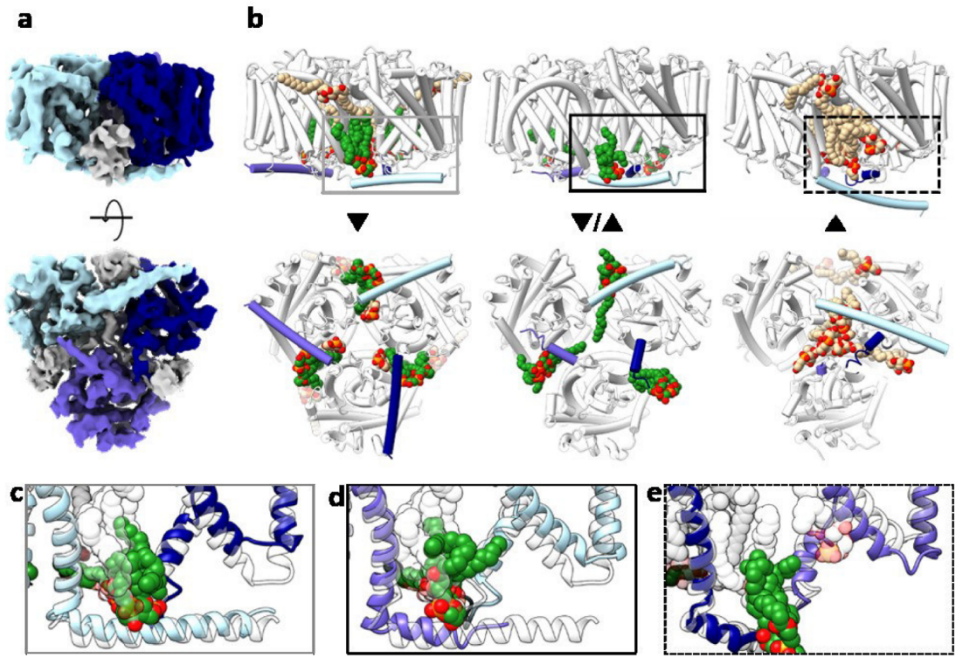

Figure 6. The effect of K^+ on the structure of BetP.
a. Asymmetric cryo-EM density map of BetP in the presence of 200 mM K^+ at a resolution of 4.3 Å. The three protomers exhibit structural differences in length and orientation of the C-terminal domains: protomer A (light blue, fully extended), protomer B (violet blue, intermediate-length) and protomer C (navy blue, short). Lipid densities are depicted in grey. **b.** Structure and orientation of the C-terminal domains (color-coded according to a) of BetP in absence (C_i^{down},▼) and presence (▼/▲) of K^+, in comparison to crystal structure 4C7R (C_i^{cryst},▲). Changes in the C-terminal domains are accompanied by altered lipid interactions with CL (green) and POPG (tan). **c.** Focus on the interaction of the C-terminal domain in protomer A (light blue) of BetP in the presence of K^+ (▼/▲) with L2 and L6 of the adjacent protomer (navy blue, grey box in b), in comparison to C_i^{down} (transparent). **d.** Focus on the interaction of the C-terminal domain in protomer B (violet blue) of BetP in the presence of K^+ (▼/▲) with L2 and L6 of the adjacent protomer (light blue, black box in b), in comparison to C_i^{down} (transparent). **e.** Focus on the interaction of the C-terminal domain in protomer C (navy blue) of BetP in the presence of K^+ (▼/▲) with L2 and L6 of the adjacent protomer (navy blue, dashed box in b), in comparison to C_i^{cryst} (transparent).

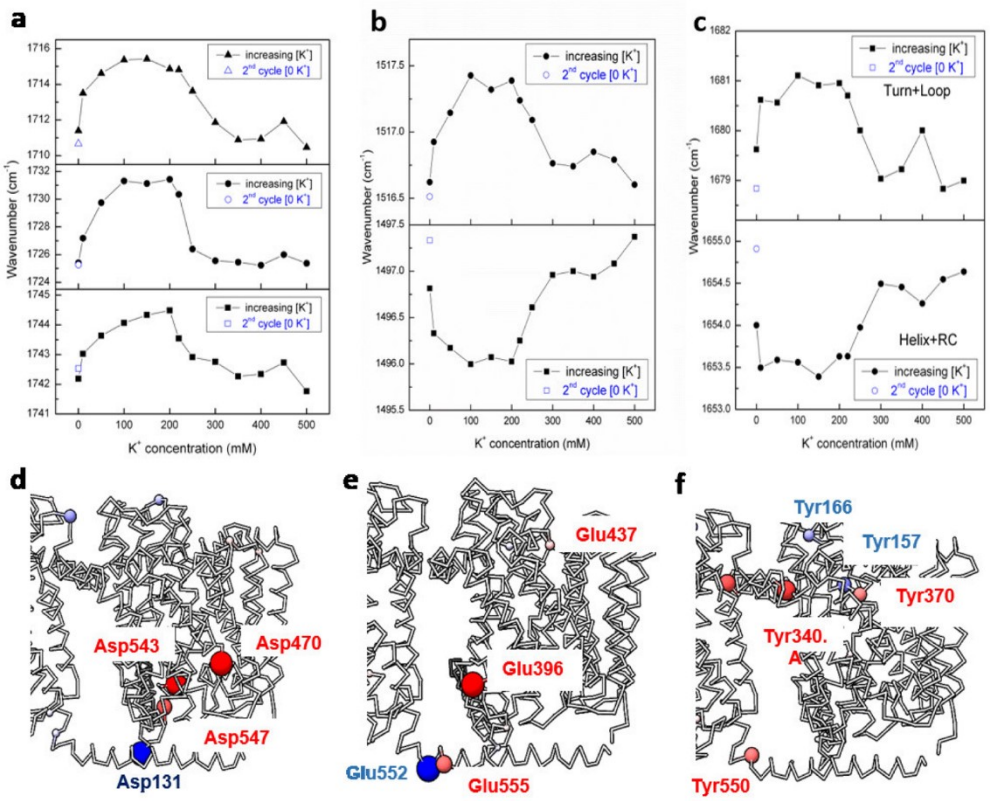

Figure 7. Changes in Asp / Glu / Tyr residues at different K^+ concentrations.

The shift of the peak positions with respect to increasing K^+ concentration for **a.** protonated Asp/Glu residues absorbing at around 1712, 1726 and 1742 cm^{-1}, **b.** Tyr absorbing at around 1517 cm^{-1} and 1497 cm^{-1}. Open signs in blue colour represent the 2nd cycle of inactive state of BetP without K^+ ions and **c.** the secondary structures absorbing at around 1680 and 1654 cm^{-1}. **d.** Aspartate and **e.** Glutamate residues, which according to the BC difference network analysis change their interaction pattern. Red spheres have stronger BC in the down-regulated state, while blue spheres have a stronger BC value in the active state. **f.** Only the cytoplasmic tyrosine residue Tyr550 showed changes from downregulated to active state. Strongest change is observed in Tyr340, which is located in h7 at the periplasmic trimerization interface. Tyr residues do not play a dominant role in the activated state except for Tyr157.

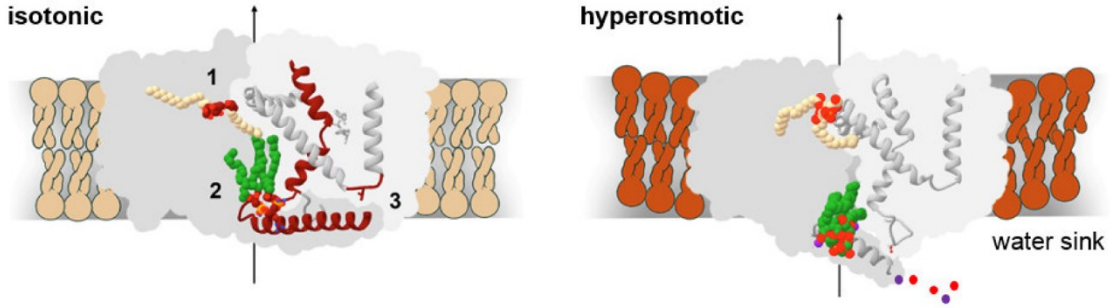

Figure 8. Regulation of BetP.
Suggested activation mechanism of BetP. At isotonic conditions, the trimer adopts a symmetric conformation with key interactions at three positions (1, 2 and 3). Under hyperosmotic conditions, release of those three interactions leads to asymmetry in the trimer.

X. Manuscript 1

Application of STEM tomography to investigate smooth ER morphology under stress conditions

V. Heinz[a], R. Rachel[b], C. Ziegler[a, ±]

[a] Department of Biophysics II / Structural Biology, University of Regensburg, Universitätsstr. 31, 93053 Regensburg, Germany

[b] Department of Molecular and Cellular Anatomy / Centre for Electron Microscopy, University of Regensburg, Universitätsstr. 31, 93053 Regensburg, Germany

± to whom correspondence should be addressed:

Prof. Christine Ziegler
Department of Biophysics II / Structural Biology
University of Regensburg
Universitätsstr. 31
93053 Regensburg
Germany
Email: christine.ziegler@biologie.uni-regensburg.de
Phone: +49 (0)941 943 3030

Key words: scanning transmission electron microscopy (STEM), tomography, endoplasmic reticulum (ER) morphology, crystalloid-ER, ER whorls, ER stress

Abbreviations:

Endoplasmic reticulum (ER), smooth-ER (sER), transmission electron microscopy (TEM), three-dimensional (3D), scanning transmission electron microscopy (STEM), human embryonic kidney (HEK), Transient Receptor Potential (TRP), polycystin-2 (PC-2), autosomal dominant polycystic kidney disease (ADPKD), unfolded protein response (UPR), organized smooth ER (OSER), bright field (BF), dark field (DF), focused ion beam (FIB), scanning electron microscopy (SEM), fetal bovine serum (FBS), high pressure-freezing (HPF), Uranyl acetate (UAc), Glutar-di-aldehyde (GA), lead citrate (PbCi), region of interest (ROI), Simultaneous Iterative Reconstruction Technique (SIRT), rough ER (rER), mitochondria-associated membrane (MAM), 3-hydroxy-3-methylglutaryl coenzyme A (HMG-CoA), microsomal aldehyde dehydrogenase (msALDH), polycystin-1 (PC-1).

Manuscript to be submitted to Journal of Structural Biology

Graphical Abstract:

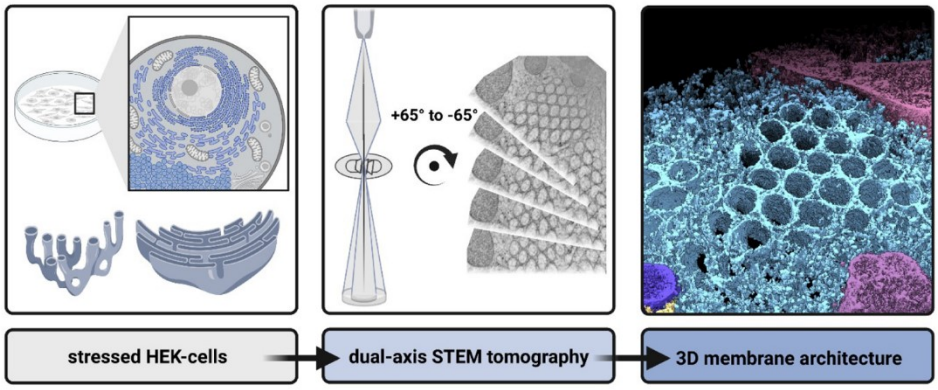

Highlights:

- Stressed HEK-cells show altered sER: tubular crystalloid-ER and lamellar ER whorls.
- Both morphotypes co-occur in the same cell but remain strictly spatially separated.
- Despite an altered morphology, their intracellular interaction networks persist.
- Dual-axis STEM tomography yielded detailed 3D reconstructions of the organelles.
- SER membrane architecture could be elucidated at an unprecedented level of detail.

Abstract

The endoplasmic reticulum (ER) is a dynamic, versatile organelle with multiple functions within eukaryotic cells, such as lipid and protein biosynthesis or Ca^{2+} homeostasis and storage. Under stress conditions, the organelle can grow substantially while severely changing its morphology. Extreme examples are ER whorls and crystalloid-ER, presumably consisting of smooth-ER (sER) membrane tubes arranged in a honeycomb-like pattern featuring an apparent hexagonal symmetry. These and other lamellar or tubular sER morphotypes have been extensively studied *via* conventional transmission electron microscopy (TEM). However, due to their large size, three-dimensional (3D) information is scarce. Electron tomography employing the scanning transmission electron microscopy (STEM) mode is a cutting-edge technique suitable to depict organelles within their cellular context at a comparably high resolution in 3D. The method benefits from a high depth-of-focus and the lack of spherical aberration during image formation, making it possible to observe larger cellular sub-volumes in thicker sections than in conventional TEM - tomography. Here, we used dual-axis STEM tomography to obtain 3D reconstructions of the crystalloid-ER described before in human embryonic kidney (HEK) cells over-expressing the ion channel polycystin-2 (PC-2), which plays a key role in autosomal dominant polycystic kidney disease (ADPKD). We successfully obtained 3D volumes not only of the crystalloid-ER, but also another sER morphotype not yet described in this physiological context, namely ER whorls. Our data allow to describe the membrane architecture of the respective organelles at an unprecedented level of detail. Furthermore, the unique possibility to investigate the organelles in their native background allowed us to identify the dynamic and diverse cellular interaction partners of the sER morphotypes. Thus, while demonstrating the applicability of dual-axis STEM tomography to investigate organellar morphology in large cellular sub-volumes in a proof – of - principle study, we could also contribute valuable ultrastructural information on membrane architecture and intracellular interactions of the sER in HEK cells under severe stress conditions.

Introduction

Eukaryotic cells constantly exposed to a variety of external and internal stress stimuli depend on sophisticated and highly coordinated stress response strategies. The ER stress response or unfolded protein response (UPR) (Harding & Ron, 2002; Schroeder & Kaufman, 2005) is triggered by elevated levels of unfolded or misfolded proteins detected within the ER luminal space. To counteract this stressful increase in workload, the ER counteracts with a concerted attenuation of protein synthesis and a progression of folding capacities, respectively (Harding & Ron, 2002; Walter & Ron, 2011). An augmented ER capacity requires both an increase of its luminal volume and membrane surface area to alleviate ER stress (Schuck *et al.*, 2009). Consequently, additional membranes are synthesized and stacked either in lamellar or tubular morphotypes referred to as organized smooth ER (OSER) (Wright *et al.*, 1988; Koning *et al.*, 1996; Voeltz *et al.*, 2002; Snapp *et al.*, 2003; Schuck *et al.*, 2009). Symmetric arrays of tubular ER are also termed 'crystalloid-ER' (Chin *et al.*, 1982; Anderson *et al.*, 1983; Takei *et al.*, 1994; Yamamoto *et al.*, 1996; Snapp *et al.*, 2003). OSER structures in cells were also observed under homeostatic conditions (Snapp *et al.*, 2003). Consequently, the presence of OSER in cells is not necessarily an indication for a dangerous stress situation but may merely reflect a phase of increased ER activity under physiological growth conditions. This is, for instance, the case in differentiated secretory cells, such as Plasma B cells or embryonic adrenal cells (Federovitch *et al.*, 2005). The molecular mechanism of OSER formation, however, is still far from understood. Diverse parameters to establish and maintain the extreme membrane curvature in crystalloid ER have been suggested, including an altered membrane lipid composition, integration of curvature-shaping membrane proteins or permanent or temporal interactions with scaffolding proteins (Anderson *et al.*, 1983; Stowell *et al.*, 1999; McMahon & Gallop, 2005; Hu *et al.*, 2008).

While the eye-catching OSER morphotypes have been studied *via* conventional transmission electron microscopy (TEM) in 2D in the past, three-dimensional (3D) information is sparse. This can be partially attributed to a lack of suitable high-throughput techniques capable to provide a resolution sufficient to elucidate the presumably complex membrane architecture of the organelles. Scanning transmission electron (STEM) tomography has shown promising results to provide higher resolution for cellular samples (Hohmann-Marriott *et al.*, 2009; Elbaum, 2018; Wolf *et al.*, 2018; Rachel *et al.*, 2020). When operated in 'biological' STEM mode, the electrons are focused into a small, nearly parallel beam, scanning across the sample. With a diameter of 2 – 3 nm in the sample plane, this beam is more than 10*x* larger than in

'standard' STEM applications (<0.2 nm). Scattered electrons are then detected on bright field (BF) and dark field (DF) STEM detectors, and the information obtained for each scanned pixel are subsequently combined to a mosaic image (Elbaum, 2018). In comparison to the 'classical' TEM tomography approach, this technique benefits from a higher depth of focus (Rachel *et al.*, 2020) and the lack of chromatic aberration in STEM mode (Hohmann-Marriott *et al.*, 2009; Sousa *et al.*, 2011; Villinger *et al.*, 2012; McBride *et al.*, 2018; Wolf *et al.*, 2018; Rachel *et al.*, 2020), as well as from a better SNR and contrast (Yakushevska *et al.*, 2007). Consequently, sections with a nominal thickness of up to 1 µm can be investigated even at high tilt angles (> ± 66°). Notably, the applicability of the STEM tomography approach for sections of this thickness at 200 keV has been demonstrated recently (Walther *et al.*, 2018; Rachel *et al.*, 2020). The method thus is ideally suited to investigate the organellar architecture of different OSER morphotypes in 3D. The use of high pressure-frozen, freeze substituted sample material in dual-axis STEM tomography has been shown to provide superior ultra-structural sample preservation suitable to investigate cellular details at high resolution in 3D (Abdellatif *et al.*, 2018; Rachel *et al.*, 2020). This preparation methods offers a number of advantages over the conventionally applied chemical fixation. First, the cells are rapidly frozen under high pressure, which helps to avoid preparation artifacts such as deformation and ultrastructural damage caused by the slow, conventional chemical fixation. Second, freeze substitution facilitates a gentle chemical fixation and en bloc-staining while maintaining the cells' integrity in the cryo-preserved state, preventing artifacts originating from washing-off soluble cytoplasmic constituents. Overall, high-pressure freezing and freeze-substitution are considered a prime method to preserve the cellular ultrastructure for subsequent electron microscopy (Rachel *et al.*, 2010; Walther *et al.*, 2013).

In this study, we aim to investigate the role and impact of OSER structures formed upon the overexpression of the Transient Receptor Potential (TRP) channel Polycystin-2 (PC-2) in HEK293S cells (Wilkes *et al.*, 2017). A previous investigation by focused ion beam (FIB) scanning electron microscopy (SEM) analysis revealed the formation of crystalloid-ER and immuno-gold labeling confirmed the enrichment of PC-2 in these crystalloid-ER membranes (Wilkes *et al.*, 2017). In the present study, by obtaining 3D reconstructions of a large cellular volume, we monitored the genesis and dynamic nature of crystalloid-ER. The use of STEM tomography results in a better resolution in the Z-dimension, and thus in a much larger reconstructed cellular volume, while dual-axis tomography minimizes the missing wedge artifact prominent in single-axis tomograms.

Material and Methods

Cell culture and protein over-expression

A stable HEK293S GnTI$^-$ cell line created by M. Wilkes and co-workers (Wilkes *et al.*, 2017) was used for the expression of WT PC-2. Cultivation of cells and expression of PC-2 were performed as described in this publication. For subsequent HPF / AFS, plasma-cleaned (Plasma Cleaner PDC-3XG, Harrick Plasma Inc., Ithaca, USA) TC 60 cell culture dishes were supplemented with 1.4 mm sapphire discs (M. Wohlwend GmbH, Sennwald, CH) prior to seeding the cells. Cells were grown in DMEM/F-12 medium (Sigma-Aldrich®, St. Louis, USA), supplemented with 10% fetal bovine serum (FBS), 5 µg/ml Blasticidin, 350 µg/ml G418, and Pen/Strep (55 u/ml Penicillin, 55 µg/ml Streptomycin). At ~40% confluence, protein expression was induced *via* addition of Tetracycline to a final concentration of 3 µg/ml. The sapphire discs were transferred into sterile cell culture medium after 72 h of expression, at ~80 – 90% confluence. Non-induced cells were grown in parallel as a negative control.

High pressure-freezing, freeze-substitution and sectioning

Subsequently, the samples were prepared by high pressure-freezing (HPF), freeze-substitution, resin embedding and ultramicrotomy, in general following the procedures outlined by R. Rachel and co-workers (Rachel et al., 2010). Cryo-fixation was performed *via* HPF at ~2048 bar and -196 °C in an EM PACT2 (Leica Microsystems GmbH, Wetzlar, DE), followed by automated freeze-substitution in an AFS2 (Leica Microsystems GmbH, Wetzlar, DE). Intracellular water was initially substituted against 0.5% (v/v) OsO_4, 0.25% (w/v) Uranyl acetate (UAc), 5% (v/v) H_2O in acetone, or 0.5% (v/v) Glutar-di-aldehyde (GA), 0.5% (w/v) UAc, 5% (v/v) H_2O in acetone. OsO_4-stained samples were used for screening and tomography, samples stained with only UAc exclusively for screening. The latter were subjected to lead citrate (PbCi) staining on the sections later on, following common procedures. Notably, special care was taken to obtain the best ultrastructural preservation of the (intra-) cellular membranes by adding H_2O to the freeze substitution solution (Walther & Ziegler, 2002; Buser & Walther, 2008). A detailed freeze-substitution protocol is presented in **Error! Reference source not found.**. After polymerization, HPF sample carriers and sapphire discs were removed from the resin blocks, and the samples were trimmed to a trapezoidal block-face shape using fresh razor blades. Subsequently, ultrathin sections (50 nm) were prepared for sample screening and thick sections (800 nm) were prepared for STEM tomography on an EM UC7 (Leica Microsystems GmbH, Wetzlar, DE) ultramicrotome using a 'histo'-type diamond knife (Diatome Ltd, Nidau, CH). The sections were picked up on pioloform-coated copper slot (1 *x* 2 mm) or P-bar grids.

For tomography, 15 nm protein A gold fiducials (University of Utrecht, Utrecht, NL) were successively applied to both sides of the sections at a dilution of 1:40, incubated for 4 min and excess gold particles were washed away with destilled H_2O. Finally, a thin, conductive carbon film of 2 – 3 nm thickness was evaporated onto the grid and section surface *via* thermal evaporation in a Cressington 208carbon (Tescan GmbH, Dortmund, DE).

Electron microscopy

Screening of grids for optimal ultrastructural sample preservation and for the presence of crystalloid ER on sections with a nominal thickness of 50 nm was performed by conventional TEM microscopy on a JEM 2100F (JEOL, Tokyo, JPN) transmission electron microscope, operated at 200 keV with a CMOS camera (TemCam-F416, 4k x 4k pixels, TVIPS GmbH, Gauting, DE) using the EM MENU (TVIPS - Tietz Video and Image Processing Systems GmbH, Gauting, DE) software package. Screening revealed good sample quality and excellent preservation of intracellular membranes. Sections with a nominal thickness of 800 nm were consequently analyzed *via* dual-axis STEM tomography, following the established procedures at the Department for Molecular and Cellular Anatomy at our university (Rachel et al., 2020). Since plastic sections shrink substantially during data collection (Luther, 2006), the samples were pre-exposed to the electron beam for several minutes ('beam showering'). Dual-axis STEM tomography was performed on the same JEM 2100F (JEOL, Tokyo, JPN) electron microscope equipped with both a bright field (BF) and a dark field (DF) STEM detector, using a Model 2040 Dual-Axis Tomography holder (Fischione Instruments Inc., Export, USA). The STEM beam was formed using special settings (Rachel *et al.*, 2020), with a 20 µm condensor aperture in place (diameter: 3-4 nm). Fine-tuning was accomplished *via* a Ronchigram generated on the pioloform support film. At a camera length of 20 cm, both BF and DF images were collected simultaneously; the signal was optimized for BF imaging. Tilt series were recorded automatically from +66° to -66° according to a modified Saxton tilt scheme (Saxton et al., 1984) presented in **Supplementary table 2** using the EM-Tools (TVIPS - Tietz Video and Image Processing Systems GmbH, Gauting, DE) software package. Eucentric height was adjusted once before data acquisition. After collection of the first tilt series completed, the sample was manually rotated in the holder by 90°. Subsequently, a second tilt series was acquired as described before from the same region of interest (ROI).

Tomogram reconstruction and visualization

Finally, tomogram reconstruction was performed in IMOD , following the inherent processing pipeline (Kremer *et al.*, 1996) and according to common procedures (McIntosh *et al.*, 2005;

Rachel *et al.*, 2020). Pre-processing included binning and image stack generation. Fine tuning of the initial, coarse image alignment requires a fiducial model. Here, manual fiducial model generation and optimization yielded superior results than automatically generated models. At least 15 fiducial markers were selected from each side of the section. Distortions were accounted for during later iterations of fine alignment. The volume was cropped, and gold fiducials were removed using the 'Bead Eraser' option. Tomogram reconstruction was performed using a Simultaneous Iterative Reconstruction Technique (SIRT) -like filter (with 15 iterations), which in this case yielded the best results. Both tomograms collected from the same ROI were reconstructed following the procedure described above, and subsequently merged using the 'Tomogram Combination' option. Alignment of the two tomograms usually worked best following the 'automatic patch fitting' method. Finally, the tomogram edges were trimmed. For tomogram visualization, the program SeggeR (Pintilie et al., 2010) in the UCSF Chimera (Pettersen et al., 2004) framework could be identified as a threshold-based approach, circumventing manual membrane tracing as commonly applied. The tomograms were imported into UCSF Chimera, scaled and binned appropriately, and the histogram display threshold was adjusted to optimally visualize the organellar membranes. Subsequently, SeggeR was used for automated, threshold based segmentation of the volume. Two or three smoothing steps were performed, very small regions (background noise < 5 to 30 voxels) were removed and the segmentation results were refined manually. The 'Ungroup' option was used to improve the quality of inaccurately segmented regions, and regions belonging to the same organelle were subsequently grouped together to obtain one separate volume per organelle.

Results

HEK cell morphology upon over-expression of WT PC-2

The morphology of HEK293S cells after 72 h of overexpression of full-length, WT PC-2 was firstly investigated *via* conventional TEM microscopy. As a control experiment, non-induced cells grown simultaneously were analyzed, and exhibited typical morphology without obvious abnormalities, i.e., the cellular ultrastructure was preserved upon the sample preparation procedure (**Supplementary Figure 1**). Under stress conditions, nuclei exhibited areas of highly electron-dense, condensed chromatin. Lamellar ER structures classified as karmellae were identified in close association to the nuclei (arrow in **Supplementary Figure 1a**) (Wright et al., 1988). We observed areas which were densely packed with polymorphic types of vesicles (**Supplementary Figure 1b**). These varied in size enclosed by well-distinguishable

membranes. Circular arrays of stacked lamellar membranes with regular spacing were observed in the cytoplasm (**Supplementary Figure 1c**). They are mostly located close to the nucleus, and mitochondria were frequently detected nearby. Based on their characteristic morphology and subcellular localization, these membrane arrays were identified as ER whorls, a lamellar OSER morphotype (Koning et al., 1996). Finally, patches of regular, putatively tubular membrane arrays could be observed (Yamamoto et al., 1996) (**Supplementary Figure 1d**), however, in 800 nm sections tubular structures were difficult to depict and discriminating between tubular, sinusoidal or hexagonal crystalloid ER remains was not possible. None of these OSER structures were observed in the control experiment without PC-2 expression. Different OSER types – whorls and putative crystalloid-ER – could be detected in approximately 10% of cells, but considering a section volume of 800 nm it can be assumed that the overall fraction of OSER in the cells is significantly higher.

OSER morphology in 2D

Thinner sections of the sample (50 nm) were investigated at higher magnifications. A gallery of different whorls is shown in **Supplementary Figure 2**. They are formed by stacked, lamellar membrane sheets arranged either as open (**Supplementary Figure 2a**) or closed (**Supplementary Figure 2b-d)** circles and reach a diameter of up to 2 µm. It should be noted, however, that both forms may also represent different section planes of the same organelle, as indicated by **Supplementary Figure 2c**. Indeed, the existence of open-circle whorls has been described before and was interpreted as partially open non-circularized whorls, denominated as loops (Snapp et al., 2003). The endpoints of whorl sheets arranged as open circles are formed *via* the membranes wrapping back by 180° and thus exhibiting extreme curvature (**Supplementary Figure 2a**). The stacked membranes feature a regular spacing, which is more pronounced in closed-circle whorls (**Supplementary Figure 2d**). Multiple whorls can occur in one cell, and vesicles are often detected enclosed by or near the circular membrane stacks (**Supplementary Figure 2a**, **c**). Whether they directly fuse to or bud from the ER membranes remains an open question, since fusion or fission were not observed in any section investigated. Moreover, mitochondria are found close to the whorls, consistent with previous studies describing clustering of mitochondria around OSER structures (Snapp et al., 2003). Whorls are often located close to the nucleus but a direct connection between whorls and nuclear envelope or whorls and karmellae, was not observed. In Lead citrate contrasted sections of *en bloc* Uranyl acetate-stained samples, electron dense spots in the size of ribosomes are sometimes observed lining peripheral membrane sheets (arrow in **Supplementary Figure 2d**, **e**). These are by far

more abundant in less well organized whorl-like structures and display the typical morphology of ribosome-decorated rough ER (rER) membranes. This finding points towards an organization of OSER structures into several functional sub-domains, which was reported previously (Borgese et al., 2006).

Two examples of putative crystalloid ER structures are depicted in **Supplementary Figure 3**. The tubular patches observed in the sample reached diameters of up to 2.5 µm. They are frequently located in proximity to the nucleus and close to mitochondria, as observed for the whorls. The membranes exhibit a regular pattern; however, the exact symmetric arrangement cannot be determined from the obtained section planes. In contrast to the lamellar whorls, cytoplasmic material was less abundant in the interspaces of the tubular arrays. As for whorl structures, also several tubular OSER organelles can occur in one cell. Whether they are separated from each other or interconnected required a 3D analysis.

3D analysis of OSER structures via STEM tomography

For a 3D analysis dual-axis STEM tomography was performed on 800 nm sections. Different types of OSER (lamellar, tubular and mixed morphologies) were analyzed. In all cases, the localization in proximity to the nucleus and in association with mitochondria could be confirmed. An in-depth analysis of the tomograms revealed further structural details. Three ROIs were identified in a reconstructed whorl tomogram (**Figure 1**): interactions with multiple vesicles, as well as with a mitochondrion. Again, no direct connection to the nucleus could be observed from the imaged sub-volume. Segmentation of the sub-volumes (**Figure 1i-iii**) provided further insights into whorl interactions. Ordered stacked membrane sheets constituting a major part of the whorl wrap around multiple vesicles (**Figure 2a**). ER whorl and vesicle membranes are in direct contact and fusion/fission of a vesicle with/from the terminal point of a whorl membrane could be observed (**Figure 2b**). Several dozen vesicles were identified in close contact to the whorl membranes. A mitochondrion is located at the whorl periphery in direct interaction, but no fusion processes were observed between the organelles (**Figure 2c**). The described contact site exhibits the typical characteristic of a mitochondria-associated membrane (MAM) site (Baumann & Walz, 2001).

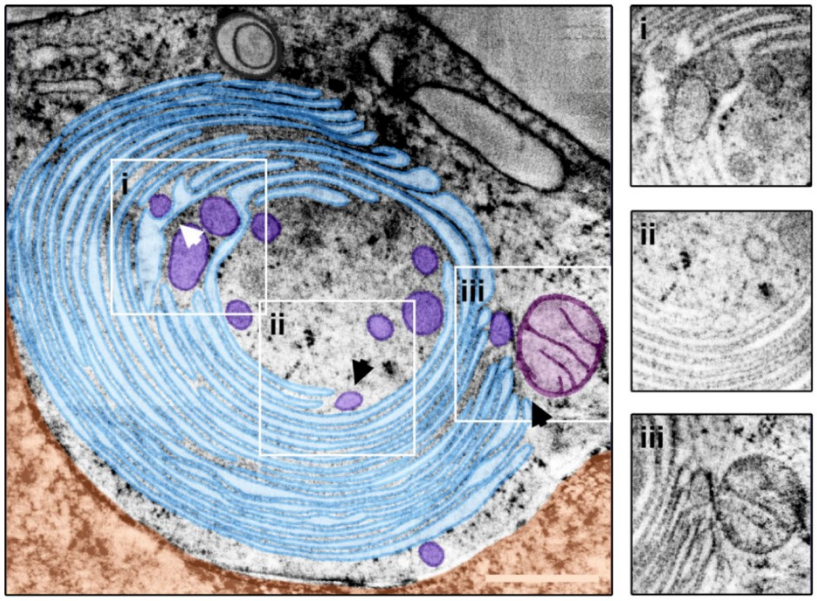

Figure 1: STEM tomography of ER whorls

Screening of the reconstructed STEM tomogram of a whorl (light blue) resulted in three ROIs, marked by boxes **i-iii**. The selected areas putatively show the integration of vesicles (dark blue) into the organelle (**i**), fusion or budding of a terminal vesicle (**ii**), and interactions with a mitochondrium (purple) (**iii**). An interaction between the nucleus (orange) and the whorl was not evident from the tomogram. Arrowheads indicate the viewing direction in the 3D close-ups depicted in **Figure 2**. Scale bar = 500 nm.

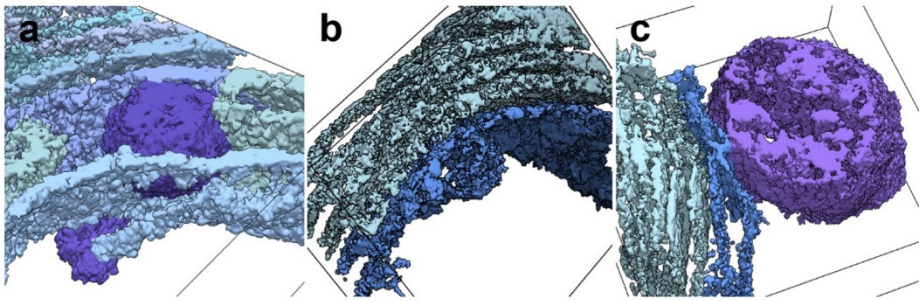

Figure 2: ER whorl morphology in 3D

Sub-volumes of a tomogram were segmented and rendered in 3D to visualize details of the ER whorl morphology. **a)** A vesicle (dark blue) embedded into a highly ordered, regular array of stacked whorl membranes (light blue). **b)** Vesicle fusion or fission to/from a whorl membrane. **c)** Direct interaction between whorl membrane (blue) and mitochondrion (violet). Black outlines indicate the sub-tomogram boundaries.

In-depth 3D analysis was also performed to reveal structural details of the tubular ER morphotype. The intracellular localization of the crystalloid-ER patch depicted and analyzed in **Figure 3** is very similar to the localization of the ER whorl described above. Surrounded by several mitochondria and vesicular structures, it is also found near the nucleus. The reconstructed tomogram revealed the presence of a vesicle wedged between the crystalloid-ER and the nucleus in the area depicted in **Figure 3i**, which is not evident from the central tomogram slice. Thus, segmentation and 3D rendering were performed to allow for a better spatial impression of the crystalloid-ER itself (**Figure 3ii**) and its intracellular interaction network. While the crystalloid-ER itself does not directly contact the surrounding mitochondria, it closely approaches the nuclear envelope (**Figure 4a**). Moreover, a singular vesicle could be identified in the contact area, interacting with both structures (**Figure 4b**). Fusion or fission of this vesicle with either organelle was not observed. In contrast to the ER whorl described above, no vesicles are present embedded within the crystalloid-ER patch. The tubular nature and regular array of the crystalloid-ER membranes can be captured best from the cut-open view (**Figure 4c**). From the reconstructed tomogram (**Figure 3**) and from the 3D visualization it becomes evident that each crystalloid-ER tube is surrounded by its own membrane. The single tubes are arranged in rows with a consistent offset of half the diameter of a tube, resulting in the most space-filling arrangement possible. The tubes' interior, equivalent to the ER lumen, appears electron-lucent in sections. Consistently, also in the reconstructed tomogram hardly any density blob was present. In contrast, the space in between the tubes is oftentimes filled with electron-dense cytoplasmic material and always confined by the membranes of three neighboring tubes.

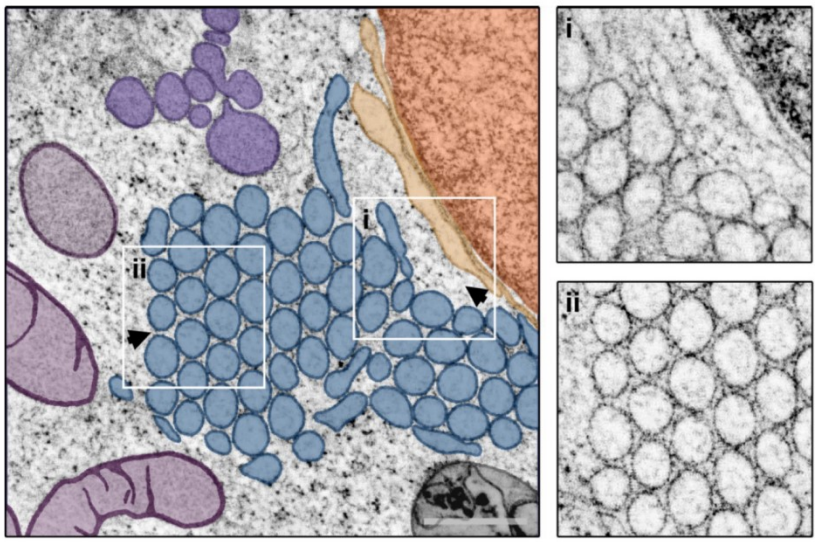

Figure 3: Crystalloid-ER morphology

The crystalloid-ER (blue), formed by a regular array of tubular ER membranes, is located in close vicinity to nucleus (dark orange) and nuclear envelope (orange) and surrounded by multiple mitochondria (violet) and vesicular structures (violet blue, grey). Putative interactions between crystalloid-ER and the nuclear envelope (**i**), as well as the tubular nature of the crystalloid-ER itself (**ii**) were analyzed further via segmentation and 3D visualization of the tomogram. Arrowheads indicate the viewing direction in **Figure 4**. Scale bar = 500 nm.

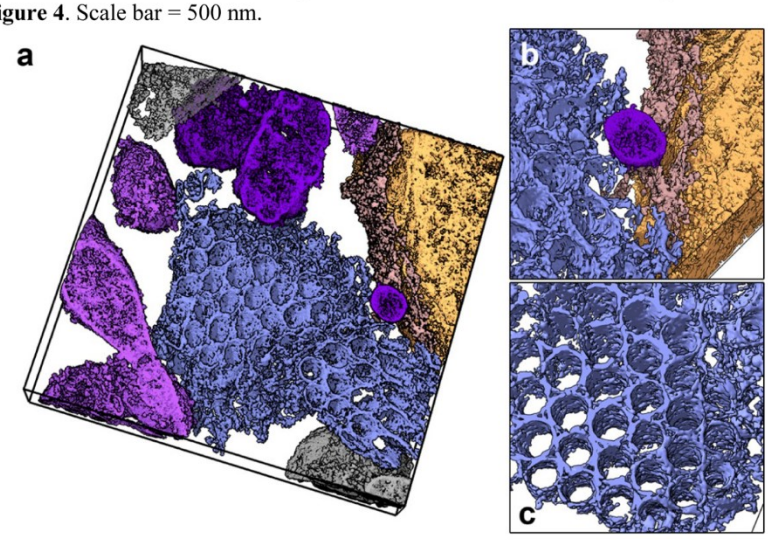

Figure 4: Crystalloid-ER morphology in 3D

a) Segmented and 3D-rendered visualization of the crystalloid-ER (blue) in its cellular context, surrounded by multiple mitochondria (violet). **b)** Detail of a vesicle (dark blue) mediating contact between the crystalloid-ER (blue) and the nuclear envelope (brown). **c)** Cut-open detail of the crystalloid-ER, highlighting the regular nature of the tubular ER membrane array.

Whorls and crystalloid-ER occur simultaneously in one cell (**Figure 5**). Interestingly, in this mixed morphotype only the crystalloid-ER exhibits direct interactions with the nuclear envelope, while the whorl does not and is localized farther away from the nucleus. Notably, crystalloid-ER and whorl are located adjacent to each other in the mixed morphotype observed here (**Figure 5i**). Again, multiple vesicles and vesicular structures are found near the ER, some of them making contact to the crystalloid-ER (**Figure 5ii**). Segmentation and 3D visualization provide further insights into the complex organization of the ER membranes in the mixed morphotype (**Figure 6a**). The tubular crystalloid-ER membranes and the lamellar whorl membrane sheets can be well distinguished and traced throughout the volume of the tomogram. Remarkably, crystalloid-ER and whorl exhibit a very pronounced interaction site with noticeable direct membrane contacts (**Figure 6b**). This further emphasizes the common origin of the morphologically very different organelles. While some crystalloid-ER tubes span the whole tomogram volume, others only reach to about half of the tomogram depth and are at least partially capped by slightly domed membranes at their end points, resulting in a presumably entirely confined crystalloid-ER lumen. This finding is further supported by the electron-lucent appearance of the crystalloid-ER tubes' interior in sections (**Supplementary Figure 3**). As described before for the single organelles, also in the mixed morphotype the ER patches are surrounded by and in close contact with multiple vesicles and vesicular structures. In the sub-volume of the cell investigated here, a prominent vesicle cluster could be identified near both the crystalloid-ER and the nucleus, potentially providing an interaction platform between the two organelles (**Figure 6c**).

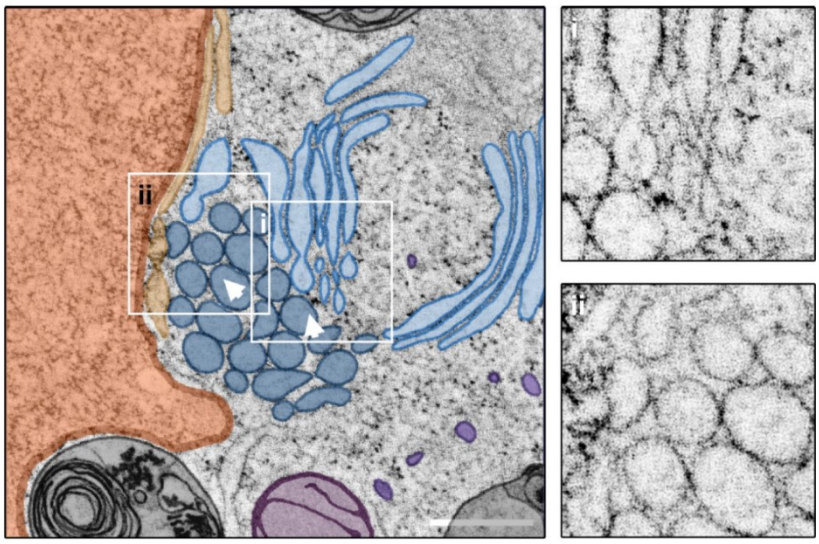

Figure 5: Mixed crystalloid-ER and whorl morphology

Central slice through a STEM tomogram showing a patch of crystalloid-ER (dark blue) located in close proximity to a putative ER whorl (light blue) in its intracellular environment. Closer inspection of the reconstructed tomogram reveals a direct connection between the two ER morphotypes (**i**), as well as the presence of multiple vesicles (not present in the central tomogram section), located near the nucleus (orange) and contacting the crystalloid ER (**ii**). Arrowheads indicate the viewing direction in **Figure 5**. Scale bar = 500 nm.

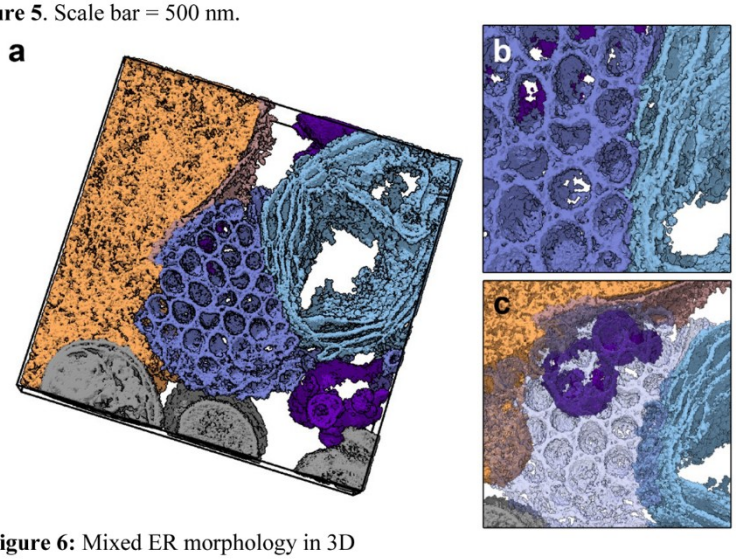

Figure 6: Mixed ER morphology in 3D

a) Segmentation and 3D rendering of a mixed ER morphotype consisting of a patch of crystalloid-ER (dark blue) and an adjacent ER whorl (light blue). Both are located in proximity to the nucleus (orange) and nuclear envelope (brown), and surrounded by multiple vesicles (violet). **b)** The direct contact between the two ER morphotypes becomes evident from the 3D visualization. **c)** The tight association of crystalloid-ER (transparent), nucleus and vesicles.

15

Crystalloid-ER and whorl architecture

ER whorls and crystalloid-ER patches are large in comparison to the ER of non-induced HEK293S cells (**Figure 7**). In all cases, the ER patches span the whole height (Z axis) of the tomogram, and consequently exceed the section thickness of 800 nm. In contrast, the organelles' maximum planar dimensions range from ~1.4 µm to ~2.2 µm for each morphotype. Since it is not possible to capture the organelles' entire dimensions in a single section, their exact volumes cannot be determined *via* STEM tomography. In addition, it has to be considered that more than one whorl or crystalloid-ER patch can be found per cell, consequently multiplying the organelles' total volume. While it is evident that ER volume and ER membrane surface both increase significantly during over-expression of WT PC-2 in HEK293S cells, it was observed that the overall cellular volume remains constant. ER whorls and crystalloid-ER always occur separated and do not intersect or alternate with each other; intermediate forms were not detected in the imaged sub-volumes. The strict segregation of sheets and tubes and the consistency of the two very different shapes requires a shaping mechanism. Thorough inspection of the tomograms reveals a nearly perfectly circular cross-section for the crystalloid-ER tubes in the X-Y-plane with a quite regular diameter of ~160 nm (average of ten tubes) (**Supplementary Figure 4a**). Each single tube is surrounded by six more tubes, resulting in an approximately triangular cross-section of the tubes' interspace. Hypothetical connections between these interspaces yield the apparent hexagonal-symmetric arrangement of the crystalloid-ER membranes (**Supplementary Figure 4b**). The resulting regular array of tubes is also determined by the constant, but moderate membrane curvature in the X-Y-plane. Curvature in the Z-direction is restricted to the terminal caps of the crystalloid-ER tubes. In stark contrast to the crystalloid-ER, whorls are composed of stacked membrane sheets arranged in a regular,

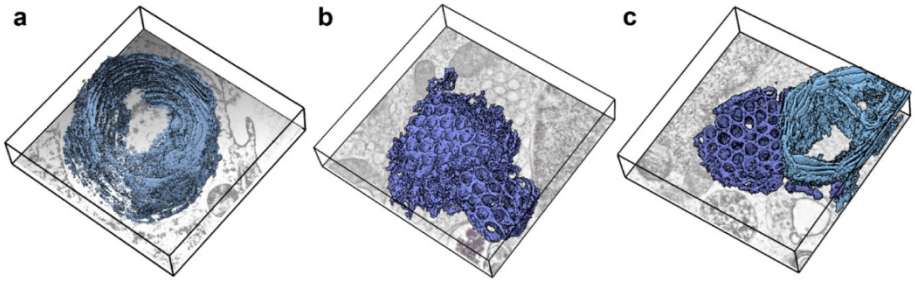

Figure 7: Crystalloid-ER and whorl dimensions

ER whorl (light blue) and crystalloid-ER (dark blue) volumes are displayed for the three STEM tomograms (**a – c**) in 3D. The tomogram dimensions are indicated by black boxes, the bottom tomogram slices are depicted for a better spatial orientation. The depictions consistently highlight the overwhelming abundance of the ER morphotypes in the respective cell sub-volumes.

lamellar array (**Supplementary Figure 4c**). At their terminal points, the membrane sheets wrap back in a 180° turn, thereby enclosing the very narrow ER lumen. This results in two opposite types of membrane curvature prevalent in whorls (**Supplementary Figure 4d**). While the major part of whorl membranes exhibits only low curvature, the terminal turns feature an extreme curvature, oriented inversely to the curvature found in the rest of the membrane. According to a prior classification these areas exhibit high positive membrane curvature with respect to the cytoplasm (McMahon & Gallop, 2005). In contrast to the crystalloid-ER, the low curvature in the whorl membrane stack does not only occur in the X-Y-plane, but also extends in the Z-dimension, resulting in a presumably almost globular shape of the entire organelle in 3D. It should be mentioned, however, that not all whorls examined in this study exhibit the same degree of order (see also **Supplementary Figure 2**).

The ER lumen is commonly described to be a continuous space, providing the ER with a defined environment tailored to the required biochemical properties. Vesicles have been found only in close proximity to the crystalloid-ER, but not integrated into the organelle itself. Thus, direct connections between adjacent crystalloid-ER tube membranes seem the most straightforward mode to establish a continuous ER lumen. Indeed, a putative connection site could be identified in a tomogram slice (**Supplementary Figure 5a**). Threshold-based isosurface representation of the respective tomogram sub-volume was successfully applied to achieve an unbiased depiction of the crystalloid-ER membranes in the respective tomogram sub-volume (**Supplementary Figure 5b**). In a tilted view (**Supplementary Figure 5c**), the narrow connection of the two tubes, approximately 20 nm in height, can be visualized, suggesting the presence of direct connections between crystalloid-ER tubes resulting in a continuous ER lumen. While no such connection could be visualized in a whorl, it should be noted that the whorl membranes are frequently found very close to each other and therefore may most probably also establish some sort of contact. It seems thus likely that also the whorl exhibits a continuous ER lumen. Moreover, multiple vesicles could be identified incorporated into the whorls, providing further potential to exchange cargo between the whorl lamella.

Discussion

Dual-axis STEM tomography to investigate organellar architecture in 3D

The use of STEM tomography at 200 kV to resolve cellular details at comparably high resolution in 3D has been demonstrated before (Walther *et al.*, 2018; Rachel *et al.*, 2020). Here, we could demonstrate that the resolution is as good to resolve the membrane architecture of OSER structures, which was not possible in our previous FIB-SEM analysis of the same sample (Wilkes *et al.*, 2017), nor in a recent FIB-SEM analysis and 3D reconstruction of ER whorls in mammalian cells (Xu *et al.*, 2020). Notably, an early freeze-fracture study pointed towards a tubular nature of the crystalloid-ER in UT-1 cells, representing a 3D-impression of the organelle but lacking the power to resolve single membranes (Anderson *et al.*, 1983). In the present study, the reconstructed cellular volumes of 800 nm unambiguously reveal the presence of membrane-enclosed tubes in the crystalloid-ER and lamellar membrane sheets in ER whorls as we can trace each of the single ER membranes (**Figure 1**, **Figure 3** and **Figure 5**). Dual-axis STEM tomography of plastic-embedded samples thus bridges the gap between cryo-TEM tomography of isolated organelles and FIB-SEM analysis of organelles in their cellular context at nm resolution on the one side and super-resolution light-microscopy on the other side. In summary, the method provided valuable insights into the diverse intracellular interaction network of OSER structures and enabled the visualization of their membrane architecture at an unprecedented level of detail.

Whorls as integral parts of the ER network

ER whorls and crystalloid ER co-exist in comparable size and abundance when PC-2 is overexpressed in HEK293S cells. Moreover, a mixed crystalloid-ER and whorl morphotype was identified (**Figure 5**, **Figure 6**). ER whorls are directly associated to mitochondria (**Figure 2c**), classifying the whorl membrane interface as MAM site, an ER domain closely involved in lipid biosynthesis (Baumann & Walz, 2001). Accordingly, ER whorls might be involved in lipid biosynthesis to account for the increased need for lipids to assemble the enormous amount of bulk ER present in both crystalloid-ER and whorls (**Figure 7**). Ribosomes were identified at peripheral ER whorl membrane sheets (**Supplementary Figure 2**). Taken together, these results point towards a role of ER whorls as locations of active protein and lipid biosynthesis and the lamellar whorl membrane sheets can be assumed to be the result of continuous ER membrane growth. It was reported that a global increase of the yeast ER membrane is issued by UPR signaling and accomplished *via* expansion of lamellar membrane sheets to overcome ER stress (Schuck et al., 2009).

Consequently, we have to ask the question whether the extreme OSER morphotypes observed upon PC2 over-expression are an indication of an acute, dangerous stress situation for the cell, or rather an ordinary cellular reaction to alleviate and tackle such condition? Given that increased PC-2 levels correlate with enhanced cell viability and proliferation, and that elevated Ca^{2+} promotes the activation of pro-survival pathways, we suggest that PC-2 expression is enhanced under conditions of stress to help protect against cell death. It was recently shown that PC-2 up-regulation occurred under pathological conditions in multiple tissue types, including the kidney, liver, brain, and hearts of both humans and animal models. *Vice versa*, PC-2 knock-down and knock-out cells showed increased susceptibility to stress-induced cell death (Brill *et al.*, 2020). Consequently, PC-2 might act in all tissues as a ubiquitous stress response protein whose expression levels correlate with cell survival in response to stress.

Crystalloid-ER architecture

Crystalloid-ER formation has been generally reported both under *in vivo* conditions and during protein inhibition or over-expression in multiple systems (Baumann & Walz, 2001). Our tomographic analysis now revealed, for the first time, the tubular nature of the crystalloid-ER at a resolution sufficient to trace the ER membranes and to distinguish the single crystalloid-ER tubes showing that they are interconnected (**Figure 3** and **Figure 4**, **Supplementary Figure 5**), supporting the idea of a continuous crystalloid-ER lumen. There is no ultrastructural evidence for active protein biosynthesis in crystalloid-ER, it appears as if PC-2 accumulates in crystalloid-ER patches (Wilkes *et al.*, 2017).

A proliferation of crystalloid-ER from lamellar ER membrane sheets was suggested in UT-1 cells upon expression of increased amounts of 3-hydroxy-3-methylglutaryl coenzyme A (HMG-CoA) reductase, the rate limiting enzyme in cholesterol biosynthesis (Pathak et al., 1986) and in COS cells upon over-expression of mouse microsomal aldehyde dehydrogenase (msALDH). Similar to PC-2, truncated versions of the msALDH protein did not induce crystalloid formation (Masaki et al., 1994; Yamamoto et al., 1996). The formation of crystalloid-ER appears to be mediated *via* homotypic soluble domain interactions (Baumann & Walz, 2001; Snapp et al., 2003). Accordingly, membrane-protein induced ER membrane curvature was later demonstrated both *in vitro* and *in vivo* (Hu et al., 2008).

The role of crystalloid-ER and whorls in the cell

Both crystalloid-ER and whorls occupy a significant portion of the cells' total volume questioning if the expanded ER is still functional. At the investigated time point, the cultivated cells showed no significant differences in overall fitness in comparison to the control, as judged e.g. from the presence of dead cells in the culture or detachment of adherent cells from the culture dish. The ER is consistently described as the largest cellular membrane system (Griffiths et al., 1984), and numerous evidence support the idea of an entirely continuous ER lumen (Baumann & Walz, 2001; Snapp et al., 2003). Our ultrastructural STEM investigations consistently revealed the presence of an intact interaction network for all ER morphotypes including the nuclear envelope, vesicles and mitochondria, opening up multiple possibilities for intracellular communication and interaction. This is in agreement with observations of a distinct co-localization of ER sub-domains with their intracellular interaction partners (Baumann & Walz, 1989). These observations suggest that both ER whorls and crystalloid-ER are indeed functional organelles.

Nevertheless, crystalloid-ER and whorls represent two very distinct morphotypes. Notably, despite the existence of a mixed morphotype, no intermediate forms, intersections between the two types or altered tube-lamella arrays were detected in the sample. Crystalloid-ER tubes and lamellar whorl membrane sheets are thus separated from each other. Based on these findings, a random formation of either crystalloid-ER tubes or whorl membrane lamella can be excluded assuming that the two morphotypes represent sub-domains accomplishing different tasks within the ER. Also, the ER itself is divided into nuclear envelope and peripheral ER, composed of rER and sER. In this study, ribosome-like structures could be identified on some peripheral membrane sheets in less well-ordered whorls (**Supplementary Figure 2**) but were not detected in crystalloid-ER patches. Moreover, a contact to a mitochondrion and the formation of the MAM site could be observed exclusively for whorls (**Figure 2c**).

Conclusions

Imaging biological samples can be a very difficult process, and the method of choice needs to be chosen with great care to finally obtain meaningful results. This is all the more the case if uncommon phenotypes are to be analyzed and depicting the object of interest in its natural background is a prerequisite to avoid faulty conclusions. Here, we demonstrate the use of dual-axis STEM tomography of resin-embedded samples at 200 keV to address this type of research questions. The method proofed suitable to investigate a larger cellular sub-volume than in the 'classical' TEM tomography approach, at a resolution sufficient to trace organellar membranes. In summary, we were able to describe the morphology of ER whorls and crystalloid-ER in 3D at an unprecedented level of detail and with great confidence.

Author contributions

VH, CZ: Conceptualization. RR: Methodology. VH, RR: Investigation. VH: Formal analysis, Visualization, Writing – Original draft. VH, CZ, RR: Writing – Review & Editing. CZ: Project administration.

Conflict of Interest

The authors declare no conflict of interest.

Acknowledgements

The authors would like to thank Ralph Witzgall for access to sample preparation equipment and the electron microscope, as well as Sabine Ruppel and Olga Maier for technical support.

Funding:

This work was supported by a DFG grant (SFB1350 / project A5) to Prof. C. Ziegler.

References

Abdellatif, M. E. A., Sinzger, C., & Walther, P. (2018): Investigating HCMV entry into host cells by STEM tomography. *J Struct Biol,* 204(3):406-419.

Anderson, R. G. W., Orci, L., Brown, M. S., *et al.* (1983): Ultrastructural Analysis of Crystalloid Endoplasmic Reticulum in UT-1 cells and its Disappearance in Response to Cholesterol. *J. Cell. Sci.,* 63:1-20.

Baumann, O., & Walz, B. (1989): Topography of Ca^{2+}-sequestering endoplasmic reticulum in photoreceptors and pigmented glial cells in the compound eye of the honeybee drone. *Cell Tissue Res.,* 255:511-522.

Baumann, O., & Walz, B. (2001): Endoplasmic Reticulum of Animal Cells and Its Organization into Structural and Functional Domains. In K. W. Jeon (Ed.), *International Review of Cytology - A Survey of Cell Biology* (Vol. 205). San Diego: Academic Press.

Borgese, N., Francolini, M., & Snapp, E. (2006): Endoplasmic reticulum architecture: structures in flux. *Curr Opin Cell Biol,* 18(4):358–364.

Brill, A. L., Fischer, T. T., Walters, J. M., *et al.* (2020): Polycystin 2 is increased in disease to protect against stress-induced cell death. *Sci. Rep.,* 10(386):1-15.

Buser, C., & Walther, P. (2008): Freeze-substitution: the addition of water to polar solvents enhances the retention of structure and acts at temperatures around –60◦C. *J. Microsc.,* 230(2):268–277.

Chin, D. J., Luskey, K. L., Anderson, R. G. W., *et al.* (1982): Appearance of crystalloid endoplasmic reticulum in compactinresistant Chinese hamster cells with a 500-fold increase in 3-hydroxy-3-methylglutaryl-coenzyme A reductase. *PNAS,* 79:1185-1189.

Elbaum, M. (2018): Quantitative Cryo-Scanning Transmission Electron Microscopy of Biological Materials. *Adv. Mater.,* 30(1706681):1-6.

Federovitch, C. M., Ron, D., & Hampton, R. Y. (2005): The dynamic ER: experimental approaches and current questions. *Curr. Opin. Cell Biol.,* 17:409-414.

Griffiths, G., Warren, G., Quinn, P., *et al.* (1984): Density of Newly Synthesized Plasma Membrane Proteins in Intracellular Membranes. I . Stereological Studies. *J. Cell Biol.,* 98:2133-2141.

Harding, H. P., & Ron, D. (2002): Endoplasmic Reticulum Stress and the Development of Diabetes. *Diabetes,* 51(3):S455-S461.

Hohmann-Marriott, M. F., Sousa, A. A., Azari, A. A., *et al.* (2009): Nanoscale 3D cellular imaging by axial scanning transmission electron tomography. *Nat Methods,* 6:729–731.

Hu, J., Shibata, Y., Voss, C., *et al.* (2008): Membrane Proteins of the Endoplasmic Reticulum Induce High-Curvature Tubules. *Science,* 319(5867):1247-1250.

Koning, A. J., Roberts, C. J., & Wright, R. L. (1996): Different Subcellular Localization of *Saccharomyces cerevisiae* HMG-CoA Reductase Isozymes at Elevated Levels Corresponds to Distinct Endoplasmic Reticulum Membrane Proliferations. *Mol. Biol. Cell.,* 7:769-789.

Kremer, J. R., Mastronarde, D. N., & McIntosh, J. R. (1996): Computer Visualization of Three-Dimensional Image Data Using IMOD. *J. Struct. Biol.,* 116(13):71–76.

Luther, P. K. (2006): Sample Shrinkage and Radiation Damage of Plastic Sections. In J. Frank (Ed.), *Electron Tomography* (Second Edition ed.). New York: Springer Science+Business Media.

Masaki, R., Yamamoto, A., & Tashiro, Y. (1994): Microsomal Aldehyde Dehydrogenase Is Localized to the Endoplasmic Reticulum via Its Carboxyl-Terminal 35 Amino Acids. *J. Cell Biol.,* 126(6):1407-1420.

McBride, E. L., Rao, A., Zhang, G., *et al.* (2018): Comparison of 3D cellular imaging techniques based on scanned electron probes: serial block face SEM vs. axial bright-field STEM tomography. *J Struct Biol.,* 202(3):216–228.

McIntosh, R., Nicastro, D., & Mastronarde, D. (2005): New views of cells in 3D: an introduction to electron tomography. *TRENDS in Cell Biology,* 15(1):43-51.

McMahon, H. T., & Gallop, J. L. (2005): Membrane curvature and mechanisms of dynamic cell membrane remodelling. *Nature,* 438:590-596.

Pathak, R. K., Luskey, K. L., & Anderson, R. G. W. (1986): Biogenesis of the Crystalloid Endoplasmic Reticulum in UT-1 Cells: Evidence That Newly Formed Endoplasmic Reticulum Emerges from the Nuclear Envelope. *J. Cell Biol.,* 102:2158-2168.

Pettersen, E. F., Goddard, T. D., Huang, C. C.*, et al.* (2004): UCSF Chimera—A Visualization System for Exploratory Research and Analysis. *J Comput Chem,* 25:1605–1612.

Pintilie, G. D., Zhang, J., Goddard, T. D.*, et al.* (2010): Quantitative analysis of cryo-EM density map segmentation by watershed and scale-space filtering, and fitting of structures by alignment to regions. *J. Struct. Biol.,* 170(3):427-438.

Rachel, R., Meyer, C., Klingl, A.*, et al.* (2010): Chapter 3 - Analysis of the Ultrastructure of Archaea by Electron Microscopy. *Methods Cell Biol.* 96:47-69.

Rachel, R., Walther, P., Maaßen, C.*, et al.* (2020): Dual-axis STEM tomography at 200 kV: Setup, performance, limitations. *J Struct Biol.,* 211(107551).

Saxton, W. O., Baumeister, W., & Hahn, M. (1984): Three-Dimensional Reconstruction of Imperfect Two-Dimensional Crystals. *Ultramicroscopy,* 13:57-70.

Schroeder, M., & Kaufman, R. J. (2005): The Mammalian Unfolded Protein Response. *Annu. Rev. Biochem.,* 74:739–789.

Schuck, S., Prinz, W. A., Thorn, K. S.*, et al.* (2009): Membrane expansion alleviates endoplasmic reticulum stress independently of the unfolded protein response. *J. Cell Biol.,* 187(4):525–536.

Snapp, E. L., Hegde, R. S., Francolini, M.*, et al.* (2003): Formation of stacked ER cisternae by low affinity protein interactions. *J. Cell Biol.,* 163(2):257–269.

Sousa, A. A., Azari, A. A., Zhang, G.*, et al.* (2011): Dual-axis electron tomography of biological specimens: extending the limits of specimen thickness with bright-field STEM imaging. *J Struct Biol.,* 174(1):107–114.

Stowell, M. H. B., Marks, B., Wigge, P.*, et al.* (1999): Nucleotide-dependent conformational changes in dynamin: evidence for a mechanochemical molecular spring. *Nat. Cell Biol.,* 1:27-32.

Takei, K., Mignery, C. A., Mugnaini, E.*, et al.* (1994): Inositol 1,4,5-Trisphosphate Receptor Causes Formation of ER Cisternal Stacks in Transfected Fibroblasts and in Cerebellar Purkinje Cells. *Neuron,* 12:327-342.

Villinger, C., Gregorius, H., Kranz, C.*, et al.* (2012): FIB/SEM tomography with TEM-like resolution for 3D imaging of high-pressure frozen cells. *Histochem Cell Biol,* 138:549–556.

Voeltz, G. K., Rolls, M. M., & Rapoport, T. A. (2002): Structural organization of the endoplasmic reticulum. *EMBO Rep.,* 3(10):944–950.

Walter, P., & Ron, D. (2011): The Unfolded Protein Response: From Stress Pathway to Homeostatic Regulation. *Science,* 334:1081-1086.

Walther, P., Bauer, A., Wenske, N.*, et al.* (2018): STEM tomography of high-pressure frozen and freeze-substituted cells: a comparison of image stacks obtained at 200 kV or 300 kV. *Histochem. Cell Biol.,* 150:545–556.

Walther, P., Schmid, E., & Höhn, K. (2013): High-Pressure Freezing for Scanning Transmission Electron Tomography Analysis of Cellular Organelles. In D. J. Taatjes & J. Roth (Eds.), *Cell Imaging Techniques: Methods and Protocols* (pp. 525-535). New York: Humana Press.

Walther, P., & Ziegler, A. (2002): Freeze substitution of high-pressure frozen samples: the visibility of biological membranes is improved when the substitution medium contains water. *J. Microsc.,* 208(1):3–10.

Wilkes, M., Madej, M. G., Kreuter, L.*, et al.* (2017): Molecular insights into lipid-assisted Ca^{2+} regulation of the TRP channel Polycystin-2. *Nat. Struct. Mol,* 24(2):123-132.

Wolf, S. G., Shimoni, E., Elbaum, M.*, et al.* (2018): STEM Tomography in Biology. In E. Hanssen (Ed.), *Cellular Imaging. Biological and Medical Physics, Biomedical Engineering* (pp. 33-60). Cham: Springer.

Wright, R., Basson, M., D'Ari, L.*, et al.* (1988): Increased Amounts of HMG-CoA Reductase Induce "Karmellae": A Proliferation of Stacked Membrane Pairs Surrounding the Yeast Nucleus. *J. Cell Biol.,* 107:101-114.

Xu, F., Du, W., Zou, Q.*, et al.* (2020): COPII mitigates ER stress by promoting formation of ER whorls. *Cell Res.,* 31:141–156.

Yakushevska, A. E., Lebbink, M. N., Geerts, W. J. C.*, et al.* (2007): STEM tomography in cell biology. *J Struct Biol.,* 159(3):381-391.

Yamamoto, A., Masaki, R., & Tashiro, Y. (1996): Formation of crystalloid endoplasmic reticulum in COS cells upon overexpression of microsomal aldehyde dehydrogenase by cDNA transfection. *J. Cell. Sci.,* 109:1727-1738.

Supplementary figures:

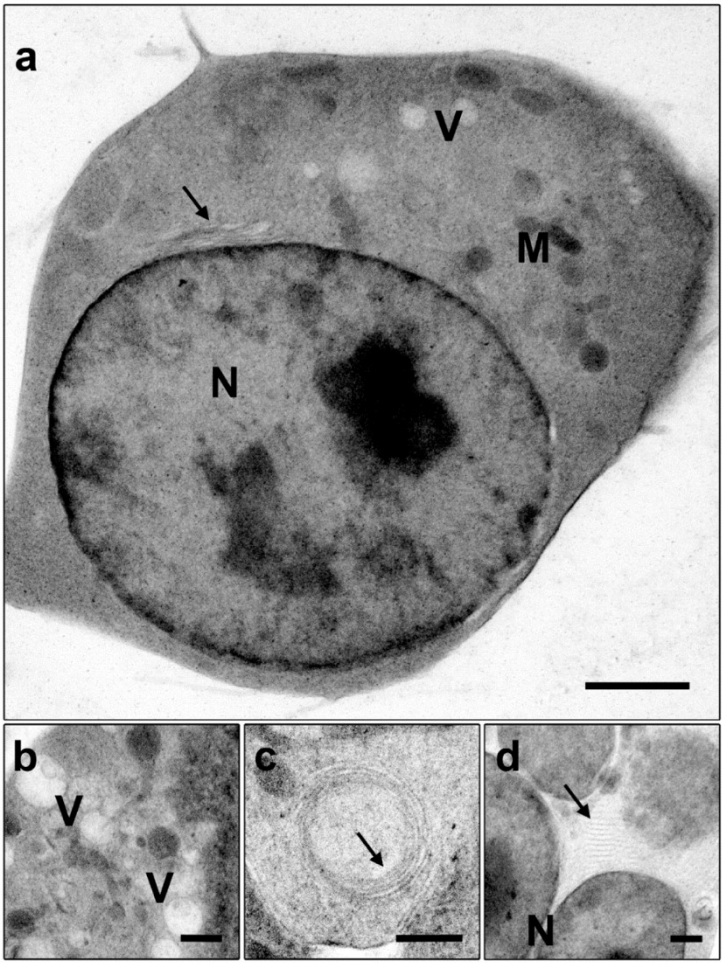

Supplementary Figure 1: Morphology of HEK cells upon over-expression of PC-2

a) TEM of an 800 nm section of a HEK293S GnTI$^-$ cell after 72 h of overexpression of WT PC-2 proofs good ultra-structural sample preservation, evident from clearly confined electron-dense mitochondria (M), electron-transparent vesicles (V), membraneous structures (arrow) and the well-defined nucleus (N). Scale bar = 2000 nm. **b, c and d)** Zooms on different areas in the sample reveal the presence of diverse membraneous organelles, such as vesicles (b), putative lamellar (c) and tubular (d) OSER structures. Scale bars = 1000 nm.

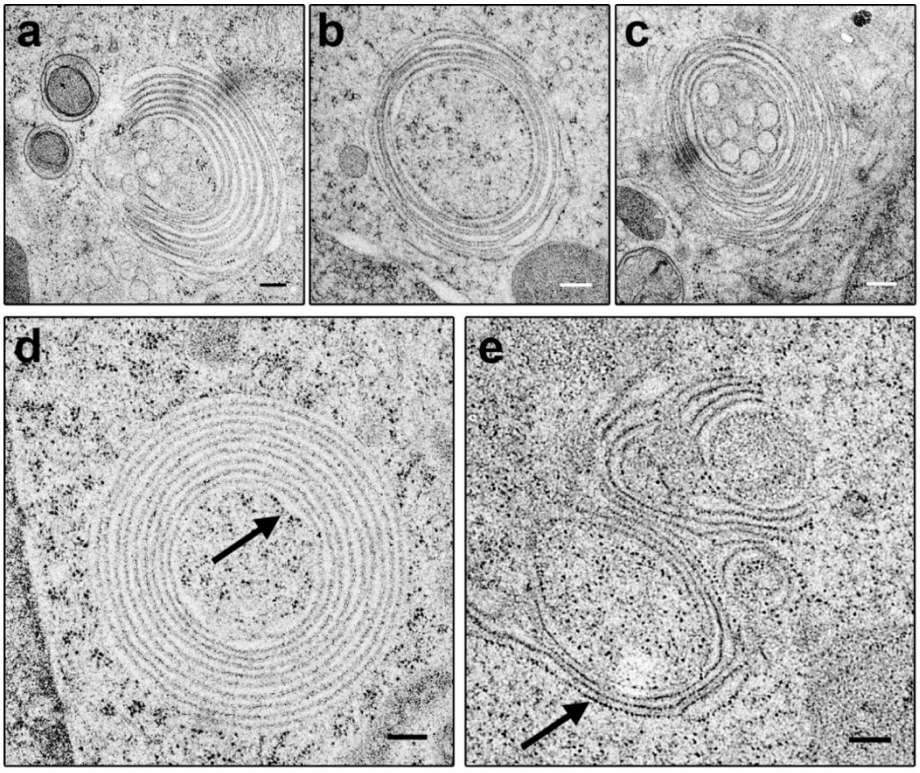

Supplementary Figure 2: ER whorl morphology

TEM of 50 nm sections of high-pressure frozen, freeze-substituted, OsO4 (a - c) or UAc / PbCi (d, e) stained and resin-embedded HEK293S GnTI- cells after 72 h of over-expression of WT PC-2. **a-c)** Examples of whorl structures. Whorls are often found in close association to vesicles and reach a diameter of up to 2 µm. The ER membranes exhibit regular spacing and enclose electron-dense cytoplasmic material. They occur as open (a) or closed (b, c) circles. **d, e)** In UAc stained and PbCi contrasted samples, electron dense spots (arrows) can be found lining up on some ER membranes, putatively representing ribosome-decorated rER. Scale bars = 200 nm.

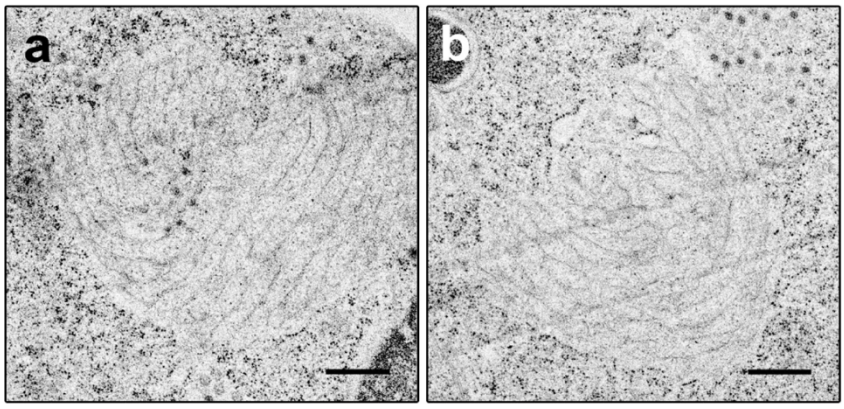

Supplementary Figure 3: Crystalloid-ER morphology

a, b) Morphology of putative crystalloid ER structures on 50 nm sections of high-pressure frozen, freeze-substituted, resin-embedded and UAc / PbCi stained HEK293S GnTI- cells after 72 h of overexpression of WT PC-2. The examples illustrate the difficulty of identifying the symmetric tubular arrays in non-perfect cross sections. Scale bars = 500 nm.

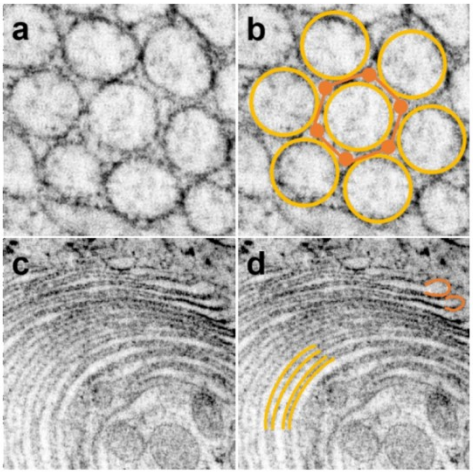

Supplementary Figure 4: Crystalloid-ER and whorl symmetry

a) Detail of a crystalloid-ER tube in cross-section, surrounded by six other tubes. The hexagonal-symmetric arrangement of the tubes is indicated in **b)** Tubes are depicted in gold, the tubes' interspaces are indicated in orange. **c)** Detail of a cross-section in a whorl, highlighting the regular array of stacked membranes and the narrow terminal turns of the ER membranes. **d)** Stacked membranes feature a steady, but low curvature (gold), while the terminal membrane turns exhibit extreme inverse curvature (orange).

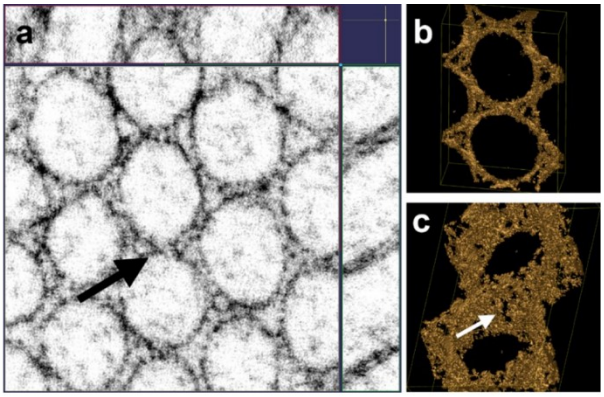

Supplementary Figure 5: Crystalloid-ER tube connection

a) Slice through a reconstructed crystalloid-ER tomogram in the X-Y-plane and the X-Z- (right) and Y-Z- (top) planes, respectively. A connection between two neighboring ER tubes is marked by an arrow. **b)** Isosurface depiction of the two connected tubes, illustrating the threshold-based tracing of the ER membranes. **c)** A tilted view of the same sub-volume, revealing a putative, narrow connection between the tubes (arrow).

Supplementary tables:

Supplementary table 1: Freeze substitution protocol

temperature	step	solution	incubation time(s)
-140 °C	stepwise substitution of intracellular H_2O, mild chemical fixation and en-bloc staining	substitution solution	1 x 30 min
-140 °C to -90 °C		substitution solution	1 x 3 h
-90 °C		substitution solution	1 x 4 h
-90 °C to -60 °C		substitution solution	1 x 3 h
-60 °C		substitution solution	1 x 4 h
-60 °C to -30 °C		substitution solution	1 x 3 h
-30 °C		substitution solution	1 x 4 h
-30 °C to 0 °C		substitution solution	1 x 3 h
0 °C		substitution solution	1 x 3 h
0 °C	removal of substitution solution	Acetone p. a.	2 x 10 min
0 °C to 4 °C		Acetone p. a.	1 x 20 min
4 °C to 25 °C	removal of Acetone and stepwise infiltration with Epon™ 812 substitute embedding resin	Acetone / resin 2 + 1	1 x 1 h
25 °C		Acetone / resin 2 + 1	1 x 1 h
25 °C		Acetone / resin 1 + 1	1 x 2 h
25 °C		Acetone / resin 1 + 2	1 x 16 h
30 °C		resin (fresh)	1 x 2 h
60 °C	resin polymerization	resin	1 x 2 d

Supplementary table 2: Tilt scheme for dual-axis tomography

	purpose	**tasks**	**acquisition scheme**	
series 1	walking up	focusing tracking	0° to +66°	5° increment
series 2	data acquisition	focusing tracking exposure	+66° to +58°	1.0° increment
			+58° to +15°	continuously increasing increment
			+15° to -15°	2.0° increment
			-15° to -58°	continuously decreasing increment
			-58° to -66°	1.0° increment
series 3	walking down	focusing tracking	-66° to 0°	5° increment

Acknowledgements

I would like to take the opportunity here to thank everyone who jointly went part of this journey with me. This thesis would not have been possible without the amazing help and support of many people; naming everybody would certainly exceed this page.

First, I want to thank my supervisor, Christine Ziegler, and my mentor, Reinhard Rachel, for their continuous personal and professional support and the outstanding possibility to actively participate in all aspects of electron microscopic research. Your trust and believe in me helped me growing into the scientific community.

I had the possibility to travel a lot and to meet fellow microscopists in many places. I would like to thank everyone for their warm welcome, dedicated support and the possibility to learn and discover a lot; namely, T. Heuser and his outstanding team in Vienna, B. Boettcher and her group in Wuerzburg, M. Strauss in Martinsried, P. Kastritis and F. Hamdi in Halle, P. Walther and his group in Ulm, and E. Katzmann at JEOL Germany GmbH, Freising.

As an exciting addition to my own work, I was also able to participate in a number of joint projects, and I would like to explicitly thank J. Pané-Farré, L. Forrest and V. Leone, G. Hagelueken and M. Peter, and D. Horinek and C. Allolio for the fruitful collaborations and the opportunity to think outside the box.

Last, but certainly not least, I would like to thank all our past and current lab members for their help, advice and enjoyable coffee breaks whenever needed – it was great fun to be part of this fantastic team!

Thank you – Merci – 衷心感谢 – Dziękuję – Grazie – Ačiū – धन्यवाद् – Tusen takk – Dankschee!

The following figures have been created with BioRender.com and are published under academic subscription:

Figures 1 - 3

Figures 6 - 7

Figure 10

Figures12 – 13

Figure 17

Manuscript 1 – Graphical Abstract

Eigenständigkeitserklärung

Ich erkläre hiermit, dass ich die vorliegende Arbeit ohne unzulässige Hilfe Dritter und ohne Benutzung anderer als der angegebenen Hilfsmittel angefertigt habe. Die aus anderen Quellen direkt oder indirekt übernommenen Daten und Konzepte sind unter Angabe des Literaturzitats gekennzeichnet.

Weitere Personen waren an der inhaltlich-materiellen Herstellung der vorliegenden Arbeit nicht beteiligt. Insbesondere habe ich hierfür nicht die entgeltliche Hilfe eines Promotionsberaters oder anderer Personen in Anspruch genommen. Niemand hat von mir weder unmittelbar noch mittelbar geldwerte Leistungen für Arbeiten erhalten, die im Zusammenhang mit dem Inhalt der vorgelegten Dissertation stehen.

Die Arbeit wurde bisher weder im In- noch im Ausland in gleicher oder ähnlicher Form einer anderen Prüfungsbehörde vorgelegt.

Hainsacker, 2022

Veronika Heinz